ΠΑΝΕΠΙΣΤΗΜΙΟ ΚΡΗΤΗΣ
UNIVERSITY OF CRETE

Device Engineering of Organic and Organic-Inorganic Solar Cells

by

Miron Krassas

Department of Materials Science and Technology

University of Crete

Thesis submitted for the degree of

Doctor of Philosophy

Heraklion, Greece, June 2020

Acknowledgements

Abstract

Organic solar cells are consider a very promising technology among the third generation solar cells. A great tailback of the organic solar cell is the high binding energy of the exciton which is responsible for the samll exciton diffusion length. So the first two works are based on the incorporation of a third component in the photoactive layer in order to increase the number of dissociated exciton. The presence of the third component led to an increasement of the current and the enhancement of the PCE of the photovoltaic device.

In the second part, in collaboration with another group, the study of low band gap polymers is shown. The OPVs absorb in the visible light of the solar spectrum, leaving the near infrared unexploited. LBG polymers, although they have small efficiencies, can be added in the photoactive layer of the device and act as a second absorber. The result will be an increasement of the absorption spectrum further from the visible and into the infrared region, which will lead in an enhancement of the current and finally of the PCE of the device.

In the final part, the stability of two different polymer was studied, P3HT and PCDTBT, two very well-known polymers in world of OPVs. Both collaborations aimed to study the effect that polymer properties, device structure (inverted/conventional and buffer layers) and encapsulation procedure have to the device stability and lifetime, and used as guidance for the fabrication of stable OPVs based on those two polymers.

Preamble

Solution-processed bulk-heterojunction (BHJ) photovoltaics enjoys immense research. The careful selection of polymer donor and fullerene acceptor materials, having in mind the proper energy level matching and appropriate degree of phase separation inside the blend, has introduced additional degrees of freedom into OSC research and scientific advancement. Polymers, including P3HT and PTB7, as well as fullerene derivatives with most notable $PC_{61}BM$ and $PC_{71}BM$ have been under study for years while demonstrating exceptional efficiencies (>5%) for $P3HT:PC_{61}BM$ and above 7% for $PTB7:PC_{71}BM$ based devices. On the other hand, a very promising subfield of OSC research employs non-fullerene acceptors (NFAs) that yield state-of-the-art OSC cells with impressive efficiencies exceeding 17%. Many polymers have been prepared through alternating copolymerization of donor (D) and electron acceptor (A) units, thereby resulting in D–A pairs that effectively (a) exhibit multiple and complementary absorptions; and (b) enhance charge transfer ability.

Another effective, yet simple strategy to enhance the OSC's photovoltaic performance is the adoption of a ternary structure into a binary system. This can be secured with the integration into the active layer of a third component. This third element could be a polymer, an organic small molecule, a dye, a fullerene derivative, a graphene and a two dimensional (2D)-based material, or a nanocrystal. The introduction and the availability of materials to be leveraged as third element support the better engineering of this architecture towards better photovoltaic OSCs' performances. The third component within ternary organic solar cells (TOSCs) may function as a charge relay for electron and hole transport, as an energy transfer step, act as a second donor, as well as create a new organic blend with new physical characteristics in conjunction with the donor.

The objectives of this thesis, we tried to enhance the efficiency of an organic solar cell by incorporating a graphene derivative and a small molecule into the photoactive layer of an inverted organic solar cell. Our goal was to try and increase the efficiency of the reference organic photovoltaic device and study the mechanism behind this enhancement. The selection of those two material was due to the functionalized groups. Both materials have nitro compounds, which can absorb light in the visible region of the solar spectrum. In addition to that, the energy levels of each materials (HOMO and LUMO) are between the HOMO and LUMO levels of the donor and

acceptor, respectively, making them a good candidate in ternary OSC for better charge transfer between donor and acceptor.

In **Chapter 1**, an introduction on the solar energy will be made, following by talking for the photovoltaic devices and the materials, which are compatible for acting as an active layer, the semiconductors. Then the three main generations of photovoltaic device will be introduced: the 1st generation based on crystalline silicon, the 2nd based on amorphous silicon and on thin film technology and finally the third, where OSCs are classified, and their aim is to improve thin film technology.

In **Chapter 2**, a small introduction on the organic photovoltaics will be made with a discussion of graphene and graphene based materials and their role in photovoltaic technology. In **Chapter 3**, the technology of OSCs will be analysed, and more specific, the materials and their role, the structures and finally the ternary organic solar cells (TOSCs).

In **Chapter 4**, we will discuss the two basic characterizations, the J-V curve from with the efficiency of a photovoltaic device is given and the External Quantum Efficiency (EQE), and we will continue on the experimental procedure that we follow in the lab to fully fabricate an organic solar cell in **Chapter 5**.

Finally in **Chapter 6**, and more specific in **Chapter 6.1.1**, we fabricate a ternary OSC, using a small molecule as a third component, while in **Chapter 6.1.2** a graphene derivative added into the Donor:Acceptor blend. As mentioned earlier, those materials where chosen due their electrical properties (favourable energy levels) and led to increased performance of the TOSC compare to the binary device.

In section **6.2**, we study various low band gap polymers which are chemical functionalized to study the effect on photovoltaic performances, while in sections **6.3.1** and **6.3.2**, the stability of P3HT and PCDTBT polymer based OSCs studied to in various architectures.

Table of Contents

List of Abbreviations

AFM	Atomic Force Microscopy
Ag	Silver
Au	Gold
Al	Aluminium
AM	Air Mass
BHJ	Bulk heterojunction
CB	Conduction band
VB	Valence band
E_g	Energy Band Gap
GO	Graphene Oxide
rGO	Reduced Graphene Oxide
MPP	Maximum Power point
MoO_3	Molybdenum Trioxide
J-V	Current density - Voltage
PL	Photoluminescence
HOMO	Highest occupied molecular orbital
LUMO	Lowest unoccupied molecular orbital
OPVs	Organic Photovoltaics

OSCs	Organic Solar Cells
ITO	Indium tin oxide
P3HT	Poly(3-hexylthiophene-2,5-diyl)
PCDTBT	Poly[N-9-hepta-decanyl-2,7-carbazolealt-5,5-(4,7-di-2-thienyl-2,1,3-benzothiadiazole)]
PTB7	Poly[[4,8-bis[(2-ethylhexyl)oxy]benzo[1,2-b:4,5-b']dithiophene-2,6-diyl][3-fluoro-2-[(2- ethylhexyl)carbonyl]thieno[3,4-b]thiophenediyl]
$PC_{71}BM$	Phenyl-C71-butyric acid methyl ester
$PC_{61}BM$	PCBM Phenyl-C61-butyric acid methyl ester
PEDOT:PSS	Poly(3,4-ethylenedioxythiophene) poly(styrenesulfonate)
SCLC	Space-charge-limited current
TEM	Transmission electron microscopy
TiO_x	Titanium Sub-oxide
WF	Work Function
V_{oc}	Open circuit voltage
FF	Fill Factor
EQE	External Quantum Efficiency
PCE	Power Conversion Efficiency
HTL	Hole transporting layer
ETL	Electron transporting layer

J_{ph}	Photocurrent density
DIO	1,8-diiodooctane
LBG Polymer	Low bang gap polymer

Chapter 1. Introduction

1.1 Solar energy

When global warming and depletion of common energy sources, such as fossil fuels started threatening the balance of human life, great attention was given to the renewable energy sources. In those alternative energy sources where wind energy, hydroelectric energy, biomass, geothermal energy and solar energy are included, solar energy has the highest amount potentially available. It should be noted, that a very small amount of sun power is capable to cover the whole energy demand worldwide.

Solar power is a clean, green and promising energy source, which is under really big investigation. As well it is constituted of three different categories: inorganic, organic and hybrid (combination of organic and inorganic, e.g. perovskites) solar devices. The efficiency of solar power can be attributed to the Photovoltaic (PV) Effect, a physical process where the semiconductor material converts electromagnetic radiation (sunlight) into Electrical Power. PV effect was first discovered by Becquerel in 1839.

The still unreachable goal of all research groups worldwide is to construct a solar cell which would be power efficient and stable, low cost manufactured and long living (lifetime). Those three parameters (efficiency, cost, lifetime) are who characterize and classify every solar device and all three of them are equally important for an efficient solar device.

The photovoltaic phenomenon was discovered from Alexandre-Edmond Becquerel[1,2], a French physicist in 1839. It took 42 years for the first photovoltaic device to appear, an event that triggered the inception of research in a field that nowadays can provide pollutant free energy and ecological solutions. Since that first device, the evolution road of the photovoltaic technology is parted in three generations.

The first generation (1G) solar cells are large scale, single junction devices. Most of the production is based on silicon wafers including single crystal and multi-crystalline silicon. About 90 % of the current photovoltaic production is based on first generation. The efficiency of the single junction cells has a theoretical limit of about 30% (the Shockley–Queisser limit)[3,4] and

currently the common silicon wafer based devices show nearly 20% efficiency with the highest reported efficiencies reaching 25 %[5]. Yet, the cost per produced Watt is nearly 4 times higher than conventional energy sources' prices due to the material's used high cost (half of the cost of 1G devices is the silicon wafer) and high manufacturing & processing expenses. Although, the cost lowers along with the progress of the technology, the 1G products will probably reach their price limit before achieving the competitive level in the market.

The second generation (2G) solar cells are addressing the cost issue and the primary task is to decrease the amount of expensive material used in the production process while keeping the efficiency of the device high. The foremost approach is producing thin film solar cells on low cost substrates (such as glass and flexible substrates such as PET). Different techniques are utilized for production process such as solution deposition, vapor deposition, electroplating and etc. Most successful materials for 2G are amorphous silicon, $CuIn(Ga)Se_2$ (CIGS), CdTe/CdS, which are being deposited on thin substrates. Devices based on these materials can deliver lab efficiencies up to 19 %, but the module efficiencies are reaching only 14 % due to difficulties in producing large-scale uniform films[7]. Although thin film technology can significantly decrease the PVs fabrication budget, 2G solar cells will be constrained by certain cost ceilings per watt due to efficiency limits and the material costs.

The third generation (3G): The alternative way to get the cost down is to increase the efficiency by multiple stacking (sandwich) of solar cells. 3G solar cells introduce the idea of multi junction solar cells, which can significantly increase the device efficiency via improvement in harvesting of photons and even overcome the theoretical limit of 30 %. Currently the highest efficiencies reported for multi-junction solar cells are over 33 %[5]. In addition, 3G utilizes completely new concepts in terms of device architectures and materials. As an example, three typical approaches of photovoltaics are Dye – Sensitized Solar Cells (DSSCs)[6,7], Perovskite Solar Cells (PeSCs) and Organic Photovoltaics (OPVs). DSSCs are based on combination of dyes with metal oxides and electrolyte. The efficiencies of DSSC are in the range of 12 % for small lab scale devices, while the lifetime of the devices is rather low compared to inorganic solar cells.

Similar to the sensitization in DSSCs, in PeSCs the perovskite material is coated onto a charge-conducting mesoporous scaffold most commonly TiO_2 – as light-absorber. The efficiencies of

PeSCs have already exceeding more than 20% and their future promises to be bright. On the other hand OPV technology in based on organic compounds such as conjugated polymers and fullerenes blended together forming heterojunctions in the nanoscale. The OPVs record certified performance has overcome the level of 17.1% using simple deposition techniques and low cost fabrication materials.
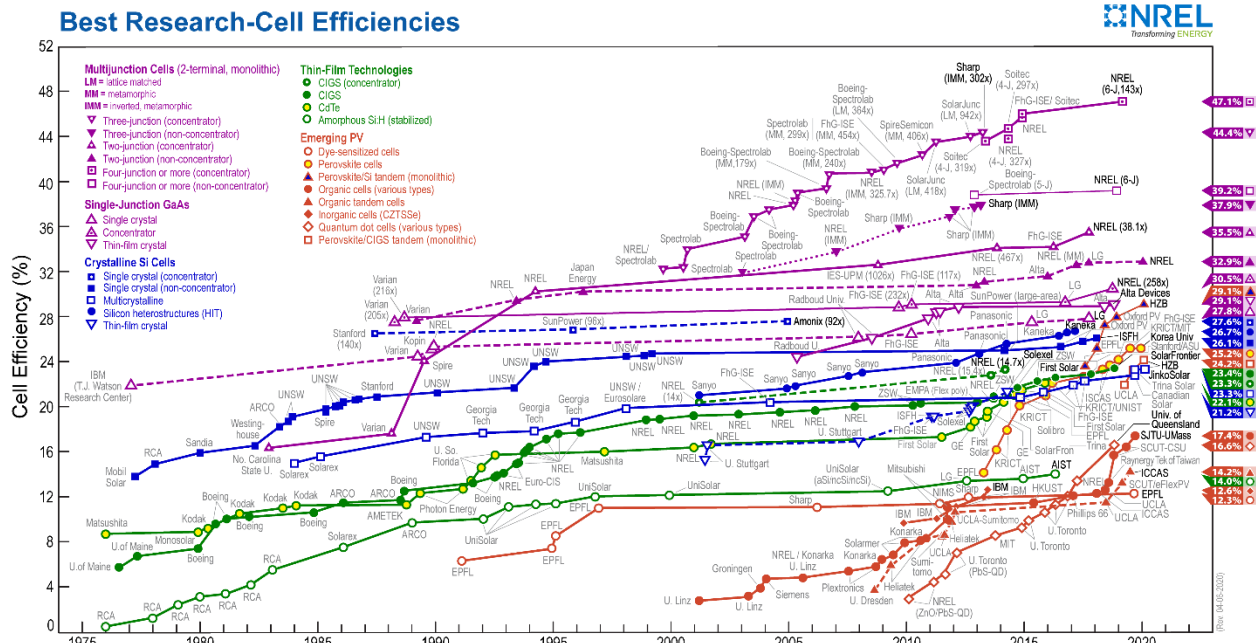
Figure 1. Best research-cell efficiencies for several technologies presented by the National Renewable Energy Laboratory. [8]

1.2 The heart of photovoltaic devices: Semiconductors

To understand what makes a material possible for photovoltaics applications, we first should talk about the energy band gap.

When atoms combine to form a molecule or a solid (in the case of photovoltaics a crystal), their atomic orbitals combine to form new orbitals (molecular) with energy levels separated from the primarily orbitals. In case of a solid, the energy of those new orbitals is so close, which is defined as an energy band. Now, these bands may or not overlap and this is due to the energy distribution, which is a reflection of the electronic properties of the atoms. The occupation of these bands

depend on the original occupation of the molecular orbitals. If the VB and the CB overlap the solid is a metal, if the two band are separated in energy the solid is a semiconductor or an insulator if the gap is large. See sketch in figure 2.
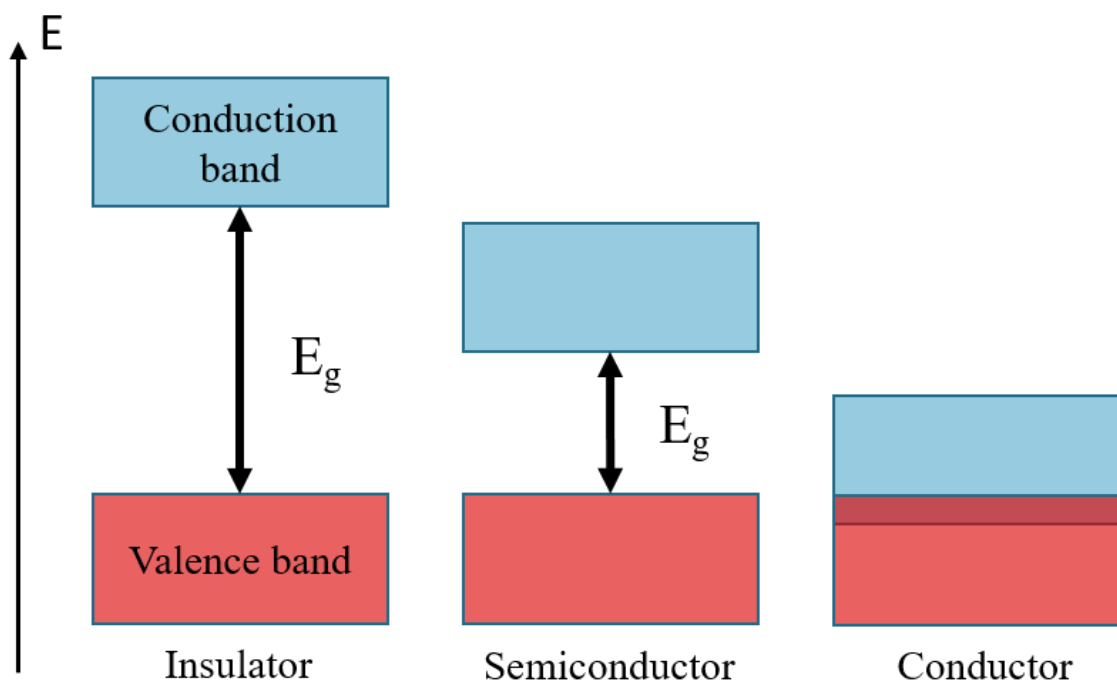
Figure 2. Nature of the band structure for a metal and a semiconductor.

The separation in energy (eV) between the two bands determine the type of material: metals – 0 eV, semimetals - less than 0.5 eV, semiconductors - between 0.5 and 3 eV, insulator more than 3 eV. When an electron is excited from the VB to the CB, an electron vacancy remains in the VB. This vacancy is usually filled by an electron in the VB and in the vicinity of this vacancy. Thus the vacancy is moving to the neighbour site. In the presence of an electric field this process can be repeated, resulting in a current represented by the movement of the vacancy in the opposite direction to the excited electron. Since this vacancy results from a lack of negative charge (missing one electron), the relative current can be described as the current of positive holes in the VB. The electron and the relative hole are charges with opposite signs. Usually these two charges are considered independent one from the other, however in some conditions they can be interacting.

In this particular conditions the Coulomb interaction, which is manifested between charges with opposite sign, bind the electron and the holes in a unique state called an exciton. These excitons can be either stationary or mobile within the material. They result in a series of intra-band gap states slightly above the VB and below the CB. Although excitonic states are not relevant for electrons and holes in isolation, they are important for the optical properties of semiconductors.

The materials for photovoltaic devices should have a band gap between the lowest unoccupied molecular orbital (LUMO) and the highest occupied molecular orbital (HOMO) in order to absorb the energy from the sun. All materials, semiconducting and insulating, have a band gap, but only semiconductors have the required bad gap to absorb the visible spectrum of the solar radiation.[9] In case of insulators, the energy band gap is too great. In the other case, metals have zero band gap and the electron don't have the time to be collected after their excitation. When a semiconductor has the right energy difference between the HOMO and LUMO, an electron is excited it quickly decays to the minimum energy of the conduction band (CB), this process takes few femtoseconds.[10] Then the recombination to the valence band (VB) occurs with a slower mechanism which takes several microseconds, giving enough time to the solar cell to extract the electron (these processes take place in the typical solid semiconductor materials) (figure 3.)
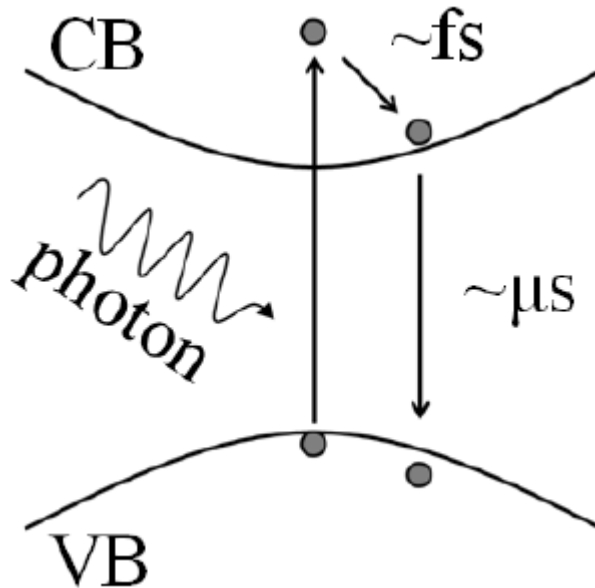
Figure 3. Excitation mechanism of an electron from the valence band (VB) to the conduction band (CB) by the absorption of a photon.[11]

1.3 Third generation photovoltaics: Organic solar cells

The absorption of the visible light and the generation of free charges are two of the three main processes of the solar cell. The third is to transport those charges into current. To achieve that, a solar cell needs an asymmetry in order to drive holes and electrons in opposite directions.

The classic model of a solar cell is the p-n junction. The semiconductor consists of a p and n type semiconductors, in which the Fermi level E_F is near the valence band edge in the p-type material and near the conduction band edge in the n-type material. When the two regions are joined together, the electrons in n-type region and holes in p-type region diffuse across the junction. These electrons and holes recombine with each other, leading to the formation of the depletion region (W), as shown in Figure 4 (c), which is depleted of mobile carriers. The internal (built-in) potential is formed as the result of the Fermi energy difference between the n- and p-type regions, as shown in Figure 4 (b). In thermodynamic equilibrium, the Fermi level of a p-n junction will be constant across the junction, which necessitates band bending through the junction (Figure 4).

Figure 4. The energy alignment for a p-n junction.[12]

The way in which the junction is realized usually characterize the type of solar cell. Third generation solar cells use a variation of the Fermi level to generate an internal electric field (the built-in field) that drives the carriers in opposi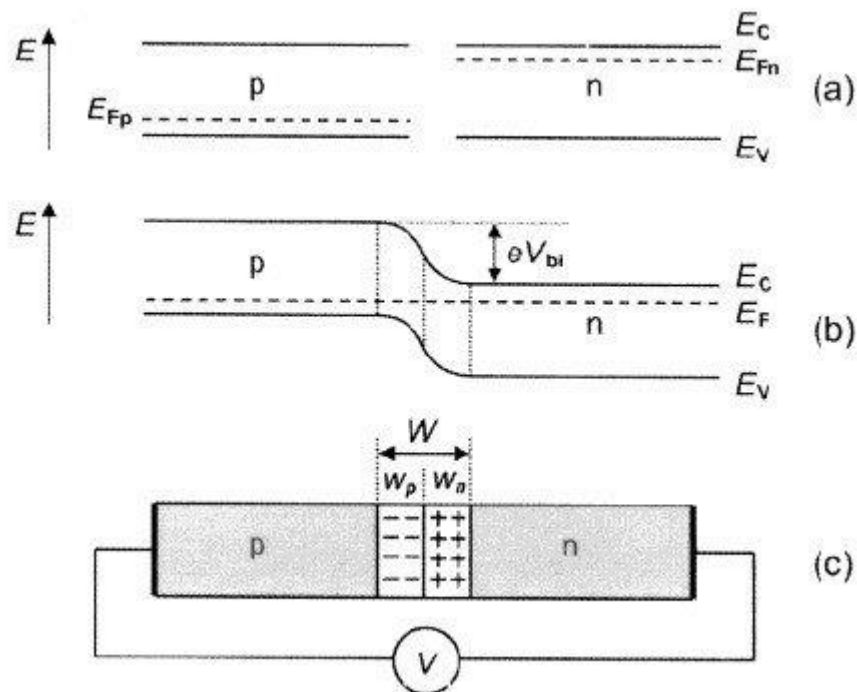te directions. This field is generated by a potential step at the interfaces between the light absorption layer and two optimized material called extraction layers. This results in the bending of the VB and CB of the absorber across the interfaces with the two extracting layers in a similar way of what happen in the p-n junction. Now, when the device is illuminated the electrons and holes are separated by the built-in field and are transported to the opposite sides. This configuration differs from the classic p-n junction and is defined as pi-n junction, where an intrinsic semiconductor layer (the i-type i.e. the photoactive material) is sandwiched between two layers intentionally doped to be p-type or n-type. The p layer presents a deep Fermi level and is responsible for the extraction of holes, the n layer on the opposite side presents a higher Fermi level and is responsible for the extraction of electrons. The built-in field generated by the p and n zones extends the electric field over the intrinsic semiconductor. Carriers that are photo generated in the i region are then driven through the electric field to the respective contacts. The band profile for an ideal p-i-n junction are reported in Figure 5.
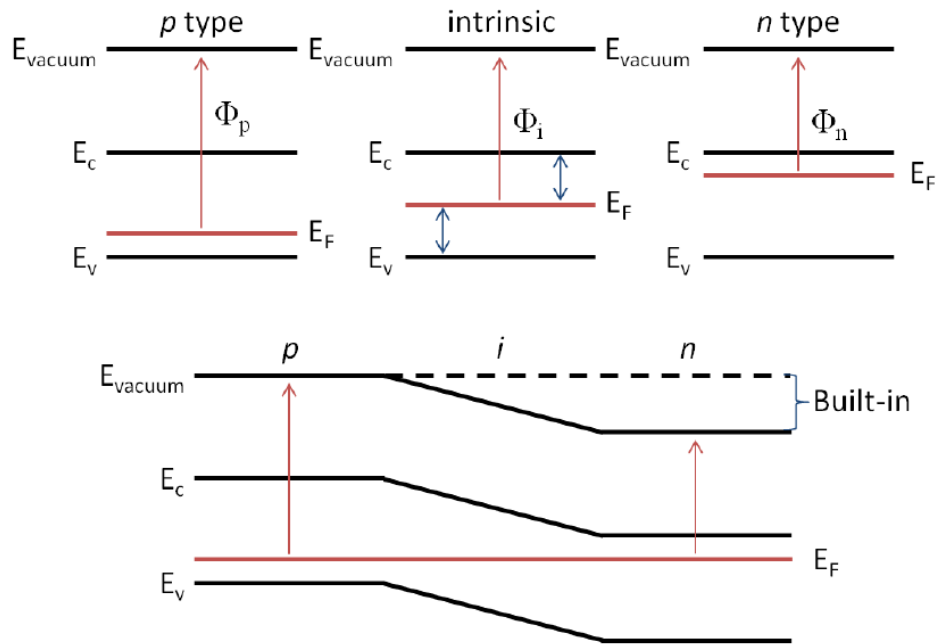
Figure 5. Band profile of a p, i and n-type semiconductors is isolation (top panel) and closed together in a p-i-n junction (bottom panel). E_F is the Fermi level, E_C, E_V the conduction and the valence band respectively while Φ represent the work function of the semiconductors.[13]

One of the most important advantages of p-i-n junction solar cells is their simple structure. Almost all of these solar cells are comprised from five components: the active material, two selective interlayers and two electrodes (the top and the bottom).

a)   The active layer, which is where the light is been absorbed leading to the excitation of an electron and the creating of the exciton.

b)   The hole transport layer. A materials with VB close to VB of the active layer, helping the transport of the holes and blocking the electrons.

c)   The electron transport layer. Has the same work as the hole transport layer, but favors the electrons and blocks the holes. The CB of the material is close to the CB of the active layer.

d)   Finally, the electrodes sandwiching all the above layers and connects the solar cell to the external circuit.

Chapter 2. Organic Solar Cells

OSCs are photovoltaics, in which the photoactive layer is based on organic semiconductors such as polymers and/or small molecules. With the ability to be tuned very easy, organic semiconductors can provide unlimited combinations of new semiconductors with different absorption spectrum and electronic properties. In addition, the ability to be used in low temperatures gives the advantage to be deposited on a large scale substrates, not only rigid but also flexible.

The first OSC was developed in 1960s and consisted by two electrodes sandwiching an organic layer, with low efficiency (<1%).[14] The first OSC with efficiencies around 1% was developed by Tang et al. in 1986 and was consisted by two organic layers, one with a p-type and one with an n-type organic semiconductor.[15] Then the concept of the bulk heterojunction (BHJ) was proposed, which led to efficiencies close to 4% for the evaporated OSCs and up to 3% for the BHJ OSCs (figure 6).[16,17,18]
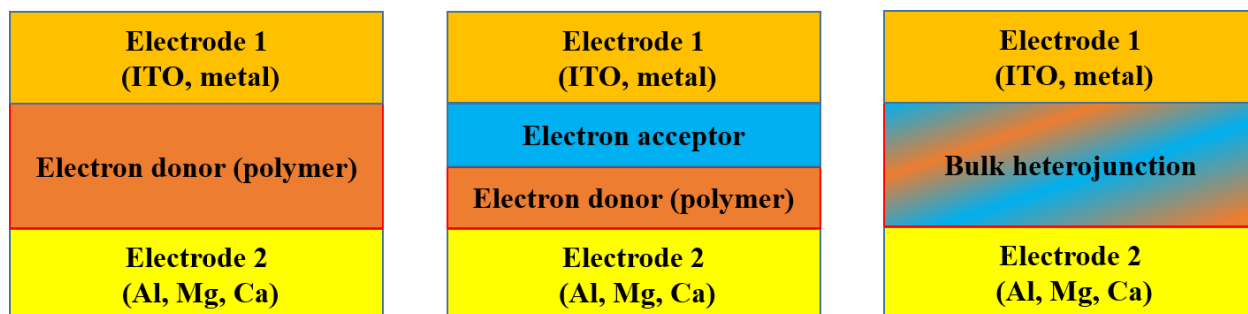
Figure 6. Evolution of OSCs from monolayer (left), bilayer (center) and BHJ (right).

The current state of the art single junction OSCs demonstrate PCEs of ~16%[19] which is close to the theoretical limit of this technology due to the fundamental limitations mainly of the photoactive materials, preventing in this way this technology from market implementation. Particularly, the high exciton binding energy, the low exciton diffusion length, the low required thickness, the relatively narrow absorption bandwidth and the high electronic disorder of the active layer materials result in low photon harvesting and voltage output thus low power generation. One

promising approach for overcoming these limitations is: a) the utilization of plasmonic metal nanoparticles and b) the ternary concept with two-dimensional (2D) layered materials.

2.1 Graphene and Graphene derivatives in photovoltaics

Graphene was first isolated from A. Novoselov and A. K. Geima at 2004[20]. From then, graphene related materials (GRMs) became the new promising materials for both the fundamental and applied physics due to their extraordinary properties[21,22,23]. GRMs can be produced with low-cost procedures, are easily processed in low temperatures and have easily tuned properties, both electrical and optical, through doping with heteroatoms and are compatible with flexible substrates and printing electronics applications. The most explored graphene derivatives are the graphene oxide (GO), reduced graphene oxide (rGO) and graphene quantum dots (GQDs), as charge carrier transporter, transparent electrodes and electron acceptor materials and all of the above arise from the unique propertied of the graphene. This 2d atomic thick material has high electron mobility ($\sim 20000 cm^2 V^{-1} s^{-1}$), large theoretical surface area ($2630 m^2 g^{-1}$), excellent thermal conductivity ($5000 Wm^{-1} K^{-1}$) and it is very light[24]. There are several chemical and physical ways to obtained graphene, those who are also with photovoltaic technologies are chemical vapor deposition[25], chemical[26], thermal reduction of GO[27] and chemical exfoliation of graphite[28,29]. Depending on the procedure, the quality of the graphene can be altered, which can affect its physical electrical and optical properties. The most common technique employed in laboratories is also the technique used to obtained rGO. This method starts from the synthesis of graphite oxide by the modified Hummers method[30], which is a chemical process that employs the oxidation of graphite in presence of strong oxidants in acidic media. When graphite is treated with a mixture of potassium permanganate, sulfuric acid and sodium nitrate, graphite oxide is formed, a compound made up of carbon, hydrogen and oxygen molecules. The increase in spacing between the sheets weakens the interactions between them, which facilitates the exfoliation of graphite oxide into graphene oxide (GO) upon sonication[31]. Subsequently, the graphene oxide can be reduced into rGO (reduced graphene oxide), in which the most common treatments used are the hydrazine hydrate reduction and thermal annealing.
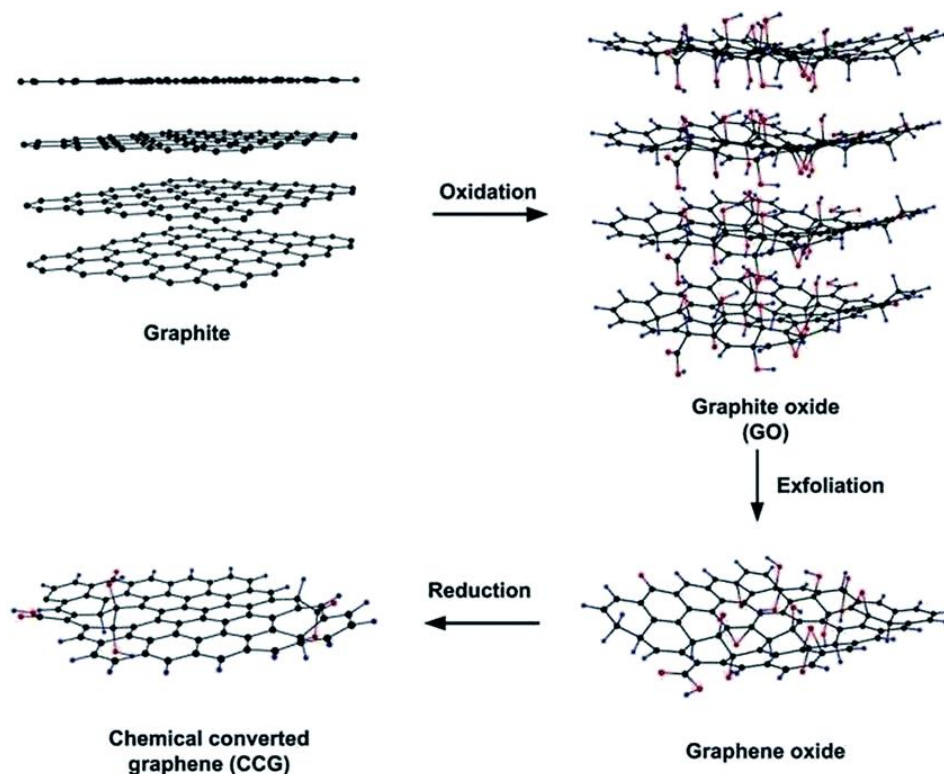
Figure 7. rGO synthesis[32]

The chemical process for obtaining GO and further rGO also requires several washing steps prior to the exfoliation, in order to remove oxidizing agents and impurities added during the modified Hummers method. It is noteworthy that the process of reduction of GO into rGO partly restores the structure and properties of a single graphene.

The final material usually brings many defects including residual oxygen groups and vacancies after the removal of functional groups, as shown in Figure 8. The reduction of GO is intended to remove the oxygen-containing groups, but it is also aimed to restore the π-conjugated network of the graphene. In addition, one must consider that the oxygen remaining groups in rGO affect its electrical conductivity, which is not the same as that of a perfect single layer of graphene. In the last years, many groups have reported the use of graphene as transparent bottom or top electrodes, hole transporting materials, electron transporting materials, charge extraction interlayers and active layer materials/components[33,34]. Recently, many carbon materials have been derived from graphene such as hydrogenated graphene (graphane), fluorinated graphene (fluorographene), and

graphene introduced by acetylenic chains (graphyne and graphdiyne). These materials are known as graphene derivatives[35]. The work function of graphene and its derivatives can be broadly tuned by doping in order to minimize the sheet resistance of graphene (or graphene oxide) films and to match the work function of these derivatives with the HOMO (VB) and LUMO (CB) level of many photoactive materials, minimizing the potential barriers at interfaces. The work function engineering is necessary to improve the device's performance and in the case of graphene and its derivatives, this can be modulated by controlling the doping level and oxygen content.

Chapter 3. Fundamental and theoretical principles

3.1 Organic semiconductor materials

In organic semiconductors materials are classified the conjugated polymers. They consists of a linear chain of carbons with alternative single and double bonds along the polymer backbone. Nowadays, conjugated polymers are used in different electronic applications, such us transistors, photodiodes, solar cells, etc. The result of the alternative bonding in those polymers is the conductive and semi-conductive behavior (Figure 8).
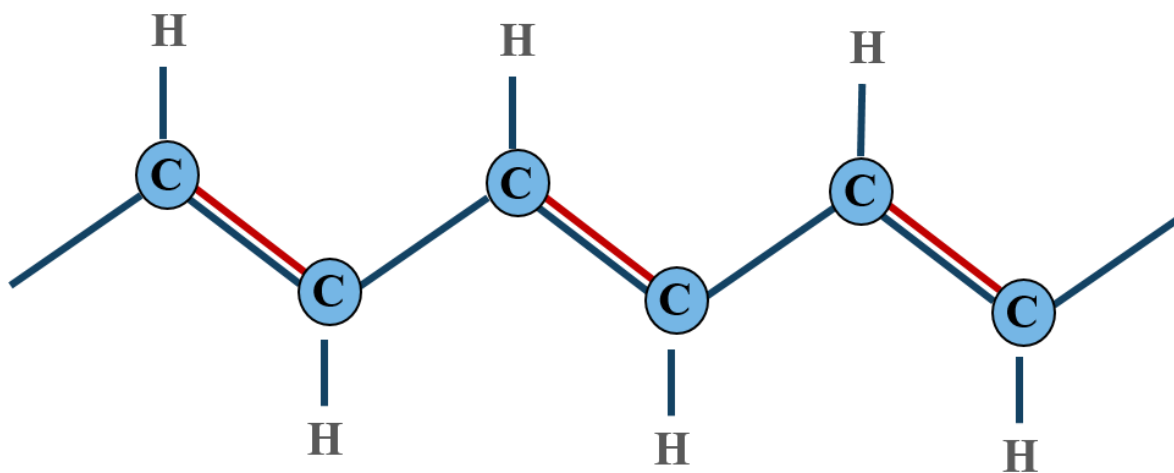
Figure 8. Linear polymer chain with alternative single and double bonds between the carbon atoms.

A single carbon atom, in the ground state, has 2 electrons in the 2s orbital and 2 in the 2p orbital. In conjugated polymers, the carbon atoms are sp^2 hybridized, where the 2s orbital are hybridized with two 2p orbitals ($2p_x$, $2p_y$), giving rise to three sp^2 orbitals and one 2p unhybridized orbital ($2p_z$). The carbon atoms can now form 2 types of bonds, the σ-bond, which is formed by the overlap of the hybridized orbitals of the adjacent atoms which are oriented along the chain. So, there are three coplanar sp^2 hybridized orbitals which are at an angle of 120° with each other. Therefore, three σ bonds are formed, two with neighbour carbon atoms and one with a hydrogen atom. The

p_z orbitals, occupied by one electron each, overlap with each other, to form bonds perpendicular to chain (Figure 9). The electrons of the p_z orbitals are delocalized through the entire length of polymer chain, which is the reason for the conductive properties of the conjugated polymers.

The set of orbitals $sp^2 + p$

Sigma (σ) bond

Overlap of p orbitals leading to pi (π) bond
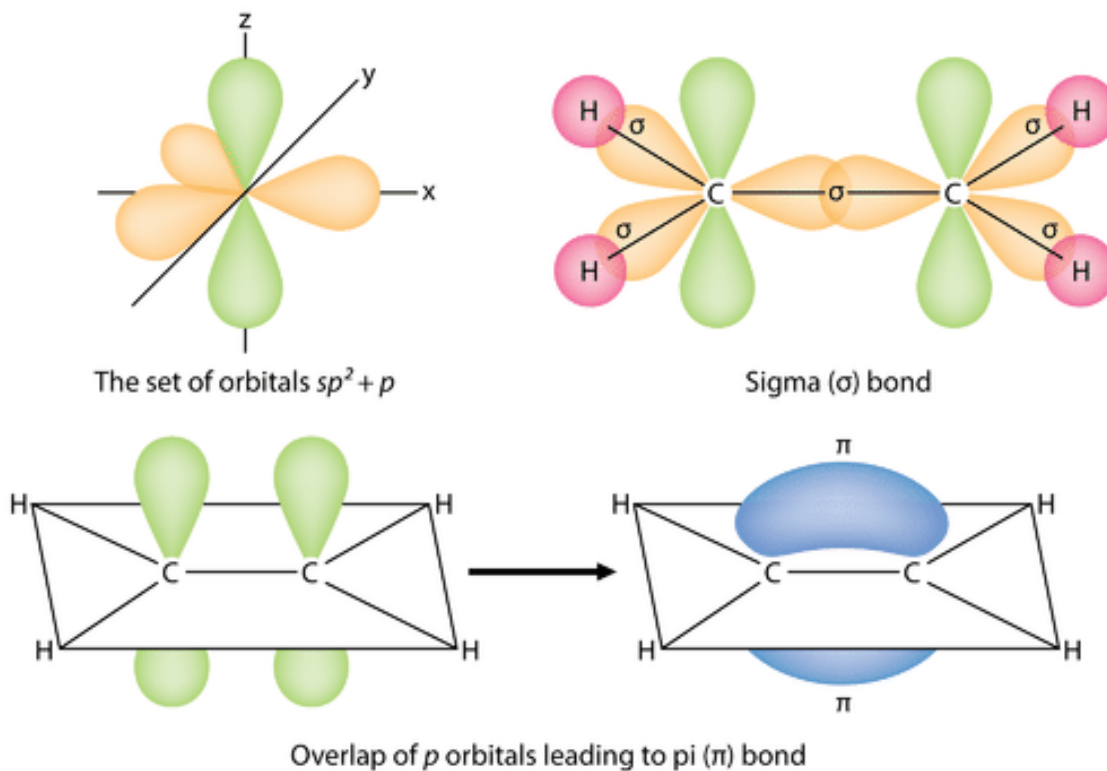
Figure 9. Chemical structure and schematic drawing of ethylene.[36]

The overlap of pz orbitals forms two molecular orbitals, a bonding π-orbital which is the highest occupied molecular orbital (HOMO) and an antibonding π*- orbital which is the lowest unoccupied orbital (LUMO). The π-orbital and π*- orbital are equivalent to the valence band and conduction band of an inorganic semiconductor, respectively. The difference between the HOMO and LUMO is called the band gap of the organic material. The optical and electrical properties of an organic material are determined by the band gap. The gap is reduced when the polymer chain is longer[37].
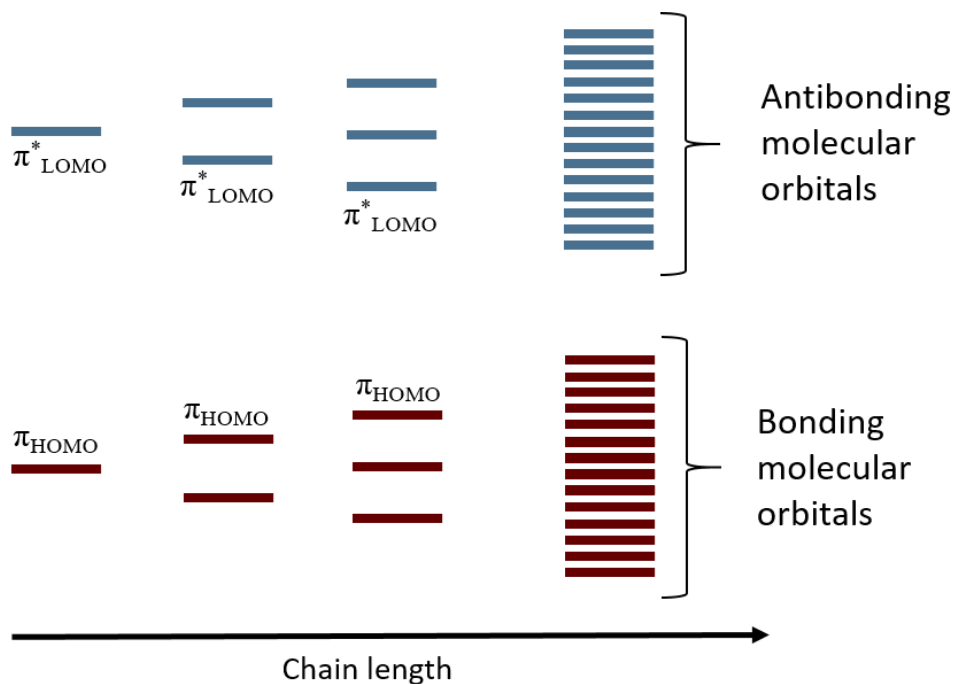
Figure 10. The polyene series with decreasing bandgaps and increasing wavelength.

3.2 Excitons in organic semiconductors

Excitons are well known in the fields of molecular crystals and inorganic semiconductors. In molecular crystals, excitons are bound electron-hole paird localized in one molecular unity (Frenkel or molecular excitond). In the field of inorganic semiconductors, excitons can be considered as electron-hole pairs, which are bound by Coulomb forces (Wannier-Mott excitons). They are electrically neutral and one characteristic is the electric dipole moment. When a photon of light interacts with an electron in the ground state, when the energy of the photon is appropriate, the electron is excited from the HOMO level (in the valence band) to the LUMO level (in the conduction bad) (π-π* transition), leaving behind an empty spot with a positive charge known as a hole. However, the resulting electron and hole are still bound, and their motion through the material is coupled[38], where the exciton extends over a few adjacent molecular units, can be called the charge-transfer exciton. Also, the terms "inter-chain" and "intra-chain" exciton are used for

polymeric semiconductors to indicate that the constituent charges are located on different or on the same polymer chains respectively.

The exciton binding energy of conjugated polymers depends strongly on their structure[39]. For highly crystalline polydiacetylene, the binding energy has been determined to be 0.5 eV, while for amorphous polymers like the polythiophene and PPV, is about 0.4 eV.[40,41]

3.3 Organic solar cells device structures

The structure of an organic solar cell is different from the one of a silicon device. The photoactive layer of the OSC is a blend between a conjugated polymer, acting as an electron donor (light absorbing material mostly in the visible spectrum) and an electron acceptor, such as fullerene (materials with higher electronegativity than the polymer donor). The active layer is placed between two electrodes with proper work function (Figure 12).
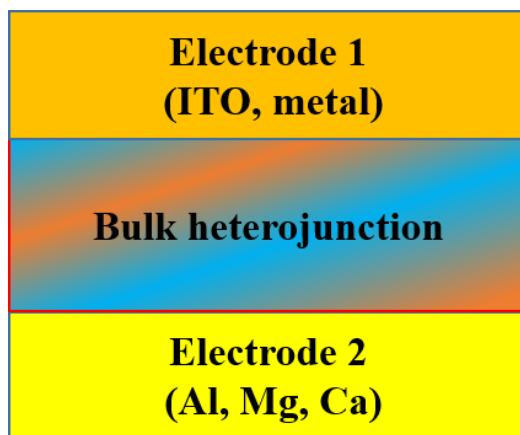
Figure 11. Device structure of OSC.

The whole device is built on a transparent substrate such as glass or PET (polyethylene terephthalate). The anode is a semi-transparent material like indium tin oxide (ITO) because it allows the light to pass through and absorbed by the active layer but also can collect the holes from the device. The cathode has role of an electron collective electrode. Aluminium is the most

common material, although silver and copper are sometimes used instead of aluminium and they deposited through thermal evaporation.

Through the years, the structure has undergone many modifications in order to achieve higher efficiencies. First, a layer of a p-type conductive polymer (usually 3,4-ethylenedioxy-thiophene)-poly (styrenesulfonate) (PEDOT:PSS) is applied between the anode and the photoactive layer. Its HOMO level should be well aligned with the HOMO level of the polymer donor. PEDOT:PSS is deposited through spin coating on top of the anode. This serves not only as a hole transport layer (HTL) but also as a blocking electron layer (EBL). In addition, it smooths the ITO surface, seals the active layer from the oxygen and prevents the diffusion of the anode material in the active layer, which can lead to trap sites[42]. Then, a solution consisting from the electron donor and acceptor is spin coated on top of the HTL. Above the active layer and before the cathode, an n-type material with wide band gap is been deposited, such as titanium dioxide (TiO_2) or zinc oxide (ZnO). The role of this layer is the facilitation of the electrons extraction from the active layer to the metal cathode and for this purpose its conduction band position should be well aligned with the LUMO level of the acceptor material.
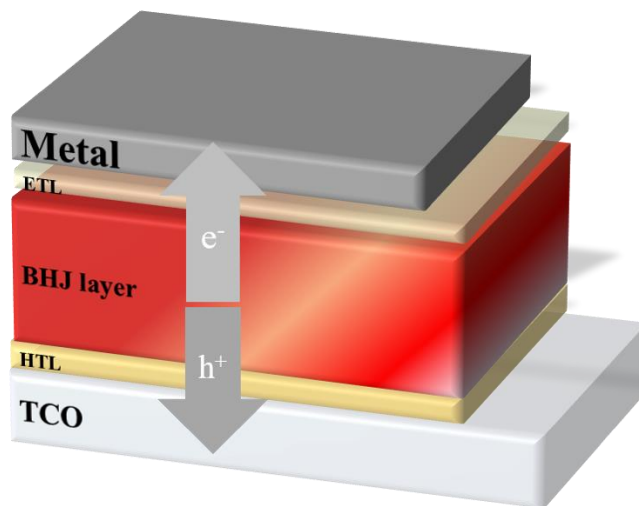
Figure 12. Schematic diagram for OPV device structure. Electron transporting layer (ETL) and hole extracting layer (HTL) is adopted to form Ohmic contact and extract charges at cathode and anode respectively. The arrows indicate the direction of electron and hole transport.[43]

3.4 Operation Principles

Due to the crystalline nature of silicon, generation and separation of charge carriers requires only a small force of interaction. Therefore, absorption in silicon leads to effectively free charge carriers. As a result of the low dielectric constant (≈3) in semiconducting polymer materials, the columbic forces of attraction between electrons and holes are very high[44,45]. This means that in organic semiconductors the excitation of the electron forms a bund pair of electron hole, in contrast to the inorganic semiconductors, in which the excitation of the electron forms a free electron and hole. In organics, a driving force is needed to break the bond between the electron and the hole. So the excitons formed in the donor material, can dissociate in the interface with the acceptor. The force required to break the exciton binding energy is provided by the energy difference between the LUMO levels between the two materials at the interface.
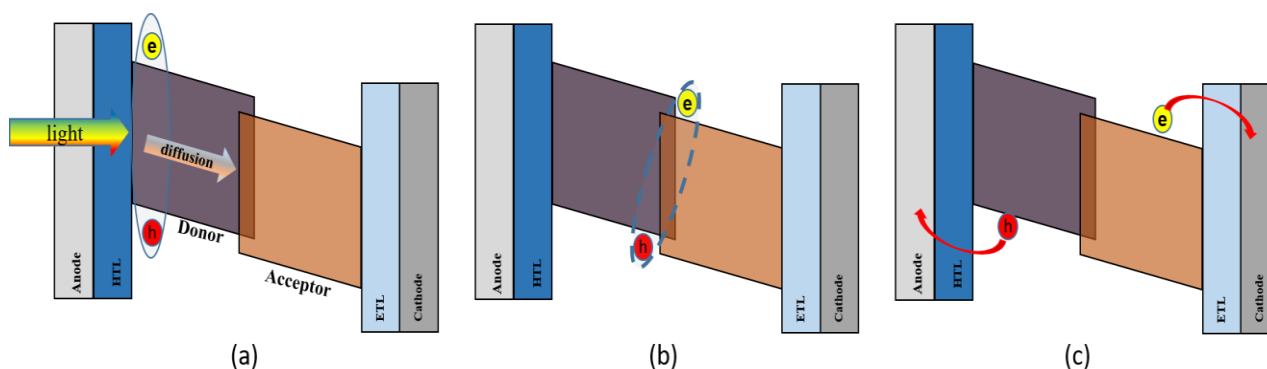
Figure 13. The energy diagram of typical organic solar cell and different stages of the photocurrent generation process (a) exciton generation, (b) charge transfer state dissociation, (c) charge transport and extraction.

In figure 13, the energy band diagram of organic solar cells is shown. This energy offset used to dissociate excitons is illustrated as ΔE_{LUMO}, which is the excited state energy offset. In order to dissociate excitons formed in the acceptor material, the energy offset of the highest occupied molecular orbital (HOMO) of the acceptor and the HOMO of the donor material is required. Excitonic dissociation due to these energy offsets occurs at the interface between the donor and acceptor phase, therefore, the arrangement of the two materials in the active layer is crucial for the

28

successful operation of the device. After the separation, the electron can be transferred to the acceptor material and from there to the cathode. From the other hand, the hole travels through the polymer and from it's been collected to the anode electrode. The same phenomenon can be occurred and in the acceptor material. There the exciton dissociates due to the energy offset of the HOMO levels between the donor and the acceptor.

The length that those electrons can travel before the electron recombine with the hole is around 10 nm[46,47,48]. Due to this small length, in bilayer organic solar cells have very poor electronic response. An approach to deal with this problem is to disperse the two materials (donor and acceptor), creating a blend and increasing the interfacial area. It is known as the bulk heterojunction structure[49]. Figure 14 displays a cross sectional illustration of both a bi-layer and BHJ device structure. Devices, based on the BHJ structure, have a large dispersion of interfaces throughout the photoactive layer, which requires smaller exciton diffusion length and achieves greater exciton dissociation yield. There exists a trade-off between increasing interfacial area via the intimate dispersion of phases and the creation of efficient conductive pathways through which free electrons and holes may be transported. The arrangement of donor and acceptor phase is thus crucial to device performance.

Bilayer Structure   **Bulk Heterojunction**

Acceptor-fullerene material
Donor-polymer material
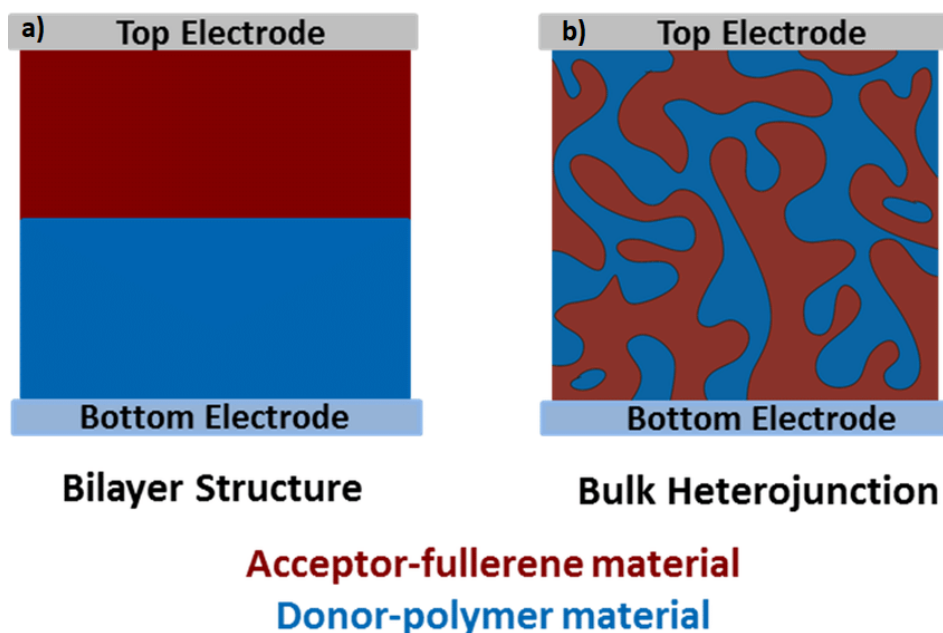
Figure 14. Schematic diagrams of (a) bi-layer heterojunction and (b) bulk heterojunction photoactive layers[50].

3.5 Ternary Organic Photovoltaics

The past decade, OPVs based on BHJ technology have achieved efficiencies greater than 15%[51,52,53,54,55,56,57]. Despite this achievement, there are still some drawbacks that could be tackled such as include a) demonstration of not intense and of spectrally narrow absorption organic semiconductor materials[58], b) excessive energy loss at donor / acceptor interfaces and limited charge transfer[59] due to energy level misalignment larger than 0.4 eV within the active layer[60], c) charge transport pathways between the donor and acceptor building blocks need significant improvement, d) Schottky contact formed between the active layer and interlayers[61] limit the efficient photogenerated charge collection and e) binary blend morphology stability issues under prolonged and continuous illumination conditionsby[62]. By introducing a third component inside the blend donor-acceptor, it addresses the majority of the binary blend devices deficiencies[63]. Depending on the physical and electrical properties of the third component, it can a) increase the intensity and/or extend the absorption spectrum of the photovoltaic device, b) enhance the charge pathways at the interface donor:acceptor, c) provide more efficient exciton dissociation pathways at the interfaces with the donor material, balance the bipolar mobility within the active layer, e) increase the crystallinity of the donor material, f) enhance the energy transfer from the donor material and g) employ the same simple fabrication techniques of the ones used in the binary devices[64].
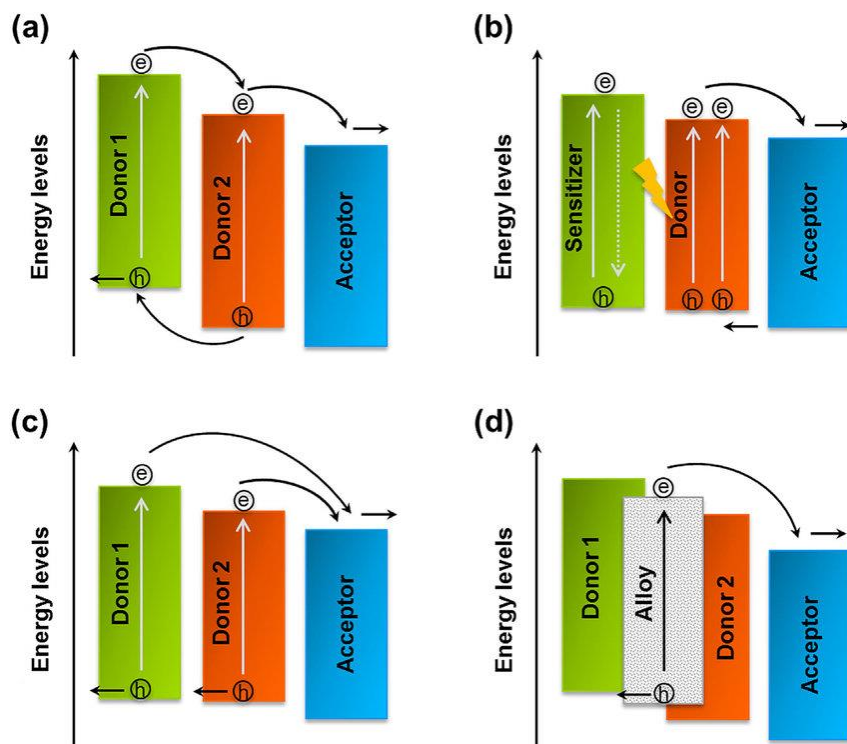
Figure 15. Schematic of the working mechanisms in ternary organic solar cells. a) The charge transfer mechanism. The additional donor functions as a charge relay for charge transport. b) The energy transfer mechanism. The photoexcited sensitizer transfers its energy to the host donor. c) The parallel-like mechanism. The additional donor forms its own independent hole-transport network. d) The alloy model. The additional and host donors electronically coupled into a new charge transfer state. The arrows indicate the possible charge charrier transfer and transport pathway[65].

The third additive in the active layer can act as a) a second donor[66], b) a second acceptor[67] and c) a non-volatile additive[68]. Figure 15 shows the four fundamental mechanisms, which can take place in ternary device depending on the physical and electrical properties of the third component, and include a) charge transfer, b) energy transfer, c) parallel like mechanism and d) alloyed structure between donor and the third component.

In the first mechanism, the role of the third component is the effective charge transfer from the donor and it's crucial for the charge collection in the respective electrodes. The properties of the additive component such us energy alignment between the donor and the acceptor and the morphological characteristics in the interfaces play an important role for the efficient charge

collection. The outcome is higher J_{SC}, V_{OC}, FF and PCE compare to the binary device. The HOMO and LUMO energy levels of the third component must be aligned between those of the donor and acceptor, as shown in Figure 16a, in order to cause high exciton dissociation and charge transfer[69].

In the second mechanism, the additive component act as a competitor to the charge transfer process[70]. Substantial overlapping between the absorption spectrum (of the low bandgap material) of one material with the emission spectrum (of the high bandgap material) of the other is desirable for the most efficient energy transfer. Thus, the ternary element, can function as "energy donor" or as "energy acceptor" within the active layer of a ternary OSC (figure 16b – energy acceptor case). Whenever the ternary element operates as 'energy donor', the holes are formed in the dominant donor material and the ternary element acts as energy absorber[71]. The energy donor should be in proximity with the energy acceptor material due to the rapid energy decay rate with the distance. In the case the third element operates as "energy acceptor", it should be distanced from the "energy donor" material and simultaneously in contact with the donor or acceptor to facilitate the excitons dissociation created by the energy transfer. The efficiency of the energy transfer between the donor to acceptor is mainly determined by how much the excited state lifetime of the energy donor is reduced by the presence of the energy acceptor material. The photogenerated excitons are dissociated at the interface of the low band gap material (energy acceptor) with the acceptor.

In the parallel like model, the third component doesn't need to align with the components of the active layer. The third component can act as a second donor or as a second acceptor. In the case of a second donor, excitons are generated in each donor and dissociates in the interfaces with the acceptor, respectively. The holes then transferred through the donor pathways and the electrons through the acceptor channels. In the case with two acceptors, the excitons will dissociate in the interfaces with either acceptor one or acceptor two. Again, the holes will be transferred through the donor pathways and the electrons through acceptor channels, regardless if those channels belongs to acceptor one or two.

In the last case, the third component creates an alloy with the donor or the acceptor, depending on the electrical properties (third composite act as a donor or as an acceptor). In both case, V_{OC}

changes due to the new energy levels of the alloy and the J_{SC} increases due to the complementary absorption spectra of the components of the ternary device active layer.

In all the above mechanisms, the third composite is selected based on its optical, electrical and physical properties, but is also crucial to be able to be used in large scale techniques and has a balanced between fabrication cost and efficiency of the photovoltaic device.

Chapter 4. Characteristics of a PV device

4.1 J-V characteristics

In this section it is going to be presented the characterization parameters that affect the quality of an OSC device. Any inference taken from those parameters could show the possible mistake be made during the experimental procedure or a new clue/discovery. There are some standard parameters that have to be calculated after the experiment as, short circuit current, open circuit voltage, fill factor, external quantum efficiency and of course power conventional efficiency, which are going to be presented below in detail.

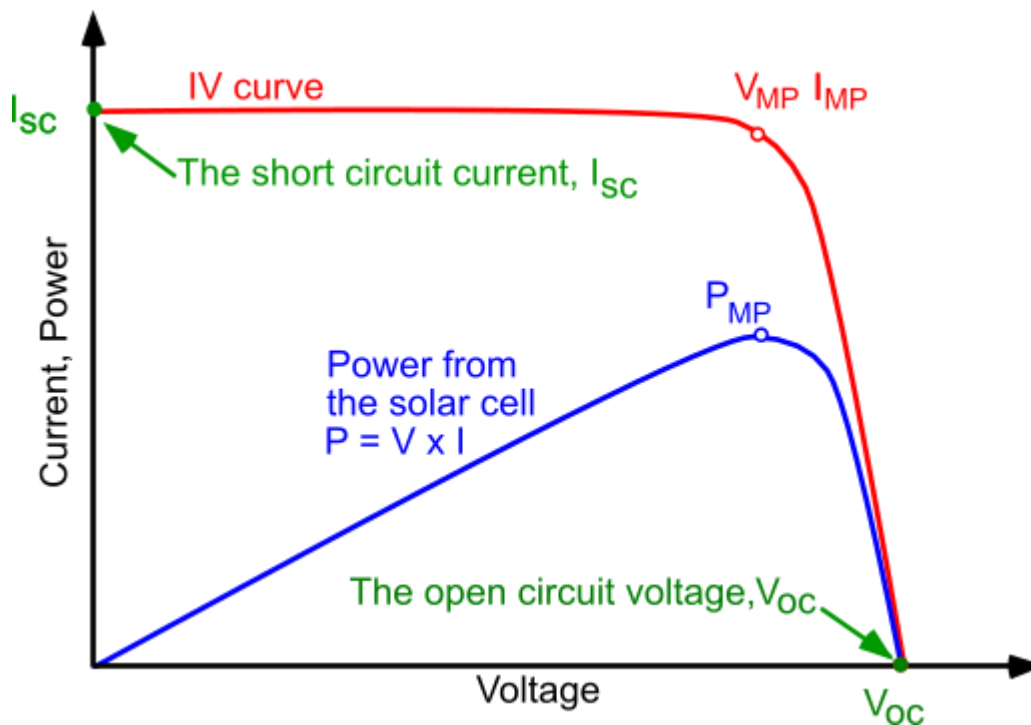*Figure 16. A typical I-V curve, where the Short circuit current and Open circuit voltage are shown[72].*

The short circuit current, the current when the voltage has a zero value, increases with light intensity, as higher intensity means more photons, which in turn means more electrons. Since the short circuit current I_{SC} is roughly proportional to the area of the solar cell, the short circuit current density,

$J_{SC} = I_{SC}/A$ is often used to compare solar cells. When a load is connected to the solar cell, the current decreases and a voltage develops as charge builds up at the terminals. The resulting current can be viewed as a superposition of the short circuit current, caused by the absorption of photons, and a dark current, which is caused by the potential built up over the load and flows in the opposite direction. As a solar cell contains a PN-junction, just as a diode, it may be treated as a diode. For an ideal diode, the dark current density is given by:

$$J_{dark(V)} = J_0[\exp\left(\frac{q*V}{n*k_B*R}\right) - 1], \text{Eq 2}$$

Here, J_0 is a constant, q is the electron charge, V is the voltage between the terminals, n is the diode ideality factor, k is the Boltzmann constant and T the temperature.

$$J = J_{SC} - J_0 \ \exp\left(\frac{q*V}{n*k_B*R}\right) - 1], \text{Eq 3}$$

The resulting current can be approximated as a superposition of the short circuit current and the dark current[73]:

$$I_{dark} = I_L - I_s[\exp\left(\frac{V}{nk_BR}\right) - 1], \text{Eq 4}$$

where, I_L is the electric current or the light-generated current and I_S is the saturation current of the diode. The saturation current (or scale current), more accurately the reverse saturation current, is that part of the reverse current in a semiconductor diode caused by diffusion of minority carriers from the neutral regions to the depletion region.

The open-circuit voltage, V_{OC}, is the maximum voltage available from a solar cell, and this occurs at zero current. The open-circuit voltage corresponds to the amount of forward bias on the solar cell due to the bias of the solar cell junction with the light-generated current.

To find an expression for the open circuit voltage, V_{OC}, we use (1.2) setting $J = 0$. This means that the two currents cancel out so that no current flows, which exactly is the case in an open circuit.[74] The resulting expression is:

$$V_{OC} = \frac{k_B*T}{q}\ln\left(\frac{J_{SC}}{J_0} + 1\right), \text{Eq. 5}$$

The built-in electric field separating the photogenerated electrons and holes can at most provide the built-in potential, V_{bi}. Hence, the built- in voltage gives the upper bound of the open circuit voltage. The effect of the parasitic series and shunt resistances, R_S and R_{SH} due to its bulk resistivity and presence of defects can included in the Shockley equation[75] as:

$$I = I_s \exp\left(\frac{q}{nk_BT}(V - IR_s)\right) - 1) + \frac{V - IR_S}{R_{SH}} - I_L, \text{Eq. 6}$$

Figure 17 shows the equivalent circuit of p-n junction solar cell, in which the I-V curve of this circuit is described by the equation above. The circuit consists of the following three parts. A current source IL that considers the light-generated current, a diode that accounts for the nonlinear voltage dependence and a shunt as well as a series resistor.
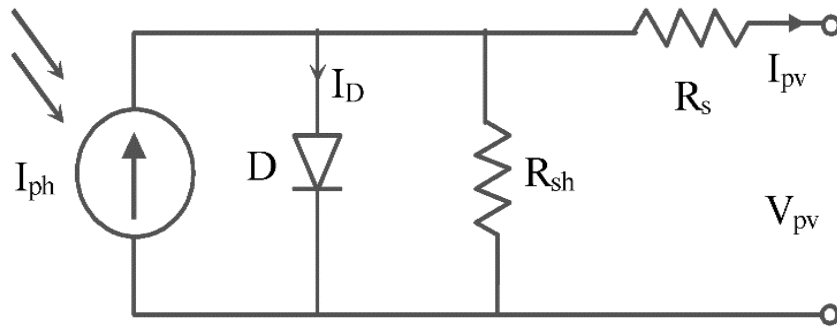
Figure 17. Solar Photovoltaic Cell Model.[76]

The current source generates a current IL up on illumination. IL can be described as the number of free electron/hole pairs immediately after generation - before any recombination can take place. The series resistance R_S is due to the bulk resistance of the semiconductor material, the bulk resistance of the metallic contacts and the contact resistance between the metallic contacts and the semiconductor. The shunt resistance RSH is caused by leakage across the p-n junction around the edge of the cell and in non-peripheral regions in the presence of defects and precipitates of foreign impurities in the junction region.

In conclusion, in the standard p-n junction solar cell, light absorption occurs via band gap excitation of electrons in the bulk of the semiconductor, charge separation in the internal electric

field of the p-n junction and charge collection by transport of electrons and holes through the bulk of the semiconductor to the electrical contacts.

Another way to find the V_{OC} from the difference of the $LUMO_{Acceptor}$ and $HOMO_{Donor}$:

$$V_{OC} = \frac{1}{e} * (LUMO_{ACCEPT} - HOMO_{DONOR}) - 0.3, \text{ Eq.7}$$

Studies have shown that the value of V_{OC} depends largely on the relative energy levels of the donor and acceptor species that form the essential heterojunction.

The short-circuit current and the open-circuit voltage are the maximum current and voltage respectively from a solar cell. However, at both of these operating points, the power from the solar cell is zero. The "fill factor", more commonly known by its abbreviation "FF", is a parameter which, in conjunction with V_{OC} and I_{SC}, determines the maximum power from a solar cell. The FF is defined as the ratio of the maximum power from the solar cell to the product of V_{OC} and I_{SC}. Graphically, the FF is a measure of the "squareness" of the solar cell and is also the area of the largest rectangle which will fit in the I-V curve. Basically, with higher FF, the performance of a solar cell is better. The FF is illustrated below:
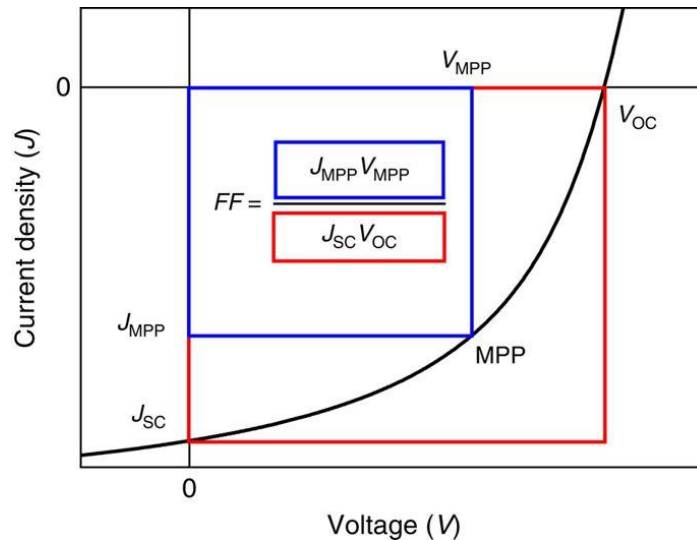
Figure 18. I-V curve with the schematic representation and the equation of Fill Factor, FF. [77]

The efficiency is one of the three key factors for an efficient OSC device. It is the most commonly used parameter to compare the performance of one solar cell to another. Efficiency is defined as

37

the ratio of energy output from the solar cell to input energy from the sun. In addition to reflecting the performance of the solar cell itself, the efficiency depends on the spectrum and intensity of the incident sunlight and the temperature of the solar cell. Therefore, conditions under which efficiency is measured must be carefully controlled in order to compare the performance of one device to another. Terrestrial solar cells are measured under AM1.5 conditions and at a temperature of 25°C.

The efficiency of a solar cell is determined as the fraction of incident power which is converted to electricity and is defined as:

$$P_{MAX} = V_{OC} * I_{SC} * FF, Eq.8$$

$$PCE \text{ or } n = \frac{V_{OC}*J_{SC}*FF}{P_{INC}} * 100\%, Eq. 9$$

Where, P_{INC} is the incident power density (sun power) = 100 mW/cm^2.

4.2 Quantum efficiency

IPCE or Quantum Efficiency (QE) is a measure of how efficiently the device converts the incident light into electrical energy at a given wavelength. There are two types of QE: External Quantum Efficiency (EQE) and Internal Quantum Efficiency (IQE).

- •EQE is the ratio between the number of collected carriers and the number of all the incident photons on the device active area at a given wavelength.
- •IQE is the ratio between the number of collected carriers and the number of all the absorbed photons by only the active absorber at a given wavelength.

The principle of EQE measurement is based on illuminating the sample by a monochromatic light and recording the device electrical current (number of generated carriers). By varying the frequency of the light the entire curve of the current as a function of wavelength can then be established. Figure 19 shows an example of an EQE curve for a typical silicon based solar device. The area under the curve will then represent the total number of carriers created by the device

under full spectrum white light illumination. In other words, the integration of the curve will give the electrical current density.
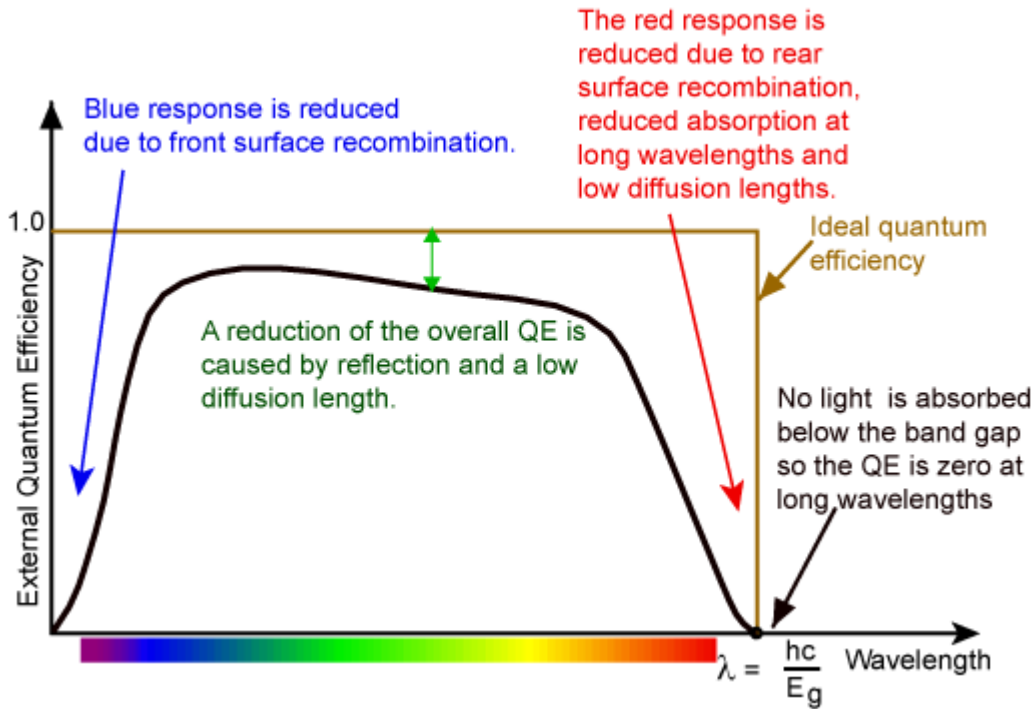
Figure 19. A typical External Quantum Efficiency curve of a silicon based solar device.[78]

In order to determine IQE the light absorbed by the active layer stack has to be identified. This is typically done by recording and excluding the light reflected from the device and using only the absorbed portion of light for the calculation of quantum efficiency. Since the absorbed light is typically less than the total incident light (as there will always be some loss of light due to reflections) then EQE will typically be less than IQE. The difference between IQE and EQE is important for distinguishing loss mechanisms between optical absorption properties of the entire device and photoconversion properties of the absorbing materials. IPCE is also useful for studying degradation properties of devices. The general reduction in the IPCE during time points to deterioration of photoconversion properties of the active material, while the change of the shape of the IPCE curve may point to morphological alterations in the absorbing layer.

Chapter 5. Experimental section

5.1 Materials

All the devices were based on rigid glass substrates coated with a ~100 nm thick Indium Tin Oxide (ITO) film as the bottom transparent conductive electrode. The glass/ITO substrates were purchased prepatterned form Naranjo Substrates B.V. and used as received.

For the buffer layers, PEDOT:PSS (Heraeus) MoO_3 (Lesker) and PTAA (Solaris Chem) were used as HTLs. Ca (Lesker) and PFN (Solenne BV) and $PC_{61}BM$ (Solenne BV) were used as ETLs. Finally, as top electrode silver from Lesker was thermal evaporated on top of the devices.

In organic photovoltaics, as electron three medium band gap polymers, i.e. the PCDTBT and PTB7 purchased from Solaris Chem. and 1-Materials respectively, while as the electron acceptor material was used the $PC_{71}BM$ fullerene derivative purchased from Solenne B.V. All the photoactive materials were used as received without any further purification step.

5.2 Fabrication procedure

In the organic photovoltaics, 2 different structures were used, the conventional and the inverted (Figure 20).
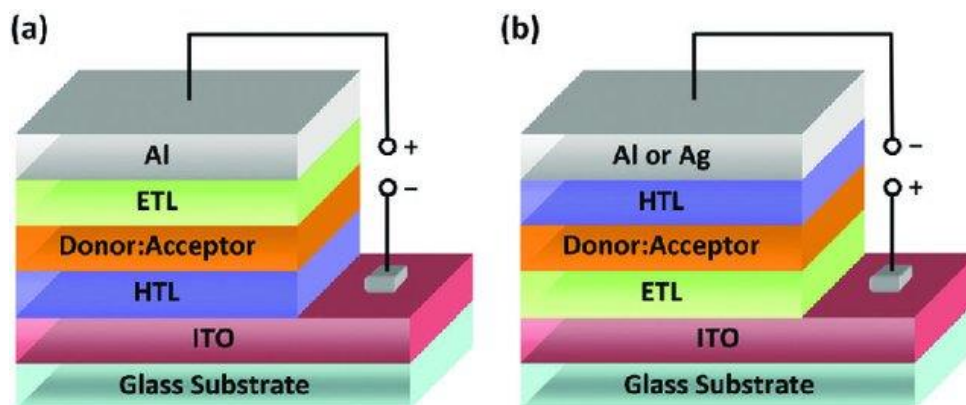
Figure 20. (a) Conventional and (b) inverted device architectures of organic bulk-heterojunction photodiodes. HTL and ETL are the abbreviations for hole-transporting layer and electron-transporting layer, respectively.[79]

In both cases, as substrate, glass substrates coated with ITO and 20x15x1.1 mm size and with 6 different ITO electrodes were purchased from Luminescence Technology Corp. Each ITO electrode represents a different photovoltaic cell. The ITO layer is of 100 nm thickness and has a surface resistance of ˜20 Ω/sq.
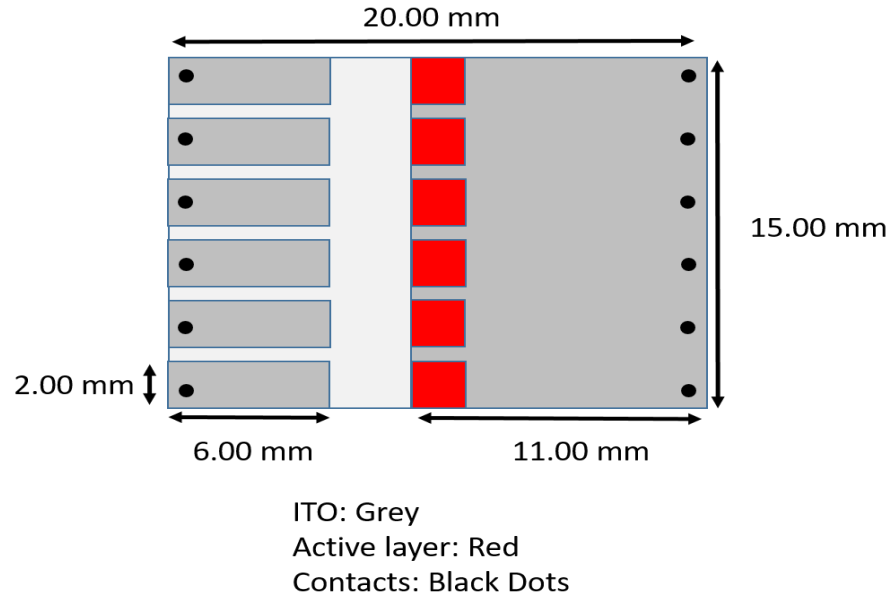
Figure 21. Schematic drawing shows physical dimensions of patterned ITO glass.

To remoce any impurities, a four step cleaning procedure was used. The substrates were placed in soap-deionized water and in ultrasonic bath for 10 minutes and washed out with deionized water afterwards. Then, they placed again in two different baths, the first with acetone and the second with propanol for another 10 minutes each. Next, transferred in Petri dish and in an oven at 120 °C for 15 minutes. Finally, before the fabrication of the solar cell, the placed in an Ozone UV Cleaner for another 15 minutes.

5.2.1 Conventional OPVs

For the HTL, filter poly(ethylene-dioxythiophene) doped with poly(4- styrenesulfonate) (PEDOT:PSS), was spin-cast from an aqueous solution on the ITO substrate at 6000 rpm for 60 s and the average thickness of the layer was 30 nm, followed by baking for 15 min at 120 °C inside

an oven. PCDTBT:PC$_{71}$BM were dissolved in 1,2- dichlorobenzene:chlorobenzene (3:1) (o-DCB:CB) with a 1:4 (4 mg:16 mg) ratio. A PTB7:PC$_{71}$BM 1:1.5 (10mg : 15mg) ratio was dissolved in chlorobenzene, followed by the addition of 1,8-diiodooctane (DIO) to give overall DIO amount of 3%. Both photoactive layers were subsequently deposited by spin-coating the blend solutions at 1000 rpm on top of PEDOT:PSS layer (under inert atmosphere). The thickness for PCDTBT:PC$_{71}$BM active layer was found to be ~80 nm and for PTB7:PC71BM blend was found to be ~100nm. The devices with PCDTBT:PC$_{71}$BM blend were then heated at 80 °C for 1 min in air, while the PTB7:PC$_{71}$BM based devices were dried inside a vacuum antichamper with dynamic vacuum for ~15 min. For the ETL, Ca was deposited through thermal evaporation. More specific, after the fabrication of the active layer, the samples are placed in a special mask whish exposes the area in which we want to deposit the Ca. Every sample is numbered in order to be distinguished. Afterwards, the mask is screwed on the arm of the vacuum chamber, in a specific distance from the cavity. Finally the cavity is filled with the amount of aluminum we desire. The chamber is sealed and the vacuum starts until it reaches 10^{-6} mbar, where the thermal evaporation can begin. We heat the thermal source until the sensor shows the desirable rate. The evaporation of Ca was with rate 0.5 Å/sec and with final thickness of 5 nm. Afterwards, sliver was thermal evaporated with rate 1,5 Å/sec and final thickness 100 nm.
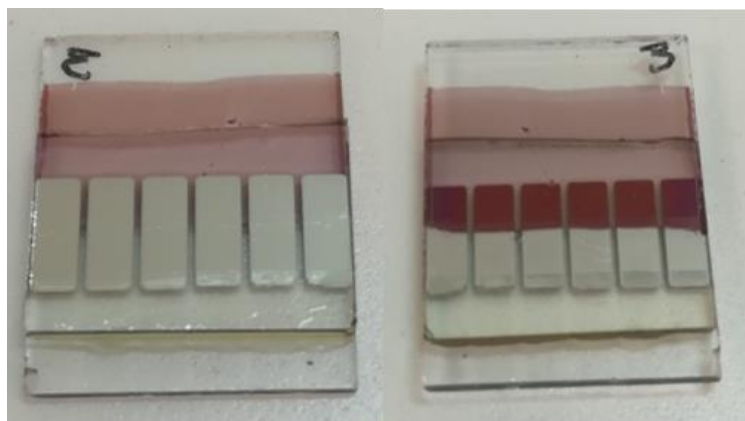
Figure 22. Final device.

5.2.2 Inverted OPVs

In the inverted structure, as ETL, a ~10 nm thick PFN (0.5 mg/ml, in 1 ml of MeOH and 2 μl of AcOH) layer (ETL) was spin-cast at 1000 rpm for 45 sec followed by thermal annealing at 150 °C

for 30 sec. Then the photoactive layer consisting of PTB7:PC$_{71}$BM at a 1:1.5 (10 mg:15 mg) ratio, dissolved in CB and 3% 1,8-diiodooctane (DIO) was spin-coated at 1500 rpm on top of the PFN layer. Finally, MoO$_3$ HTL layer (rate 0.3 Å/sec and thickness 8 nm) and the top Ag electrode (rate 1.5 Å/sec and thickness 100 nm) were thermally evaporated through a shadow mask, defining an active area of 4 mm^2 for each device.

5.3 Characterization

The performances of the devices were measured under inert atmosphere with an Air Mass 1.5 Global (A.M. 1.5 G) Oriel solar simulator at an intensity of 100 mW cm^{-2} using a Solar Cell I-V Test System (both dark and light I-V curves were collected). A reference monocrystalline silicon solar cell from Newport Corp. was used to calibrate the light intensity at one sun irradiation conditions.
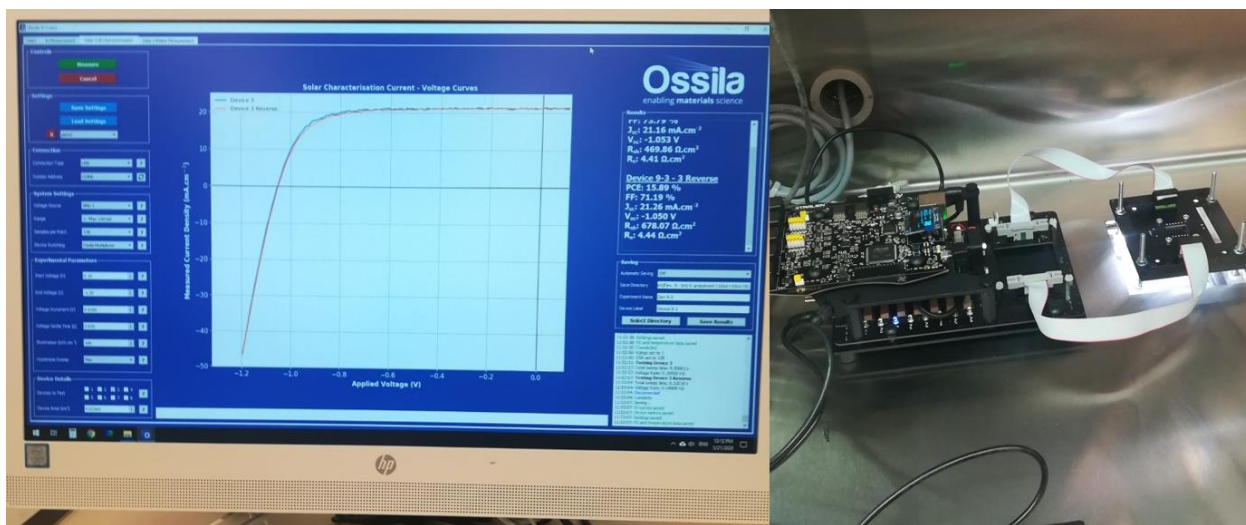
Figure 23. Ossila multiplexer system for Solar Cell I-V Test System.

The external quantum efficiency measurements were conducted immediately after device fabrication using an integrated system (Enlitech, Taiwan) and a lock-in amplifier with a current preamplifier under short-circuit conditions. The light spectrum was calibrated using a monocrystalline photodetector of known spectral response. The devices were measured using a Xe lamp passing through a monochromator and an optical chopper at low frequencies (~200 Hz) in order to maximize the signal/noise (S/N) ratio.
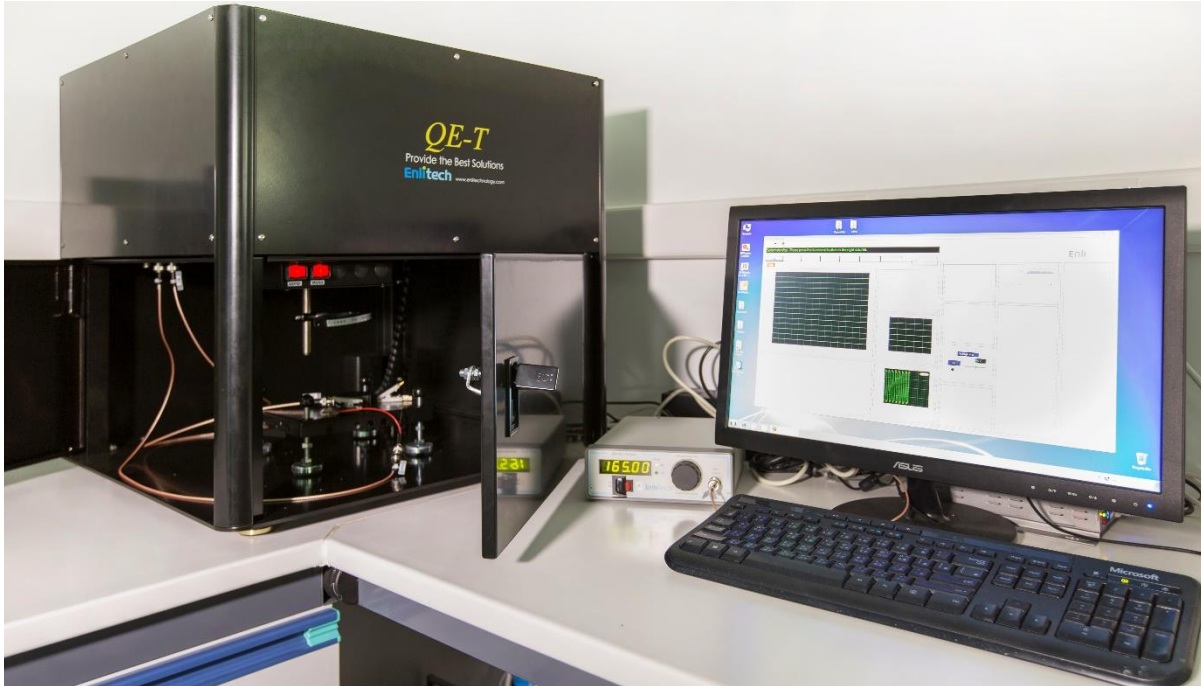
Figure 24. Enlitech EQE measurement system.

The photoluminescence (PL) measurements of the thin films were carried out at room temperature and resolved by using a UV grating and a sensitive, calibrated liquid nitrogen cooled CCD camera, in the wavelength range from 600 to 950 nm using a He-Cd CW laser, at 325 nm with a full power of $P_0 = 35$ mW, as the excitation source. UV-vis absorption and reflectance spectra were recorded using a Shimadzu UV-2401 PC spectrophotometer over the wavelength range of 300-800 nm.

The absorbance, transmittance and reflectivity measurements of the samples were recorded using a Shimadzu UV-2401 PC spectrophotometer over the wavelength range of 300-850 nm.

The Raman spectroscopy of the samples was performed onto a 0.5x0.5 cm Si/SiO_2 wafer (LDB Technologies Ltd.) and dried under vacuum. Raman measurements were collected with a Renishaw in Via confocal Raman microscope using an excitation line of 514 nm with a 100X objective lens, and an incident power of ~1 mW on the sample. The spectra are analyzed using Wire 4.4 software.

The Atomic Force Microscopy (AFM) of the samples was performed onto the device, depending on the layer that was examined. AFM images are acquired with Bruker Innova® AFM in tapping mode using silicon probes (frequency = 300 kHz, spring constant = 40 Nm^{-1}).

The X-ray diffraction measurements (XRD) measurements were performed by means of a Panalytical Empyrean Diffractometer, equipped with a ceramic Cu-anode (40kV-40mA). A parallel plate collimator is used as incident optical pathway to maximize diffracted signal response from layered samples and devices, whilst a unique 2D solid-state hybrid pixel detector (Pix'cel 3D) accomplished the signal detection. The samples, allocated into an Eulerian cradle, are studied in reflection mode and gonio-collections, performed at different angular ranges ($5° < 2\theta < 80°$).

The energy dispersive X-ray reflectivity measurements were performed on an especially designed X-ray spectrometer (Patent No. RM 93 A000410, 1993, R. Felici, F. Cilloco, R. Caminiti, C. Sadun, and V. Rossi Albertini, Italy) characterized by a non-symmetric configuration, the detection optical path being much longer than the incident one in order to maximize the Reflectivity and reduce the undesired scattering/noise. A polychromatic incident radiation produced by a W-anode is used as probe (operating Energy range 10-55keV), and the reflected signal was collected by means of an energy sensitive Solid State High purity Ge-single crystal detector cooled to cryogenic temperatures by means of an electro-mechanical cooler. The samples are mounted into an appropriate sample holder (transparent to the incident radiation) on top of a two axes cradle used to optimize the reflectivity conditions. A controlled N_2 atmosphere is kept inside the sample holder during the data collection to prevent materials degradation. Experiments are conducted in the following experimental conditions: E =55 keV, I = 30 mA and the samples are kept in controlled N_2 atmosphere in an appositely designed sample holder during the completely experimental procedure.

Chapter 6. Studies

6.1 Ternary OPVs

6.1.1 Ternary Organic photovoltaics using a small molecule as a third component

__Miron Krassas__, Christos Polyzoidis, Pavlos Tzourmpakis, Dimitrios M. Kosmidis, George Viskadouros , Nikolaos Kornilios , George Charalambidis, Vasilis Nikolaou, Athanassios G. Coutsolelos, Konstantinos Petridis, Minas M. Stylianakis and Emmanuel Kymakis, Benzothiadiazole Based Cascade Material to Boost the Performance of Inverted Ternary Organic Solar Cells, Energies 2020, 13(2), 450.

The prevalent research rush of the scientific community towards cost-effective and reliable alternative energy sources involves the whole spectrum of research on photovoltaic technologies and corresponding material science. Recent progress in the subfield of organic solar cells (OSCs) highlights and even updates their potential as ideal, low-cost alternatives to the conventional inorganic silicon technology. This is attributed to their advantages, such as light-weight and solution-processability, as well as their compatibility with flexible substrates and upscaling techniques[80,81,82]. The emergence of novel materials[83,84,85,86], advancements of device's engineering[96,87,88] for enhanced light harvesting and trapping by extending the absorption spectrum or introducing optical cavities[89,90], and additionally leading theoretical studies[91,92], have so far skyrocketed their efficiency over 13%.

Solution-processed bulk-heterojunction (BHJ) photovoltaics constitute a subcategory of OSCs that already enjoys immense research. The careful selection of polymer donor and fullerene acceptor materials, having in mind the proper energy level matching and appropriate degree of phase separation inside the blend, has introduced additional degrees of freedom into OSC research and scientific advancement[93,94,95]. Polymers, including P3HT[96] and PTB7[97], as well as fullerene derivatives with most notable $PC_{61}BM$[98] and $PC_{71}BM$[99] have been under study for years while demonstrating exceptional efficiencies (>5%) for $P3HT:PC_{61}BM$[100] and above 7% for $PTB7:PC_{71}BM$ based devices.[101] On the other hand, a very promising subfield of OSC research employs non-fullerene acceptors (NFAs) that yield state-of-the-art OSC cells with impressive

efficiencies exceeding 16%.[102,103,104] However, NFA based OSCs remain partially explored and extensive optimization efforts are required, in order to counter the competitive advantages of conventional fullerene-based materials. For instance, PC71BM-based active blends result to OSCs that yield better photostability under operational conditions.[105,106,107] On top of that, tailor-made polymer fabrication is an additional way of research towards efficient OSCs. Many polymers have been prepared through alternating copolymerization of donor (D) and electron acceptor (A) units, thereby resulting in D–A pairs that effectively (a) exhibit multiple and complementary absorptions; and (b) enhance charge transfer ability.

Another effective, yet simple strategy to enhance the OSC's photovoltaic performance is the adoption of a ternary structure into a binary system. This can be secured with the integration into the active layer of a third component.[108,109,110,111] This third element could be a polymer[112,113,114], an organic small molecule[115,116,117,118,119,120,121,122,123,124,125,126,127,128], a dye[129,130,131], a fullerene derivative[132], a graphene and a two dimensional (2D)-based material[133,134,135,136,137], or a nanocrystal[138]. The introduction and the availability of materials to be leveraged as third element support the better engineering of this architecture towards better photovoltaic OSCs' performances. The third component within ternary organic solar cells (TOSCs) may function as a charge relay for electron and hole transport, as an energy transfer step, act as a second donor[139], as well as create a new organic blend with new physical characteristics in conjunction with the donor. In the cases where the charge transfer mechanism prevails, the third component needs to be placed at the interface of the host donor and the acceptor in order, efficient charge transfer to take place; the so-called energy level "cascade" phenomenon. Careful design and selection of the third component, as a function of its energy levels, electrical conductivity, electron mobility and chemical properties, necessitate to ensure efficient charge transfer through the active layer of TOSC[140]. The careful selection and introduction of the third element impacts the photovoltaic properties of the resulting solar cell such as optical properties, the extension of the absorption's bandwidth and intensity, the improved charge or energy transfer efficiency, by regulating the local environment at the D:A interfaces, thereby securing a better exciton generation and dissociation. As a consequence, an improvement in efficiency may end up to power conversion efficiency (PCE) values of the order of 8–10%[141].

2,1,3-Benzothiadiazole (BT), an electron-deficient unit, is among the most common building blocks utilized for the lowering of potential and electron affinity of electron- transport materials[142,143]. BT is a n-type building block consisting of a benzene ring fused to one of thiadiazole[144,145], that can be coupled with an electronically rich molecule to form low bandgap functional polymers or small molecules[146]. Moreover, the cyano groups bound to the benzene ring can operate as electron scavenging units. Following this recipe, the lowest unoccupied molecular orbital (LUMO) level of the polymer can be reportedly lowered due to the benzene ring in an effective way[147].

In this work, a ladder-type vinyl complex based on cyanovinylene bonds, 4,7-dithien-benzothiadiazole as central unit and thiophene rings as terminal units, was synthesized and characterized in terms of its photophysical and electrochemical properties. The synthesized conjugated small molecule (CSM), named compound T[148], was integrated as the third component, into a binary BHJ PTB7:PC$_{71}$BM active layer in different concentrations (3–15%) ratio to the polymeric donor. Upon the incorporation of compound T in 5% as optimum determined concentration, a PCE of 8.34% was achieved for the champion inverted TOSC device, improved by 12% with respect to the control inverted binary device.

Synthesis and characterization of compound T

1. Synthesis of 2,1,3-Benzothiadiazole (1)[149]

o-phenylenediamine (9.25 mmol) and triethylamine (37 mmol) were added to a 100 mL roundbottom flask. Then, CH$_2$Cl$_2$ (30 mL) was added, and the mixture was stirred until total dissolution of diamine. Afterwards, SOCl$_2$ (18.5 mmol) was added dropwise to the reaction flask and the mixture was heated at reflux for 6 h. Then, the solvent was removed and deionized water (70 mL) were added. The pH value was tuned to 1 by adding conc. HCl. Then, water was added to the reaction mixture, and the desired compound was purified by distillation. The distilled mixture was extracted with CH$_2$Cl$_2$ (3 x 20 mL), dried with MgSO$_4$ and directly filtered. In the last step, the solvent was removed to afford pure 2,1,3-Benzothiadiazole (yield ~90%, 8.5 mmol).

2. Synthesis of 4,7-Dibromo-2,1,3-benzothiadiazole (2)

A 100 mL two-necked round bottom flask was charged with (1) (7.34 mmol) and 48% HBr (15 mL). Then, a solution of Br_2 (22 mmol) in HBr (10 mL) was added very slowly to the reaction flask, using a dropping funnel. Upon the total addition of Br_2, the solution was refluxed for 6 h. Next, the reaction mixture was cooled down at room temperature and a saturated solution of $NaHSO_3$ was added to the reaction flask, to remove Br_2 excess. The reaction solution was then filtered under vacuum and washed thoroughly with D. water. Finally, the yielded solid was washed once with cold diethylether and dried in an oven at 50 °C for 6h to afford 4,7-Dibromobenzothiadiazole (~95%, 7 mmol).

3. Synthesis of 4,7-Dithien-2-yl-2,1,3-benzothiadiazole (3)[150]

A Stille coupling reaction was conducted for the synthesis of 4,7-Dithien-2-yl-2,1,3-benzothiadiazole. More analytically, a 100 mL round bottom flask was charged with (2) (5 mmol), $PdCl_2(PPh_3)2$ (0.05 mmol), tributyl(thien-2-yl)-stannane (12 mmol) and 35 mL of THF. Afterwards, the reaction mixture was refluxed for 6 h. Next the solvent was removed under reduced pressure and the residue was purified by column chromatography on silica gel (eluent CH_2Cl_2/hexane, 1:1). The final yield was recrystallized from ethanol-toluene and gave 4,7-Dithien-2-yl-2,1,3-benzothiadiazole in red needles (yield ~80%).

4. 5,5-(2,1,3-Benzothiadiazole-4,7-diyl)-bis-2-thiophenecarboxyl-aldehyde (4)[151]

A Vilsmeier-Haack reaction was conducted for the synthesis of 5,5-(2,1,3-Benzothiadiazole-,7-diyl)-bis-2-thiophenecarboxylaldehyde. More specifically, (3) (1 mmol), was dissolved in 30 mL of CH_2Cl_2 into a 250 mL round bottom flask. Then, a mixture of DMF (5 mmol) and $POCl_3$ (5 mmol) was added dropwise to the reaction flask and the mixture was refluxed for 18 h, under inert atmosphere. After cooling at room temperature, 50 mL of CH_2Cl_2 and 100 mL of saturated aqueous solution of sodium acetate were added into the reaction mixture. After 2 h of constant stirring at room temperature, the organic phase was separated, washed with water and dried over $MgSO_4$. Finally, it was purified by column chromatography (silica gel/CH_2Cl_2), and the solvent was evaporated under vacuum to afford 5,5-(2,1,3-Benzothiadiazole-4,7-diyl)-bis-2-thiophenecarboxyl-aldehyde (4), as an orange solid (yield ~90%).

5. Synthesis of Compound T[152]

A condensation reaction was conducted in order to afford the final product, compound T. A 250 mL three-neck round bottom flask was charged with (4) (3 mmol) in absolute EtOH (50 mL). The mixture was stirred for 1h. Afterwards, a dropping funnel containing a solution of 2-Thiopheneacetonitrile (10 mmol) in absolute EtOH (40 mL) was placed on the left neck of the reaction flask. The right neck of the reaction flask was charged with an additional dropping funnel containing a solution of NaOH (4.00 mmol), in absolute EtOH (40 mL). The reaction mixture was then constantly stirred under inert atmosphere (N_2). Both 2-Thiopheneacetonitrile and NaOH were added simultaneously dropwise in the reaction mixture, in order to avoid any byproducts formation. After 6 h, a purple solid was precipitated, filtered off and washed thoroughly with water. Finally, it was dried in an oven at 65 °C to afford the final compound T (yield ~55%).
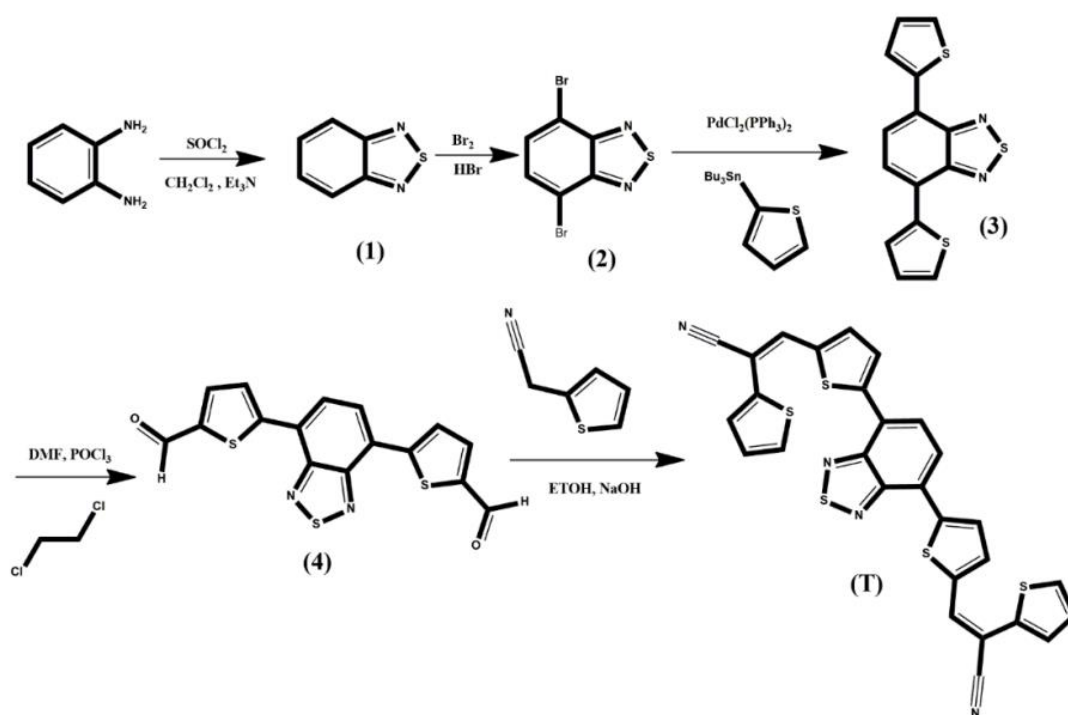
Figure 25. Five-step synthesis of compound T.

The chemical structures of PTB7, compound T and PC$_{71}$BM, employed in the ternary BHJ, are illustrated in Figure 26. Such an approach is popular and is widely utilized to reduce the band gap

of conjugated semiconductors[153,154]. The exact synthetic procedure of compound T can be found in another publication of our research team and is analyzed in Figure 25.
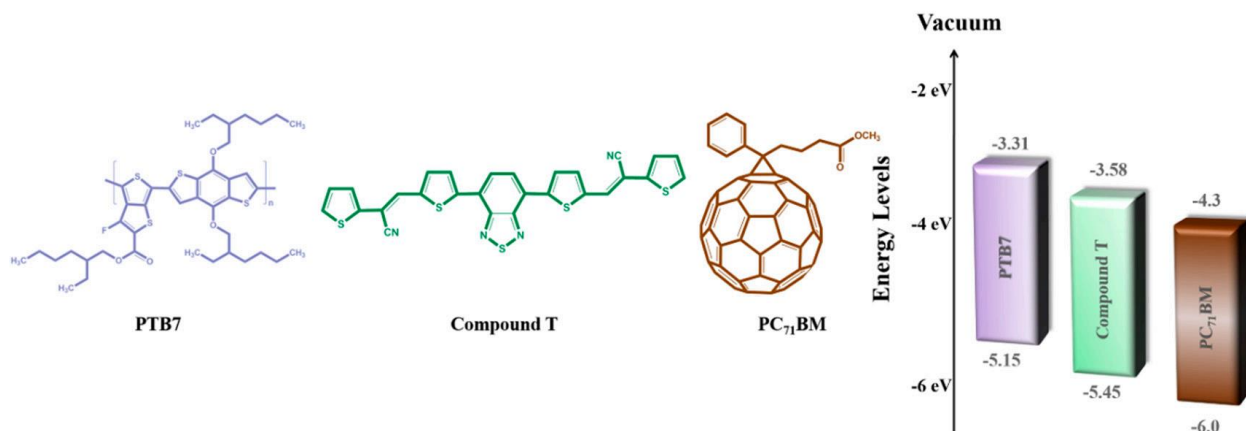
Figure 26. Chemical structures and energy levels of ternary blend's component.

Compound T was characterized using UV-vis, FT-IR and PL spectroscopy. The UV-vis absorption spectrum of a thin film pristine compound T exhibited two main peaks at 398 nm and 485 nm, respectively (Figure 27), which were both due to the $\pi \rightarrow \pi^*$ electron transition.
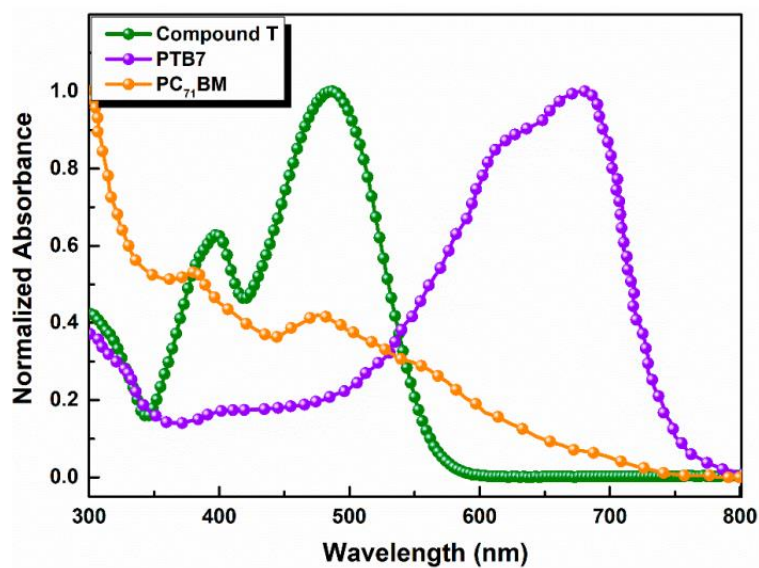
Figure 27. Normalized UV-Visible absorption spectra of Compound, PTB7 and PC$_{71}$BM in thin films.

According to the FT-IR spectrum of compound T (Figure 28) a characteristic peak at 2214 cm^{-1} appears, due to the CN-stretching bond. The peak at 3103 cm^{-1} is ascribed to aromatic C–H stretching, while the absorption bands at 1652 cm^{-1}, 1577 cm^{-1}, 1533 cm^{-1}, 1520 cm^{-1}, 1479 cm^{-1} and 1441 cm^{-1} correspond to C=C aromatic stretching bonds, respectively. Finally, peaks at 1267 cm^{-1}, 1252 cm^{-1}, 1243 cm^{-1}, 1224 cm^{-1}, 1203 cm^{-1}, 1189 cm^{-1}, 1097 cm^{-1}, 1080 cm^{-1} and 1048 cm^{-1} are attributed to the benzene ring of benzothiazole. On the other hand, the PL spectrum of compound T in solid state was recorded in the range of 600−900 nm, upon photoexcitation at 485 nm, as depicted in Figure 29. Compound T exhibited a broad peak at 700 nm.
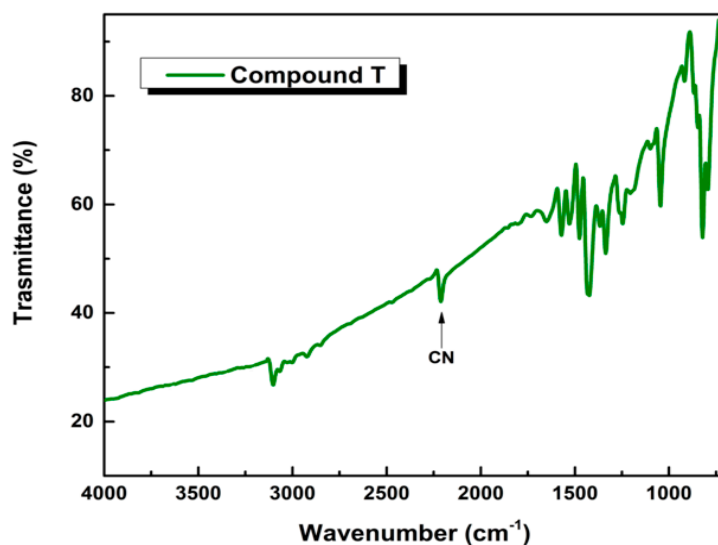
Figure 28. FT-IR spectrum of compound T.
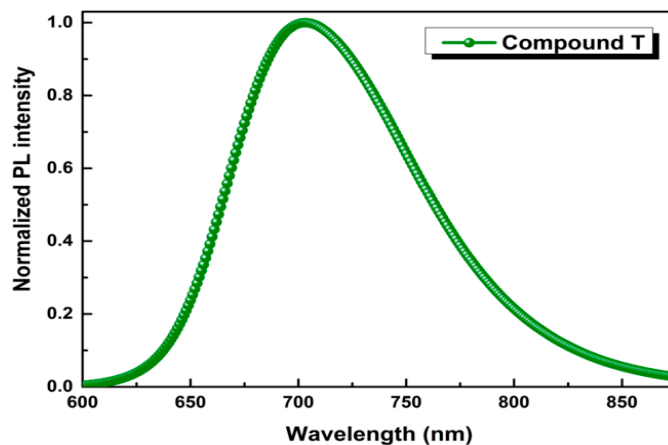
Figure 29. Normalized PL spectrum of compound T in thin film.

In Figure 30 the absorption spectra of the ternary active layers are illustrated. It is observable that the absorption intensity slightly increased as the concentration of compound T got 5% across the full spectrum range and especially between 400 and 560 nm, where the host PTB7 and compound T spectra overlapped. Moreover, the common peak of compound T and fullerene derivative $PC_{71}BM$ got higher values, while the absorption peak of PTB7, decreased. According to relevant existing literature[155], two broad absorption peaks at around 614 and 682 nm are attributed to the characteristic π–π* transition of the PTB7 polymer.
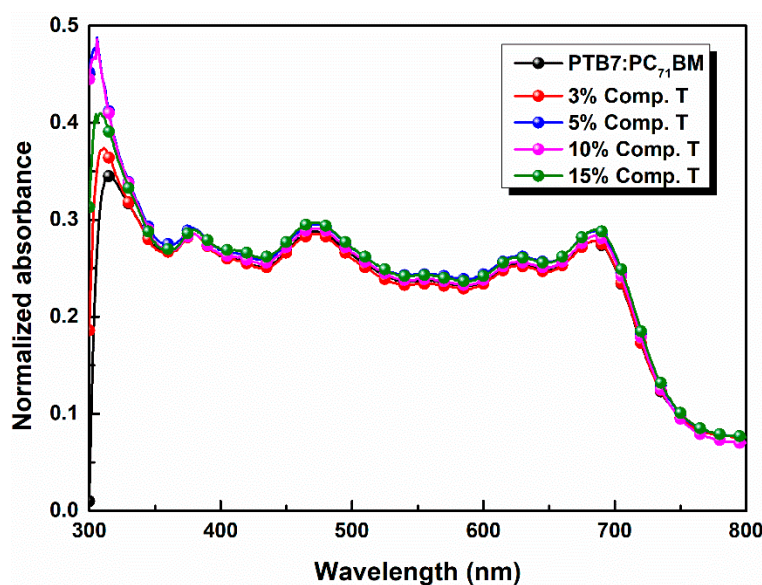
Figure 30. Normalized UV-vis absorption spectra of PTB7:PC₇₁BM blends incorporating compound T in different concentrations.

In the latter, the photoluminescence (PL) spectrum of PTB7:compound T was quenched as an optimum concentration value of the third element was approaching its optimum value. The PL quenching is clear evidence of the improved exciton dissociation, between compound T and PTB7, as the emission of the latter quenched (Figure 31). The best charge extraction was observed after the addition of 5% v/v Compound T, compared to the reference binary system (PTB7:PC$_{71}$BM). This is a possible reason for the enhanced PV parameters in the case of 3% and 5% ternary devices, as demonstrated below in Table 1. This fact proves that compound T could act as an electron

cascade material that facilitates the higher electron extraction from PTB7 towards PC$_{71}$BM compared to the binary reference system.
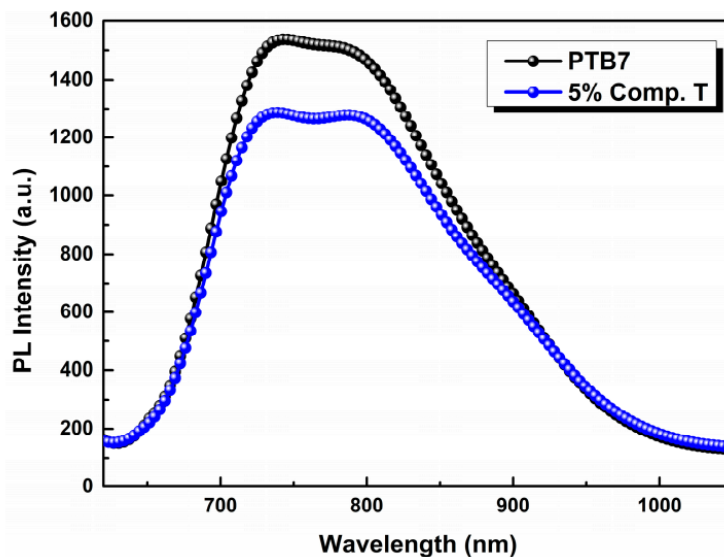
Figure 31. Photoluminescence (PL) spectra of PTB7 (black) and PTB7:compound T (5%; blue) thin film on Si substrate.

A schematic representation of the inverted ternary OSC structured as ITO/PFN/PTB7:compound T:PC$_{71}$BM/MoO3/Al is depicted in Figure 32, while the respective configuration and energy diagram of the device with the HOMO and LUMO energy levels of the materials selected are depicted in Figure 29. Due to the energy level offset between PTB7[156], compound T and PC$_{71}$BM (3.31 eV, 3.58 eV and 4.3 eV in LUMO level and 5.15 eV, 5.48 eV and 6.0 eV in the HOMO level, respectively) the charge transfer is enhanced. This is clear evidence, that the addition of compound T up to an optimum concentration, promoted the electron-cascade effect. More specifically, excitons are dissociated at the D:A interfaces throughout the blend layer. Since the HOMO levels of compound T and the conjugated polymer PTB7 perfect match, holes' transport was facilitated through the compound T en route to the anode electrode. In Figure 5, current-to-voltage characteristics based on the PTB7:PC$_{71}$BM and the ternary PTB7:compound T:PC$_{71}$BM active layers, are also depicted. The corresponding PV performance parameters are listed in Table 1. The reference binary device exhibited a short circuit current density (J$_{SC}$) of 16.10 mA cm^{-2}, an open circuit voltage (V$_{OC}$) at 0.72 V, a fill factor (FF) at 64.6% and a PCE of 7.51%.
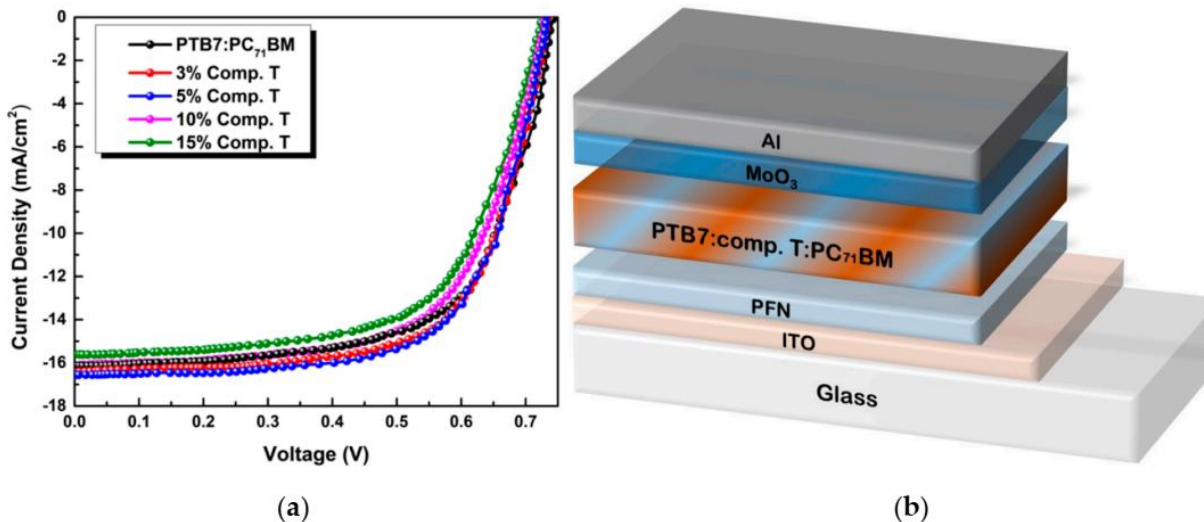
Figure 32. Current density to voltage characteristics of different concentrations of compound T in PTB7:PC$_{71}$BM blend (a) and a schematic representation of the ternary bulk heterojunction device structure (b).

As shown, J$_{SC}$ did not follow the rising trend of compound T concentration, but instead it increased from 3% to 5% and then started to decay as the concentration of compound T got higher values. This was attributed to the degradation of the interfaces between compound T and the polymer donor material. On the other hand, the V$_{OC}$ obtained in the ternary cells was almost identical to the binary PTB7:PC$_{71}$BM, reflecting that charge transfer state energy (E$_{CT}$) does not change upon the addition of Compound T[157].

Table 1. Summary of solar cell parameters of PTB7:PC$_{71}$BM and ternary PTB7:compound T:PC$_{71}$BM blend with different concentrations *

Concentration of Compound T	Calc. *Jsc* (mA cm^{-2})	*Jsc* (mA cm^{-2})	*Voc* (V)	FF (%)	PCE (%)
Reference	15.23	16.10 ± 0.08	0.72 ± 0.04	64.6 ± 0.6	7.51 ± 0.12
3% v/v	15.60	16.44 ± 0.11	0.73 ± 0.02	65.9 ± 0.3	7.96 ± 0.11
5% v/v	15.72	16.70 ± 0.05	0.73 ± 0.01	67.7 ± 0.4	8.25 ± 0.09
10% v/v	15.12	16.06 ± 0.11	0.73 ± 0.02	64.0 ± 0.3	7.50 ± 0.11
15% v/v	14.26	15.61 ± 0.13	0.72 ± 0.01	63.3 ± 0.1	7.11 ± 0.09

*The data were averaged from ten identical organic solar cell (OSC) devices with six cells each.

In view of further investigating the origin of the J_{SC} increase upon the addition of the compound T up to an optimum concentration, the incident photon to electron conversion efficiency was measured (IPCE) for each device (Figure 33). From EQE curves, it was deduced that the 5% concentration (v/v) had the best response at both main absorption peaks, which indicates that this ratio might yield the most efficient charge transportation and collection due to a better domain engineering within the active layer of the ternary system.
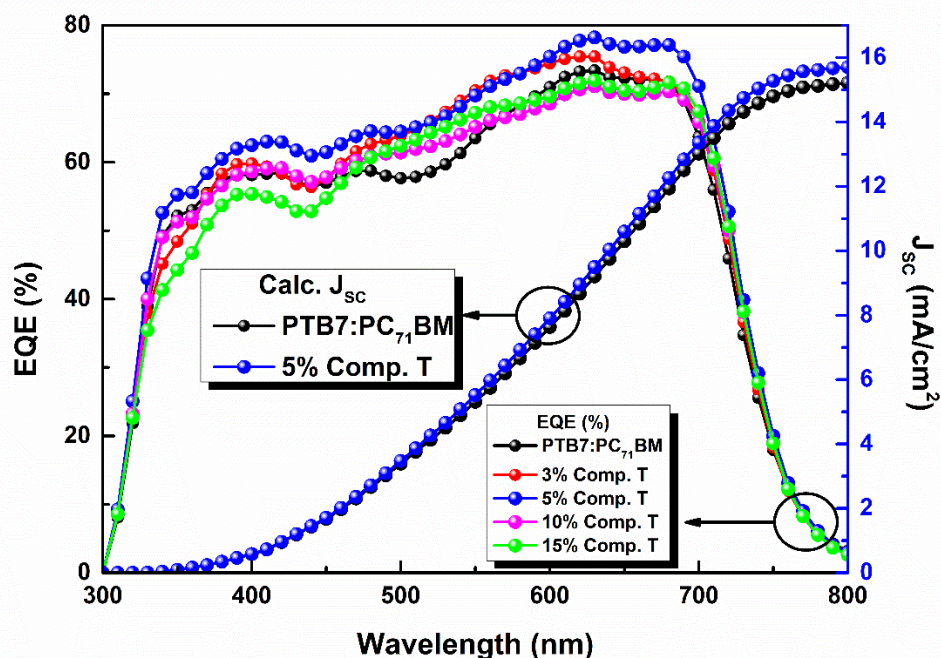
Figure 33. External quantum efficiency (EQE) curves of the reference (black), 3% (red), 5% (blue), 10% et) and 15% (green) compound T based OSC devices.

For hole mobility determination, a hole-only device was fabricated. The building concept of this device is the replacement of the ETL by an HTL; in our case the PFN ETL was replaced by PEDOT:PSS that acts as an HTL. The hole-only device of the structure Glass/ITO/PEDOT:PSS/active layer/MoO₃/Au was fabricated according to the same parameters as the fully operational BHJ OSC. More specifically, PEDOT:PSS was spin coated in static mode at 5000 rpm, 50 µL of the active layer's blend was dynamically spin coated at 2500 rpm for 30 s,

8 nm of MoO_3 were deposited by thermal evaporation and finally 100 nm of Au were deposited via thermal vacuum deposition.

Respectively, the electron-only device of the structure ITO/PFN/active layer/Ca/Al was fabricated by replacing the MoO_3 HTL with a 5 nm thick Ca ETL deposited through thermal evaporation.

Carriers' mobilities of the reference device (PTB7:PC$_{71}$BM) and the ternary one, incorporating 5% compound T, were also obtained by space charge limited current (SCLC) method. To this end, hole and electron only devices of the structure ITO/PEDOT:PSS/active layer/MoO_3/Au and ITO/PFN/active layer/Ca/Al were respectively fabricated and J-V^2 characteristic curves are reported (Figure 34). Calculations were based on the Mott–Gurney equation[158]:

$$J = \frac{9}{8}\mu_h\varepsilon_o\varepsilon_r \frac{(V-V_{bi})^2}{L^3}, \text{Eq. 10}$$

where ε_r is the relative dielectric constant, ε_0 is the permittivity of free space, μ is the charge carrier mobility, V is the applied voltage, V_{bi} is the built-in potential and d is the thickness of the active layer.
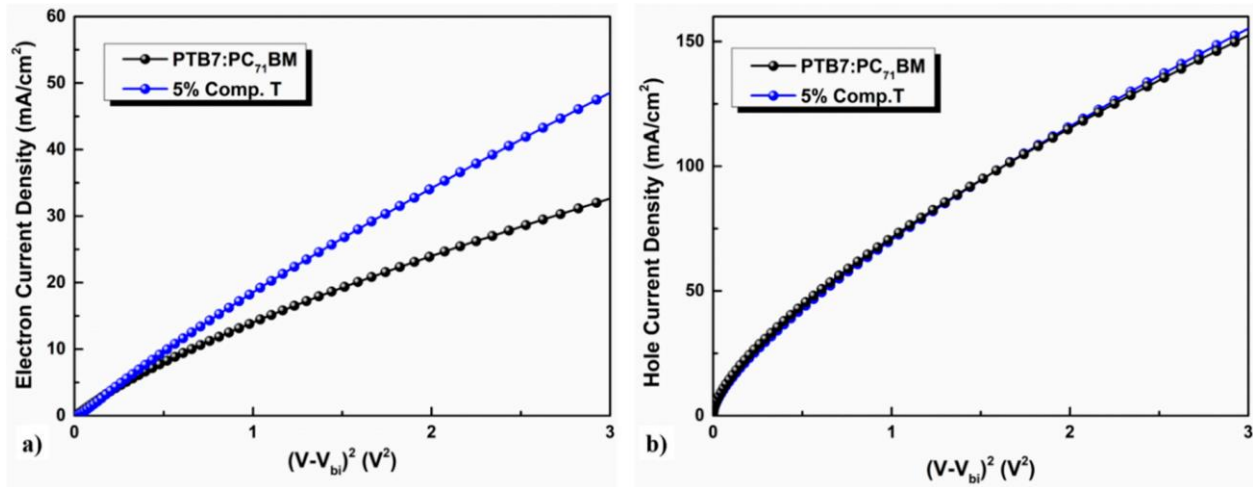
Figure 34. J-V^2 characteristics of the fabricated a) electron-only and b) hole-only devices, upon the addition of 5% compound T, for the determination of carriers' mobilities.

The μ_h and μ_e values for holes and electrons mobilities of the reference and 5% compound T ternary device are summarized in Table 2, respectively. It is obvious that the incorporation of compound T into the binary solution resulted to the improvement of hole mobility, an even higher increase in electron mobility and most important the more balanced ratio between hole and electron mobilities. Moreover, the fact that the μ_h/μ_e ratio is closer to one for the case of the ternary device, is a key prerequisite in avoiding charge accumulation in the device and thus higher photovoltaic performances. The aforementioned result confirms the previous assumption for the electron-cascade-role of compound T.

Table 2. Hole and electron mobilities of PTB7:PC$_{71}$BM and ternary blend PTB7:compound T (5%):PC$_{71}$BM*.

Active layer	μ_h $(cm^2 \cdot V^{-1} \cdot s^{-1})$	μ_e $(cm^2 \cdot V^{-1} \cdot s^{-1})$	μ_h/μ_e
PTB7:PC$_{71}$BM	9.91 x 10^{-5}	8.01 x 10^{-5}	1.24
5% compound T	1.01 x 10^{-4}	8.61 x 10^{-5}	1.17

*The data were averaged from ten identical organic solar cell (OSC) devices with six cells each.

In order to study the effect of compound T on active layer's morphology, a reference and a ternary blend layer of 5% (v/v) concentration were subjected to AFM measurements. Subsequent results (Figure 35) indicate a better morphology together with a reduction in roughness (RMS) for the ternary device containing 5% of compound T, by approximately 9.1%. In particular, the RMS value for the reference binary layer was 1.4 nm, whereas the ternary layer demonstrated an RMS value of approximately 1.28 nm. This is proof that the addition of compound T enhances the interface quality between the active layer and hole transport layer, thereby indicating an improvement in FF and other PV parameters[159].
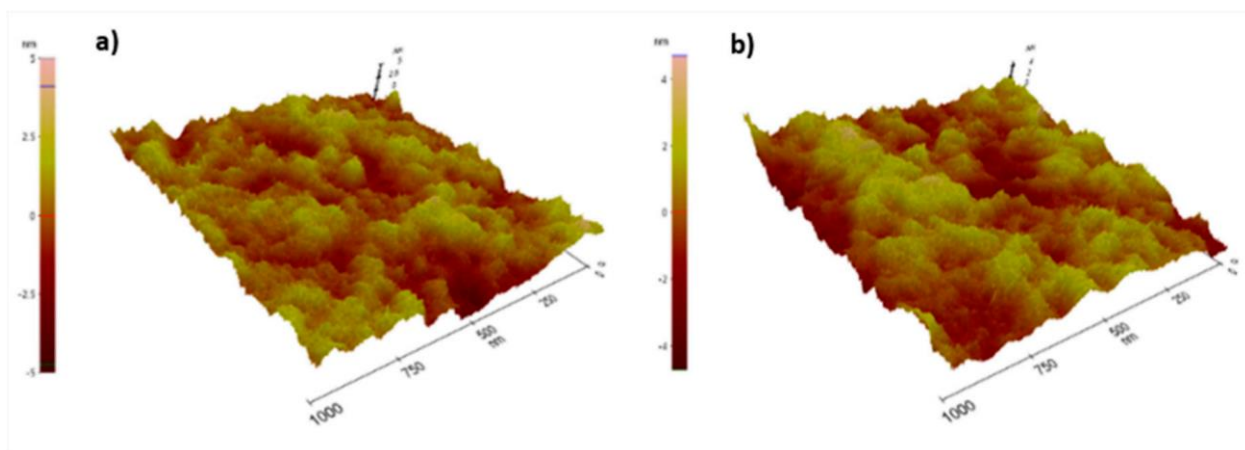
Figure 35. AFM images of a) binary and b) ternary bulk heterojunction film with 5% compound T content.

Conclusions

In conclusion, simple ternary inverted organic solar cells incorporating the soluble compound T, into the photoactive layer of the binary PTB7:PC$_{71}$BM blend were fabricated by differentiating additive's concentration from 3% to 15%. The incorporation of the compound T led to a favorable energy alignment between the energy levels of PTB7 donor and PC$_{71}$BM acceptor, thus facilitating the electron-cascade effect. The champion ternary blend device based on the ITO/PFN/PTB7:compound T:PC$_{71}$BM/MoO$_3$/Al structure, with a 5% (v/v) concentration of compound T, resulted in a PCE of 8.34%, with an enhancement of 12% compared to the reference device. Therefore, since compound T had a wide optical bandgap and low HOMO level, it demonstrated the potential for boosting device performance of other visible, as well as the near-infrared non-fullerene blends like, which are of great interest for the OSC community.

6.1.2 Graphene-Based Ink for Ternary OPVs

*Minas M. Stylianakis, Dimitrios M. Kosmidis, Katerina Anagnostou, Christos Polyzoidis, **Miron Krassas**, George Kenanakis, George Viskadouros, Nikolaos Kornilios, Konstantinos Petridis and Emmanuel Kymakis*

Due to the highly increased global demand for low-cost energy generation during the last three decades, significant research efforts took place towards the development and progress of organic solar cells (OSCs), in order to boost their competitiveness over silicon technology[160,161]. Owing to several attractive properties, including light weight, flexibility, low manufacturing costs, and compatibility with large-area processes, OSCs is considered as one of the most prominent photovoltaic technologies for sustainable energy production[162]. Very recently, alternative optimized architectures such as tandem structures, novel donors and non-fullerene acceptor design and synthesis, as well as ternary systems have escalated the performance of OSCs over 14%[163,164,165,166].

Unlike to the typical binary OSC configuration, that is based on a donor-acceptor bulk heterojunction (BHJ) blend, the ternary one contains a third component which can function as: i) second donor, ii) second acceptor and iii) non-volatile additive. The operation of a ternary OSC device relies on one of the four existing dominant mechanisms including: (1) charge transfer, (2) Forster resonance energy transfer, (3) parallel-linkage and -last but not least- (4) alloyed donor structure mechanism[167]. Thus, according to the above mechanisms, small molecules[168,169,170,171,172], polymers[173,174], dye molecules[175], graphene-based materials[176,134] or 2D materials[177] could be chosen and incorporated as additives within the binary active layer.

This study discusses for the first time the design and synthesis of a novel graphene-based material (GO-TNF) through simple chemical processes as well as its direct incorporation in ink form within the binary active layer (PTB7:PC$_{71}$BM) for the realization of inverted ternary OSC devices. GOTNF consists of GO as core and TNF side groups linked with ethylenediamine (EDA) aliphatic spacers. Since the energy levels of the synthesized graphene-based molecule and these of PTB7 and PC$_{71}$BM perfectly match, GO-TNF ink was incorporated in different ratios ranging from 1 to 3%. Upon GO-TNF incorporation, charge transfer operational mechanism dominated (cascade effect), while the photovoltaic performance was boosted in all ternary devices compared to the

reference cell. The champion device, containing 2% v/v GO-TNF ink, exhibited a significant enhancement by ~13%, leading to a power conversion efficiency (PCE) of 8.71%.

Synthesis and characterization of GO-TNF

Foer the preparation, 9-oxo-fluorene-4-carboxylic acid 97%, 1,2-ethylenediamine (EDA) puriss. p.a., absolute, $\geq$99.5% (GC), graphite synthetic, H_2SO_4 95-97%, fuming HNO_3 70%, $SOCl_2$ ReagentPlus >99%, were purchased from Sigma Aldrich.

The preparation of GO-TNF took place into several steps, as it is depicted in Figure 39. First, 9-oxo-fluorene-4-carboxylic acid was nitrated using a mixture of concentrated sulfuric acid (H_2SO_4, 95-97%) and fuming nitric acid (HNO_3, 70%), yielding 2,5,7- trinitro-9-oxo-fluorene-4-carboxylic acid (TNF-COOH). Afterwards, the carboxyl group of TNF was chlorinated using thionyl-chloride ($SOCl_2$), to get 2,5,7-trinitro-9-oxo-fluorene-4-acyl-chloride (TNFCOCl). The linkage of TNF-COCl with 1,4-ethylenediamine (EDA) was held via a typical nucleophilic substitution reaction to obtain TNF-EDA. In the second parallel step, GO was prepared via a modified Hummers' method and was subsequently acylated, using $SOCl_2$ to get GO-COCl. The final GO-TNF was extracted upon the coupling between GO-COCl and TNF-EDA through a nucleophilic substitution reaction. Finally, GO-TNF ink was prepared as described in the SI. Below, the above steps will be analyzed in detail.
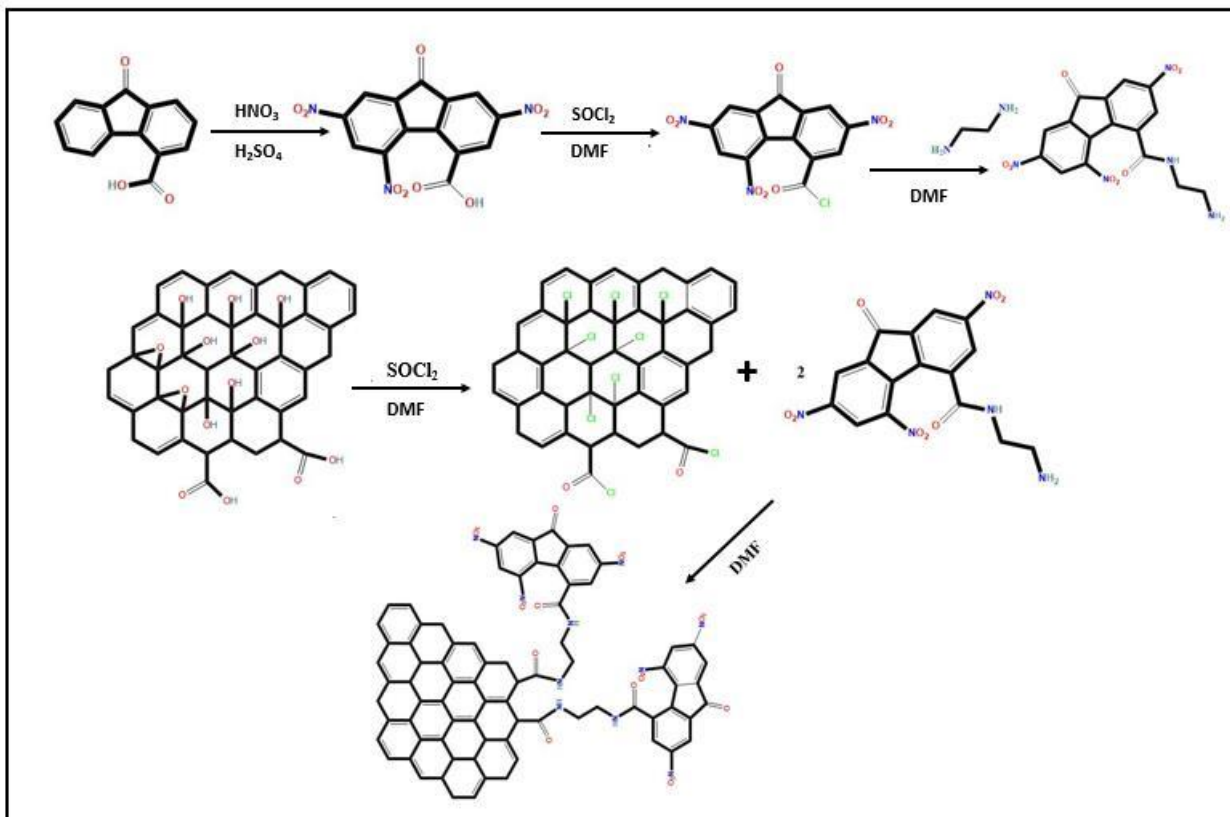
Figure 36. Schematic representation of the chemical synthetic procedure.

1. Preparation of TNF-COOH

8 ml of concentrated (95-97 %) sulfuric acid (H_2SO_4) were added slowly to a separation funnel containing 1 g of 9-oxo-fluorene-4-carboxylic acid. The color of H_2SO_4 changed immediately after the addition from colorless to dark red. The solution was firmly mixed and added dropwise, over a 15 minute period of time, to a refluxing mixture of 13 ml fuming nitric acid (HNO_3) and 8 ml of concentrated H_2SO_4. The temperature of the refluxing mixture of concentrated H_2SO_4 and fuming HNO_3 was 85 °C. Afterwards, a mixture of 9 ml fuming HNO_3 and 11 ml of concentrated H_2SO_4 was added dropwise over a 4.5 hours period of time. After cooling to room temperature, the reaction mixture was left under N_2 atmosphere and stirring overnight. Subsequently, the reaction solution was poured into ice water (100 mL) and the yellow solid which precipitated was collected onto a G5 filtration funnel. The yellow solid was washed with 5 ml of 0.05 % aqueous solution of sodium bicarbonate in order to remove any amount of residual acid. Then it was dried overnight at 40 °C. Afterwards, it was collected and recrystallized with methanol. The recrystallization

process occurred with the dissolution of the product to the smallest possible amount (5-7 ml) of methanol that was brought to reflux, followed by the placement of the solution flask to the refrigerator overnight. The residual precipitate was then collected on a G5 filtration funnel and dried at 40 °C overnight. TNF-COOH in powder form was characterized by ATR FT-IR (Figure 40).
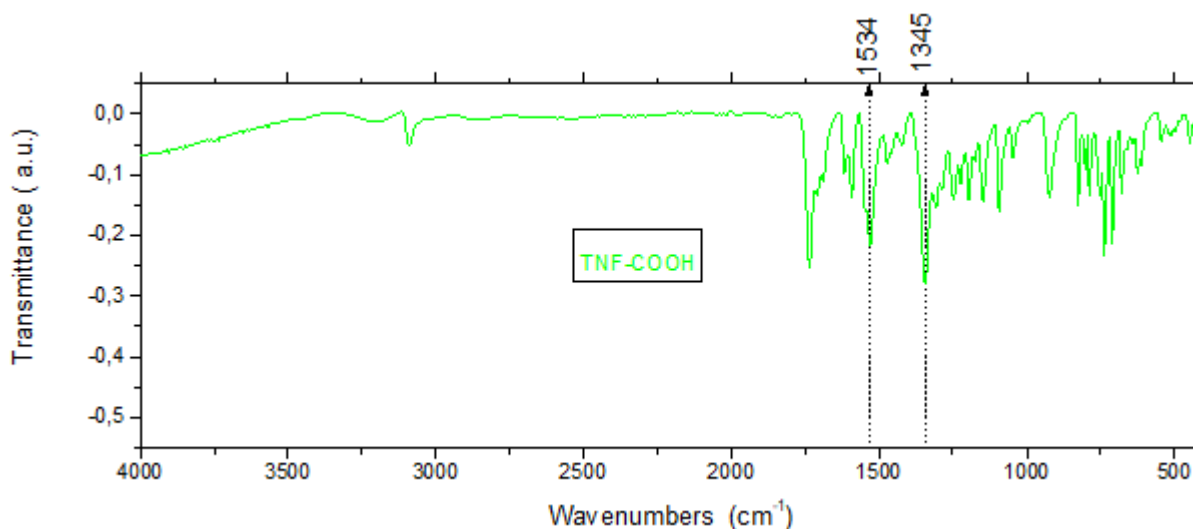
Figure 37. ATR FT-IR spectrum of TNF-COOH. The peaks at 1534 and 1345 cm^{-1} are attributed to NO$_2$ stretching vibrations, which strongly indicate the successful nitration of 9-oxo-fluorene-4-carboxylic acid.

2. Preparation of 2,5,7-trinitro-9-oxo-fluorene-4-acyl-chloride (TNF-COCl)

0.5 g of TNF, 25 ml of thionyl chloride (SOCl$_2$) and 1 ml of DMF were added to a 50 mL round bottom flask. Subsequently, the reaction solution was brought to reflux condition (75 °C) under N$_2$ atmosphere for 18 hours. Afterwards, SOCl$_2$ was removed via distillation at 85 °C and the residual precipitate was washed with diethyl-ether, in order to completely remove any amount of SOCl$_2$ that remained after the distillation process was completed. Finally, the product of TNF-COCl was recrystallized with a very small amount of toluene and dried overnight at 60 °C. The product was used immediately after its preparation in order to avoid degradation.

3. Preparation of TNF-EDA

0.3 g of TNF-COCl and 12 ml of THF were added in a dried 50 ml round bottom flask. Then, the reaction mixture was placed in an ice bath until the temperature dropped to 3 °C. Subsequently,

0.2 ml of ethylenediamine (EDA) was added under continuous stirring. A sharp color change was observed after the addition from yellowish to light brownish. During the next hour, 1 ml of triethylamine was added dropwise, in order to adduct the producing HCl, precipitate as a salt and increase the reaction yield. The reaction mixture was centrifuged, and the residual precipitate was washed with slightly acidified water. Thereupon, several washes with 2D water of the solid were conducted and the product was placed in the oven at 60 ^{o}C for 6 h to dry. TNF-EDA in powder form was characterized by ATR FT-IR (Figure 38).
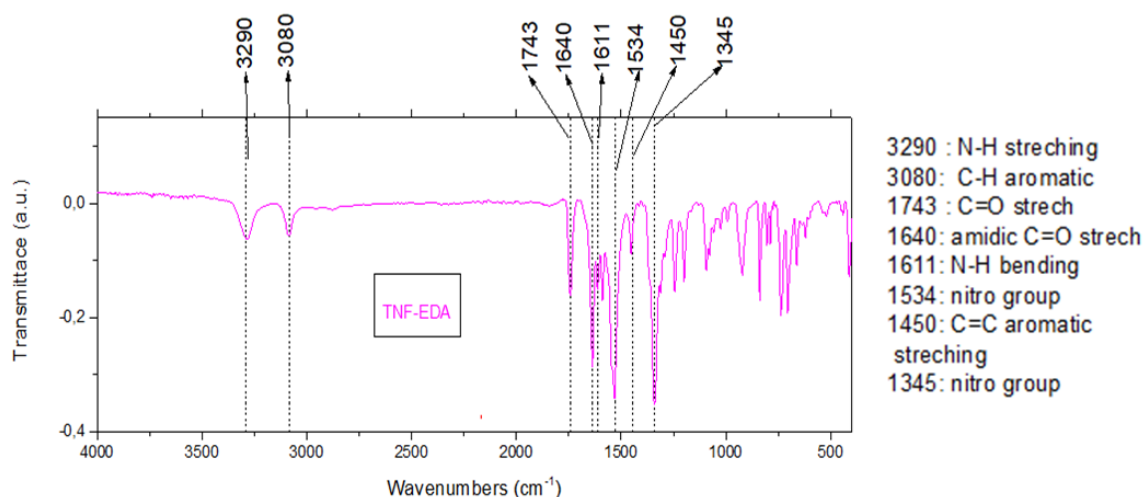
Figure 38. ATR FT-IR spectrum of TNF-EDA

4. Preparation of Graphene Oxide (GO)

GO was synthesized from graphite powder according to the modified Hummer's method. 1 g of graphite was placed in a 400 ml reaction beaker. Then the beaker was placed in an ice bath and 40 ml of concentrated H_2SO_4 were added. The mixture was left under stirring for 20 minutes and 1 g of $NaNO_3$ was added slowly while the ice from the ice bath was being frequently replaced. After another hour of stirring in low temperature, 6 g of $KMnO_4$ were added very slowly to the reaction mixture. The solution was left under stirring overnight and then it was heated for 100 minutes at 35 ^{o}C. Afterwards, the mixture was heated to 90 ^{o}C and 80 ml of water was added. Continuously, it was left under stirring for another 40 minutes. Thereupon, the heating was turned off and 200 ml of water were added very slowly. Subsequently, 20 ml of H_2O_2 were added very slowly in order to react with the residual $KMnO_4$. The reaction mixture was left to cool down to room temperature and then was centrifuged. The residual precipitate was washed with 200 ml of hot water (65 ^{o}C).

64

Several washes with water (25 °C) followed until the pH of the supernatant was 7. The precipitate was dried for 5 days at 80 °C. Afterwards, it was pulverized and stored in vials for further use.

5. Acylation of GO, preparation of graphene oxide acyl-chloride (GO-COCl)

30 mg of GO, 20 ml $SOCl_2$ and 0.5 ml of DMF were added in a dried 100 ml round bottom flask. The mixture was sonicated for 1 hour and was left under N_2 atmosphere in reflux condition for 24 h. Afterwards, the solvent was removed via distillation and the resulting precipitate was washed with THF multiple times. Then, the product was dried in an oven overnight at 60 °C.

Synthetic procedure of the final GO-TNF

13 mg GO-COCl and 42.4 mg of TNF-EDA were dispersed in 15 ml of dimethylformamide by a 10-minute ultrasonication at room temperature. Subsequently, 2 ml of triethylamine were added to the reaction flask. The mixture was stirred and refluxed (137 °C) for 72h, under N_2 atmosphere. Afterwards, the mixture was cooled at room temperature and poured in a centrifugal funnel, along with the solid product that was collected from the walls of the reaction flask. The reaction solution was centrifuged for 1.5 h and the solid was collected and washed with 2-4 ml of methanol (primary product). The supernatant was mixed with 15 ml of anhydrous diethyl-ether in order to boost the precipitation of the secondary product. Then, the residual precipitate was centrifuged for 100 minutes, washed with ethanol 5 times and put to the oven at 45 °C overnight.

Finally, GO-TNF ink preparation GO-TNF was dispersed in anhydrous CB (0.5 mg/mL) through ultrasonication for 45 minutes, using an Elmasonic S_30H sonication bath. Afterwards, the dispersion was centrifuged at 4200 rpm for 30 minutes and a concentrated supernatant (GO-TNF ink) was isolated and decanted. The final GO-TNF ink was used without further purification. The solvent's selection (anhydrous CB) for GO-TNF ink preparation was done by taking into account that the binary blend ($PTB7:PC_{71}BM$) of the active layer of the inverted OSC was also dissolved in anhydrous CB.

GO-TNF thin films preparation for microscopic characterization

Cleaning process of glass substrates

The glass substrates were cleaned using a 5-step cleaning process. Firstly, the glass substrates were sonicated into an aqueous solution of detergent for 15 minutes. Afterwards, the residual amount of aqueous detergent solution was wiped and blown away from the glass substrates. Subsequently, the same procedure was followed using different solvents with the following order: 1) deionized water 2) acetone 3) isopropanol. Then the glass substrates were dried in the oven for 30 minutes. Thereafter, the glass substrates underwent a UV-ozone treatment in an M-BRAUN glovebox in order to be more furtherly purified and for their hydrophilicity to be increased.

GO-TNF thin films fabrication

Immediately after the UV-ozone treatment of the 5-step cleaning process, the glass substrates were sprayed with an infinity CR Plus spray gun filled with 4 ml of the wanted dispersion. The spray gun was mounted onto a custom made, automatically moving axis, 12 cm above the glass substrates which were constantly heated at 180 °C. After each spray cycle, the substrates were given one minute in order for the solvent to be evaporated. The pressure of the air that was fed into the spray gun was 2 bar.

The morphology of GO-TNF was examined using field emission scanning electron microscopy (FE-SEM). Representative SEM images of its flakes coated on silicon substrates are demonstrated in Figure 39. The size of the wrinkled GO-TNF flakes varies ranging from 100 nm to 1 μm while it should be reported that no charging was observed during SEM imaging, thus indicating that the formed network was electrically conductive.
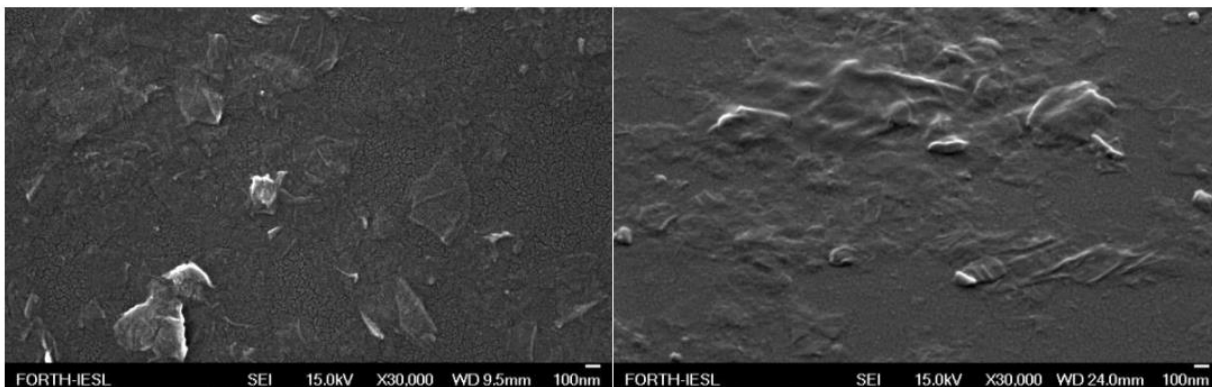
Figure 39. FE-SEM images of GO-TNF.

OSC Device Fabrication

All OSC devices were fabricated in a typical sandwich inverted geometry consisting of a bottom indium tin oxide (ITO) coated glass substrates electrode, poly [(9,9-bis(3'-(N,N-dimethylamino)propyl)-2,7-fluorene)-alt-2,7-(9,9–dioctylfluorene)] (PFN) as the ETL, a PTB7:PC$_{71}$BM BHJ thin film as the active layer, a MoO$_3$ as the HTL and a top metal (Al) electrode. GO-TNF ink was directly incorporated within the binary photoactive layer, in ratios ranging from 1 to 3% ratio to the polymer for the fabrication of the ternary devices. The schematic representation of the device and the respective energy level diagram are depicted in Figure 40.
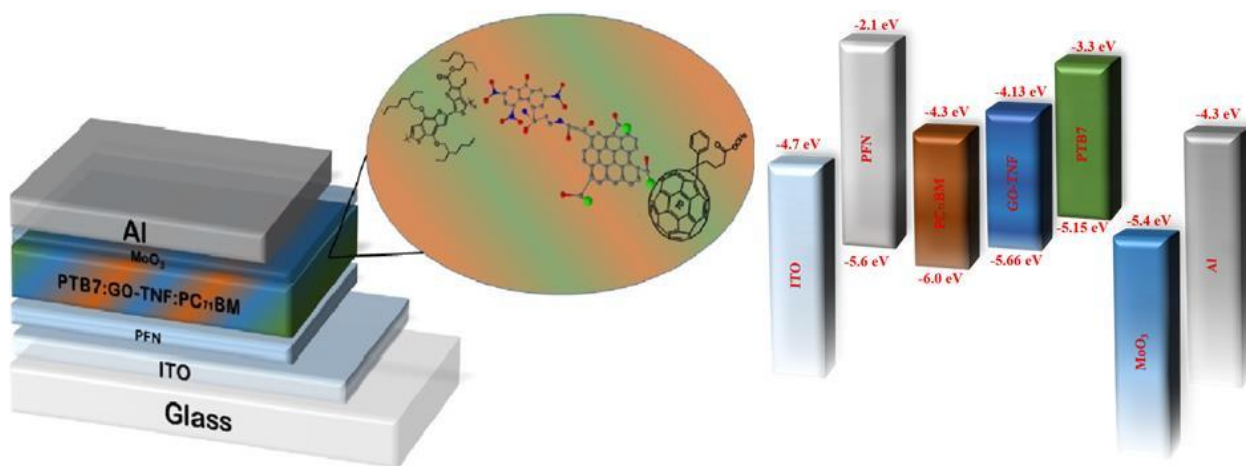
Figure 40. Schematic representation of the ternary OSC device (left) and energy levels diagram (right).

Results and Discussions

ATR FT-IR spectra of GO and GO-TNF, in powder form, are presented in Figure 41. Pristine GO (black line) shows a broad and strong peak at 3390 cm^{-1}, which is attributed to O–H stretching vibration of the OH- moieties. Furthermore, stretching vibration of C=O moieties is appeared at 1706 cm^{-1}, while the remaining graphitic domains (C=C) stretching vibration are shown at 1568 cm^{-1}. In addition, C-O-H bending vibration due to COOH groups are presented at 1394 cm^{-1}. The peaks at 1143 cm^{-1} and 1027 cm^{-1} represent C-OH stretching vibration of the hydroxide domains and the stretching vibration of C-O-C groups, respectively. On the other hand, GO-TNF (red line), exhibits a broad peak of low intensity at 3331 cm^{-1}, indicating a N-H stretching vibration. Next, a peak at 1697 cm^{-1} is attributed to C=O stretching vibration deriving from the carbonyl moiety of trinitrofluorenone. Moreover, two peaks occurred at 1652 cm^{-1} and 1575 cm^{-1} are due to amidic C=O stretching vibration. NO$_2$ asymmetric and symmetric stretch vibrations are shown at 1525 cm^{-1} and 1334 cm^{-1}, respectively, as well as the peak at 1446 cm^{-1} corresponds to the aliphatic a-CH$_2$ bending vibration of ethylenediamine moiety. Finally, C-N stretching vibration of the ethylene diamine moieties appears at 1105 cm^{-1}.
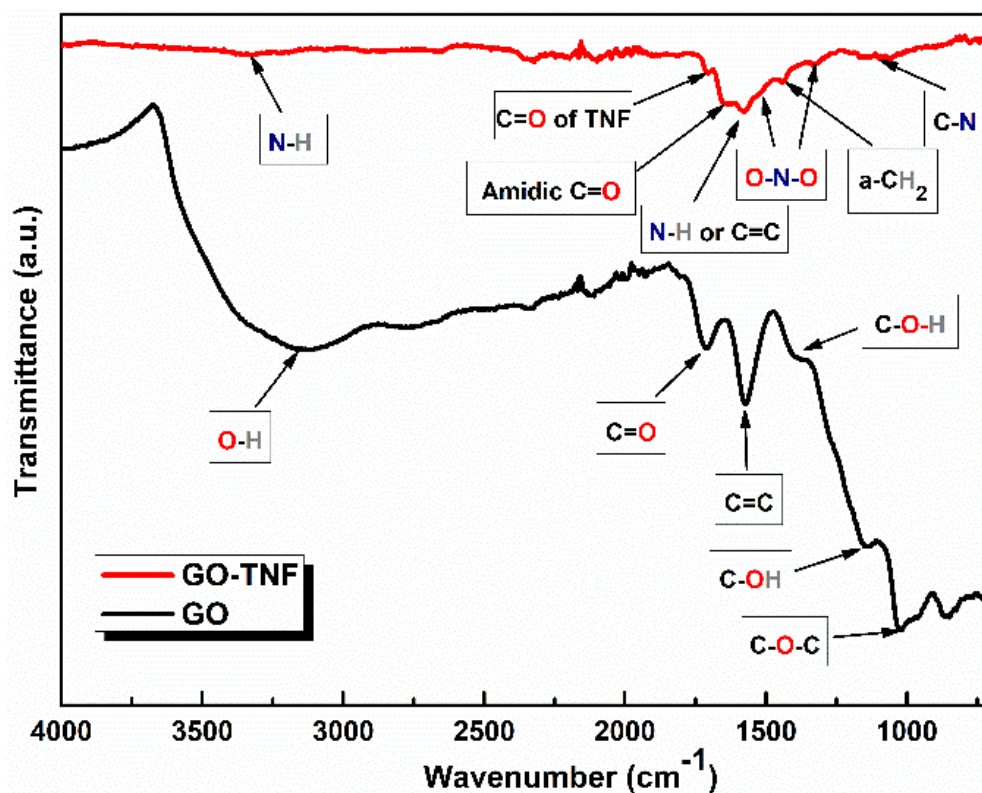
Figure 41. ATR FT-IR spectra of GO (black line) and GO-TNF (red line) in transmission mode.

In Figure 42, UV-vis spectra of GO and GO-TNF in solid state are presented. Due to the strong attachment of TNF moieties to the edges of the lattice of GO, the absorption spectrum of GO-TNF is broader than that of the pristine GO, exhibiting a shoulder at ~365 nm. This fact indicates that there is a strong interaction between the GO lattice and TNF moieties, which is mainly attributed to the enhanced electron delocalization caused by TNF.
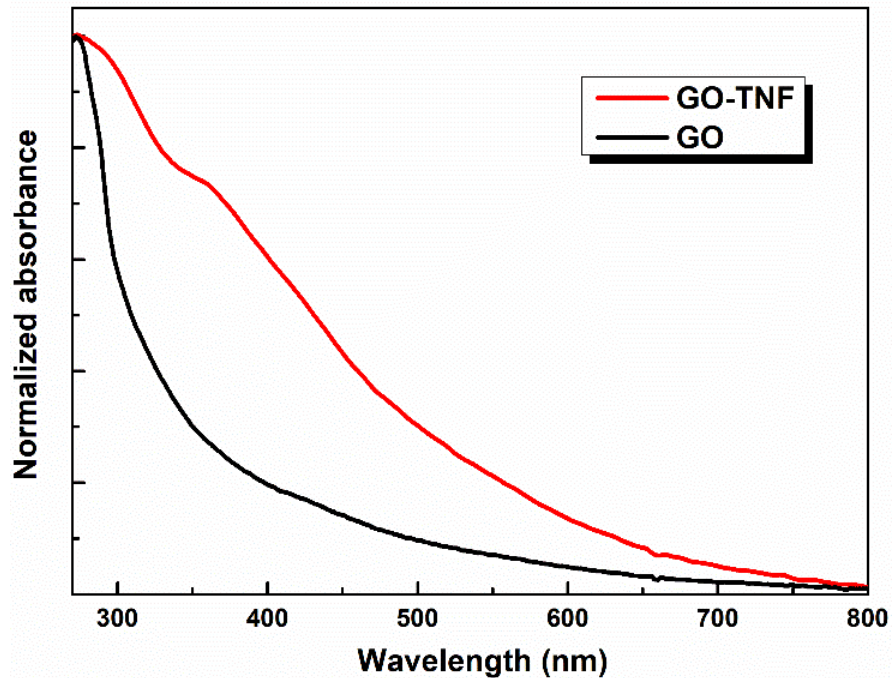
Figure 42. UV-vis spectra of GO (black line) and GO-TNF (red line).

Raman spectra of GO and GO-TNF are shown in Figure 43. No shift is observed for both D and G peaks of GO compared to the respective ones of GO-TNF; D bands occurred at ~1340 cm^{-1}, while G bands at ~1580 cm^{-1}. However, a difference in the relative intensity ratio (I_D/I_G) was observed from 0.92 for GO to 1.04 for GO-TNF, indicating that the linking between GO and TNF increased disorder and defects in the graphitic lattice.
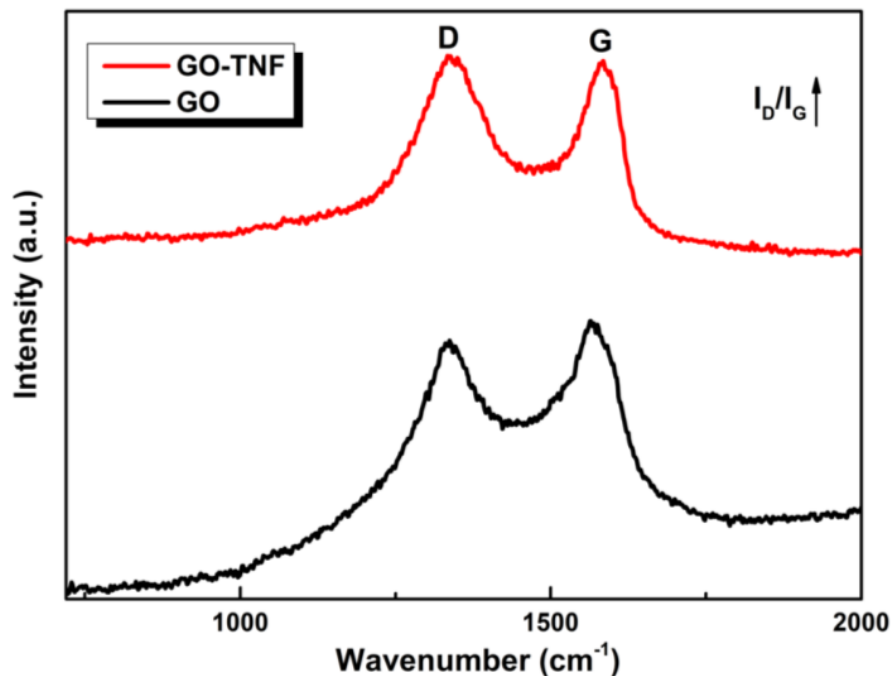
Figure 43. Raman spectra of GO and GO-TNF.

Photoluminescence (PL) measurements were conducted to evaluate charge transfer mechanism upon the incorporation of GO-TNF within the active layer, and the respective PL spectra are depicted in Figure 44. In this context, PTB7 and PTB7:GO-TNF thin films were excited at 471 nm presenting an emission band around 760 nm corresponding to radiative decay of photogenerated excitons from the excited state to ground state[178]. When 2% v/v GO-TNF ink was added, PL intensity quenching is significant owing to the better energy offset between the LUMO levels of PTB7 and GO-TNF that enhances the charge transfer mechanism. In our case, the incorporation of GO-TNF ink with an optimum concentration of 2% v/v, facilitates exciton dissociation at the PTB7:PC_{71}BM interface thus leading to a higher number of electrons that can be collected by the cathode, which is in agreement with the champion current density value achieved so far (17.65 mA cm^{-2})[179].
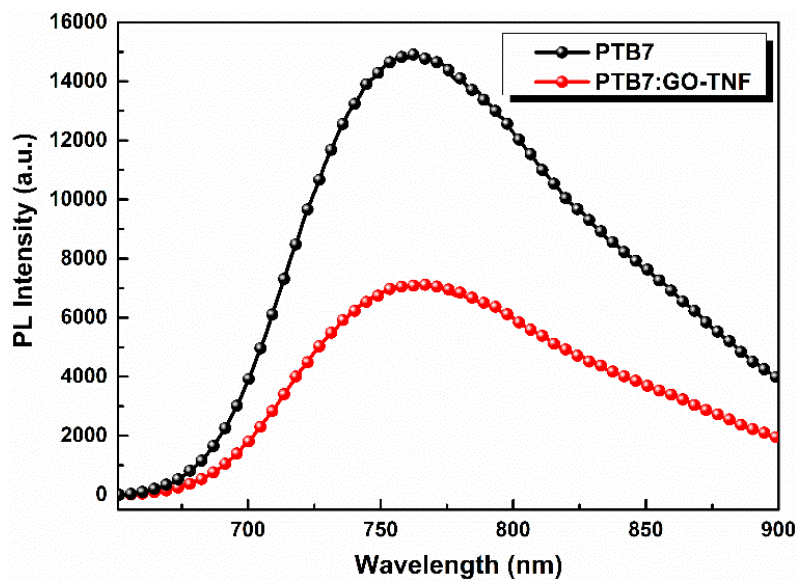
Figure 44. PL spectra of PTB7 (black) and PTB7:GO-TNF (2%) (red).

The crystallinity of pristine GO and GO-TNF was investigated by X-ray diffraction (XRD) in a 2θ range from 5º to 60º (Figure 45). GO displays a narrow peak at 9.51o which is attributed to the main reflection (002) of its stacks with an interlayer d-spacing of ~ 8.2 Å , while a second weak peak appearing at 42.69º is due to the turbostratic band of disordered carbon materials[180]. On the other hand, GO-TNF exhibits a broad peak at 24.99º referring to (002) reflection with a slightly increased d-spacing of 9.1 Å which is attributed to GO covalent bonding with TNF moieties.
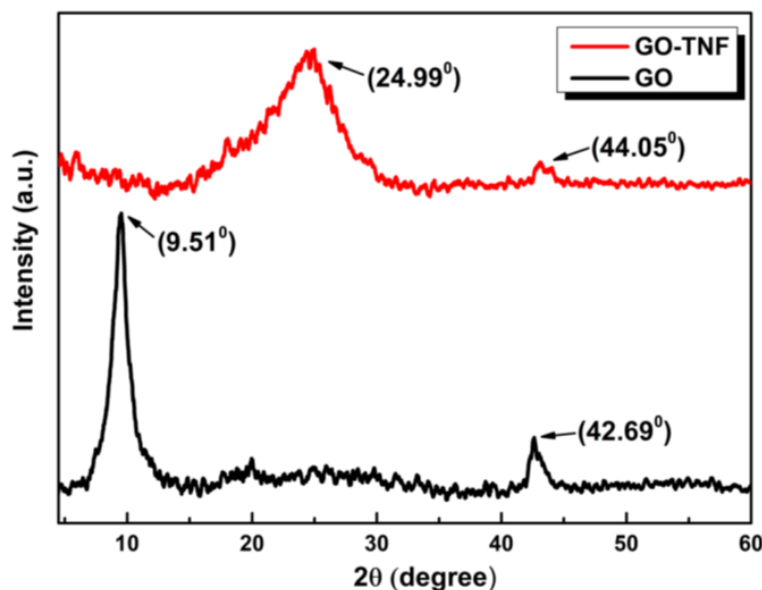
Figure 45. X-ray diffraction patterns of GO (black) and GO-TNF (red).

Figure 46 displays TGA curves of GO and GO-TNF obtained under inert atmosphere with a heating rate of 10 ^{o}C/min, while the maximum temperature limit was set at 800 ^{o}C. First, GO exhibited a moderate weight loss of 5% at a 210 ^{o}C, which was followed by a steep weight loss of 37% at about 270 ^{o}C due to oxygen functional groups' pyrolysis. Its total mass loss was 40% at 800 ^{o}C. On the other hand, GO-TNF presented an improved thermal stability when compared to GO, since the total loss did not exceed 22% of its initial weight. The improved thermal stability of GO-TNF was attributed to successful amide bond formation between GO and TNF that enhance thermal stability[181].
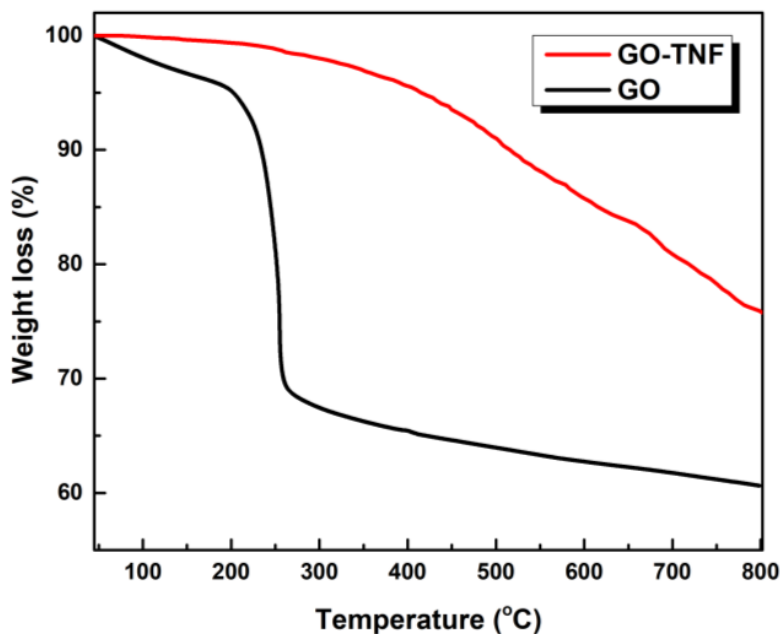
Figure 46. TGA curves of GO (black) and GO-TNF (red) taken under N2 atmosphere and 10 °C/min

To determine the energy levels of GO-TNF, cyclic voltammetry measurements were carried out using an electrolytic solution of TBAPF$_6$ in CH$_3$CN 0.1M, with a scan rate of 10 mVs^{-1}, between the potential sweep window of -2 V to +2V, as demonstrated in Figure 47. The energy HOMO and LUMO levels of GO-TNF were calculated using the empirical relations below[182]:

$$E_{HOMO}= - (E_{(onset,ox \text{ vs } Fc+)Fc]} + 5.1)(eV), \text{ Eq. 11}$$

$$E_{LUMO}= - (E_{(onset,red \text{ vs } Fc+)Fc]} + 5.1)(eV), \text{ Eq. 12}$$

The HOMO level was approximately -5.66 eV as calculated by the oxidation peak onset 0.53 V, while its LUMO level was extracted from the onset of the reduction peak (0.85 V) and was -4.13 eV.
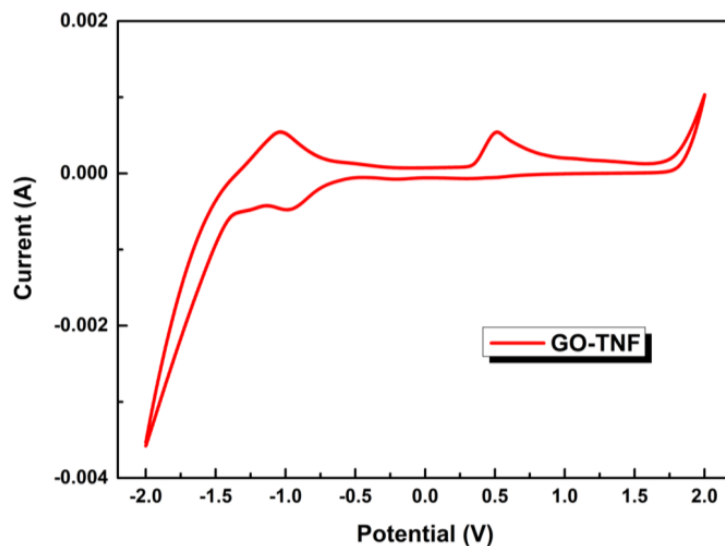
Figure 47. Cyclic voltammogram of GO-TNF.

Several OSC devices were fabricated by incorporating GO-TNF ink within the binary PTB7:PC$_{71}$BM photoactive layer (Figure 40) in various ratios (1, 2 and 3%) and J-V characteristic curves were exported to evaluate its operational role into device's PV performance (Figure 48). It is obvious that the presence of GO-TNF was beneficial, as stated below in Table 3.

Table 3. PV characteristics summary of the OSC devices based on PTB7:GO-TNF:PC$_{71}$BM ternary blends*

GO-TNF content (%)	J$_{sc}$ (mA/cm^2)	Calc. J$_{SC}$ (mA/cm^2)	V$_{oc}$ (mV)	FF (%)	PCE (%)
Reference	16.20 ± 0.45	15.72	760 ± 10	61.8 ± 0.7	7.61 ± 0.11
1	16.54 ± 0.54	16.21	760 ± 50	63.0 ± 0.4	7.92 ± 0.26
2	17.21 ± 0.44	16.78	760 ± 11	64.0 ± 0.1	8.37 ± 0.34
3	16.53 ± 0.35	16.21	760 ± 90	62.4 ± 0.6	7.84 ± 0.17

*The data were averaged from 10 identical devices with 6 cells each
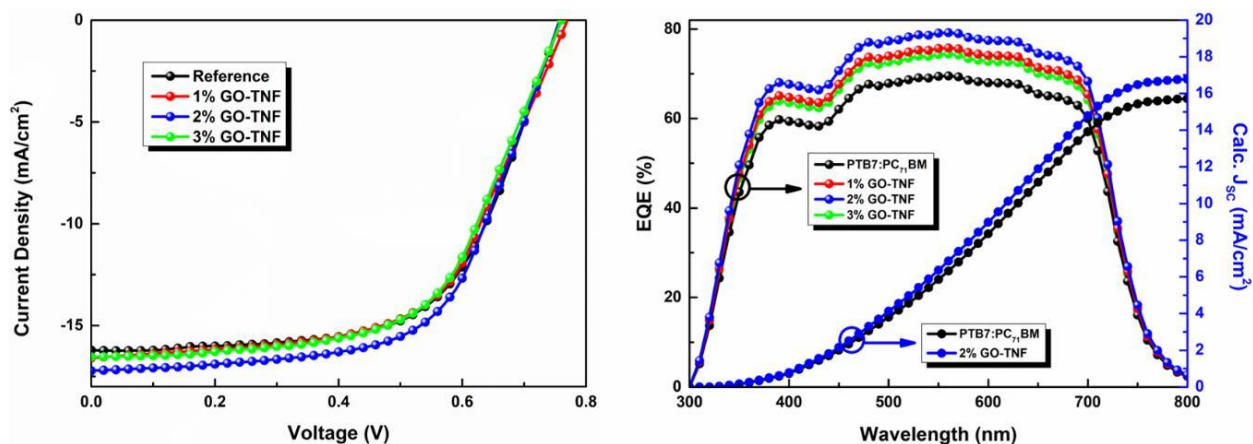
Figure 48. J-V characteristics (left) and EQE curves (right) of the reference (PTB7:PC$_{71}$BM) and the devices incorporating different GO-TNF ink content. The calc. J$_{SC}$ curves (inset in EQE) correspond to the reference and the champion device with 2% GO-TNF ink content.

All ternary devices showed an improved performance, especially the device containing 2% v/v GO-TNF ink. In particular, the champion device exhibited a current density (J$_{SC}$) of 17.65 mA/cm^2 and a power conversion efficiency (PCE) of 8.71% that show an improvement of ~10% and ~13% respectively when compared to the reference device.

To further confirm the experimental J$_{SC}$ improvement due to the incorporation of GO-TNF, external quantum efficiency measurements were conducted to determine the calculated J$_{SC}$. Figure 48 depicts the external quantum efficiency (EQE) curves of the reference, as well as the champion ternary OSC device incorporating 2% v/v GO-TNF ink.

It can be seen that the EQE enhancement is mainly due to J$_{SC}$ increase. The accuracy of the PV measurements was checked, by calculating the J$_{SC}$ values of the OSCs from the integration of the EQE spectra. The calculated J$_{SC}$ was found to be -15.72 mA cm^{-2} and -16.78 mA cm^{-2} for the binary and the 2% GO-TNF ink content ternary devices, respectively, which are within the standard deviation from the J$_{SC}$ obtained from the J–V curves. It should be also noted that any concentration of GO-TNF ink higher than 3% wt. resulted to short circuit, probably due to the occurrence of local shunts. This undesired effect could be linked with the concentration of GO-TNF ink in the blend that becomes enough to allow a direct bridging with the ITO electrode.

To get a more accurate insight into the influence of GO-TNF blend into the charge transfer process in the ternary approach, hole-only and electron-only cells were fabricated to calculate the hole and electron mobility, respectively. Measurements were based on space charge limited current method. Hole-only cells and electron-only cells were fabricates using the architecture indium tin oxide ITO/PEDOT:PSS/PTB7:GO-TNF:PC$_{71}$BM/MoO$_3$/Al for holes and ITO/PFN/PCDTBT:GOTNF:PC$_{71}$BM/Ca/Al for electrons, respectively. The evaluation of the charge carrier mobilities was based on the Mott–Gurney equation[183]:

$$J = \frac{9}{8}\mu_h\varepsilon_o\varepsilon_r \frac{(V-V_{bi})^2}{L^3}, \text{Eq. 13}$$

where ε_r is the relative dielectric constant, ε_0 is the permittivity of free space, μ is the charge carrier mobility, V is the applied voltage, V_{bi} is the built-in potential, and d is the active layer thickness.

Figure 49 illustrates J–V^2 characteristics under dark conditions for a) electron-only and b) hole only devices, respectively, where the black line refers to the control device (PTB7:PC$_{71}$BM), while the red line corresponds to the champion ternary one PTB7:GO-TNF (2%):PC$_{71}$BM. According to J–V^2 characteristics, although hole mobility did not present any significant change upon the addition of GO-TNF, the respective electron mobility has shown a significant improvement, passing from 7.80×10^{-5} cm^2 V^{-1} s^{-1} to 9.93×10^{-5} cm^2 V^{-1} s^{-1} (Table 4). This improvement in electron mobility obviously originates from the presence of GO-TNF that provided energy levels' perfect match, as well as better exciton dissociation interfaces, as presented in the next section. Hence, the observed electrons' mobility enhancement is directly associated with the cascade effect facilitating electrons' transition from PTB7 to the ITO electrode.
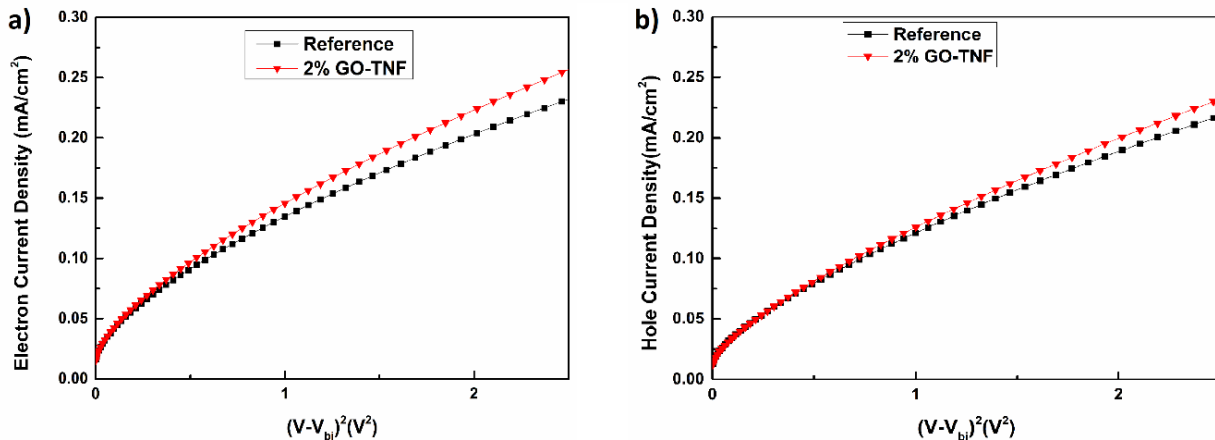
Figure 49. J-V^2 characteristics of the fabricated a) electron-only and b) hole-only devices. The black line refers to the control device (PTB7:PC$_{71}$BM), while the red line corresponds to the ternary PTB7:GO-TNF (2%):PC$_{71}$BM.

Table 4. Hole and electron mobilities of PTB7:PC$_{71}$BM and ternary blend PTB7:GO-TNF:PC$_{71}$BM.*

Active layer	μ_h (cm^2 V^{-1} s^{-1})	μ_e(cm^2 V^{-1} s^{-1})	Ratio (μ_h / μ_e)
PTB7:PC$_{71}$BM **(reference)**	1.28×10^{-4}	7.80×10^{-5}	1.64
1% GO-TNF	1.31×10^{-4}	8.71×10^{-5}	1.50
2% GO-TNF	1.39×10^{-4}	9.93×10^{-5}	1.39
3% GO-TNF	1.34×10^{-4}	8.03×10^{-5}	1.67

*The data were averaged from 10 identical devices with 6 cells each.

Conclusions

We reported the synthesis and characterization of a new graphene-trinitrofluorenone derivative, named GO-TNF, as well as its operational role as the cascade material between the LUMO energy levels of PTB7 and PC$_{71}$BM, in efficient ternary OSCs. Due to its ideal energy levels, it was directly incorporated, as the third component, within the binary photoactive layer providing a significant improvement in current density of the champion device (2% v/v GO-TNF ink) by ~10%. Respectively, the PCE value of the same device was higher by ~13%, leading to a champion

efficiency of 8.71%. Our efforts proved that the insertion of graphene derivatives is a very promising way towards the fabrication high performance OSCs.

6.2 Low band gap polymer for OPVs

Christos L. Chochos , Athanasios Katsouras, Sofia Drakopoulou, Christina Miskaki, **Miron Krassas***, Pavlos Tzourmpakis, George Kakavelakis, Christian Sprau, Alexander Colsmann, Benedetta M. Squeo, Vasilis G. Gregoriou, Emmanuel Kymakis, Apostolos Avgeropoulos*

Low-bandgap (LBG) semiconducting polymers with bandgaps smaller than 1.4 eV and absorption cut-off in the near infrared (NIR) are of great interest for organic photovoltaics (OPV), organic photodetectors, ambipolar field-effect transistors (FETs) and bio-imaging applications.[184,185,186,187,188] Intense efforts have been devoted to the synthesis of new polymers for such applications, and tremendous progress has been made. Among the various classes of LBG conjugated polymers, diketopyrrolopyrrole (DPP) polymers have attracted considerable attention, today yielding power conversion efficiencies (PCEs) above 8% in polymer solar cells[189,190,191] and hole and electron mobilities of 17.8 and 6.3 cm^2 V^{-1} s^{-1} in FETs.[192,193] Currently, enormous number of new DPP-based conjugated polymers have been reported, which are presented in some excellent reviews. One of the most promising class of DPP-based polymers are those consisting of quarterthiophene as the electron donating (D) unit. Janssen et al. first reported a DPP quaterthiophene copolymer for organic solar cells, which exhibited an optimal PCE of 4.0% with a Jsc of 11.3 mA/cm^2, a Voc of 0.61 V, and a FF of 0.58.[194] DPP copolymers offer a wide range of structural optimization opportunities as they can be tuned via their aromatic substituents, their alkyl side chains, and the nature of the p-conjugated segment-linking units along the polymer backbones.[195]

The rigid backbone of conjugated polymers and their characteristic feature to aggregate via p-p stacking lend a reduced solubility to these materials in common organic solvents.[196] To cope with this challenge, often various alkyl side chains are screened and attached to the polymer backbone.[197] Alkyl chains are the most commonly used side chains in polymeric semiconductors. Whereas their initial role was to ensure polymer solubility in organic solvents and good processability toward thin-film formation[198], today, more and more studies have demonstrated the substantial impact of the flexible chains on the supramolecular self-assembly through different intermolecular interactions of the polymer chains[199,200] and consequently on their device performances. Even subtle changes of the flexible chains may greatly influence the device

performance.[201,202,203] Parameters that influence the molecular packing include the length of the side chains[204,205] as well as the substitution position,[206] their density,[207,208] and the bifurcation point of branched alkyl chains.[209,210] The optimum choice of alkyl side chains is not universal. For each semiconducting polymer, an extensive screening of structural modifications is required. Specifically, for DPP copolymers, very few studies on alkyl side chain optimization have been presented so far in the field of OPV.[211,212,213]

In this contribution, we set out to study the relation of molecular structures, optoelectronic properties, and solar cell performance to optimize alkyl side chain positioning and aromatic substituents in LBG DPP-based copolymers. We examine the influence of anchoring two linear dodecyl side chains in two different positions, namely tail-to-tail (TT) and head-to-head (HH), at the two outer thiophene units in the backbone of a quaterthiophene-based DPP copolymer (DPP4T) by the synthesis of DPP4Ta (TT) and DPP4Tb (HH) (Fig.50). Then, to study the impact of the flanked aromatic substituent of DPP, the thiophene rings have been replaced with the thieno[3,2-b]thiophene units through the synthesis of the DPP2TT2Ta (TT) and DPP2TT2Tb (HH) copolymers (Figure 50).
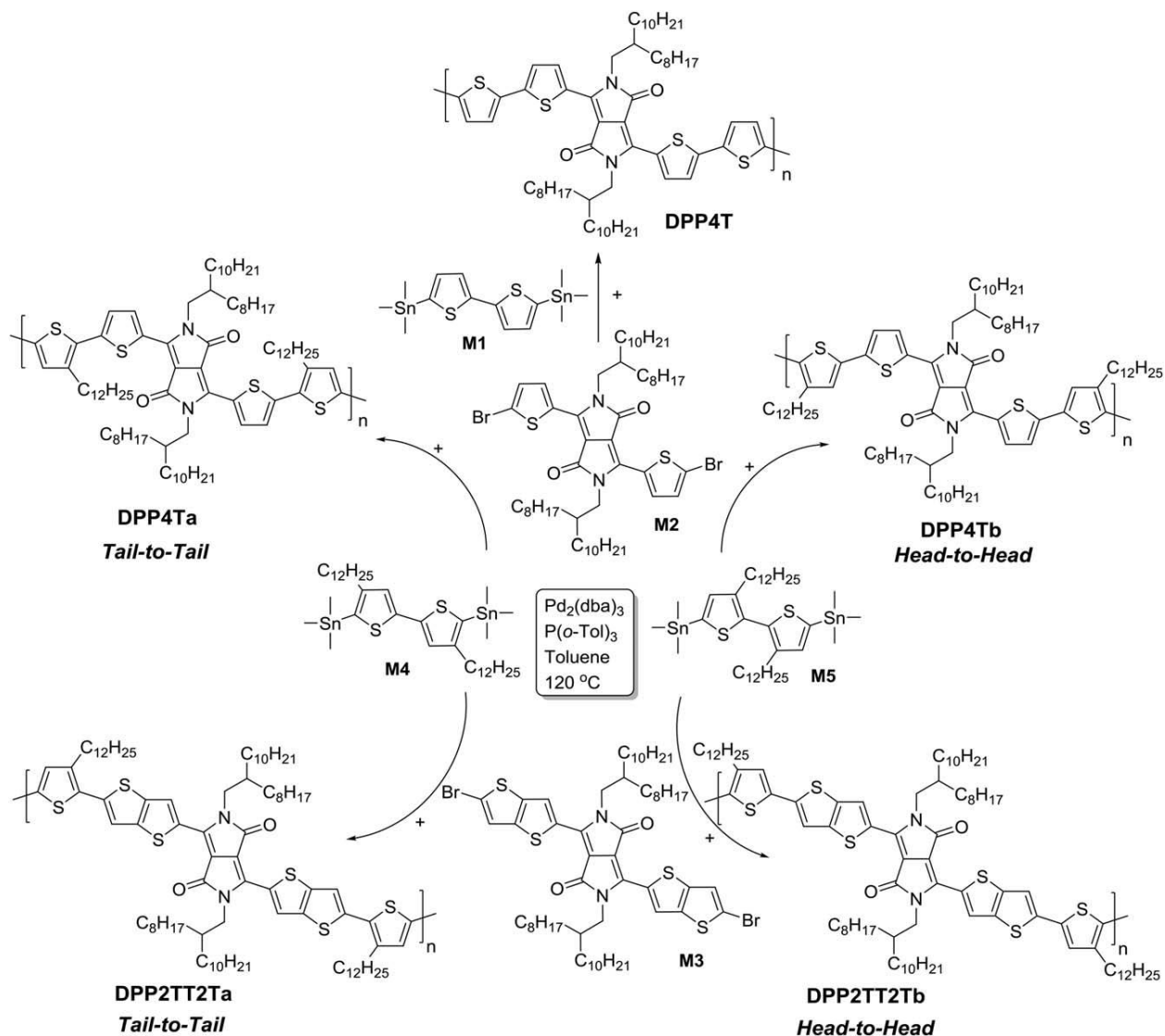
Figure 50. Reaction procedures towards the new DPP-based copolymers.

Experimental

Materials

All reactions are air and light sensitive and, therefore, were performed under argon and in the dark. All glassware was washed using detergent (Teepol), rinsed with water, acetone, and methylene dichloride, and dried in an oven at 120 °C. All solvents and reagents were purchased from Aldrich. Toluene was distilled using calcium hydride (CaH_2).

The syntheses of 5,5'-bis(trimethylstannyl)-2,2'-bithiophene (M1), 3,6-bis(5-bromothiophen-2-yl)-2,5-bis(2-octyldodecyl)pyrrolo[3,4-c]pyrrole-1,4(2H,5H)-dione (M2), 3,6-bis(5-bromothieno[3,2-b]thiophen-2-yl)-2,5-bis(2-octyldodecyl)pyrrolo[3,4-c] pyrrole-1,4(2H,5H)-dione (M3) were performed following previous reports.[214,215,216] (4,4'-didodecyl-2,2'-bithiophene-5,5'-diyl)bis(trimethylstannane) (M4) and (3,3'-didodecyl-2,2'-bithiophene-5,5'-diyl)bis(trimethylstannane) (M5) (Figure 50) were purchased from Solarmer Materials.

Dibromo-DPP monomers (0.5 mmol) and bis(trimethylstannane)thiophene derivatives (0.5 mol) were dissolved in dry toluene (0.025 M). Then, tris(dibenzylideneacetone)dipalladium(0) [Pd$_2$(dba$_3$)] (0.02 equiv) and tri(o-tolyl)phosphine [P(o-tol)$_3$] (0.08 equiv) were added, and the reaction mixture was stirred at 120 °C under argon atmosphere for 48 h. The polymers were purified by precipitation in methanol, filtered, and washed using a Soxhlet apparatus with methanol, acetone, hexane, and chloroform (CF). The hexane (DPP4Ta, DPP4Tb) and CF (DPP4T, DPP2TT2Ta, DPP2TT2Tb) fractions were evaporated under reduced pressure, and the polymers were precipitated in methanol, filtered through 0.45 mm PTFE filters, and finally dried under high vacuum, producing a greenish solid with yields of DPP4T = 83%, DPP4Ta = 78%, DPP4Tb = 91%, DPP2TT2Ta = 71%, and DPP2TT2Tb = 84%.

Instrumentation

Gel Permeation Chromatography (GPC)

Average molecular weights per number (M_n) and polydispersity indices (D) were determined with GPC at 150 °C on a high temperature PL-GPC 220 system using a PL-GEL 10 lm guard column, two PL-GEL 10 lm Mixed-B columns and ortho-dichlorobenzene (o-DCB) as the eluent. The instrument was calibrated with narrow polystyrene standards with M_P ranging from 4,830 to 3,242,000 g/mol.

Absorption Spectrometry

UV/vis absorption spectra were measured on a Cary 5000 UV–vis-NIR spectrophotometer (Agilent Technologies) in dual beam mode.

Photo-Electron Spectroscopy in Air (PESA)

Data was collected on a Riken Keiki AC-2 on thin polymer films at room temperature.

Theoretical Calculations

All calculations of the model compounds studied in this work have been performed using the Gaussian 03 software package.[217] The alkyl side chains substituents anchored onto the DPP and the peripheral thienyl rings have been replaced with methyl groups in the model compounds for our calculations. While the presence of these long alkyl chains enhances the solubility of these polymers and affects the charge carrier mobility and photovoltaic behavior of the polymer[218] from a computational point of view their replacement with shorter chains does not affect their optoelectronic properties (HOMO, LUMO, and band gap) and thus the optimized structures of the molecules.[219,220] The ground-state geometry of each model compound has been determined by a full optimization of its structural parameters using the DFT calculations, upon energy minimization of all possible isomers. In this work, the DFT calculations were performed using the Becke's three-parameter hybrid functional, B3, with nonlocal correlation of Lee-Yang-Parr, LYP, abbreviated as B3LYP in conjunction with the 6–311G(d,p) split valence polarized basis set. All calculations were performed taking into account that the system is under vacuum conditions. No symmetry constraints were imposed during the optimization process. The geometry optimizations have been performed with a tight threshold that corresponds to root mean square (rms) residual forces <1025 au for the optimal geometry. The energy level of the HOMO and the LUMO of the repetitive units of each polymer were carried out by using the same set of calculations. In our studies, the theoretical calculations performed on trimer model compounds. The visualization of the molecular orbitals has been performed using GaussView 5,0.

Atomic Force Microscopy (AFM)

AFM in tapping mode (Dimension ICON, Bruker) using a TESP-HAR tip was performed on thin polymer:$PC_{71}BM$ blend films on glass substrates, which were fabricated according to the Photovoltaic Devices description below.

Fabrication of Photovoltaic Devices

The photovoltaic devices were fabricated on pre-patterned indium-tin-oxide (ITO) glass substrates (Naranjo Substrates) with a sheet resistance of 20 Ω/sq. The ITO coated substrates were cleaned in a 3-step cleaning process (detergent, deionized water, acetone, 2-propanol). Before the deposition of the electron transport layer, the ITO coated substrates were placed inside an ultraviolet ozone cleaner to remove any organic contamination and to increase their surface hydrophilicity. Afterwards, a poly[(9,9-bis(3'- (N,N-dimethylamino)propyl)-2,7-fluorene)-alt-2,7-(9,9–dioctylfl uorene)] (PFN) solution (PFN, 0.5 mg/mL in methanol/acetic acid) was spun onto the ITO substrate at 1000 rpm for 45 s followed by sample annealing for 30 s at 150 $^{\circ}$C. This procedure was repeated three times. DPP4Ta, DPP4Tb, DPP2TT2Ta, and DPP2TT2Tb were dissolved in chlorobenzene (CB) and stirred for 1 h on a hotplate at 40 $^{\circ}$C, except DPP4T that was dissolved in CB and stirred for 1 h on a hotplate at 75 $^{\circ}$C. Afterwards, the fullerene [6,6]-phenyl C_{71}-butric acid methyl ester (PC$_{71}$BM) was added to the polymer solutions, yielding blend solutions with overall concentrations of 15 mg/mL and polymer:fullerene ratios of 1:3. Three hours before the photoactive layer deposition, 2% of 1,8- diiodooctane were added to the blend solution. Then the solutions were placed on a hotplate at 80 $^{\circ}$C and stirred. Before deposition of the active layers, the substrates were placed on a hotplate at 80 $^{\circ}$C for 10 min. By keeping both the concentration and the spin coating conditions (1500 rpm for 60 s) identical for all the polymer:PC$_{71}$BM systems, the photoactive layers were deposited on top of the PFN layer. Afterwards, the as-deposited polymer:PC$_{71}$BM films were first dried in a vacuum chamber for 20 min and afterwards were thermally annealed (at ambient pressure) at 85 $^{\circ}$C for 5 min. Molybdenum oxide (MoO$_3$, 8 nm)/aluminum (100 nm) counter electrodes were thermally evaporated through a shadow mask defining the photoactive area of 4 mm^2 of each device.

Current Density-Voltage (J-V) Measurements

The solar cell performance was measured in inert atmosphere under illumination from an Air Mass 1.5 Global (A.M. 1.5 G) solar simulator at an intensity of 100 mW cm^{-2} using an Agilent B1500A Semiconductor Device Analyzer. A reference monocrystalline silicon solar cell (Newport Corp) was used to calibrate the light intensity at 1 sun irradiation. An aperture mask with holes of 2.56 mm^2 is used to accurately define the photoactive area of the pixels during the measurements.

External quantum efficiency (EQE) measurements were conducted immediately after device fabrication on encapsulated devices in ambient conditions, using an integrated system (Enlitech, Taiwan) and a lock-in amplifier together with a current preamplifier under short-circuit conditions. The illumination intensity was calibrated using a monocrystalline photodetector of known spectral response. The solar cells were measured using a Xe-lamp, a monochromator and an optical chopper at low frequencies (200 Hz) to maximize the signal/noise (S/N) ratio.

Results

Synthesis

To relate structure, optoelectronic properties and solar cell performance, we investigated the combinations of M2 with M1 (DPP4T), M2 with M4 (DPP4Ta), and M2 with M5 (DPP4Tb). In addition, M3 was combined with M4 or with M5 to afford DPP2TT2Ta and DPP2TT2Tb, respectively. The synthesis of DPP4Ta, DPP4Tb, DPP2TT2Ta, and DPP2TT2Tb enabled us to study the impact of anchoring two linear dodecyl side chains in TT or HH conformation. We strived to determine the optimum alkyl side chain positioning in the polymer backbone as well as the flanked aromatic substituent around the DPP core, and to study their influence on the optoelectronic properties, the energy level adjustment, and the device performance. The copolymers were synthesized by Stille aromatic crosscoupling polymerization[221] utilizing tris(dibenzylideneacetone)dipalladium(0) [$Pd_2(dba)_3$] in 2% per mole and tri(o-tolyl)phosphine [$P(o$-$tol)_3$], 8% per mole, as the catalytic system in toluene solution. After purification, using Soxhlet extraction, DPP4Ta and DPP4Tb are received from the hexane fraction, whereas DPP4T, DPP2TT2Ta, and DPP2TT2Tb are obtained from the CF fraction. The average molecular weights per number (M_n), per weight (M_w), and the polydispersity index (D) of the copolymers as measured by GPC (Figure 51), based on monodispersed polystyrene standards at 150 ºC and using o-DCB as eluent, are summarized in Table 5. All copolymers exhibit monomodal GPC profiles with no appearance of residual monomers or oligomer chains and exhibit high Mn ranging from 30,000 up to 115,000 g/mol with D between 1.95 and 2.69; except DPP2TT2Ta with D = 4.45.
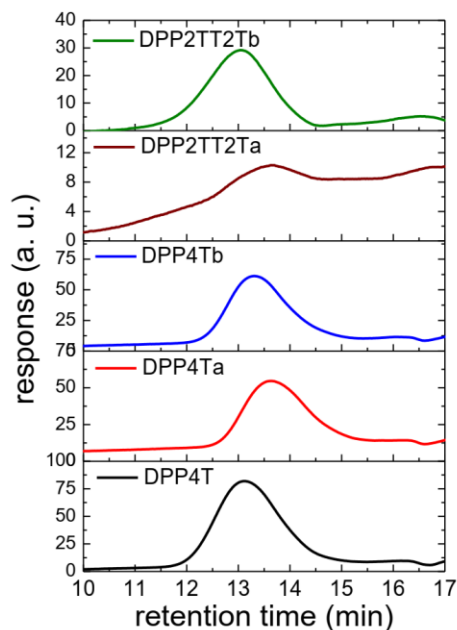
Figure 51. Gel permeation chromatography (GPC) profiles of the synthesized copolymers.

Table 5. Molecular Weight and Optoelectronic Characteristics of the Synthesized Copolymers.

Polymer	Average Molecular Weight per Number [Mn] (g/mol)	Average Molecular Weight per Weight [Mw] (g/mol)	Polydispersity Index [D]	λ_{max} (nm)	E_g^{opt} (eV)	IP (eV) (PESA)[a]	EA (eV)[b]
DPP4T	68,600	152,100	2.22	442, 791	1.35	5.24	3.89
DPP4Ta	30,300	65,300	2.16	433, 752	1.35	5.14	3.79
DPP4Tb	55,000	107,100	1.95	376, 687	1.37	5.21	3.84
DPP2TT2Ta	31,200	138,700	4.45	442, 730	1.40	5.13	3.73
DPP2TT2Tb	114,900	309,100	2.69	405, 695	1.46	5.23	3.77

[a]EA = IP – E_g^{opt}

[b]IP based on the onset of photoelectron yield, with an estimated error of 0.02 eV.

Optical Properties and Energy Level Estimation

The absorbance of the copolymers in thin-films is presented in Figure 52, and the corresponding optoelectronic properties are summarized in Table 5.

For each copolymer, two major absorption peaks are observed, a feature which is commonly observed for alternating donor-acceptor (D-A) copolymers. The short wavelength peaks were detected at 442 nm for DPP4T, at 433 nm for DPP4Ta, and at 376 nm for DPP4Tb, while the long-wavelength peaks which are related to an intramolecular D-A charge transfer[222] were observed at 791 nm for DPP4T, at 752 nm for DPP4Ta, and at 687 nm for DPP4Tb.
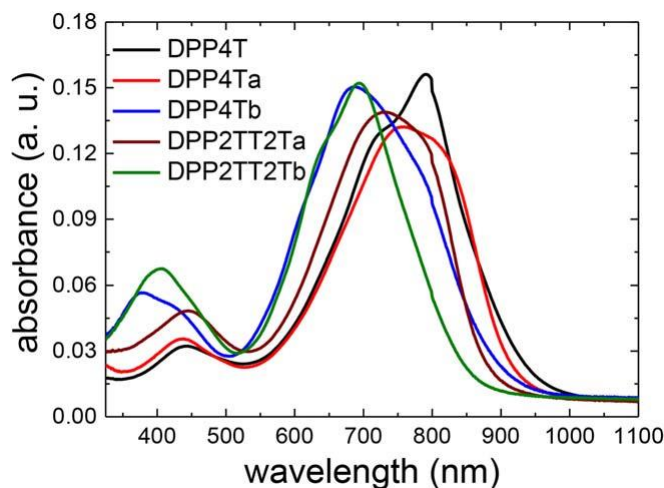
Figure 52. Absorbance spectra of DPP copolymer thin-films.

This shows that the introduction of the didodecyl side chains in the polymer backbone, either as TT or HH, results in blueshifted absorption maxima as compared to the unsubstituted derivative DPP4T. When the positioning of the didodecyl side chains present HH conformation, the blue-shift appears even stronger, indicating a higher degree of polymer chain distortion. To support our assumption quantum chemical density functional theory (DFT) calculations were performed to estimate the dihedral angles, to predict the molecular energy levels and to model the distribution of the frontier molecular orbitals of the copolymers. The DFT calculations using the B3LYP/6–311G(d,p) performed on trimer model compounds and the chemical structures of the copolymers as obtained by the theoretical calculations are presented in Figure 56 and the estimated dihedral angles in Table 6.

Table 6. Calculated Dihedral Angles (Θ_1, Θ_2, Θ_3, Θ_4, and Θ_5) of Some Representative Bonds That Are Shown in Scheme 1 for the Studied Copolymers

	Θ_1	Θ_2	Θ_3	Θ_4	Θ_5
DPP4T	9.4º	8.2º	10.3º	18.4º	1.6º
DPP4Ta	11.6º	11.1º	18.7º	17.3º	19.2º
DPP4Tb	13.4º	15.2º	18.9º	58.5º	19.9º
DPP2TT2Ta	23.2º	22.5º	26.9º	20.8º	17.9º
DPP2TT2Tb	22.9º	22.5º	21.7º	63.0º	18.5º

As expected, the estimated dihedral angles of DPP4T are significantly lower than all the other copolymers. By the introduction of the alkyl group, the theoretical calculations demonstrate increased dihedral angles for DPP4Ta and DPP4Tb versus DPP4T. In particular, the most important alteration is detected on θ_4 dihedral angle where the rotation between the adjacent units in DPP4Tb is 58.5º as compared with 17.3º in DPP4Ta. Similar observation is also presented for the θ_4 dihedral angle between DPP2TT2Ta and DPP2TT2Tb. In this case, the rotation between the adjacent units in DPP2TT2Tb is 60.3º as compared with 20.8º in DPP2TT2Ta. The lower θ_4 dihedral angles between the adjacent didodecyl thiophene rings when the positioning of the didodecyl alkyl chains present TT conformation can minimize the steric hindrance along the axis, which is beneficial towards enhanced optoelectronic and charge transporting properties. [223],[224] These findings are in agreement with the aforementioned observation on the absorption maxima variation (Fig. 52 and Table 5) among DPP4T, DPP4Ta, and DPP4Tb.

Likewise, we observed some influence of the positioning of the didodecyl side chains in DPP2TT2Ta and DPP2TT2Tb. Again, the shift is more pronounced in DPP2TT2Tb than DPP2TT2Ta. Yet, the short-wavelength peaks of both DPP2TT2Ta (442 nm) and DPP2TT2Tb (405 nm) are redshifted by 9 and 29 nm as compared with DPP4Ta and DPP4Tb, respectively (Table 5). We attribute this to the extension of the p-conjugation along the polymer backbone induced by replacing the thiophene rings in DPP4Ta and DPP4Tb with the thieno[3,2-b]thiophene units in DPP2TT2Ta and DPP2TT2Tb (Figure 53). Moreover, the long-wavelength peak of

DPP2TT2Ta at 730 nm is blue-shifted by 22 nm as compared with DPP4Ta which is in agreement with recent work: the stronger the coupling between the D and A moieties[225] or the shorter the conjugation length between two electron withdrawing units (A1 and A2) within the polymer chain,[226] the longer is the wavelength of the absorption maximum. As a matter of fact, the theoretical calculations show that the replacement of the thiophene rings around the DPP unit by thieno[3,2-b]thiophene rings results to enhanced θ_1 and θ_2 dihedral angles (Table 6) for the DPP2TT2Ta (23.2°, 22.5°) and DPP2TT2Tb (22.9°, 22.5°) versus the corresponding DPP4Ta (11.6°, 11.1°) and DPP4Tb (13.4°, 15.2°), respectively indicating less efficient coupling between the D and A moieties in DPP2TT2Ta and DPP2TT2Tb as compared with DPP4Ta and DPP4Tb. In contrast, the long-wavelength absorption peak of DPP2TT2Tb at 695 nm is red shifted by 8 nm as compared to DPP4Tb. We attribute this shift to the positioning of the didodecyl side chains in HH conformation on DPP4Tb that may cause severe steric hindrance in the polymer backbone. This steric hindrance is minimized in DPP2TT2Tb. The extension of the repeat unit length through the insertion of the fused thieno[3,2-b]thiophene rings may assist the increased planarity of the polymer backbone, yielding better overlap between the molecular orbitals of the electron donating and electron withdrawing units.
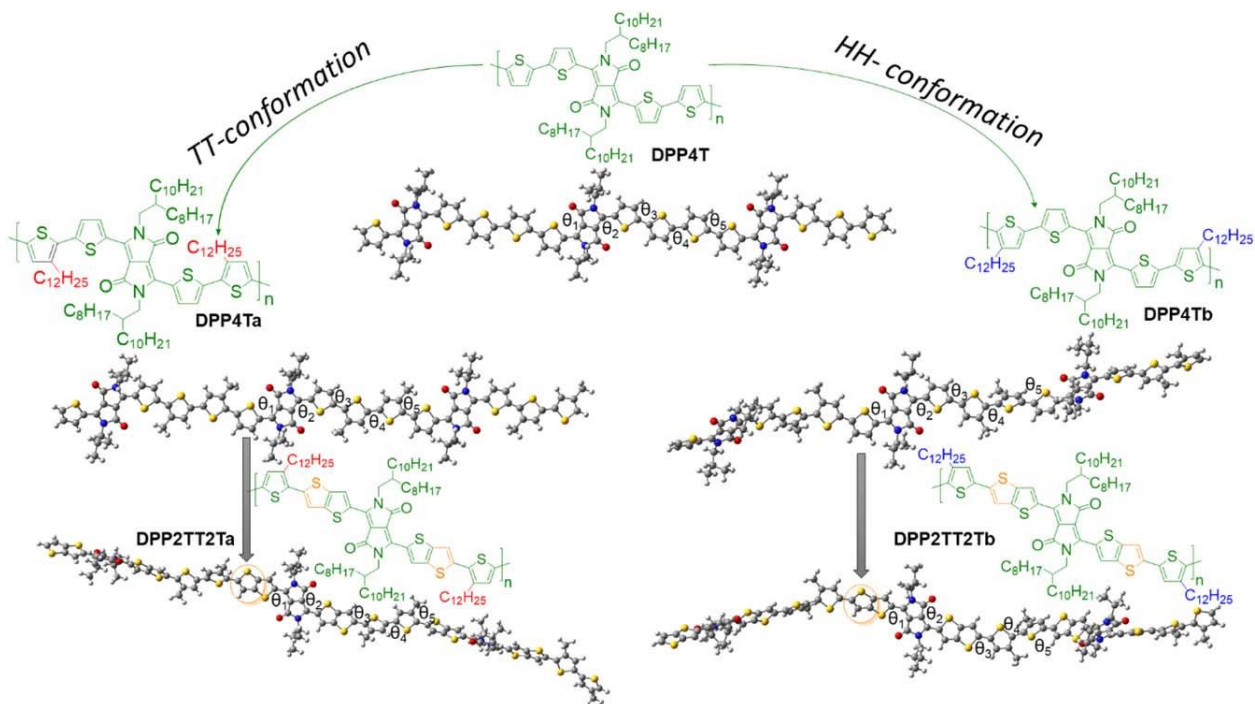
Figure 53. Chemical structures and theoretical optimized chemical structures of the studied LBG DPP-based copolymers.

The optical bandgap of DPP4Ta is 1.35 eV, slightly lower than the optical bandgap of DPP4Tb (1.37 eV) and matches the optical bandgap of DPP4T, showing that the insertion of the alkyl side chains in TT conformation does not influence the optical bandgap of the copolymers but only the position of the absorption maxima. The optical bandgaps of DPP2TT2Ta (1.40 eV) and DPP2TT2Tb (1.46 eV) are slightly higher than the optical bandgaps of DPP4Ta and DPP4Tb but show the same trend. The positioning of the didodecyl side chains in HH conformation results in an increase of the optical bandgap as compared to the TT regardless the presence of thiophene or thieno[3,2-b]thiophene rings around the DPP core in the studied copolymers. The thin-film absorbance of the various LBG copolymers blended with $PC_{71}BM$ are depicted in Figure 55. Upon addition of $PC_{71}BM$, DPP4T:$PC_{71}BM$ exhibits the highest optical density at the long-wavelength region (650– 1000 nm), then the DPP4Tb:$PC_{71}BM$ absorption peak shows an intermediate amplitude, and finally DPP4Ta:$PC_{71}BM$ exhibits the lowest optical density. On the contrary, the optical densities of the long-wavelength absorbance (650–1000 nm) of both DPP2TT2Ta:$PC_{71}BM$

and DPP2TT2Tb:PC$_{71}$BM are similar. Around 500 nm, the absorbance of all blends is dominated by PC$_{71}$BM.[227]

The ionization potentials (IPs) of all DPP-based copolymers were determined by PESA. The measurements are depicted in Supporting Information Figure 54, and the data are summarized in Table 5.
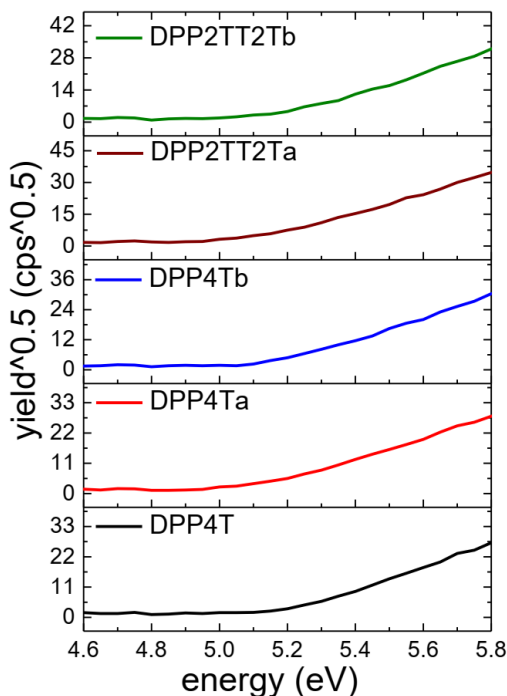
Figure 54. Photon-Electron Spectroscopy in Air (PESA) of the DPP-based copolymers,

The electron affinities (EAs) of the polymers were estimated from the IPs and the optical bandgaps. The IPs of DPP4T, DPP4Ta, DPP4Tb, DPP2TT2Ta, and DPP2TT2Tb are 5.24, 5.14, 5.21, 5.13, and 5.23 eV, respectively. These results indicate that the positioning of the didodecyl side chains in TT conformation (DPP4Ta) decreases the IP by 0.1 eV as compared with the unsubstituted DPP4T. In the case of the HH conformation (DPP4Tb), no significant variation in IP is observed (DPP4Tb versus DPP4T). A similar trend is observed for DPP2TT2Ta and DPP2TT2Tb. For these specific examples, anchoring of the didodecyl side chains in TT conformation leads to a decrease of the IP in higher degree as compared to the HH conformation.

Furthermore, we find no variation on the IP upon replacing the thiophene rings with thieno[3,2-b]thiophene units next to the DPP core in the copolymers regardless the TT (DPP4Ta-DPP2TT2Ta) or the HH (DPP4Tb-DPP2TT2Tb) conformation. This indicates that a small increase in the p-conjugation along the polymer backbone of these DPP based copolymers does not change the IP of the copolymers significantly. The predicted highest occupied molecular orbital (E_{HOMO}) and lowest unoccupied molecular orbital (E_{LUMO}) energy levels as well as the distribution of the frontier molecular orbitals of the copolymers are presented in Figure 55. It is possible to observe that in all the copolymers both the E_{LUMO} and E_{HOMO} levels are fully delocalized along the polymer chain axis with those of E_{LUMO} assuming a more quinoidal form as shown by the presence of orbital lobes in the bonds between the thiophene rings along with a significant localization of the E_{LUMO} on the DPP unit. Moreover, a good agreement in the variation of the predicted E_{HOMO} levels and the resulting IPs of the copolymers is observed. The predicted E_{HOMO} of the DPP4Ta is 24.82 eV, which is 0.13 eV increased as compared with DPP4Tb (–4.95 eV). Furthermore, the predicted E_{HOMO} of DPP4Tb is similar to that of DPP4T (–4.91 eV). Finally, the predicted E_{HOMO} of the DPP2TT2Ta is 24.97 eV, which is 0.06 eV increased as compared with DPP2TT2Tb (–5.03 eV). All these findings are in accordance with the observed IP variation of the copolymers in Table 5 and Figure 54.
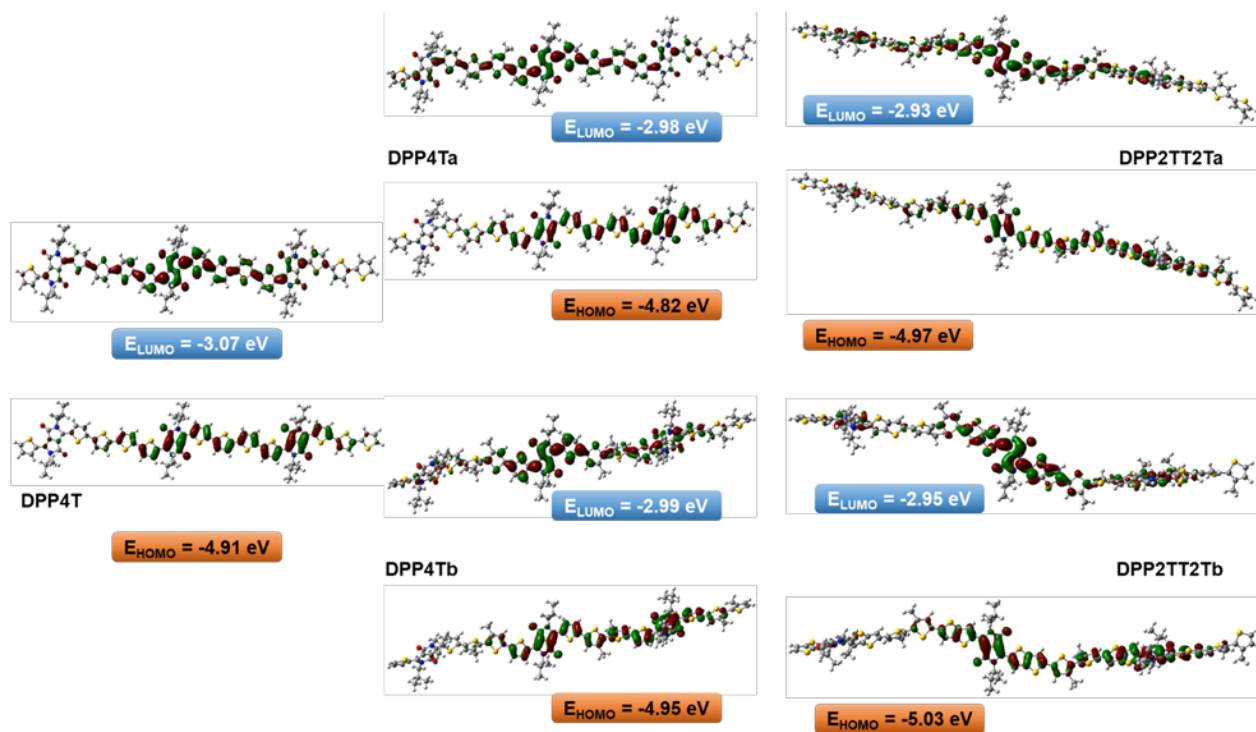
Figure 55. DFT [B3LYP/6-311G(d,p)] calculated frontier molecular orbitals of the EHOMO and ELUMO for the trimers of DPP4T, DPP4Ta, DPP4Tb, DPP2TT2Ta and DPP2TT2Tb.

Photovoltaic Performance

The main energy levels of the copolymers, modulated by the position of the didodecyl side-chains and the thieno[3,2-b]thiophene moieties in the polymer backbone, partly determine the optoelectronic properties of the respective solar cells. To study the impact of the side-chains on the photovoltaic device properties and processability, we investigated organic solar cells with an inverted ITO/PFN/active layer/MoO$_3$/Al device architecture. The beneficial role of the alkyl side chains positioning of the processability is highlighted in the fact that DPP4Ta, DPP4Tb, DPP2TT2Ta and DPP2TT2Tb were dissolved at much lower temperature (40 ºC) than DPP4T (75 ºC). The J-V curves and the photovoltaic properties of the devices are presented in Figure 56a and Table 7, respectively.
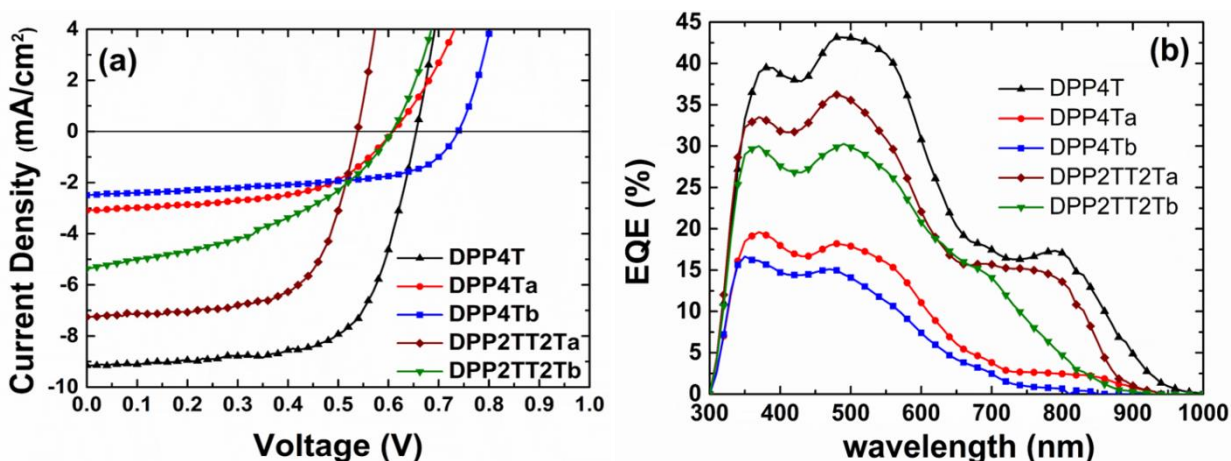
Figure 56. (a) Current density-voltage characteristics under solar simulator illumination (AM1.5G, 100 mW cm^{-2}) and (b) EQEs of inverted organic solar cells comprising DPP4T:PC$_{71}$BM, DPP4Ta:PC$_{71}$BM, DPP4Tb:PC$_{71}$BM, DPP2TT2Ta:PC$_{71}$BM or DPP2TT2Tb:PC$_{71}$BM.

Table 7. Properties of Inverted Solar Cells under 1 Sun Illumination (AM1.5G, 100 mW cm^{-2}) in Polymer:PC$_{71}$BM Blends

Polymer	J_{SC} (mA/cm2) [J-V]	J_{SC} (mA/cm2) [IPCE]	V_{OC} (V)	FF (%)	PCE (%)
DPP4T	9.2 ± 0.3	8.6	0.66 ± 0.02	65.5 ± 1.5	4.0 ± 0.3
DPP4Ta	3.1 ± 0.3	2.9	0.61 ± 0.02	52.8 ± 1.9	1.0 ± 0.2
DPP4Tb	2.5 ± 0.5	2.1	0.74 ± 0.01	56.7 ± 1.7	1.1 ± 0.3
DPP2TT2Ta	7.2 ± 0.4	6.8	0.54 ± 0.02	64.7 ± 2.0	2.5 ± 0.8
DPP2TT2Tb	5.3 ± 0.7	5.5	0.61 ± 0.01	42.4 ± 1.6	1.4 ± 0.6

In the case of the HH conformation (DPP4Tb or DPP2TT2Tb), the respective solar cells exhibit almost 0.1 eV enhanced V_{OC} versus solar cells comprising DPP4Ta or DPP2TT2Ta (TT conformation). This observation is well in agreement with the IP of DPP4Tb and DPP2TT2Tb. In contrast, the Jsc of solar cells comprising DPP4Ta or DPP2TT2Ta are higher than the J_{SC} of the DPP4Tb and DPP2TT2Tb solar cells, rendering the alkyl side chains in the TT conformation favorable for improved photocurrents. These results can be supported by the theoretical findings that minimization of steric hindrance is estimated when the didodecyl side chains are in the TT

95

conformation. In addition, the thieno[3,2-b]thiophene moieties in the polymer backbone impact on J_{SC}: both DPP2TT2Ta and DPP2TT2Tb exhibit enhanced Jsc and hence increased PCEs versus DPP4Ta and DPP4Tb even though they have slightly higher optical bandgaps. Finally, among all the studied DPP-based systems, the solar cells comprising unsubstituted DPP4T or DPP2TT2Ta demonstrate the highest EQE in the long-wavelength spectral regime where the absorption of polymers dominates [Fig. 56(b)].

To better understand the origin of the variations on the photovoltaic performance of the studied copolymers we examine the surface of the active layer by AFM (Figure 57). The topography AFM images of the active layers (Figures 57a-e) reveal rather smooth films (±5 nm scale covers topography) for DPP4T:PC$_{71}$BM, DPP4Tb:PC$_{71}$BM, DPP2TT2Ta:PC$_{71}$BM, and DPP2TT2Tb:PC$_{71}$BM, except DPP4Ta:PC$_{71}$BM that shows a slightly rougher topography (well shown on ±15nm scale). One clear differentiation is observed on DPP2TT2Tb:PC$_{71}$BM that presents very different features observed in topography.
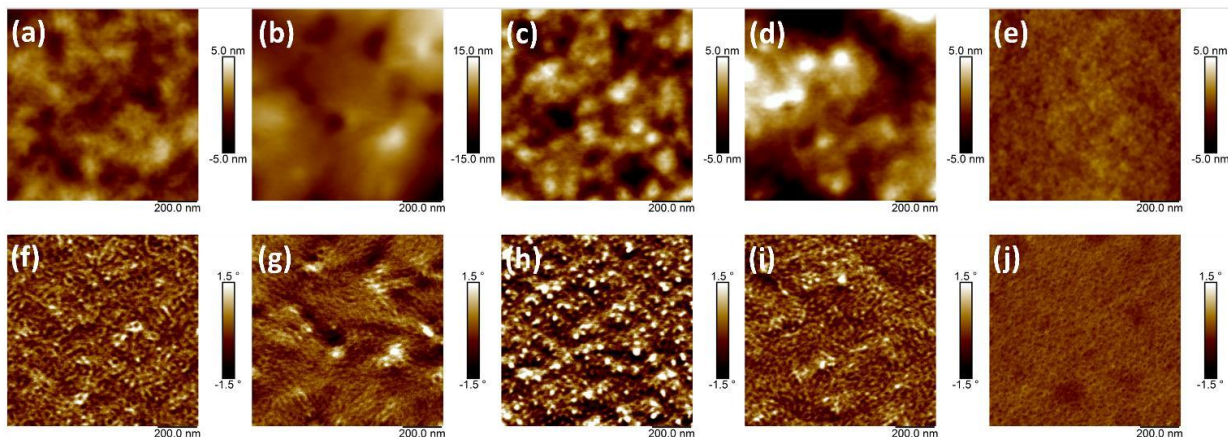
Figure 57. Atomic force microscopy images of the studied copolymers in polymer:PC$_{71}$BM blend films. Topography (top) images of DPP4T (a), DPP4Ta (b), DPP4Tb (c), DPP2TT2Ta (d), DPP2TT2Tb (e). Phase images (bottom) of DPP4T (f), DPP4Ta (g), DPP4Tb (h), DPP2TT2Ta (i), DPP2TT2Tb (j).

Table 8. Roughness of the different active layers.

Polymer:PC$_{71}$BM blend	Rq (nm)
DPP4T	1.4
DPP4Ta	3.5
DPP4Tb	1.9
DPP2TT2Ta	2.3
DPP2TT2Tb	0.5

Moreover, by comparing the AFM phase images in the Supporting Information, Figures 57f-j, we observe some kind of fibrillar network for DPP4T:PC$_{71}$BM, DPP4Ta:PC$_{71}$BM, DPP4Ta:PC$_{71}$BM, and DPP2TT2Ta:PC$_{71}$BM on a very similar phase signal of $\pm 1.5^{\circ}$ relative. For the DPP2TT2Tb: PC$_{71}$BM, we observe an even smoother film and less contrast in the phase image, which may hint to more intermixing of the components, thus reduced charge extraction probability and in line with the observed low FF. Therefore, the observed differences in the photovoltaic performance between the DPP4T:PC$_{71}$BM, DPP4Ta:PC$_{71}$BM, DPP4Ta:PC$_{71}$BM and DPP2TT2Ta: PC$_{71}$BM devices cannot be readily attributed to a distinct morphological variation, but we hypothesize it might be related to vertical phase segregation of the components. However, the higher PCE of the DPP2TT2Ta:PC$_{71}$BM versus the DPP2TT2T: PC$_{71}$BM device might be attributed to morphological variations.

Conclusions

In summary, we performed an initial chemical structure optimization in terms of alkyl side chain positioning and a DPP-based oligothiophene copolymer that is solution processable in much lower temperature than DPP4T, which is beneficial towards large scale fabrication of organic solar cell devices was presented. Even if the PCE of DPP4T is higher than DPP2TT2Ta, additional chemical structure optimization of DPP2TT2Ta in terms of molecular weight enhancement, length, and type of alkyl side chains for improvement of the p-p stacking are in progress towards boosting the PCE further. Moreover, a detailed chemical structure—optoelectronic properties—solar cell

performance study has been carried out on LBG DPP-based copolymers through the combination of alkyl side chain positioning and aryl substituents next to DPP. We show that the introduction of the didodecyl side chains in two different conformations in the polymer backbone results in blue shifted absorption maxima as compared to the unsubstituted reference polymers. In particular, in the TT conformation the absorption maxima are blue shifted in a lower extent as compared to the HH-conformation. Quantum chemical DFT calculations demonstrated that the dihedral angles between the adjacent didodecyl thiophene rings can minimize the steric hindrance along the axis, when the didodecyl alkyl chains are anchored in TT conformation, which is beneficial towards enhanced optoelectronic and charge transporting properties. Moreover, in the TT conformation (DPP4Ta) the optical bandgap is similar to the unsubstituted derivative. Anchoring of the didodecyl side chains as TT conformation leads to an IP decrease as compared with the HH conformation. A small increase in the p-conjugation along the polymer backbone does not significantly alter the IP of these DPP-based copolymers. From the OPV performance study, we observed that, if the alkyl side chains are reveal HH conformation, the Voc of the corresponding devices increases by 0.1 V as compared with the devices containing the polymers with TT conformation. This observation is in agreement with the copolymers' IPs. In addition, if the alkyl side chains are anchored as TT conformation, the photocurrents are improved.

6.3 Stability of OPVs

6.3.1 Impact of P3HT materials properties and layer architecture on OPV device stability.

Rico Meitzner, Tobias Faber, Shahidul Alam, Aman Amand, Roland Roesch, Mathias Büttner, Felix Herrmann-Westendorf, Martin Presselt, Laura Ciammaruchi, Iris Visoly-Fisher, Sjoerd Veenstra, Amaia Diaz de Zerio, Xiaofeng Xu, Ergang Wang, Christian Müller, Pavel Troshin, Martin D. Hager, Sandra Köhn, Michal Dusza, Miron Krassas, Simon Züfle, E. Kymakis, Eugene A. Katz, Solenn Berson, Filip Granek, Matthieu Manceau, Francesca Brunetti, Giuseppina Polino, Ulrich S. Schubert, Monica Lira-Cantu, Harald Hoppe.

We report a cooperative study conducted between different laboratories to investigate organic solar cell degradation with respect to P3HT material properties and different solar cell architectures. Various batches of P3HT were collected from different suppliers reflecting commercial availability as well as properties variability. Among the materials properties explicitly considered were the molar mass, dispersity, regio-regularity, impurities by trace metals and intrinsic doping evaluated from radical concentrations. Each of the participating laboratories contributing test devices applied their own layer stack, i.e. their own device architecture and layout. This variation was appreciated as another parameter for evaluation. Even though a large amount of devices failed due to extrinsic degradation effects, indeed, some materials properties were found to be more important than others for obtaining long lifetimes and high stability of P3HT-based polymer solar cells.

Experimental

Five different commercial P3HT samples were acquired from 1 M, BASF, Merck, Plextronics and Rieke Metals Inc. and named P3HT-I through P3HT-V, without following the producer order above. Commercial P3HTs were chosen to study the viability of these materials available from suppliers broadly used labs within the OPV community. Their intrinsic properties were evaluated in detail via chemical, thermal and optical analysis. Thus their properties, reported in the results section, are the only parameters to enter into the evaluation. $PC_{61}BM$ of 99% purity or better was used in all cases for the suppliers of the used $PC_{61}BM$.

In Fig. 1 the procedure of the initial experimental phase, including ordering and distribution of P3HTs, manufacturing of the solar cells and characterization, is depicted. Chemical characterization including ^{1}H nuclear magnetic resonance spectroscopy, size exclusion chromatography, induction coupled plasma optical emission spectroscopy, electron spin resonance spectroscopy, thermal characterization like differential scanning calorimetry and thermogravimetric analysis, as well as optical characterization methods like UV/Vis spectroscopy and photothermal deflection spectroscopy, were performed. Additionally, electronic characterization including current-voltage (IV) and external quantum efficiency (EQE) measurements, as well as different characterization methods performed with PAIOS by Fluxim (see section 2.7.3), were done. The results of these experiments are reported in Sections 2.6 and 2.7.
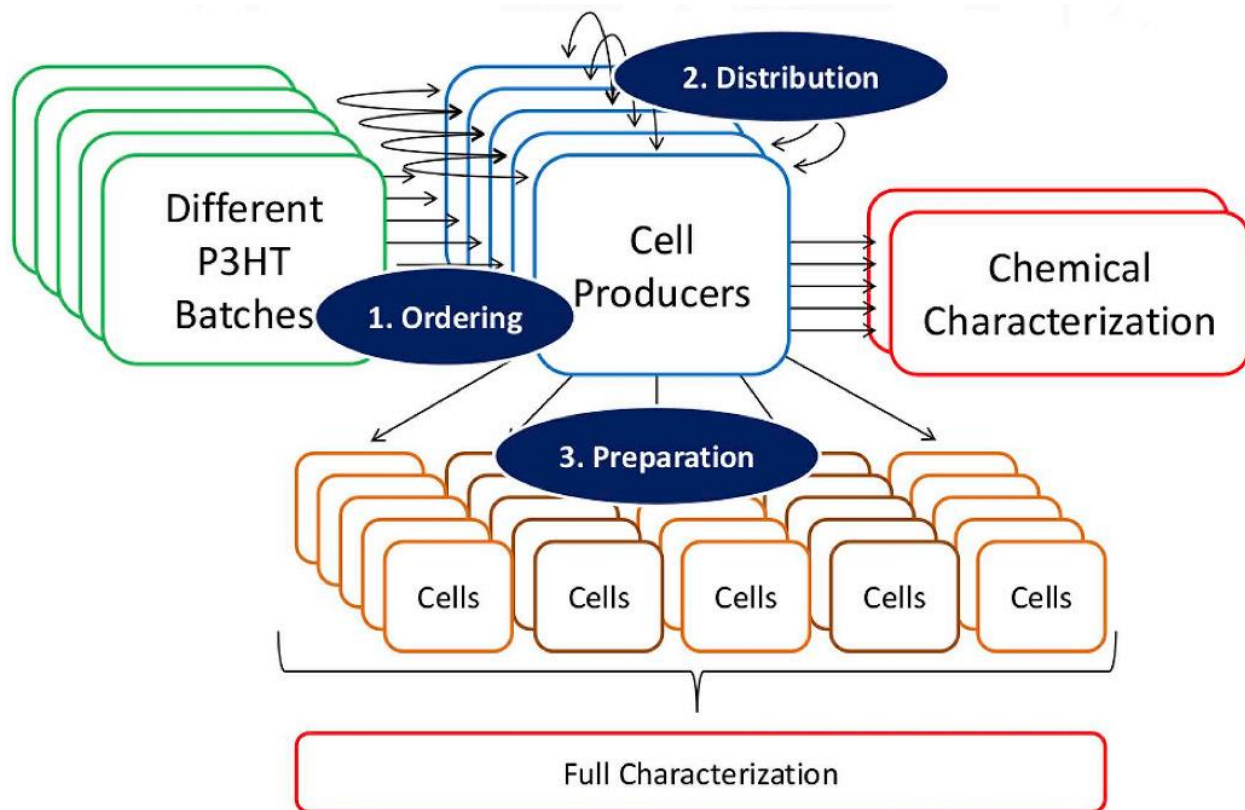
Figure 58. Schematic of the experimental proceedings before aging.

In Fig. 58 the experimental procedure after cell manufacturing and initial characterization is shown. The produced solar cell devices (see section 2.1) were distributed to the respective labs for

aging (see section 2.3) and some were sent to Fluxim for characterization with the PAIOS instrument. Aging was performed at different labs according to ISOSL2, ISOS-D2 and ISOS–O1 protocols[228], as explained in detail in Section 2.3. Samples aged at L2, D2 and O1 were also sent to Fluxim after aging to determine their electrical properties.

At the end of the experiment the polymer properties determined from chemical and thermal analysis were correlated with the extracted lifetime parameters. For ease of reading the results, a unified color code for the different P3HT batches was defined and is shown in Table 9.

Table 9. Color coding for the materials used in the experiment.

Material	*Color code*
P3HT-I	Black
P3HT-II	Red
P3HT-III	Blue
P3HT-IV	Green
P3HT-V	Orange
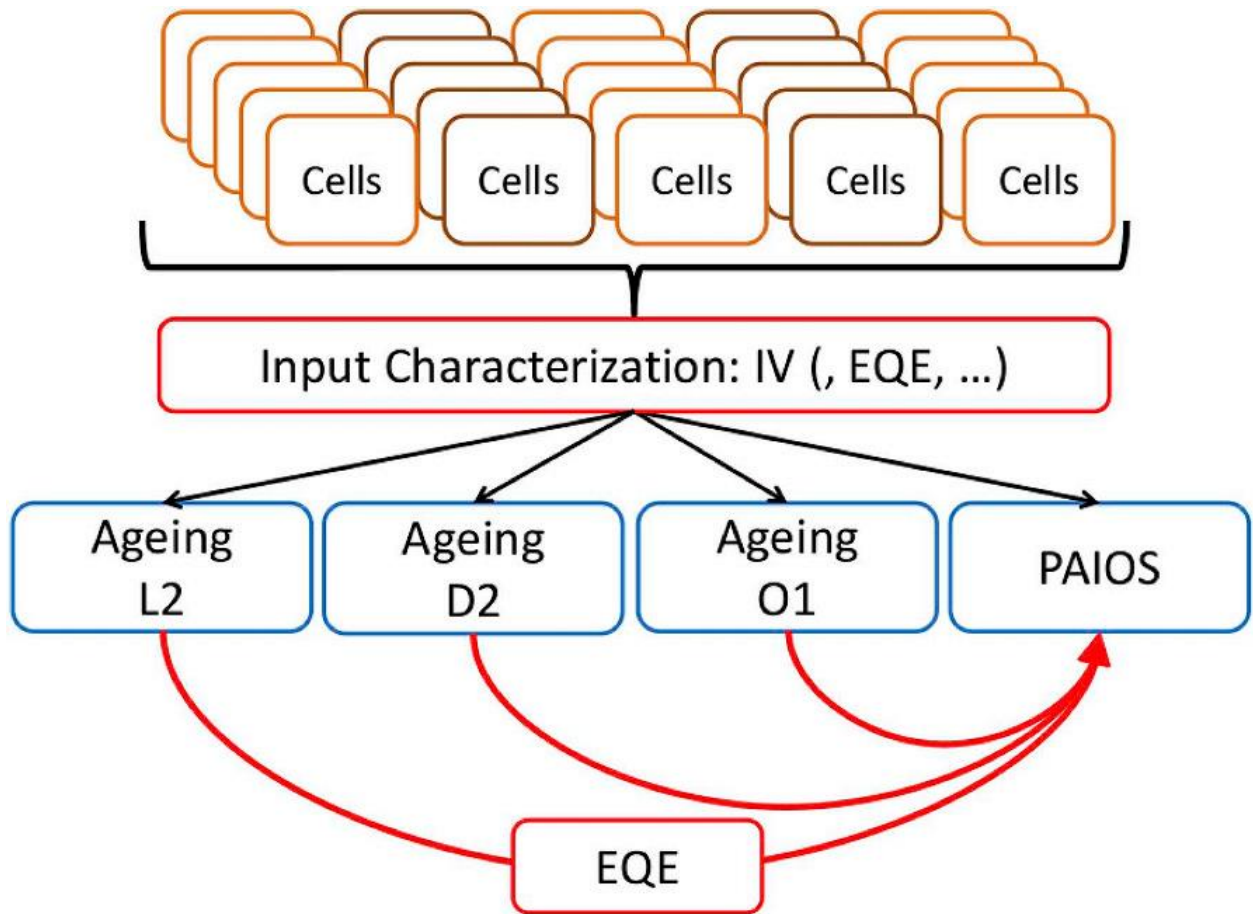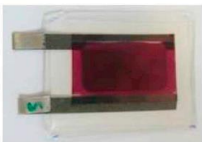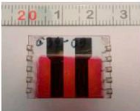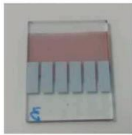
Figure 59. Further experimental procedure after production and initial characterization of the devices.

Materials and layer stacks

We deliberately allowed a large variation in layer stacks/device layout– including substrates – providing additional parameters impacting device stability. This was made possible by the fact that each cell producer prepared devices based on all the different P3HT batches using their preferred device layout. Five different labs served as cell producers: Commissariat à l'énergie atomique et aux énergies alternatives (CEA), Wroclaw Research Centre EIT+ (EIT+), Institut Català de Nanociència i Nanotecnologia (ICN2), Technological ducational Institute Crete (TEIC) and University Torr Vergata Rome (UTV). The different P3HT batches were contributed by different collaborators of the experiment. Three of the cell producers used ITO coated glass as substrates, one lab used FTO coated glass (ICN2), and one lab used ITO coated PET foil (CEA). Further variations were in the device architecture, including mainly inverted layer stacks (electron extraction via semi-transparent electrode) as well as one example for conventional layer stack (hole

extraction via semitransparent electrode). The charge extraction layers were varied as well: ZnO, MoO_3, V_2O_5, PEIE, and PEDOT:PSS were used. Calcium, aluminum and silver served as opaque back electrodes. Physical vapor deposition was used for evaporation which will be called evaporation for short from here on. Three producers used epoxy as sealant for cell encapsulation (EIT+, TEIC and ICN2), while CEA used a fully flexible encapsulation and UTV used parafilm for sealing. All layer stacks as well as device layouts are reported in detail in Table 10.

Table 10. Producers of OPV devices, layer stack, layout (photo) and single device area.

Manufacturer	Layer Stack	Photo	Active Area (mm²)
CEA, France	Ag / PEDOT:PSS / P3HT:PCBM / ZnO / TCO / PET		140
EIT+, Poland	Ag / MoO_3 / P3HT:PCBM / ZnO / ITO / Glass		4.5
ICN2, Spain	Ag / V_2O_5 / P3HT:PCBM / ZnO / FTO / Glass		20
TEIC, Greece	Al / Ca / P3HT:PCBM / PEDOT:PSS / ITO / Glass		4
UTV, Italy	Ag / MoO_3 / P3HT:PCBM / PEIE / ITO / Glass		10

Processing of active layer solutions

The active layer solutions were provided by various labs involved in the study and were distributed including detailed preparation recipes among all cell producers. These recipes were

followed largely, though small adaptations were allowed concerning processing temperatures in order to incorporate for specific layer stack requirements. In general, solutions were handled around 50 °C for storage and processing; details can be found in the Supporting Information.

Aging methods

Aging of the photovoltaic devices was performed following largely the published ISOS recommendations. Three different aging protocols were applied: laboratory weathering (L2), outdoor aging (O1) and dark aging (D2). This allowed us to investigate the impact of different stress conditions on the device stability.

ISOS-L2 degradation

Samples were aged at the CEEC Jena under conditions close to ISOSL2. The setup in Jena consists of a metal halide lamp, whose illumination spectrum is close to AM 1.5G, as can be seen in Fig. 60. The light intensity was set to 1000 W/m^2 with help of a pyranometer. The intensity was logged by a silicon sensor at all times, demonstrating that the operation of the lamp was very stable. The temperature was set to 55 °C in a shady region of the chamber and monitored as well. Unfortunately, a higher temperature could not be reached and therefore remained 10 K below the ISOS recommendations. However, the acceleration for 10 K higher temperature can be estimated to be roughly a factor of two[229]. Furthermore, as the devices were illuminated, their temperature was considerably higher than in the shadow, yielding 65 °C or higher inside the cells. Humidity was monitored and remained constant at around 5% r.H within the setup due to the elevated temperature. The samples were electrically connected via crocodile clamps to a multiplexing unit (Keithley 2700). Periodic current-voltage (IV) characterization was performed automatically every 30 min with a Keithley 2400 via computer control. When multiple cells on a substrate were available, the innermost cells were chosen for aging, as they were considered to be least affected by extrinsic degradation mechanisms.
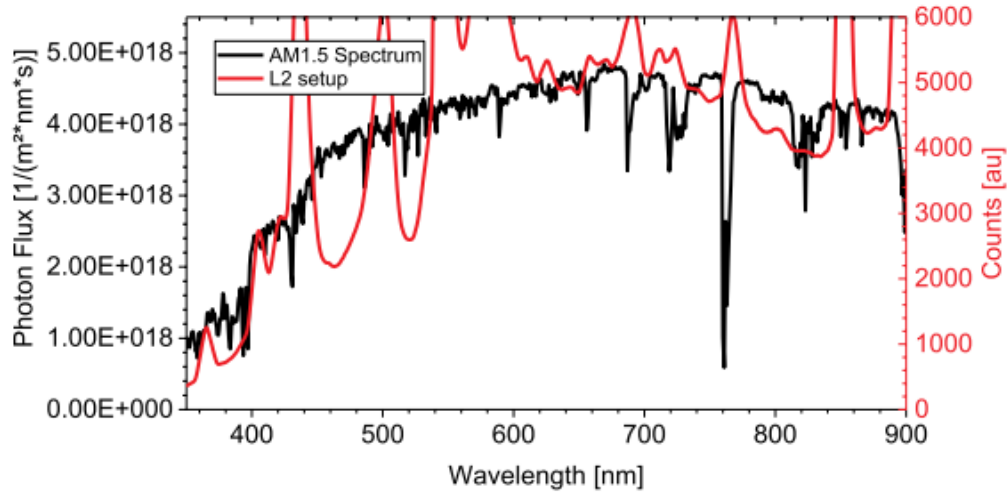
Figure 60. Comparison of the spectrum of the metal halide lamp used in the L2 aging setup at CEEC Jena with AM 1.5G showing a good match.

ISOS-D2 degradation

Dark storage degradation was carried out Solliance in Eindhoven under a solar simulator equipped with a sulphur plasma light source (Solaronix), under which the samples were shaded by a metal plate. The samples were occasionally uncovered, computer-controlled automated IV measurements took place during the whole aging process every hour and the collected data was stored in a database. The IV measurements recorded under one sun illumination were later filtered from the complete data set. During the aging process the temperature was set to 65 °C and relative humidity stayed at around 5% at that temperature. Solar cells on substrates with more than one device were chosen based on maximum performance.

ISOS–O1 degradation

The cells were mounted on a fixed angle (30° to horizontal) stand and the global intensity of incident sunlight was measured with a calibrated thermopile pyranometer (Eppley PSP) mounted on the same plane. It should be noted that the spectrum measured at noon time ± 2–3 h of a cloudless day at Sede Boqer, Israel (Lat. 30.8°N, Lon. 34.8°E, Alt. 475 m), matches almost perfectly to the standardized AM 1.5G spectrum[230]. The cells were exposed between November 2015 and February 2016 and only during light hours (between ± 9:30 and 15:30) for a total of ~210 h, in order to avoid potential encapsulation breaking or contact oxidation problems due to

night-time humidity. After the daily exposure the cells were stored in the dark at shelf life conditions (lab environment).

The photovoltaic parameters of the solar cells were periodically monitored indoor with an AM1.5 class AAA Newport Oriel Verasol LSH- 7520 solar simulator (70 mW/cm^2) and a Keithley 2410 source-measure unit. Before aging the cells were kept in the dark inside a glove box (O2 < 0.1 ppm).

Materials characterization

Dynamic scanning calorimetry (DSC), size exclusion chromatography (SEC), nuclear magnetic resonance spectroscopy (NMR)

Differential scanning calorimetry (DSC) was carried out under nitrogen between −20 to 300 °C at a scan rate of 10 °C/min using a Mettler Toledo DSC2 calorimeter equipped with a HSS7 sensor and a TC-125MT intracooler. DSC was used to determine the peak melting and crystallization temperature as well as the enthalpy of melting. Thermogravimetric analysis (TGA) was carried out under nitrogen between 20 to 550 °C at a scan rate of 10 °C/min using a Mettler Toledo TGA/DSC 3 + instrument. TGA was used to determine the decomposition temperature. The molar mass was measured with size exclusion chromatography (SEC) on an Agilent PL-GPC 220 Integrated High Temperature GPC/SEC System in 1,2,4-trichlorobenzene at 150 °C using relative calibration with polystyrene standards. SEC was used to determine the molar mass and the dispersity (PDI) of the polymers. ^{1}H nuclear magnetic resonance (NMR) spectroscopy was measured on a Varian Inova 400 MHz NMR spectrometer by using chloroform-d (CDCl$_3$) as solvent and tetramethylsilane (TMS) as internal reference. The head-to-tail (HT) and head-to-head (HH) protons from α-CH$_2$ on the hexyl side chain give a peak at around δ = 2.8 ppm and δ = 2.6 ppm, respectively. The regioregularity of P3HT was calculated from the 1H NMR integral of the different α-CH2 protons on the hexyl of P3HT by following the equation (14) below[231]:

$$\text{RR}_{P3HT}(\%) = \frac{\text{Integral}_{\text{HT}}}{\text{Integral}_{\text{HT}}+\text{Integral}_{\text{HH}}}, \text{Eq. 14}$$

Inductively coupled plasma optical emission spectroscopy (ICP-OES)

ICP-OES was used to determine the trace metal content of the polymers. 200–250 mg polymer were digested in nitric acid (65%, purity p.A., Merck Schuchardt OHG) and hydrogen peroxide (33%) in a microwave (Biotage Initiator+, instrument settings 15 min, 180 °C, vial 0.5–2 mL, absorption level very high, fixed hold time OFF). This process was repeated three times with altogether 2 mL nitric acid and 400 µL hydrogen peroxide. The combined solutions were refilled to 25 mL with water and filtered through nylon syringe filter (0.45 µm, Applichrom). The resulting solution was utilized for the measurements with the ICPOES (Varian 725-ES) to determine the trace metal contents.

Electron spin resonance (ESR)

Standard 5 mm OD NMR tubes (which are ESR silent within the g = 2.00 region) were loaded with the P3HT powder (10–20 mg) inside the argon glovebox and tightly closed under inert atmosphere before taking them out for measurements. The weights of the empty sample tubes and those with the introduced material were determined with a high accuracy (± 0.01 mg). The ESR spectra were recorded using a benchtop Adani CMS8400 spectrometer. Integration of the signals in the ESR spectra was performed using EPR4K software developed by National Institute of Environmental Health Science (NIEHS). Each sample was characterized by average number of spins per repeating unit following the previously published approach[232].

Optical spectroscopy – ultraviolet/visible-spectroscopy (UV/Vis), photothermal deflection spectroscopy (PDS)

A custom-made spectroscopy setup was used to determine UV/Vis spectra. In the setup a glass fiber above the sample, which captures light reflected from the sample, is surrounded by a ring of several other fibers which carry the light from a white light source containing a halogen lamp and a deuterium arc lamp. Below the sample there is another glass fiber collecting the light transmitted through the device. The fibers are connected to two spectrometers from Avantes AvaSpec-ULS3648, which record the spectra. A custom-made setup for photothermal deflection spectroscopy (PDS) was used to determine the sub-bandgap absorption of all investigated P3HT films as done in previous works[233]. The measurement principle and basic setup of PDS is described

elsewhere[234]. The used monochromatic light source (obtained from LOT-Quantum Design) contains a 450 W Xenon lamp and a monochromator with a focal length of 260 mm). The monochromator is equipped with three gratings providing maximum intensity from 300 to 2000 nm, while the resolution is kept at 10 nm up to 1000 nm and 20 nm above 1000 nm. The light is modulated by a chopper operating at a frequency of 5 Hz. Deflection of a 0.7 mW HeNe-laser is measured by a $10 \times 10mm2$ lateral effect sensor obtained from Thorlabs. The measured deflection is frequency selective and amplified by a SR850 Lock-In amplifier. The samples are dispersed in perfluorohexane and graphite is used as standard to calibrate the data. A self-written Labview program automatically collects and calibrates the data.

Device characterization

Current-voltage-characterization (IV)

Devices were initially IV characterized upon arrival e.g. at CEEC Jena under a solar simulator using a metal halide lamp. The metal halide lamp was calibrated to 1000 W/m^2 with a pyranometer. The setup uses a computer-controlled Keithley 2400 SMU. Samples were connected using crocodile clamps.

External quantum efficiency (EQE)

EQE characterization of the samples was done at CEEC Jena upon arrival and after aging. The EQE setup used is a BENTHAM PVE 300. EQE measurements were generally performed without additional bias light. Hence, if the device performance decays during aging, but the EQE remains constant, the loss mechanism could be due to increased bimolecular recombination or series resistance losses, only showing under higher excitation densities. On the other hand, if EQE decreased upon ageing, but photocurrent remained on a higher level within the L2-setup, the low light level conditions within the EQE measurement point to extraction problems, e.g. due to insufficient trap filling.

PAIOS characterization

JV, CELIV, TPC, TPV, DIT, impedance, C–V, temperature dependence and numerical simulation details. Transient and impedance techniques can help to characterize charge transport.

Qualitative comparison of nominally identical devices, and between fresh and aged cells may contribute to the understanding of the underlying degradation processes. Current-voltage (IV), charge extraction by linearly increasing voltage (CELIV), transient photocurrent (TPC), transient photovoltage (TPV), double injection transient (DoIT), impedance spectroscopy, capacitance - voltage curves (C–V), and further optoelectrical characterization methods were performed at Fluxim AG using their All-in-one characterization platform Paios for Solar Cells[235,236]. For this purpose, Fluxim received a batch of fresh devices as well as aged cells from the L2 and O1 tests. The devices were illuminated with a high-power white LED (with an intensity above 1 sun illumination) allowing for pulsed and light-intensity dependent experiments.

Analysis method for L2 aging results: lifetime energy yield (LEY)

After the experiments were finished the aging data was analyzed to extract different relevant parameters, like the end of the burn-in period (at stabilized efficiency ES) (T_S), the lifetime (T_{80}) or lifetime after stabilization ($T_{S,80}$) and the lifetime energy yield (LEY). It was considered useful here due to its capability to depict a relevant parameter for an energy producing device, i.e. its energy output throughout its nominal lifetime. In the case of an ISOS-L2 experiment the LEY is straightforward as the light intensity is stable throughout the whole experiment. In case of O1 and D2 aging we restricted ourselves to analyze the performance decay as is.

Results

Polymer properties characterization

The initial characterization concerned polymer materials properties and the corresponding parameters obtained for the different P3HT batches investigated are summarized in Table 11 The molar masses varied roughly by a factor of three, whereas the dispersity (Đ, or polydispersity index – PDI) exhibited smaller variations with values between 2.0 and 2.7. The lowest molar mass, P3HT-III exhibited also the lowest PDI – together with P3HT-I. Concerning the regio-regularity (RR) generally all samples showed high values between 94% and 96%; only the sample with the highest molar mass and the highest PDI, P3HT-IV, had a rather low value with 90%. Also for crystallization (T_C) and melting temperatures (T_M) the same sample differed considerably from the others, exhibiting the second lowest value of $T_C = 189 \,°C$ and the lowest value of $T_M = 222 \,°C$. In

accordance with its low RR, P3HT-IV exhibits the lowest melting enthalpy (ΔH_M) of all samples, indicating and confirming that it is less ordered. The decomposition temperatures were – as expected for the same chemical structure – almost identical for the different P3HT batches.

Table 11. Polymer properties of the P3HT batches determined by GPC, TGA and DSC at Chalmers University.

Polymer	M_n (kg/mol)	M_w (kg/mol)	D(-) [PDI]	RR (%)	T_D (ºC)	T_M (ºC)	T_C (ºC)	ΔH_M (J/g)
P3HT-I	30	59	2.0	96	455	237	201	18
P3HT-II	24	54	2.3	94	455	227	184	17
P3HT-III	11	22	2.0	96	455	227	197	20
P3HT-IV	26	71	2.7	90	456	222	189	14
P3HT-V	25	60	2.4	95	455	236	198	21

Trace metal content analysis of the P3HT batches

The results for the trace metal content determined by ICP-OES are summarized in Table 12. They show a certain variation between the different polymer samples, which might stem from different synthetic approaches used for the polymerization, the equipment used to handle them and the purification methods applied. The standard synthetic procedures for regioregular P3HT include the McCullough method, which is a Kumada coupling, as well as the Rieke method based on activated zinc (Rieke zinc).[237,238] Moreover, the Grignard metathesis reaction (GRIM) was developed by McCullogh.[239] All these reactions are based on nickel catalysts. Furthermore, also palladium-catalyzed reactions have been applied: Stille coupling, Suzuki coupling as well as the dehydrogenative polycondensation.[240,241] For a very ubiquitous element like sodium, which is basically everywhere, there are barely any variations between the different P3HT samples. Palladium content was below the detection limit for all samples (Pd-catalyst are only used for the

non-standard polymerizations). Residual palladium is known to cause shunting problems [80]. The nickel content, the main catalyst for the standard polymerizations (e.g., in the GRIM) is also very low for all polymer samples. Only P3HT-I exhibited a comparably high magnesium content, which might be caused by residual magnesium salts from utilized Grignard reagents. Noteworthy, the zinc content was also rather low for all polymers. On the other hand, P3HT-IV exhibited the highest iron (Fe) content but otherwise did not differ much from all other batches. The iron could originate from the catalyst (dppf as phosphine ligand), however, this ligand is rather unusual. Alternatively, the synthesis might also have been performed in steel reactors.

Table 12. Trace metal content of the different P3HTs used in the experiment. Determined by ICP-OES (nn = below detection limit).

P3HT Batch	Ca mg/L	Cu mg/L	Fe mg/L	K mg/L	Mg mg/L	Na mg/L	Ni mg/L	Pd mg/L	Sn mg/L	Zn mg/L
Blind values	0.115	0.009	0.116	0.115	0.013	0.51	nn	nn	0.06	0.015
	0.101	0.008	0.092	nn	0.009	0.49	nn	nn	0.06	0.013
P3HT-I	0.806	0.024	0.083	0.33	0.481	3.158	0.046	nn	0.182	0.037
	0.789	0.025	0.084	0.347	0.487	3.135	0.057	nn	0.177	0.038
P3HT-II	1.077	0.014	0.153	0.145	0.131	3.081	0.045	nn	0.132	0.024
	1.085	0.014	0.15	0.168	0.132	3.082	0.043	nn	0.144	0.024
P3HT-III	1.051	0.01	0.179	0.173	0.107	3.41	0.013	nn	0.091	0.072
	1.035	0.01	0.188	0.177	0.106	3.367	0.014	nn	0.078	0.072
P3HT-IV	1.116	0.01	0.512	0.155	0.112	3.183	0.045	nn	0.068	0.072
	1.124	0.01	0.521	0.159	0.113	3.185	0.044	nn	0.076	0.073
P3HT-V	0.934	0.014	0.203	0.257	0.093	3.588	0.031	nn	0.133	0.021
	0.949	0.014	0.203	0.224	0.094	3.591	0.029	nn	0.155	0.022

Optical spectroscopy

Optical spectroscopy can yield information about the crystallinity of the different P3HT batches used. In this case films were cast from pristine P3HT solutions and characterized as is. In Fig. 61 P3HT-III stands out as the most crystalline batch as can be seen by the multiple distinct peaks near the absorption onset. This is consistent with its material properties as stated in Table 11, specifically the low PDI, high regio-regularity (RR) and the high melting enthalpy. However, the overall correlation between spectroscopic information and structural parameters reported above is not strong. In general it could be expected that more crystalline materials would be more stable and exhibit a slower degradation, in case blend stability dominates the degradation.
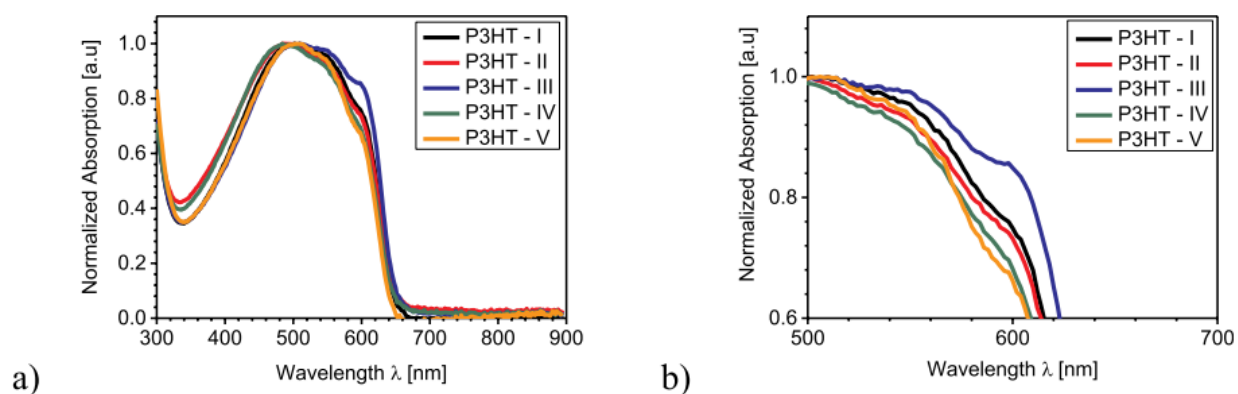
Figure 61. UV/Vis spectroscopy results for pristine P3HT thin films of the respective P3HT batches, a) overview and b) details of the films. P3HT-III shows the highest crystallinity

Photothermal deflection spectroscopy, of which results are depicted in Fig. 62, showed an increased absorption below the bandgap for P3HTII, in agreement with the results from electron spin resonance spectroscopy (see below). The sub-bandgap absorption of the P3HT batches show several known features. The first one is the peak centered at around 1000 nm which can be assigned to the P2 polaron transition, indicating minor p-doping of all batches of the pristine P3HT. It seems that this is most pronounced for P3HT-IV, and least pronounced for P3HT-I and –III. While P3HT-I contained relatively high content of trace metal impurities, P3HT-III had fewer impurities making an assignment of the polaron peak to trace metal contents difficult. However, P3HT-IV exhibited the highest content of Iron. Furthermore, we see an unstructured absorption between 700 and 900 nm which is most prominent in P3HT-II and -V. This might be caused by amorphous morphology

resulting in increased tail absorption. However, interestingly, the most disordered P3HT-IV batch exhibits a lower absorption in this range. A shallow defect state arising e.g. from chemical impurities could also explain this feature, which might increase the recombination rate in P3HT.
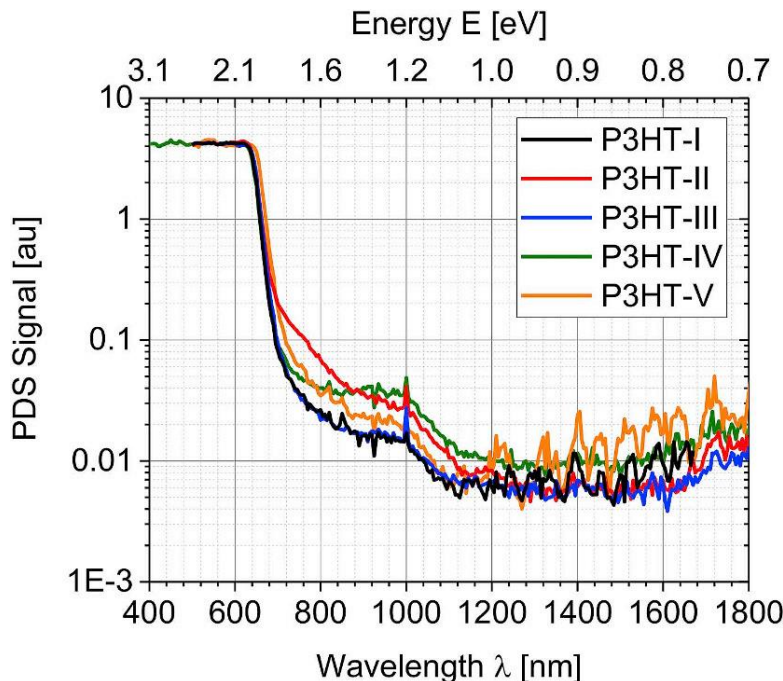
Figure 62. Results of the photothermal deflection spectroscopy measurement on pristine P3HT films. All of them show some signature of doping, visible by the peak around 1000 nm

Electron spin resonance spectroscopy

Electron spin resonance is a useful method for determining radical concentrations in the material under investigation. In this study, radicals might originate from defects at the chain capping groups, some structural defects (e.g., stabilized tri(hetaryl)amine type radicals) or certain impurities possibly stemming from the synthesis and insufficient purification. Alternatively, radicals can belong to the polymer polaronic state formed as a result of the material oxidation (oxidative doping) while handling it in air. The concentrations of persistent radical species for the P3HT-batches was estimated using ESR spectroscopy (Table 13). We did not find any correlation with the molar masses of the polymer samples, which would be a reasonable expectation if the radicals are mostly induced by defected chain capping groups. The obtained radical concentrations could also not be related with the findings from the ICP-OES measurements (Table 12), as P3HT-

II generally showed relatively small levels of trace metals, but exhibits the highest radical concentration by ESR. However, some correlation could be found when comparing radical concentrations with PDS data: here P3HT-II showed the highest radical concentration in ESR, and also exhibited the strongest absorption between 700 – 900 nm in the sub-bandgap region of the PDS spectrum. On the other hand, P3HT-III exhibited not only the lowest sub-bandgap absorption, but also showed the lowest radical concentration obtained via ESR. However, the correlation does not hold very well for the other batches, e.g. P3HT-I, exhibiting the lowest concentration of polarons as by PDS (like P3HT-III), had a relatively high radical concentration. These observations suggest that radical species identified in different samples of P3HT apparently have different origins.

Table 13. Experimental results of the ESR measurements on the pristine P3HT films.

P3HT Batch	Concentration of the radicals (spin/r.u.)
P3HT-I	7.94E-6
P3HT-II	3.98E-5
P3HT-III	1.45E-6
P3HT-IV	4.82E-6
P3HT-V	3.13E-6

Finally, it should be emphasized that concentration of radical species in all investigated P3HT samples is relatively low and should not impair the efficiency of the photovoltaic devices based on these materials. The results of other characterization methods applied to the P3HT batches are displayed in the Supplementary Information, sections 5-8.

Results of controlled aging

ISOS-L2 degradation

1 Performance over time versus P3HT batches. The ISOS-L2 protocol provides an efficient way of accelerated testing of lifetimes. Stress factors like heat (here 55 °C in the shadow) and light (including UV-light) reveal operational weaknesses of photovoltaic devices. Due to space constraints here only the power conversion efficiency (PCE) over time curves are being displayed; see section 4 for the time development of the other photovoltaic parameters.

Considering the characterization data from above, it might be expected that P3HT-I (for metal contamination) and P3HT-II batches (for radical concentration and sub-bandgap absorption) would lead to the fastest decay in performance. However, specifically these two batches yielded the best values for stability. Similarly, if we consider the extreme cases of the molecular properties, P3HT-III representing one of the most highly ordered, and P3HT-IV representing the least ordered among all, we can find a layer stack (TEIC) in which both perform similarly well and better than all others. These results – and the fact that there was no agreement among the different sets of devices originating from different cell producers concerning which P3HT batches lead to slower or faster degradation, makes correlating the lifetime data and the P3HT properties difficult.

The performance decay for the different cell producers, respectively their layer stacks applied, are shown in Fig. 63, while the corresponding ageing parameters based on various fit functions are summarized in Table 14. In order to check whether P3HT-batches do yield similar decay curves in different layer stacks, the ageing data is replotted with respect to the materials itself (Fig. 64). However, no clear correlation is found between P3HT-batch and ageing slopes, thus the decay slopes generally seem to depend more on the layer stack (i.e., cell producer) than on the actual P3HT-batch used.

Table 14. Results of curve fitting of the performance decay over time. Given are the fit function, the burn-in time TS, efficiency after burn-in ES, operational lifetime TS,80 (or T80) and efficiency at the end of nominal lifetime ES,80 (or E80). Finally the calculated lifetime energy yields (LEYs) for the L2 aged solar cells are given. See S59–S80 for the respective fits. (* - lifetime from data is infinite and thus was limited to the tenfold stressing time, # denotes catastrophic failure).

Manufacturer	P3HT Batch	Fit Function	E_S (%)	T_S (h)	$E_{S,80}$ or E_{80} (%)	$T_{S,80}$ or T_{80} (h)	LEY (kWh/m^2)
CEA	P3HT-I	Exp	-	-	2.32	2241	52.9
	P3HT-II	Lin	-	-	0.55	355	2.16
	P3HT-III						
	P3HT-IV	BiExp	0.56	172	0.44	826	4.44
	P3HT-V	BiExp	1.84	24	1.47	509	9.56
EIT+	P3HT-I	Exp	-	-	0.93	229	2.39
	P3HT-II	BiExp	1.44	16	1.15	1594	20.5
	P3HT-III	Lin	-	-	0.65	1088	8.01
	P3HT-IV	Lin	-	-	0.53	1547	9.18
	P3HT-V	LogLin	0.85	180	0.56	784	5.81
ICN2	P3HT-I	BiExp	0.22	35.9	0.17	10000*	14.6
	P3HT-II	Exp	-	-	0.76	458	3.9
	P3HT-III	-	-	-	-	-	-
	P3HT-IV	Exp	-	-	0.55	114	0.70#
	P3HT-V	BiExp	0.15	437	0.12	7248	9.83
TEIC	P3HT-I	BiExp	1.02	21	0.81	733	6.71
	P3HT-II	BiExp	1.6	24	1.27	454	6.56
	P3HT-III	Lin	-	-	1.79	458	9.23
	P3HT-IV	BiExp	1.47	11	1.26	546	7.71
	P3HT-V	BiExp	1.46	22	1.16	155	2.11
UTV	P3HT-I	Lin	-	-	0.91	34#	0.35
	P3HT-II	-	-	-	-	-	0
	P3HT-III	Lin	-	-	2.43	17#	0.45

P3HT-IV	Lin	-	-	0.67	14[#]	0.1
P3HT-V	Lin	-	-	3.62	40[#]	1.61
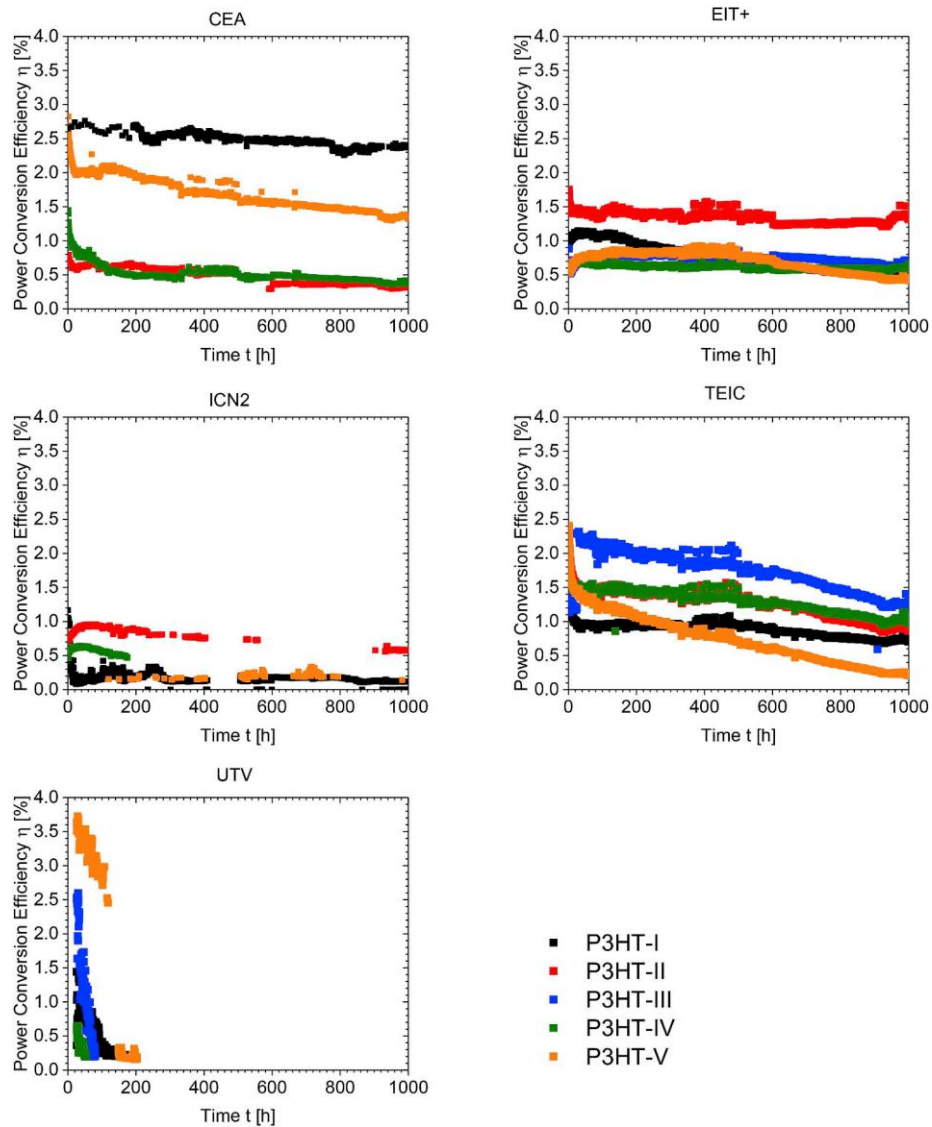
Figure 63. Aging curves for organic solar cells of the different manufacturers (indicated in the title of each panel) from the ISOS-L2 measurements performed at CEEC Jena, with different P3HT-batches.
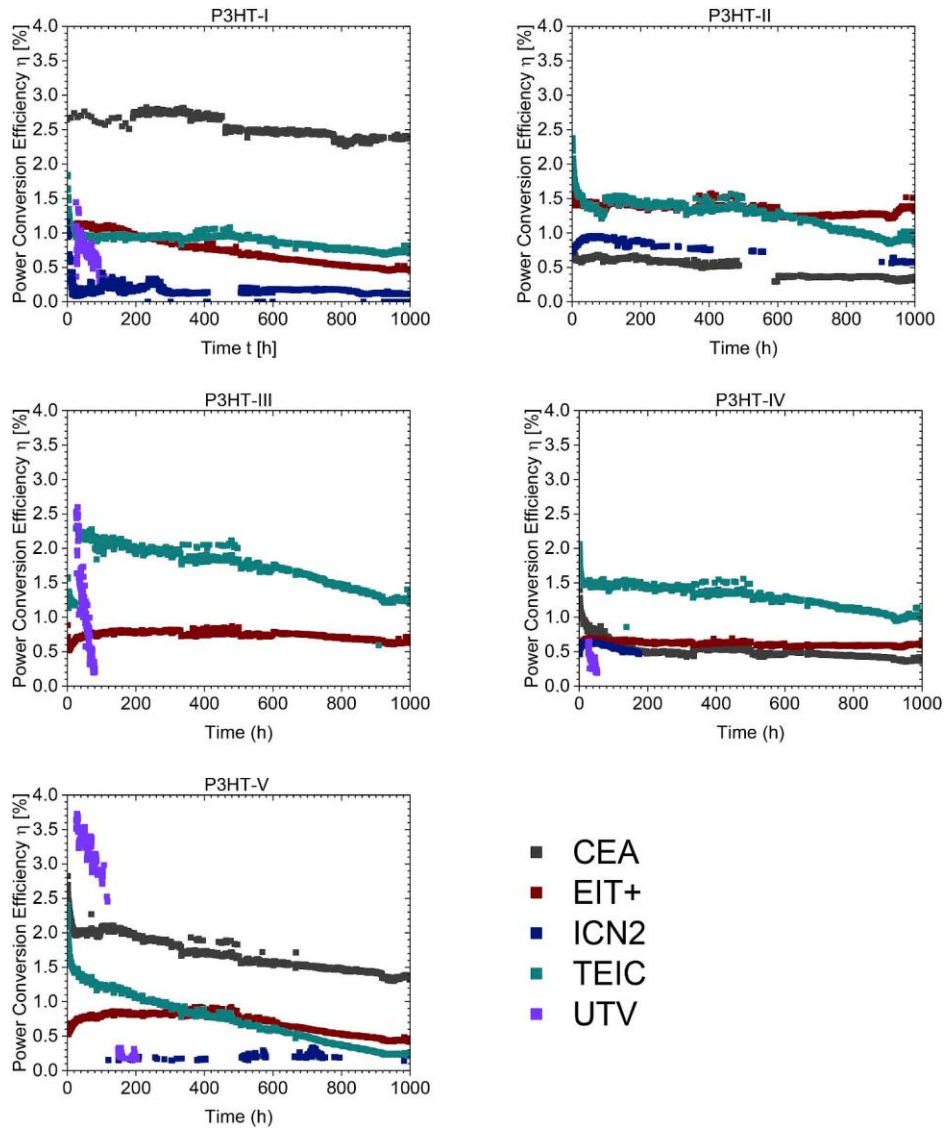
Figure 64. ISOS-L2 aging data plotted for individual P3HT-batches (indicated in the title of each panel) for solar cell producer, respectively, their device layout.

A more consistent behavior was found for the rather stable (but sometimes at lower performance) operation of P3HT-I and P3HT-V, which seemed to degrade generally faster (smaller lifetime) than the other batches. Unfortunately, this behavior could not be related to any P3HT property, as the latter batch had no distinct properties under all of the characterization methods reported above. It is interesting to note that cell producers who provided their own active layer material, obtained the most stable operation with exactly these materials. Thus, we may conclude here that experience with the material system seems to play a more dominant role in obtaining stable devices than the actual choice of P3HT-batch.

The most consistent ageing behavior was found for the devices made by TEIC, which always showed a bi-exponential decay function under ISOS-L2. Furthermore, TEIC cells demonstrated that with a sufficiently good encapsulation it is also possible to reach a relatively high lifetime with conventional architecture. The outstandingly highest device stability was reached by CEA with the self-provided P3HT batch (P3HT-I), leading to similar LEY values as reported in the literature.[242] It is interesting to note that also poorly encapsulated inverted devices failed faster than the conventional devices, which was most pronounced in the case of the UTV and ICN2 devices. This observation suggests the need to re-assess the inverted layer stacks concerning their inherent intrinsic stability problems.

The low stability observed for the UTV devices might be connected with the encapsulant Surlyn, as its glass transition temperature (Tg) is below 60 °C. Though the heating in the chamber was set to 55 °C in the shadow, the cell temperature can be expected to be considerably higher owing to direct exposure to full light spectrum and associated heating effects. As diffusivity suddenly increases above Tg, especially oxygen ingress might have happened at an increased rate. This assumption is supported by the fact that the Surlyn encapsulation layer is thicker than the epoxy layers used and thus can lead to higher ingression rates and then serve as a larger reservoir for oxygen.

2 Performance over time versus cell producer. In Fig. 64 it is clearly visible that the cell producer, i.e. the device layout, is more dominating the aging behavior than the P3HT. The same P3HT batch exhibits strongly varying aging behavior for the different producers, like P3HT-I which shows a nearly linear decay for EIT+, though showing a biexponential decay behavior for TEIC and a more or less constant operation in case of CEA. The burn-in behavior for the individual P3HTs is independent of the P3HT batch used as can be seen from the aging curves of each producer. Hence the degradation of the interfaces and interfacial and electrode materials (partially influenced by the sealing) have a larger impact, than the variation of polymer properties found in the P3HTs used for the experiment.

3. Evaluation of lifetime energy yield (LEY). CEA and EIT + demonstrated record LEYs of ~53 kWh/m^2 and 20 kWh/m^2 based on devices built with their self-provided material P3HT-I and P3HT-II, respectively (Tables 14). This fact is unexpected, as P3HT-II exhibits considerably

different material properties than P3HTI, and the low performance in EIT + devices cannot be explained. Among the other materials, maximum LEY values of ca. 10 kWh/m^2 were reached, for P3HT-III by TEIC, for P3HT-IV by EIT+ and for P3HT-V by ICN2. In general, the aging characteristics obtained by one producer were not identical for the different materials used. In case of P3HT-I based solar cells built by CEA the first 200 h are missing due to some contact problem observed only later. As no burn-in was observed, it may be highly probable that this device completed burn-in before reconnection occurred. From the best stabilities obtained for the record devices of CEA and EIT + some further conclusion concerning the hole extraction layer can be made: CEA used inverted architecture with PEDOT:PSS, while EIT + used MoO$_3$ for hole extraction. Thus, at least PEDOT:PSS cannot be claimed responsible for yielding insufficient OPV stability. For completeness it should be mentioned that the total device area is not a relevant parameter for stability, as these two cell producers delivered the largest and the (nearly) smallest solar cell areas.

4. Remarkable exceptions. The highest stability in terms of lifetime was generally shown by P3HT-I cells. A remarkable exception was observed for P3HT-I cells provided by ICN2: while devices generally suffered from insufficient encapsulation, this device basically showed an "eternal" lifetime (no slope), however, at a very low performance level ($< 0.2\%$ PCE). We decided to cut the lifetime at 10000 h, as further extrapolation to longer lifetimes is not really supported by an about 1000 h lasting ageing experiment.

5. Usefulness of L2 for stability experiments. The ISOS-L2 protocol allows determining the photostability of devices in an accelerated way. In combination with ISOS-D2 characterization the effect of the elevated temperature can be deconvoluted in order to learn about the pure light stability. Hence the performance decay observed in L2 should be expected to be more than for O1 and D2, assuming a perfect encapsulation and a sufficiently long measurement period. L2 ageing might also allow for drawing conclusions about the lifetime of a device under realistic operation in the field (outdoors). It is assumed that a lifetime of 1000–2000 h under L2 roughly corresponds to a lifetime of 1 year in the field under stable sealing. Thus the most stable devices of this study correspond to about 1–5 years operational stability in the field.

External quantum efficiency for L2-Ageing

Besides the pure stability and performance information, external quantum efficiency (EQE) measurements can yield additional information. In accordance with its high crystallinity, solar cells processed with P3HT-I commonly have an absorption onset towards longer wavelengths than those of the other P3HT batches (see Fig. 65). In case of the inverted device structure (here CEA, EIT+, and ICN2) the spectral response remains stable in its qualitative characteristics. However, for the only conventional device architecture (TEIC) an interesting effect is observed: upon aging the regions exhibiting highest absorption by P3HT-I show lower charge extraction for the L2 aged device. This may refer to an unfavorable vertical material gradient that inhibits charge extraction from a certain region of the device, where a higher P3HT-I concentration is present. This could be due to a build-up of a space charge region within the active layer, where a higher concentration of P3HT-I is present. However, this effect takes place already early during aging, specifically during the burn-in process, and thereafter the performance remains fairly stable – in fact this was the most stable of all devices processed in conventional architecture. Thus this type of burn-in degradation might be best related to the relatively high number of metal impurities, as well as radical concentrations, as found by ICP-OES and ESR. However, in unprocessed pristine P3HT-I fairly low polaron densities (PDS) were found, indicating that only the combination of light and metal impurities may play a dominant role here for the generation of space charge. As the overall behavior of all devices cast from this P3HT-I is relatively stable (as seen by the long lifetimes), the observed losses should in all cases be related to space charge built up due to inherent impurities present in the material from the beginning. Thus, we may speculate that the same P3HT without the space charge would yield much higher performances for longer times.
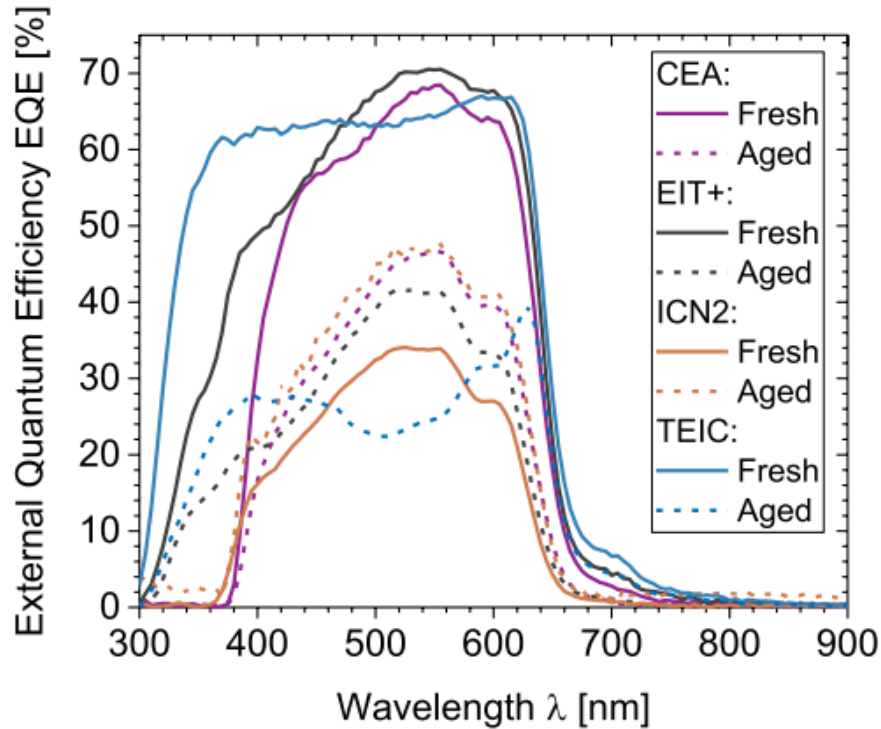
Figure 65. EQE spectra for P3HT-I solar cells from different manufacturers before and after L2 aging

Upon comparison of the EQE-data with the ageing data of the photocurrent from ISOS-L2 we can find a severe deviation for the CEA P3HT-I sample between the photocurrent measured under the solar simulator ($\sim$8 mA/cm^2) and the one from integration of the EQE-curve and multiplication with a hypothetic AM 1.5 spectrum: the EQE-curve delivers only 5.72 mA/cm^2. This deviation could be assigned to trapassisted charge recombination or an extraction barrier in the low-light level case, which can be overcome by trap-filling for higher excitation densities. It is interesting to note that already in the beginning of the experiment, light bias yielded a gain in photocurrent for the same device, see Fig. 66. Unfortunately, no EQE with bias measurements were performed after the L2-ageing.
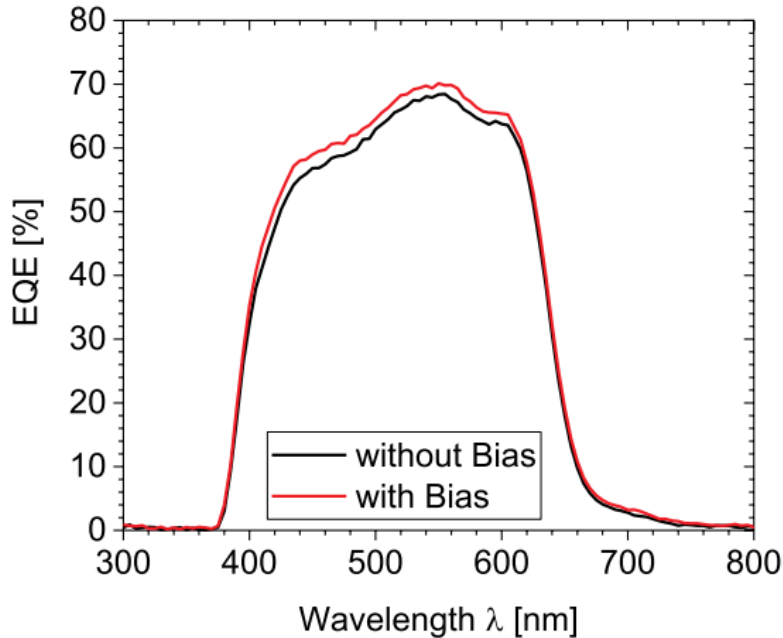
Figure 66. EQE measurement with and without bias light for CEA-P3HT-I cell before L2 degradation determined at CEEC Jena.

ISOS-D2 degradation

In contrast to our expectation, the photovoltaic devices suffered on average more degradation under dark storage at elevated temperatures (ISOS-D2), seen in Fig. 67, than under accelerated laboratory weathering (ISOS-L2). Notable exceptions were found only for EIT+ and TEIC devices, which showed higher performances than under L2. In case of the EIT + solar cells drastic device failure is visible for P3HT-II, indicating breakage of the sealing. This hints that for these configurations the thermal stability is much more relevant than the light stability. However, even for the case presented here, where the L2 ageing took place at slightly lower temperatures of 55 °C in the shadow, similar temperatures are to be expected within the devices for L2, as the light absorption itself must inevitably lead to heating. Further this means that EIT + cells show a good thermal stability, while their photo-stability is lower than those of the other cells. This might be connected to light-induced doping effects arising from the MoO_3 hole transport layer. On the other hand, devices produced by UTV and ICN2 exhibited similarly low stability as under L2, indicating degradation mechanisms to be independent of light. In general, it should be noted that insufficient

123

sealing effects may have played a more important role under D2 than under L2 aging, as for D2 not the innermost devices were chosen, but rather the best performing ones.
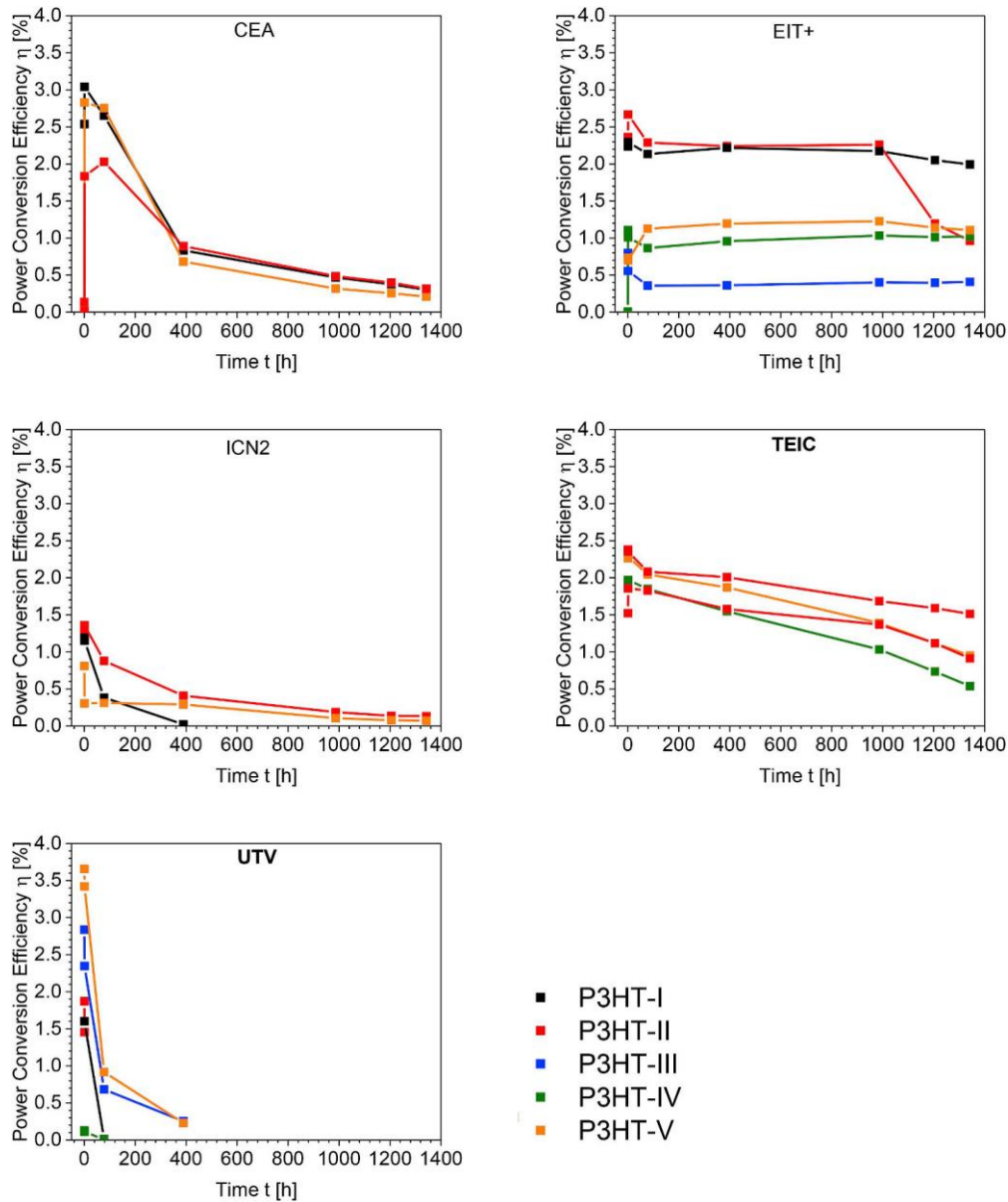
Figure 67. Aging data from ISOS-D2 experiment done by Solliance in Eindhoven.

An interesting deviation appeared for the TEIC solar cells, which did not show a fast burn-in, but rather a linear long-term decay. This hints to a light induced rather than a thermally induced process for the burnin, independent of the P3HT batch used. Furthermore, the CEA cells degraded severely, independent of the P3HT batch, indicating a thermally driven process that might be

124

prevented (at least for the most stable P3HT-I batch) under illumination. Finally, it should be noted that the highest performing devices (yielding also highest hypothetical LEYs) provided by EIT+ were obtained with the already identified superior P3HT-batches I and II.

ISOS–O1 degradation

The observations made for dark ageing under elevated temperatures could in part also be found for ISOS–O1, see Fig. 68. As a matter of fact, the EIT + devices outperformed in terms of stability for this ageing condition those aged under L2. Again, the identified superior P3HT batches, namely I and II, yielded the best performance over time here. Noteworthy are the devices provided by TEIC: although they showed considerable degradation following exponential decays, there was no indication of drastic failure. This confirms the superiority of the encapsulation used in this case over the other device layouts. In case of the remaining cell producers, drastic failure was observed in all cases, independent of the P3HT batch used. Hence the conditions even under this modified outdoor ageing seemed to be dominated by environmental impacts such as water or oxygen ingress. Interestingly, ICN2 solar cells based on the P3HT-batches I and II also outperformed the other batches, confirming their superiority. However, such exceptions were not observed in case of CEA, TEIC and UTV, where rather a material independent degradation was found.

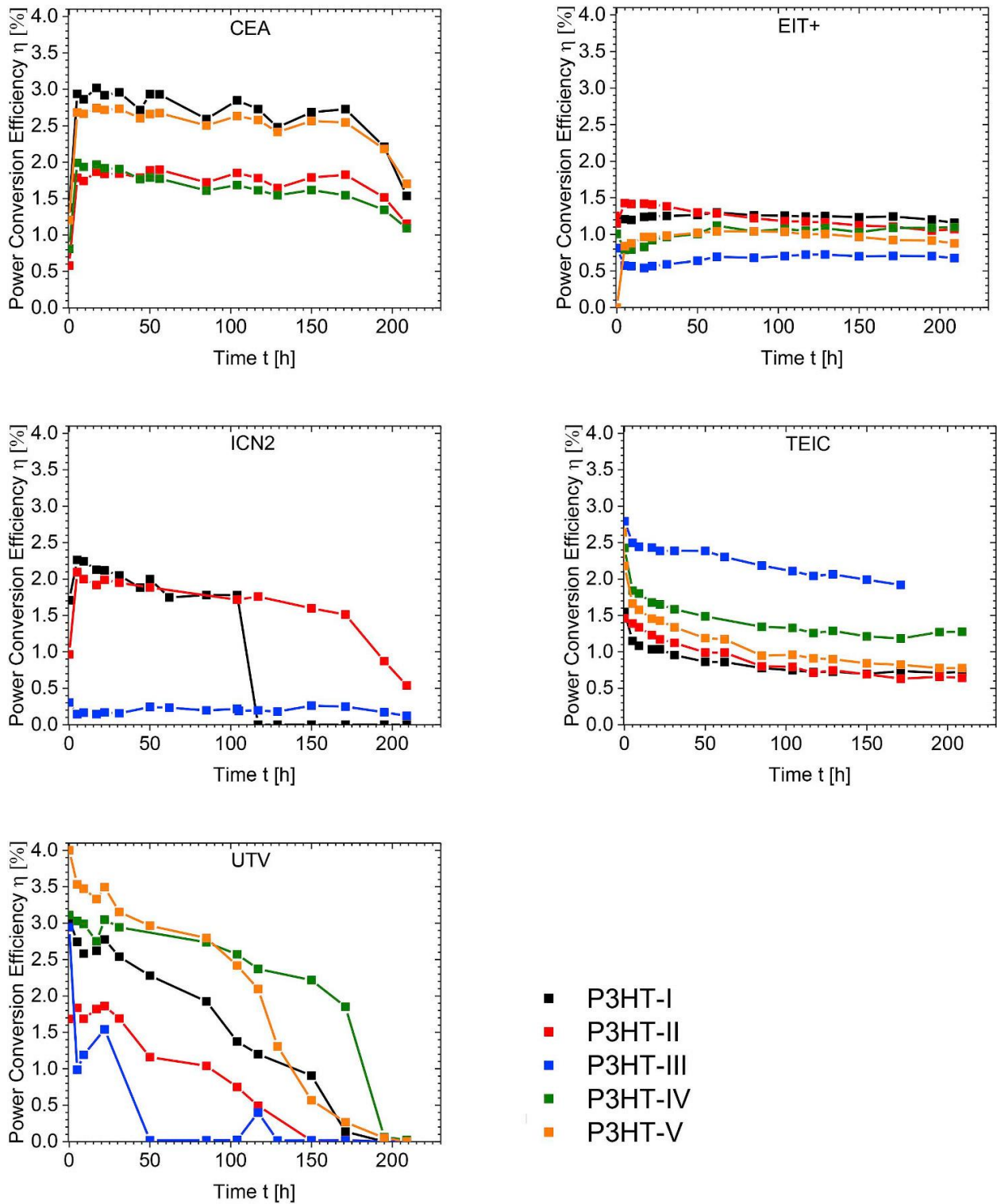*Figure 68. Aging data for ISOS–O1 measurements performed at BGU in Sede Boqer in Israel.*

Paios results

It has been shown that by a combination of various transient and impedance experiments, and a complementary data analysis, certain aging mechanisms can be revealed by their specific signatures. For example, an overshoot observed in the transient photocurrent is a trace of charge accumulation (space charge), which can occur due to trapping or an energetic barrier for charge extraction. The impedance signal of the two cases (trapping or energetic barrier), however, looks different, and therefore allows distinguishing between the two mechanisms. Another example is charging of the active layer (doping), which can be determined by combining impedance and CELIV measurements. Unfortunately, no systematic behavior for devices of the same producer or using the same P3HT batch could be found. We identified two main reasons for this: i) the low reproducibility in cells obtained make a cell-to-cell comparison erroneous, ii) the significantly differing stack architectures and sample geometries turn out to have an enormous impact on the initial cell performances and their stability. Yet, several conclusions can be drawn from this supplementary experiment.

In order to perform transient measurements small devices with a low RC time constant are required. This is, however, not only a necessary condition for analytic models to be valid, but also impacts any electrical measurement on the device. Large resistance values have been found in all cells produced by EIT + using the Osilla layout, which is mainly due to the un-metallized ITO contact. A series resistance of 200 Ohm already affects the steady-state performance of the device and should therefore be avoided. This observation nicely agrees with the observed low fill factors. The UTV layout, on the other hand, showed negligible contact resistances.

We further found shunting by leakage currents to be a major failure mechanism. Here devices by UTV, ICN2, and EIT+ were most sensitive, and the O1-aged devices showed more severe shunting than L2-aged ones. The underlying mechanisms for this behavior are however not understood.

Another important conclusion from the Paios measurements is that encapsulation failure, leading to the lateral in-diffusion of oxygen and water vapor, can superimpose to the degradation process of the active layer and will induce additional pathways for degradation which should be prevented. The inhomogeneous oxidation of the metal electrode from the sample edges forms an insulating

oxide layer hampering charge extraction. A prominent signature of this process is a strong overshoot in the transient photocurrent signal.

Fig. 69 shows an example of a TEIC sample, where the outer devices show more severe degradation due to the failure of the encapsulation adhesive. The further to the edge the cells were, the weaker was the measured signal, which shows there was ingress of oxygen and moisture through the encapsulation. This effect was found more pronounced in cells aged under L2 at CEEC Jena than under O1 in the Negev. We therefore speculate that it is driven by the oxygen diffusion, supported by elevated temperatures under L2 conditions.
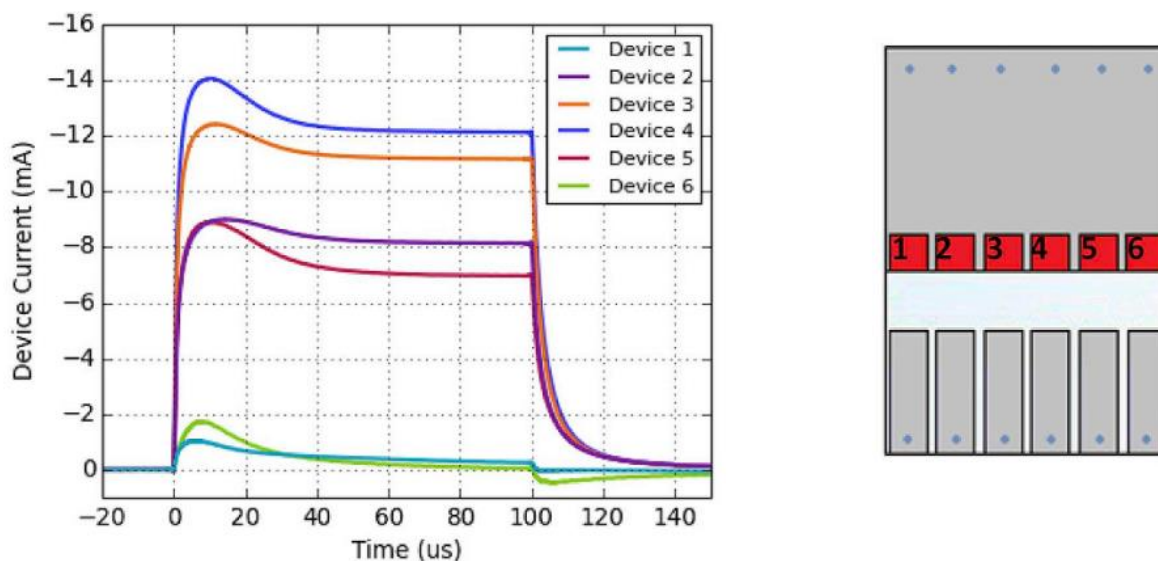
Figure 69. Transient photocurrent results for TEIC solar cells after aging.

Discussion

Two P3HT-batches showed in several cases – however, not consistently over all cell producers – exceptional stability: P3HT-I and P3HT-II. However, these two batches exhibit significantly different materials properties:

P3HT-I, yielding the exceptionally high LEY of 53 kWh/m^2 under accelerated ISOS-L2 ageing, is distinguished from the other batches by its high crystallinity; however, P3HT-III showed in the optical characterization the strongest aggregate absorption. Furthermore, P3HT-III remained similarly inconspicuous concerning sub-bandgap absorption like P3HT-I. However, except for

128

TEIC cells based on P3HTIII under outdoor degradation (ISOS–O1), this P3HT-batch rather underperformed in all stress tests compared to the other cell producers. The fact that P3HT-III exhibited the lowest radical and trace metal concentrations of all batches, seems to make this material property rather insignificant concerning its impact on yielding stable organic solar cells. Thus, the only remaining material parameter that could be blamed for the low stability can be the exceptionally low molar mass of this batch, roughly three times lower than all others. Microscopically, the low molar mass might be connected to an unfavorable phase behavior; either unsuitable crystallization leading to phase separation and thus loss in charge generation and diode characteristics, or vertical phase segregation reducing the fill factor and potentially the open-circuit voltage as well. It is known that lower molar mass P3HT samples lead to high crystallinity, while higher molar mass result in different crystallites due to chain backfolding. Besides the fact that several devices based on P3HT-III were missing out from the studies, this batch gave usually the lowest open-circuit voltages, except for the UTV devices where it yielded the highest ones. The difference that UTV devices showed with respect to all others must be connected to its electron extraction layer, which consisted of PEIE. This seems to make a big difference, potentially preventing interfacial recombination otherwise leading to a reduction of the quasi-Fermi level splitting. Getting back to P3HT-I and its properties, we may take the sub-bandgap absorption as the only remaining factor to take into account. Thus, low intrinsic doping levels and well-ordered domains, while keeping the molar mass large enough, seem to display a necessity for reaching long lifetimes at appreciable performances.

The second best result for lifetime energy yields was obtained with P3HT-II (by EIT+), although it exhibited rather opposite material properties than P3HT-I in all cases. However, its LEY remained below one half of that obtained by CEA with P3HT-I under ISOS-L2 conditions, clearly making this batch second choice. Part of the explanation for a LEY of $\sim$20 kWh/m^2 thus should be assigned to the experience by EIT+ with this material, as it was (as in the case of P3HT-I and CEA) provided by this lab. This reason might be also responsible for comparable performances between P3HT-I and –II obtained by EIT+ in the other ageing tests (D2, O1). Thus it may be concluded that experience with a material system plays a major role in getting stable performances.

Unfortunately, not all cell producers could reproduce these results: in two cases (ICN2, UTV) this was not possible due to insufficient encapsulation of the devices, leading to extrinsic

degradation becoming dominant. However, concerning the layers involved it might be indicated that PEIE is less suitable than ZnO for long-term stable electron extraction and V_2O_5 might be less stable than MoO_3 and PEDOT:PSS. The most reliable sealing of samples could be demonstrated by EIT+ and TEIC, specifically for the ageing tests obtained under ISOS-D2 and ISOS–O1. This means that – at least for glass-glass sealing – also conventional devices exhibiting PEDOT:PSS layers can reach substantially high intrinsic stabilities.

The experience gained from this collaboration experiment could be summarized as follows: if cell producers are confronted with new material systems with which they have no processing experience, a longer preparation and training time before providing devices for ageing tests is required. Of course a proper sealing method and corresponding encapsulation materials are required. Furthermore, improved statistics obtained by averaging over more devices may provide more reliability in ageing characteristics. The fewer devices take part in such an ageing experiment, the higher is the risk of losing devices due to catastrophic failures, which drastically lowers the chance for finding correlations between materials or layer stack properties. Finally, the design of the ageing experiments should be such that a sufficient amount of data points ($\gg$10) over time to enable a reliable fitting procedure, leading to a well-predictable long-term behavior.

According to the data, large lifetimes alone seem not to be an appropriate way of expressing the stability, since severe performance losses during burn-in would be disregarded. Hence we have chosen to use the determination of the lifetime energy yield (LEY), as this parameter combines lifetime and performance into one figure of merit, which expresses the usefulness of the solar cells in applications. This analysis is also of vital importance for solar cells with reversible degradation, for instance for perovskite-based photovoltaics[243].

Conclusion

In conclusion, though the overall statistics in this experiment were challenging due to partially insufficient encapsulation and thus extrinsic degradation, some rules concerning the materials properties could be found, which can help to develop intrinsically more stable organic photovoltaic devices. In case of the semi-crystalline organic semiconductor poly(3-hexyl-thiophene), high crystallinity, sufficiently high molar mass and minimum intrinsic doping levels, as well as minimal disorder as found by photothermal deflection spectroscopy, are beneficial parameters contributing

to stable photovoltaic operation. Interestingly, trace metal contents and radical concentrations seem to have no remarkable impact on device stability.

Furthermore, we found that the burn-in behavior of organic solar cells is mostly dependent on the layer stack. This means that part of the burn-in may stem from a) electrodes, b) transport layers, c) interfacial changes at the layer boundaries, d) differences in phase segregation of the active layer (i.e. stratification) due to different surface energies of the adjacent layers, or from e) a combination of the aforementioned factors.

In addition, experience with a certain material system seems to be an important parameter contributing to achieving relatively stable solar cells. Finally, the common suspect for insufficient organic solar cell stability, PEDOT:PSS, seems to perform better than its reputation, since the best devices in this comparison obtained with it in an inverted device architecture show competitive lifetime energy yields of more than 50 kWh/m^2.

6.3.2 Stability of OPVs based on PCDTBT donor polymer

*Laura Ciammaruchi, Ricardo Oliveira, Ana Charas, Tulus, Elizabeth von Hauff, Giuseppina Polino, Francesca Brunetti, Rickard Hansson, Ellen Moons, **Miron Krassas**, George Kakavelakis, Emmanuel Kymakis, José G. Sánchez, Josep Ferre-Borrull, Lluis F. Marsal, Simon Züfle, Daniel Fluhr, Roland Roesch, Tobias Faber, Ulrich S. Schubert, Harald Hoppe, Klaas Bakker, Sjoerd Veenstra, Gloria Zanotti, Eugene A. Katz, Pälvi Apilo, Beatriz Romero, Tülay Aslı Tumay, Elif Parlak, Luciano Mule Stagno, Vida Turkovic, Horst-Günter Rubahn, Morten Madsen, Vaidotas Kazukauskas, David M. Tanenbaum, Santhosh Shanmugam and Yulia Galagana.*

This work is part of the interlaboratory collaboration to study the stability of organic solar cells containing PCDTBT polymer as a donor material. The varieties of the OPV devices with different device architectures, electrode materials, encapsulation, and device dimensions were prepared by seven research laboratories. Sets of identical devices were aged according to four different protocols: shelf lifetime, laboratory weathering under simulated illumination at ambient temperature, laboratory weathering under simulated illumination, and elevated temperature (65 °C) and daylight outdoor weathering under sunlight. The results generated in this study allow us to outline several general conclusions related to PCDTBT-based bulk heterojunction (BHJ) solar cells. The results herein reported can be considered as practical guidance for the realization of stabilization approaches in BHJ solar cells containing PCDTBT.
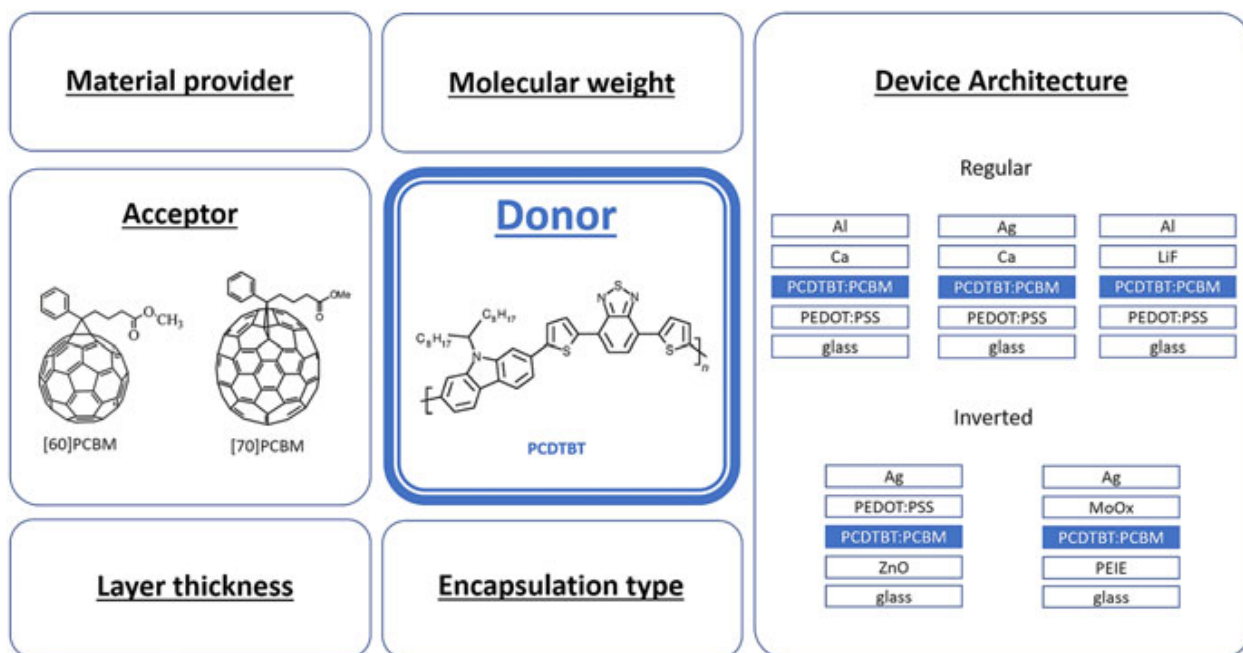
Figure 70. Overview of the tested device types and varied active layer parameters, along with the chemical structures of the PCDTBT donor and fullerene derivative acceptors used.

Experimental

The research laboratories participating in this study each have produced at least 10 identical devices, which have been encapsulated and shipped to the partners for aging and characterization. The main idea was that BHJ solar cells should be based on the PCDTBT absorber, whereas other parameters such as the type of charge transport layer (CTL), solar cell architecture, encapsulation type, etc. were varied depending on the laboratories (Fig. 70). In this way, the device producers used the architectures and materials in which they already had a solid experience. This guaranteed high efficiency and reproducibility of the devices, thus giving a high level of credibility to the performed research. Vice versa, asking device producers to use identical device architecture and materials might have given a lower level of credibility, as these architectures and materials would have been new for the laboratories and in lack of time-extensive process, optimization might have resulted in suboptimal devices.

Thus, seven research laboratories produced 10 identical devices each. With the aim of keeping objectivity, the names of producers are kept anonymous, and the devices will be referred to as Type 1, Type 2, . . ., Type 7. The layer structure consists of anode/CTL/PCDTBT:PCBM/

CTL/cathode, as detailed in Table 15. Five device structures in this study have a "standard" layout (Types 1, 3, 5, 6, and 7), and two have an "inverted" one (Types 2 and 4). Devices are fabricated on top of ITO-covered glass and are encapsulated using different methods. The area of the devices ranged between 4 mm^2 and 3.75 cm^2. The typical PCE values of each device type are shown in Fig. 71

Table 15. Summary of the device types under study

Identifier	Architecture	Area (cm^2)	Cell stack layers [thickness]	Encapsulation
Type 1	Standard	0.24	ITO + PEDOT:PSS [40 nm] + PCDTBT:PC$_{61}$BM [90 nm]+ Ca [20 nm] + Al [100 nm]	Glass + Delo-Katiobond (LP655) UV
Type 2	Inverted	3.75	ITO + ZnO [30 nm] +PCDTBT:PC$_{70}$BM [250 nm] + PEDOT:PSS [100 nm] + Ag [100 nm]	Metal lid + Araldite epoxy
Type 3	Standard	0.16	ITO + PEDOT:PSS [??] + PCDTBT:PC$_{60}$BM [250 nm]+ Ca [20 nm] + Al [100 nm]	Glass + Araldite epoxy
Type 4	Inverted	0.1	ITO + PEIE [10 nm] +PCDTBT:PC$_{70}$BM [70 nm] + MoO$_3$ [5 nm] + Ag [100 nm]	Glass + parafilm
Type 5	Standard	0.045	ITO + PEDOT:PSS [40 nm] + PCDTBT:PC$_{70}$BM [90 nm]+ LiF [0.3 nm] + Al [100 nm]	Glass + Ossila epoxy glue
Type 6	Standard	0.04	ITO + PEDOT:PSS [30] + PCDTBT:PC$_{60}$BM [80 nm]+ Ca [5] + Al [100 nm]	Glass + epoxy UV
Type 7	Standard	0.09	ITO + PEDOT:PSS [30] + PCDTBT:PC$_{60}$BM [90 nm]+ Ca [25 nm] + Ag [100 nm]	Glass + glue (LOCTITE 358) UV
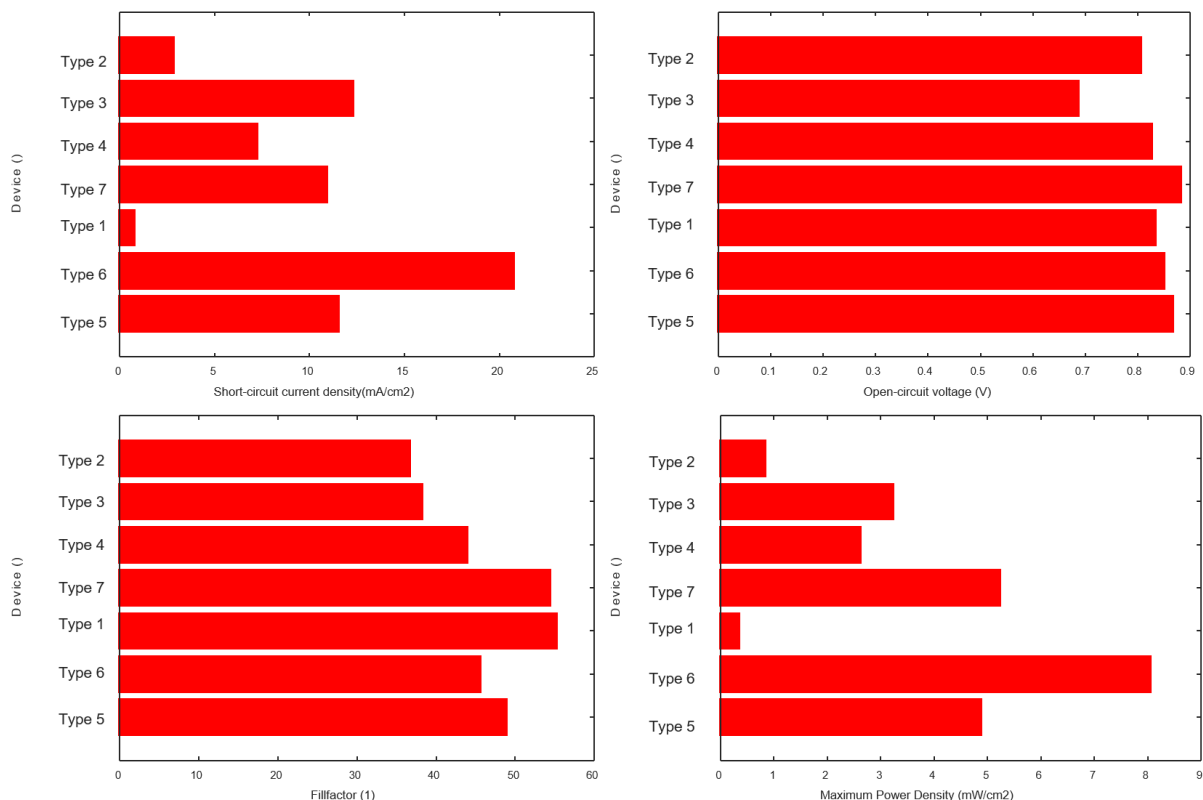
Figure 71. Snapshot of initial FOMs of selected devices of each Type.

Standard cells use ITO as anode and PEDOT:PSS as the hole transport layer (HTL). Regarding electron transport layer (ETL) and cathode, Types 1, 3, and 6 use Ca/Al, Type 5 uses LiF/Al, and Type 7 uses Ca/Ag. Inverted structures use ITO as cathode and ZnO (Type 2) or PEIE (Type 4) as the electron extraction layer (EEL). The anode is Ag and HTL is PEDOT:PSS (Type 2) or MoO_3 (Type 4).

After standard cleaning and drying processes, the substrates were treated with UV-oxygen plasma for several minutes (from 3 to 20 min). In standard devices, PEDOT:PSS was spin-coated and thermally annealed for several minutes over 100 °C to remove any residual water. Next, the blend PCDTBT:PCBM prepared in chlorobenzene or dichlorobenzene was spin-coated on top of the PEDOT:PSS. Details of the blend ratio, concentration, and deposition parameters are given in Table 16. The ETL (Ca or LiF) and cathode (Al or Ag) were thermally evaporated in high vacuum. In inverted devices, the EEL was spin-coated (PEIE or ZnO) on top of the ITO. The blend is then spin-coated and dried. In Type 2, PEDOT:PSS is spin-coated on top of the blend and annealed for

135

10 min at 120 °C. The cathode was always thermally evaporated. In Type 4, both MoO_3 and Ag cathodes were thermally evaporated on top of the blend.

Table 16. Details of the active layer composition and fabrication parameters

Identifier	PCDTBT:PCBM ratio	Blend concentration (mg/ml)	Spin coating speed (rpm)/time(s)	Annealing temperature /time
Type 1	1:2	12	1600/15 + +1800/45	110°C/5 min
Type 2	1:4	15	1000/60	
Type 3	1:4	30	1500/60	Vacuum dry/ 20 min
Type 4	1:4	40	2400/14	Vacuum dry/ 1 h
Type 5	1:4	20	750/100	
Type 6	1:4	20	1200/110	60ºC / 3 min (inert atmosphere)
Type 7	1:4	9	1000/60	120°C/20 min

The number of cells available for testing varied from one PCDTBT producer to another, due to some accidental cell breakdown, but at least two identical devices per producer were tested for each aging protocol. We note here that it was not possible to realize complete tests on Type 1 and Type 7, due to their sudden failure/breakdown during the series of testing. Therefore, Type 1 will not appear in the results and will not be discussed any further, while Type 7 will only appear in two of the aging protocols performed.

The devices were aged according to 4 different protocols[244]: (i) ISOS-D1: laboratory weathering in the dark at ambient temperature (shelf lifetime); (ii) ISOS-L1: laboratory weathering under simulated illumination at ambient temperature; (iii) ISOS-L2: laboratory weathering under simulated illumination and elevated temperature (65 °C); (iv) Daylight outdoor weathering under sunlight with measurements under simulated illumination. All devices were initially characterized at the aging laboratories before starting the actual degradations, and time = 0 was defined as the starting point of each test. Devices characterized according to the ISOS-D1 protocol were stored in the dark and monitored weekly for the first 12 weeks, and thereafter with the characterization

sequence of 5, 4, and 7 weeks. The I–V measurements were performed under AM1.5G illumination by using a solar simulator equipped with a xenon lamp and the Keithley 2400 source meter (Tektronix, Cleveland, Ohio). The aging following ISOS-L1 and ISOS-L2 protocols were prepared with a home-built stability setup enabling periodic in situ I–V characterization. The setup consists of ATLAS KHS 1200 W solar simulator (ATLAS, Linsengericht, Germany), under which solar cells can be placed and connected to a computer-controlled sourcemeasure unit. The automatic periodic I–V characterization was implemented by multiplexing. For the daylight outdoor degradation experiment, the cells were mounted on a 30° tilted rack from the horizontal. The intensity was measured with a calibrated thermopile pyranometer (Eppley PSP, The Eppley Laboratory Inc., Newport, Rhode Island) set to the same angle as the cells. This protocol differs from the ISOS-O1 protocol only by the fact that the cells were exposed to sunlight only during daylight (i.e., 6 h per day) until their T80 was reached, amounting to a total exposure time of ~120 h, between February 14th and March 30th 2016. The cells were measured with a solar simulator (AM1.5 class AAA Newport Oriel Verasol LSH-7520 solar simulator, Newport Corporation, Irvine, California) and a Keithley 2410 sourcemeter (Tektronix, Cleveland, Ohio). Between the light hours, the cells were stored in the dark in shelf life conditions. This was done to inhibit humidity-related breach/contact oxidation problems during the night. It is noteworthy to mention that the spectrum measured at noon time ±2–3 h of a cloudless day at Sede Boker (the Negev desert, Israel, Lat. 30.8°N, Lon. 34.8°E, Alt. 475 m) is nearly identical to the AM 1.5G spectrum. The details of similar outdoor degradation experiment are described elsewhere.[245,246] Devices under the same condition were stressed side-by-side. All devices were aged at V_{OC}.

The devices aged following the ISOS-L1 and ISOS-L2 protocols were characterized before and after aging using photoluminescence imaging (PLI). The luminescence imaging is based on the detection of luminescent radiation from a solar cell with a camera. Here, a silicon charge coupled device camera (Si-CCD, ANDOR iKonM, Andor Technology Ltd., Belfast, U.K.) was used during PLI, and the devices were excited with a blue solid-state diode array emitting at 470 nm, leading to efficient photon absorption and exciton formation within the PCDTBT with subsequent radiative decay. To block the excitation light of the LED array, a cutoff filter was placed in front of the Si-CCD. As the overall luminescence intensities are relatively small, the whole setup was placed into a light blocking housing.

Analysis of the experimental results

Figure 72 collects the main parameters defined as lifetime markers of a solar cell, as reported earlier.[247] T_{80} is commonly defined as the time when the device is degraded by 20% from the initial efficiency $PCE(T_0)$. T_S is the starting time of the more stabilized portion of the efficiency curve, while T_{s80} is the time when the efficiency reaches 80% of its stabilized value [80% of $PCE(T_S)$], as shown in Fig. 70. All solar cell parameters shown in this paper are normalized with respect to their value at T_0.
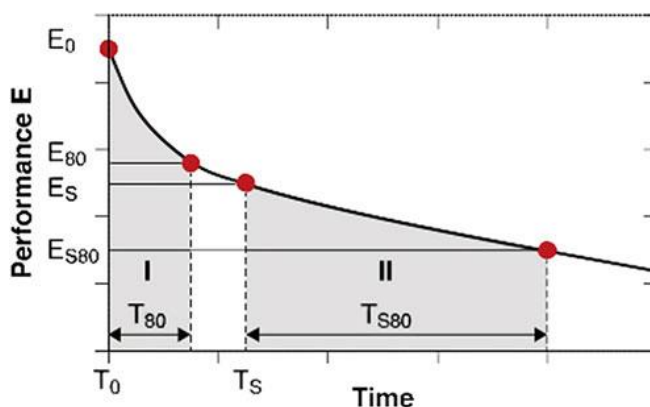
Figure 72. Lifetime curve defined with the characteristic parameters. Reproduced with permission from Wiley-VCH.[248]

The efficiency curves were fitted with either a onephase (ISOS D1 conditions) or two-phase (ISOS L1, L2, and O1 conditions) exponential decay function. For devices with slower decay dynamics, when the T_{S80} was not reached within the duration of the measurements, the lifetime markers were extrapolated from the available data points. Within the same aging test and for devices comprising more than one pixel, single figures of merit (f.o.m.) were measured for each pixel and then averaged for all identical pixels per each time point. Generally, standard deviations obtained for Type 5 and Type 6 devices are the widest, with a tendency to increase even more over the time, which we attribute to the poorer encapsulation in those device types. In these cases, the upper edge corresponds to the most stable device of this type and the lower edge corresponds to less stable device.

Results

Figure 73 shows the T_{80} behavior of the tested device as a function of the molecular weight of the PCDTBT. Despite the absence of some data points due to the mechanical breakdown of devices, the plot reveals some interesting relationships between the properties of the donor molecule and the lifetimes of the devices. The general outcome is that the time in which the devices reach their T_{80} point is strongly dependent on the aging condition, and it is in the order $T_{80}(D1) > T_{80}(L1) > T_{80}(L2) > T_{80}$(daylight outdoor). This is true for all tested device types—inverted and standard architecture—and regardless of the molecular weight of the polymer or the type of interlayers implemented.
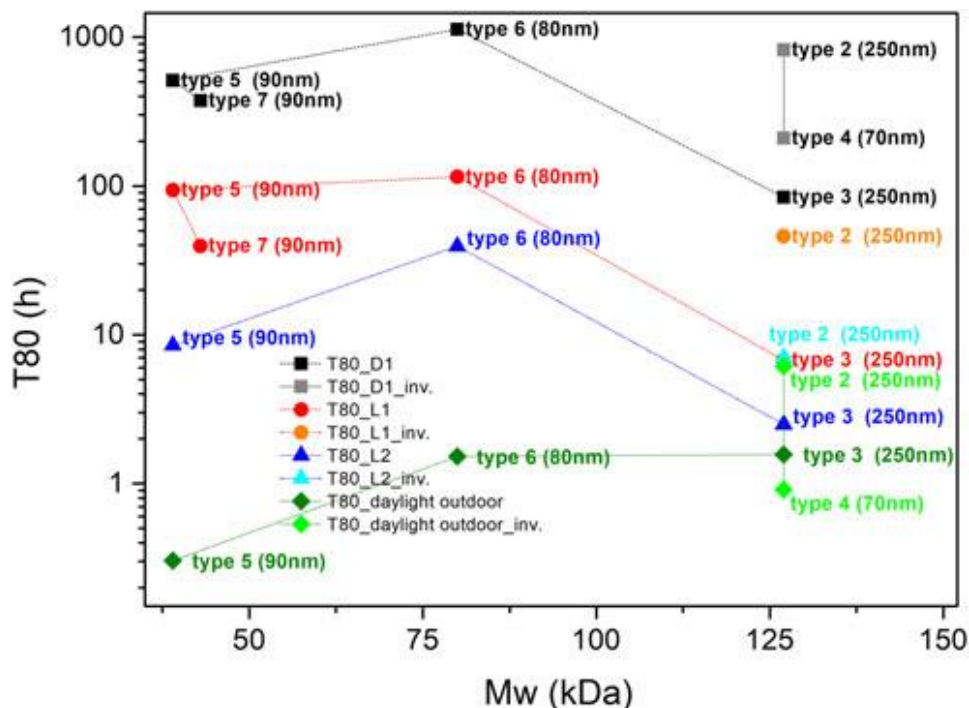
Figure 73. T_{80} parameter of devices (inverted architecture is named "inv.") degraded under different stress conditions, correlated with molecular weight of the PCDTBT. Degradation conditions are denoted as follows: square for ISOS D1, circle for ISOS L1, triangle for ISOS L2, and rhombus for daylight outdoor weathering.

It has been demonstrated that the molecular weight of specific donor polymers has an important impact on the morphology and polymer ordering (p-stacking) of OSC devices,[249,250,251,252,253] but also on the stability of the cells.[254] Ding et al.[254] showed that solar cells based on PTB7 with higher molecular weight were more stable over time and exhibited better operational stability. Using EPR spectroscopy, it was found that the higher molecular weight polymer samples contained a lower

density of radical species in the material. As shown by Troshin et al., such radical species might act as deep traps for mobile charge carriers, therefore diminishing the electrical performance of the cells.[255,256,257] In Fig. 73, it is also seen that increasing the molecular weight from 39 to 80 kDa, while maintaining the same active layer thickness, appeared beneficial for the device stability, as manifested by a longer T_{80} time. It should also be noted that this result is obtained despite the calcium-based cathodes used in Type 6, which is known to be a particularly unstable contact material.[258,259,260,261,262] When increasing the molecular weights to 127 kDa, however, devices having the same standard architecture (Type 3) show a drop-in device stability. We attribute this behavior to the thicker Ca layer used in the Type 3 cells. Moreover, Type 3 cells have thicker active layers, which could have an impact on the device stability as well. Therefore, there seems to be an interconnection between Mw and cell T_{80} up to a certain threshold value, after which the excessively high molecular weight may affect the device stability. When comparing standard versus inverted device architectures for molecular weights of 127 kDa, it is clear that the inverted cells outperform the standard configuration devices, as it has also been demonstrated for many other material systems in OSCs.[263] Such improved stability is mainly due to the use of high work function cathodes. We point out here that the T_{80} parameter utilized for our analysis does not reflect the overall device reliability but is rather one of the typical indicators for looking at certain initial dynamics related to OPV stability. Nevertheless, even by looking at the stabilized time of the devices against Mw (Fig. 74, we do find a similar—even if less defined—trend, where a $[T_S–M_W]$ optimum seems to be recognizable. Therefore, we feel confident in correlating the M_W to the "rate of degradation" (T_{80} versus M_W), but also to the time the device gets to a stabilized value of efficiency (T_S versus M_W), after which the degradation process proceeds on a much slower pace.
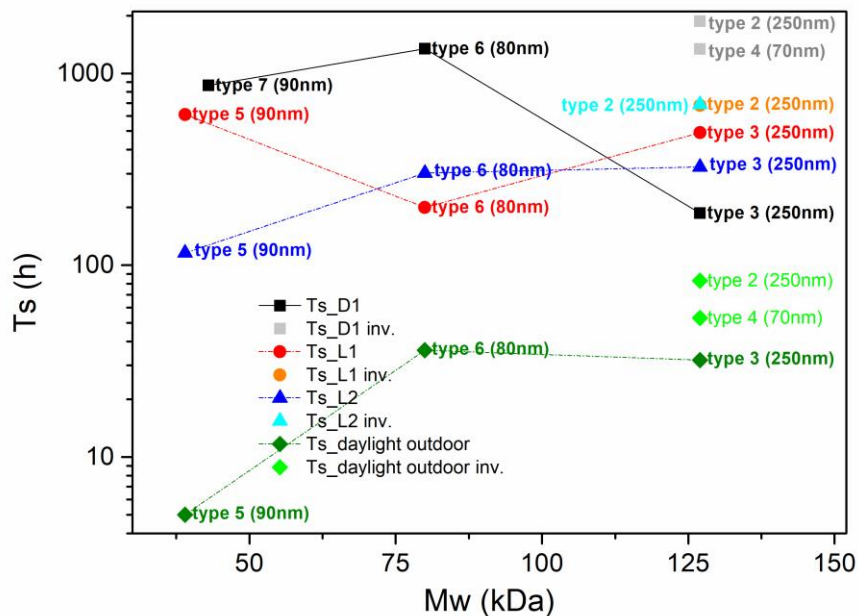
Figure 74. Stabilized time of the devices against M_W.

In Fig. 75, the PCEs of different device types and aging protocols are plotted as a function of time. Unfortunately, device failures are found for some of the investigated cells. This is seen for example at a very early stage for the Type 4 cell under ISOS-L1 conditions and for Type 5 at later stages under ISOS-L2 conditions. We ascribe these failures to mechanical breaks of the encapsulation during the experiments.

Figure 75. Comparison of long-term PCEs of the different types of devices measured under the four degradation conditions.

In the following sections, detailed performance comparisons for the different ISOS degradation conditions will be given. First of all, we note that in some cases, small increases in PCE are seen at the beginning of degradation, which result from an increase in V_{OC}. To emphasize this, in Fig. 76, we plot Voc as a function of time for the different ISOS degradation conditions. The small increase is seen for Type 5 devices under all degradation conditions and for Type 3 devices under the ISOS-L2 conditions. Such an increase in Voc has also been observed in previous OSC stability investigations, and it was found to be the result of cathode oxidation, as in contact with air, a thin oxide layer can be formed at the cathode interface, minimizing interface recombination effects,[264,265] which could also explain the observed effects for the specific cases mentioned here.
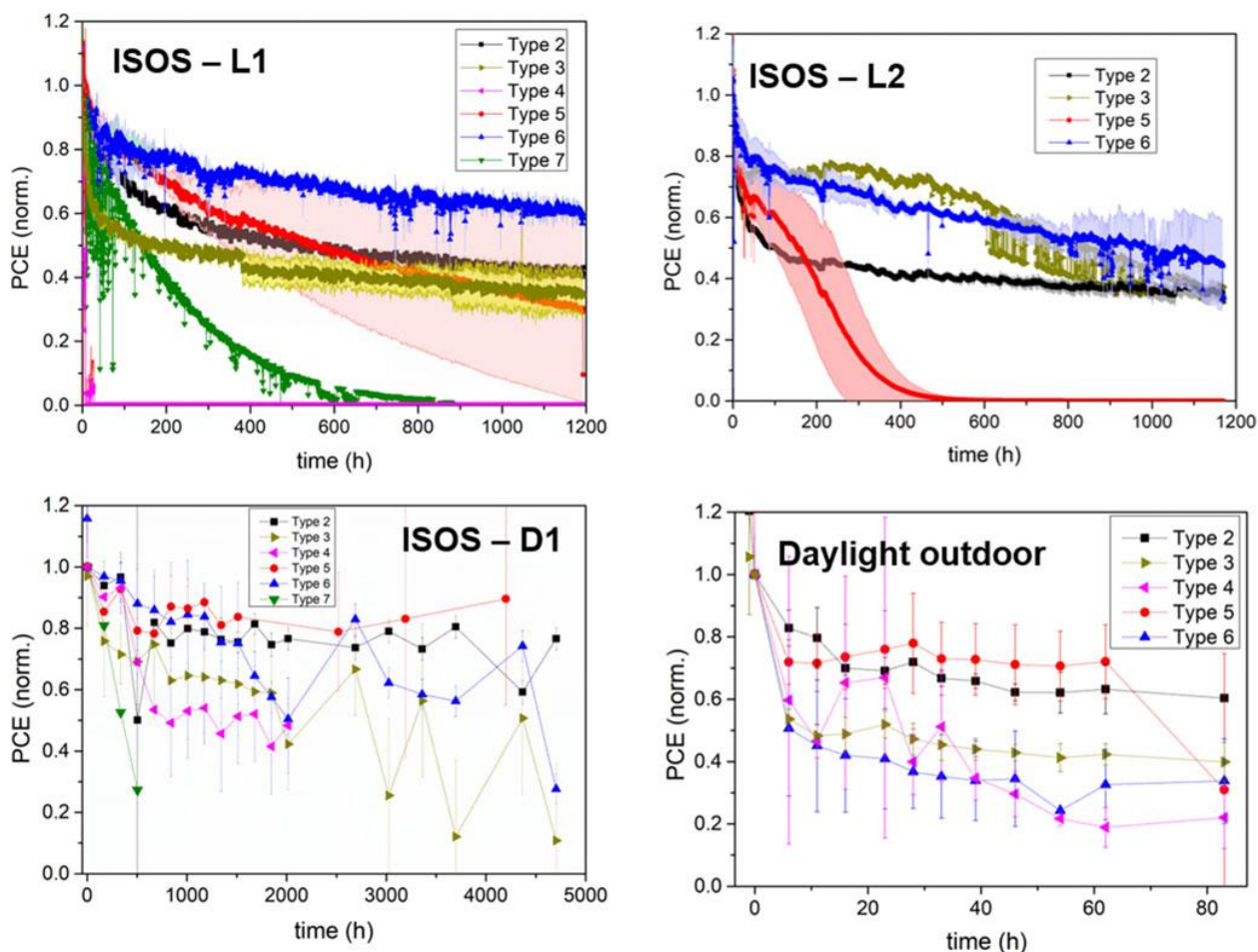
142
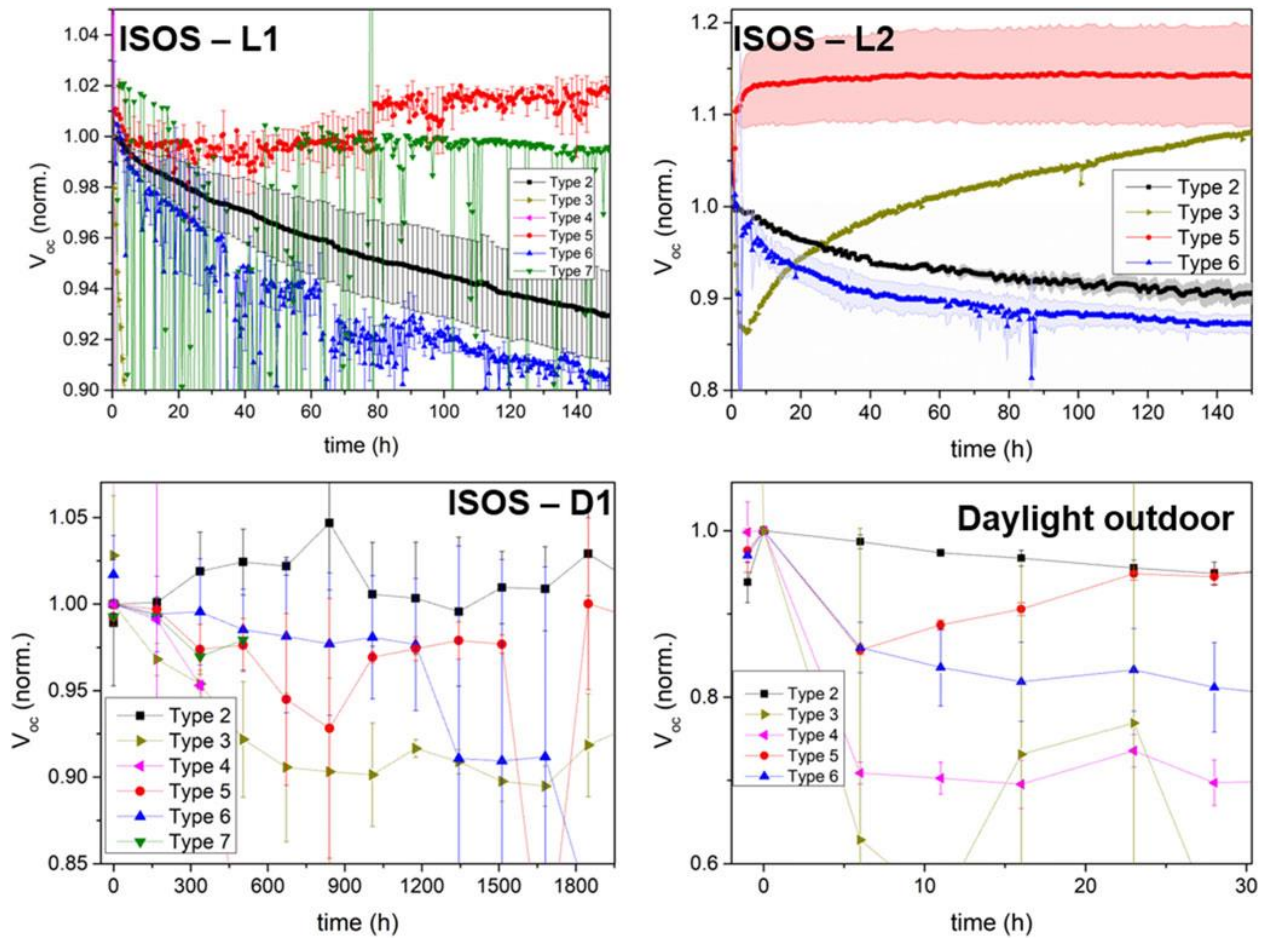
Figure 76. Comparison of long-term open circuit voltages of the different types of devices measured under the four degradation conditions (only the initial 0–100 h are represented).

D1—degradation

The ISOS-D1 conditions resulted (see Fig. 77) in the longest lasting degradations, with all but one PCE best fit displaying a single exponential decay with time constants given in Table 15. The PCE trends were mainly dictated by the J_{SC}, and the single time constant parameter could indicate one major degradation process affecting the cells, even though at a very low rate. In this respect, the edge-ingress of water and moisture through the encapsulation system has already been reported as the principal factor responsible for the performance drop of cells under similar conditions.[266,267] We may speculate that for these degradation conditions, intrinsic differences in the polymer, like molecular weight, morphology, or solubility limits, are of less importance with respect to the extrinsic mechanisms (permeable encapsulation) responsible for the PCE drop. As ISOS D1 is the mildest degradation condition experienced by the cells, we attribute the fast (~500 h) PCE drop of

143

Type 7 to the defective or insufficient encapsulation adopted, which proved to be inadequate also under the other aging conditions.
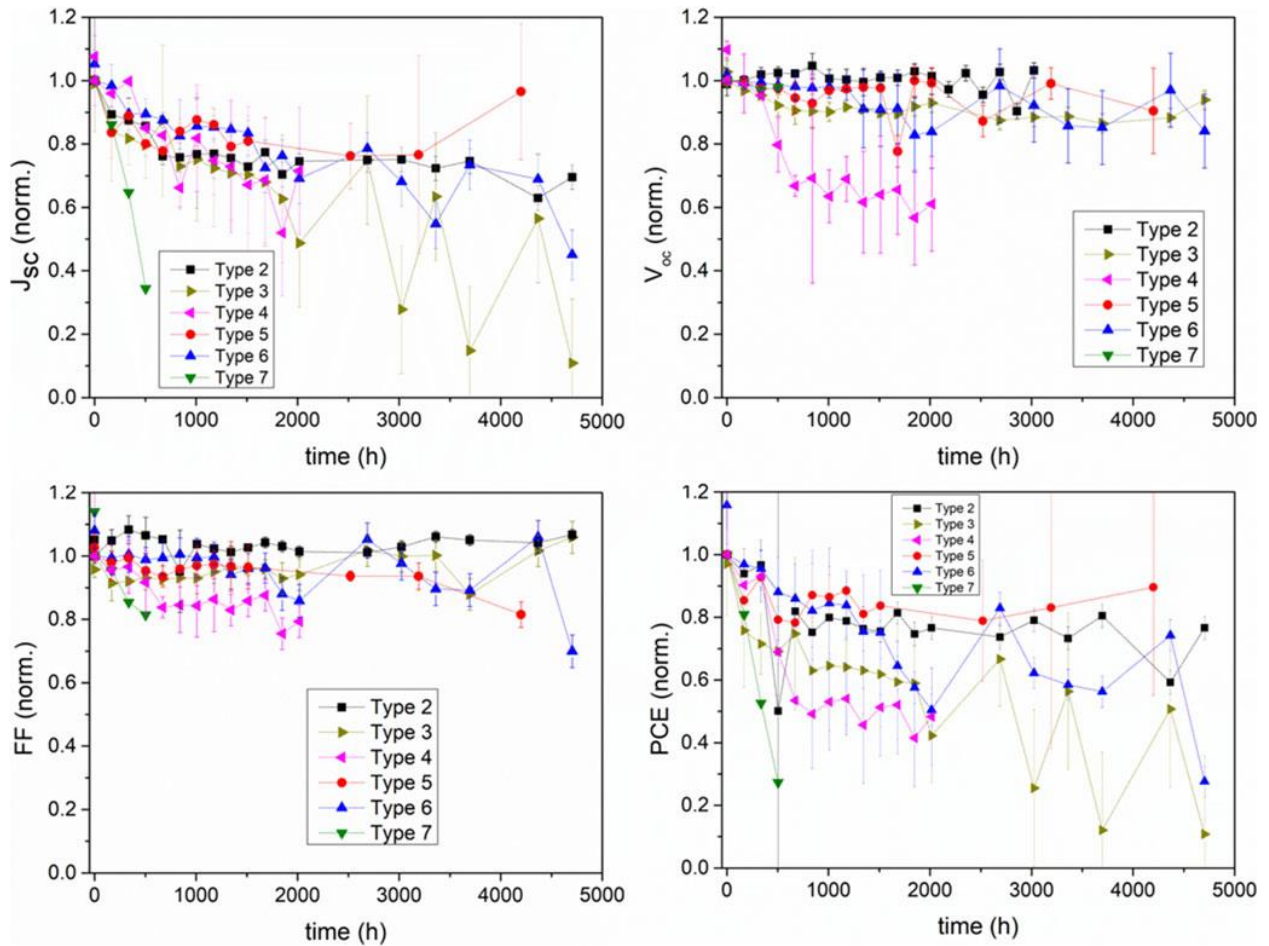
Figure 77. Solar cell parameters of the different device types measured under ISOS D1 conditions (in the dark at room temperature).

L1—light-soaking indoor

The ISOS-L1 testing was performed indoors, under constant 1 Sun light-soaking and ambient temperature and humidity, and due to the heat from the simulated light, the temperature of the devices was 45 °C. As expected (see Fig. 78), all the long-term PCE curves show a pronounced initial drop due to the light-activated burning reactions.[268,269,270] The efficiency decrease seems mostly dominated by J_{SC}, and less by V_{OC} and FF, which are mainly dropping in the burn-in period and are otherwise stable.

Figure 78. Solar cell parameters of the different device types measured under ISOS L1 conditions (1 Sun illumination at room temperature).

The photo-oxidation processes taking place in PCDTBT is governed by combined chain-scission and cross-linking reactions. The process starts by chain scission of the C–N bond between the carbazole group and the tertiary carbon atom, bearing the alkyl side chain, followed by cross-linking between the carbazole unit and the fullerene acceptor. Based on EPR spectroscopy measurements, it has been demonstrated that the burn-in period is correlated with these cross-linking reactions and with the formation of defects along the polymer chain. Following the burn-in, the modified system enters a more stable phase with minimum degradation over time. Comparing again Type 5 and Type 6 devices which possess comparable active layer thicknesses but different molecular weights, it seems that Type 6 devices with a molecular weight of 80 kDa are experiencing a much weaker burn-in than Type 5 devices with a molecular weight of 39 kDa. Since radical defects can be expected to be present mostly on the polymer chain ends, the larger

molecular weight would imply having less radical defects. Thus, one can speculate that the described chain-scission and cross-linking processes will be dependent on the molecular weight of the polymer, and that more pronounced chain-scission and cross-linking processes will take place in the lower molecular weight polymer as it has a higher density of radical defects. That would explain the small burn-in for Type 6 devices, experiencing a very slow Jsc decrease over the whole aging period. As mentioned earlier, the influence from the thick calcium-based cathode in Type 3 devices could overshadow the contribution of the larger molecular weight donor in this device type.

L2—light-soaking indoor @ 65 ˚C

Besides the V_{OC} effect, which was commented on earlier, it is clear from the ISOS-L2 testing (see Fig. 79) that under increased heat, the cell degradation further accelerates compared to the ISOS-L1 tests. Indeed, high temperature proves to be a detrimental factor for PCDTBT-based solar cells. Interestingly, we see in the ISOS-L2 stability tests that the long-term stability of the inverted cells, Type 2, is worse than for some of the devices with the standard configuration. It is known that the PCDTBT:PCBM morphology is more stable when comprising ZnO layers as compared to PEDOT:PSS layers,[271] which cannot explain this observed effect. In addition, the large molecular weight of the polymer used in the inverted cells should also lead to the lower radical defect density and thus improved device stability. Also, employing $PC_{70}BM$ as the acceptor should lead to more stable cells as compared to $PC_{60}BM$, which also does not correlate with the inverted cells investigated in this study. In fact, comparing the inverted device stack investigated here with a similar one from the literature possessing high device stability, the only difference is that the HTL used here is PEDOT:PSS instead of MoO_X, therefore we speculate that PEDOT:PSS could be the main reason for the observed device instabilities seen for the inverted cell here.[272]
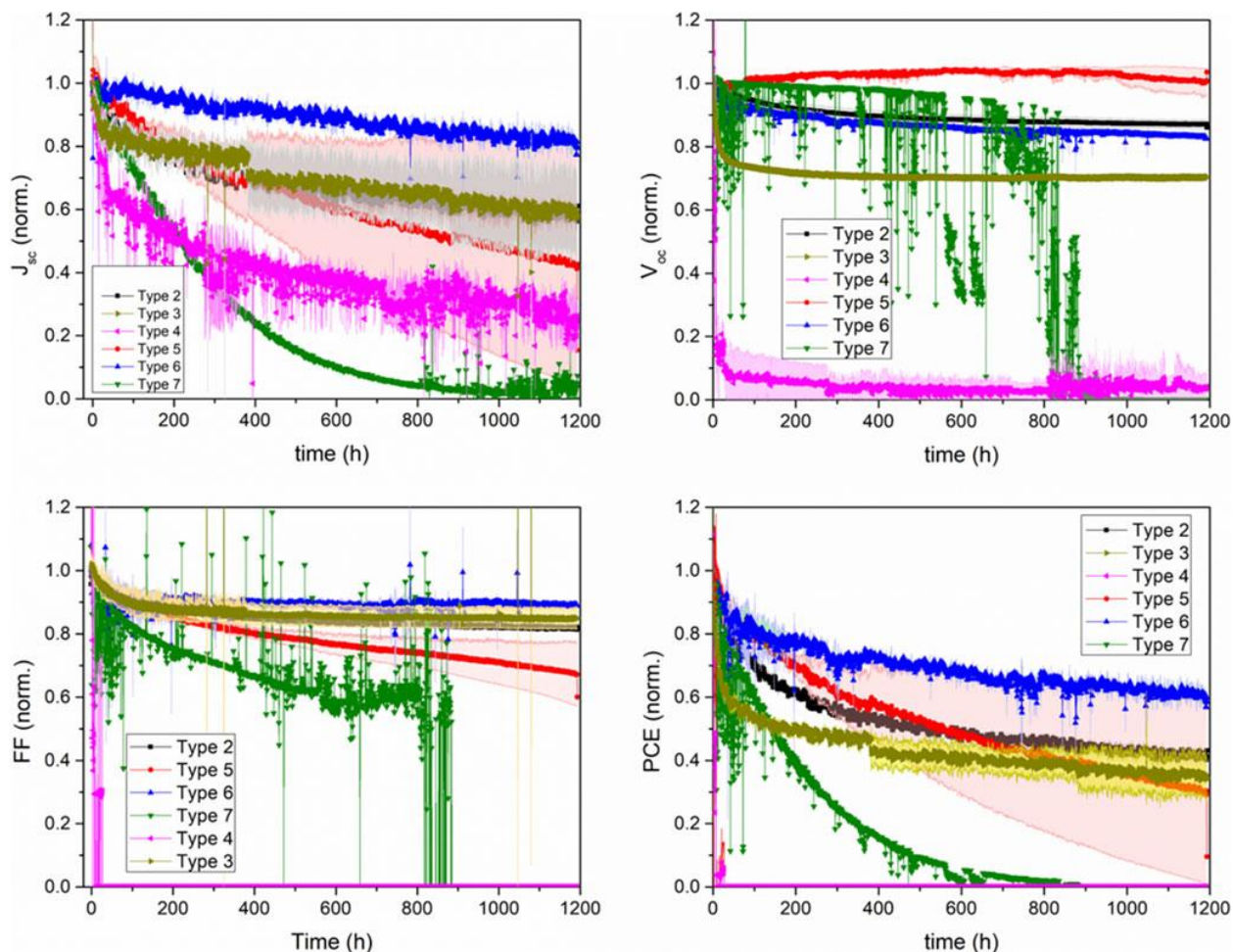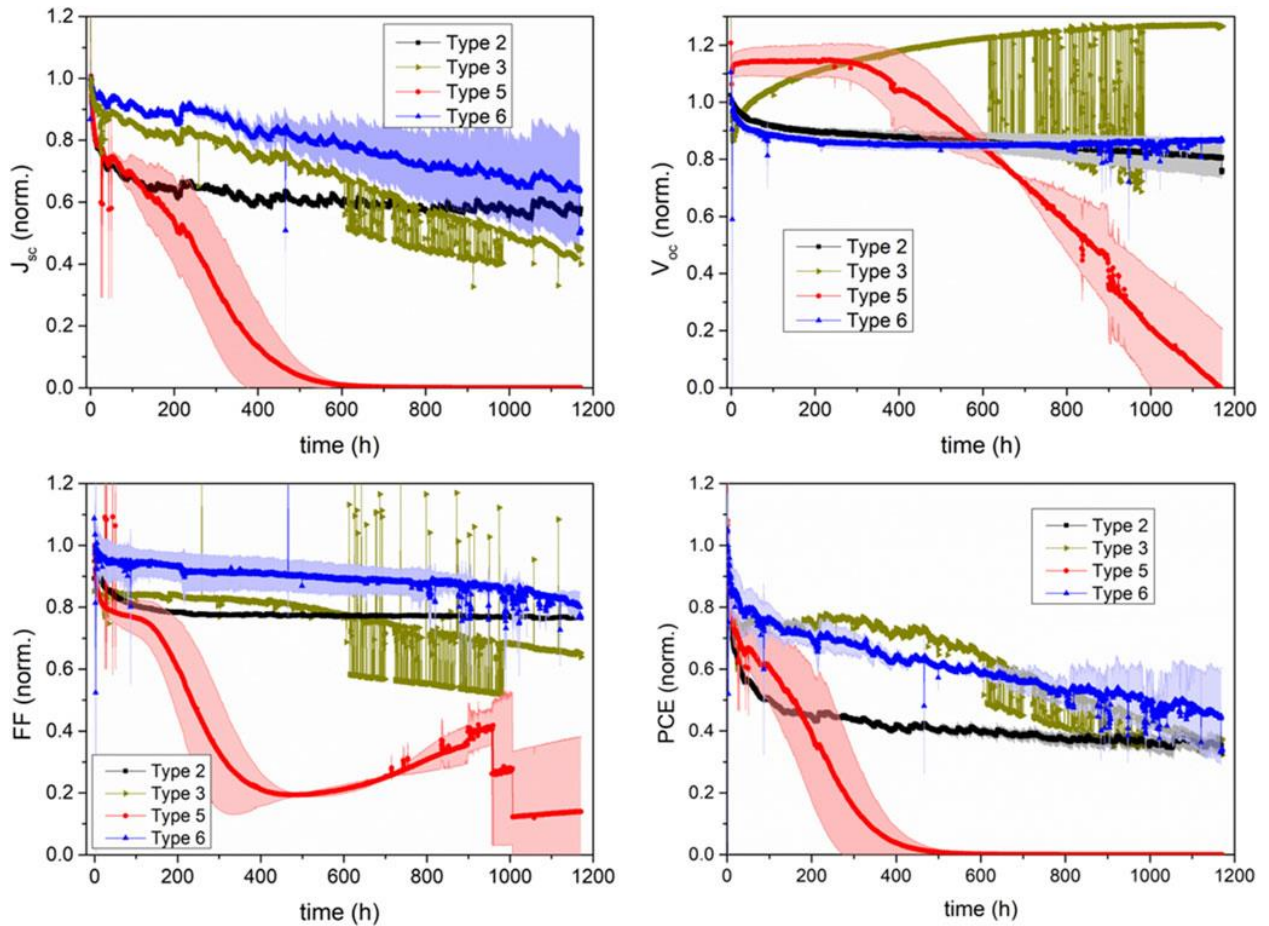
Figure 79. Solar cell parameters of the different device types measured under ISOS L2 conditions (1 Sun illumination at 65 °C).

For all devices undergoing this specific ISOS-L2 aging test, the periodic I–V characterization was complemented with pre- and post-aging PLI. In most cases, PLI revealed no luminescence changes due to side ingress of water or oxygen; thus for the majority of devices investigated here, only intrinsic degradation processes need to be considered. As an example, the PLI images for a Type 2 device before and after aging are shown in the upper row of Fig. 80. Only a slight decrease in the overall intensity coming from the active layer can be detected. This can be attributed to the very slight, homogeneous degradation of the photoactive layer. In contrast to that, Type 4 devices showed severe side ingress, presumably of water and oxygen from the ambient air (compare with the lower row of Fig. 80). Along the edges of the back contact of the solar cell (six dark stripes), a contrast change can be detected: the outer, presumably degraded parts appear darker in between those contacts, while to the center of the sample luminescence yields a brighter and thus more intense signal, indicating the nondegraded portion of the active layer. This finding is in good

147

agreement with the already reported fast degradation of the Type 4 devices under L1 and L2 aging conditions and provides an explanation for that: photo-oxidation of the active layer and possibly further degradation processes at charge extraction layers.
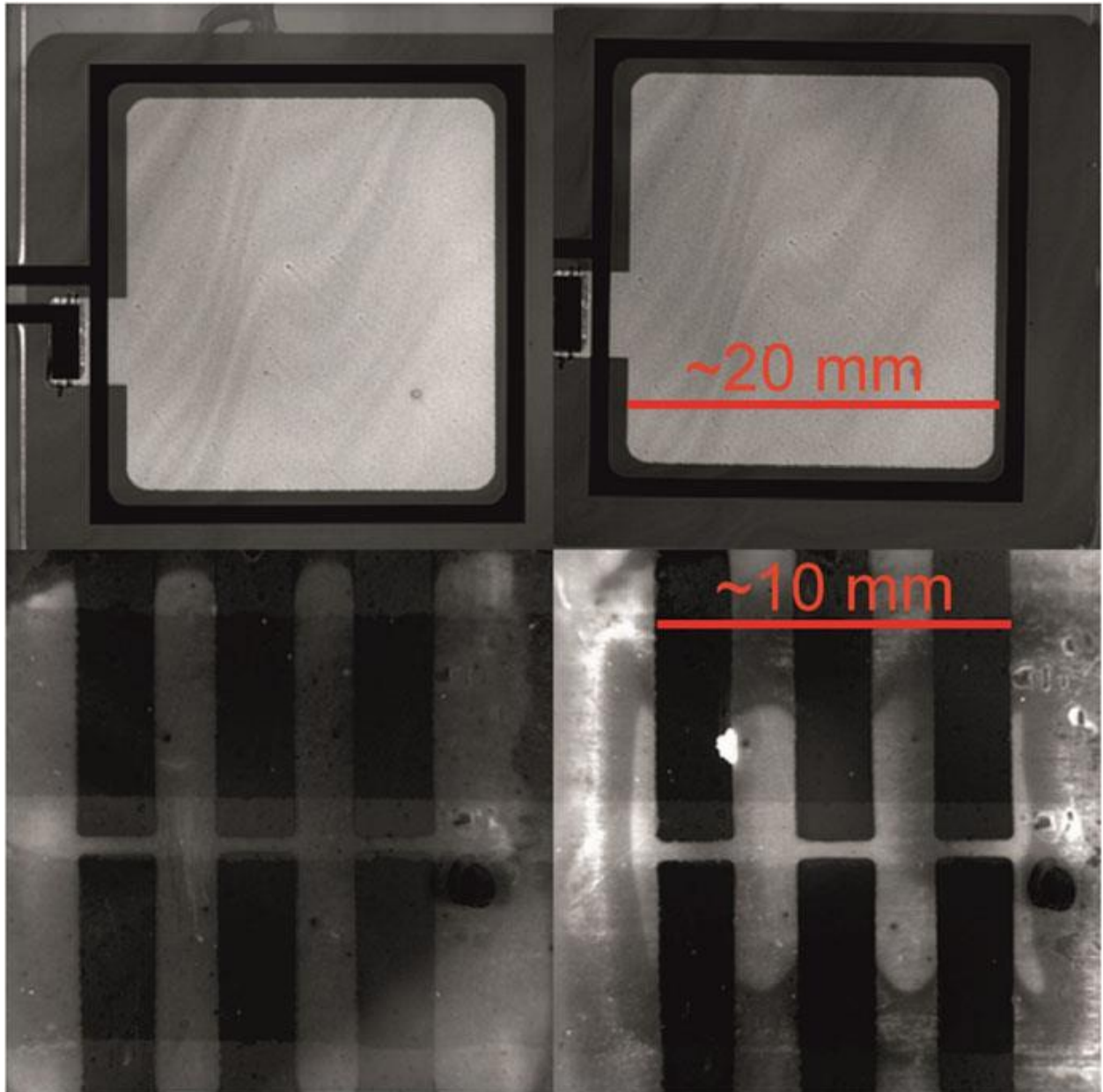
Figure 80. Photoluminescence images of Type 2 devices (upper row) and Type 4 devices (lower row) of fresh (left column) and aged (right column) samples. The aging was done under ISOS L2 conditions for 1200 h. The scale bar for PL intensity of the upper two images is exactly the same, while the scale for the lower two images is very comparable.

Daylight outdoor light-soaking

For the outdoor stability tests, degradation of J_{SC} dominates the PCE for all the investigated device types (Fig. 81). The burn-in period is in all cases followed by a more linear behavior, and it is on average less than 10 h long. Comparing the different aging conditions, the outdoor tests clearly lead to the fastest degradation of the cells, which suggests that external effects are dominating the degradation process. Therefore, comparing molecular weights, morphology, and even electrode interlayers and device configurations may lead to the wrong conclusions. Here, we point to the device encapsulation as one of the key factors for the observed outdoor stability effects. Thus special care should be given to the implementation of ultra-low moisture permeation encapsulation with effective oxygen and humidity barriers, as well as to the addition of stabilizing compounds that may alleviate the rapid degradation arising from the presence of reactive radical species.[273,274,275,276]
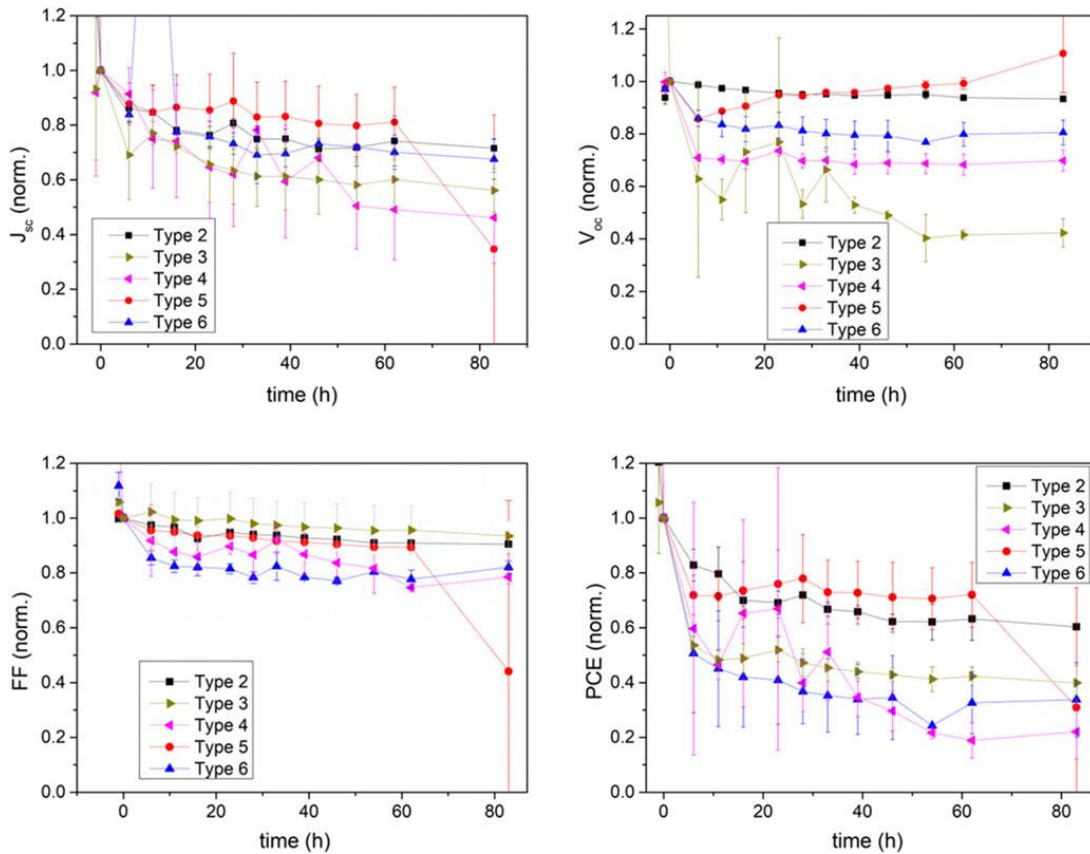
Figure 81. Solar cell parameters of the different device types measured under ISOS daylight outdoor weathering.

Conclusions

In conclusion, we have shown that multiple effects should be considered when comparing the device stability of PCDTBT-based solar cells. Although the lifetimes presented here still do not always meet the stringent industry standards as required for product commercialization—mostly due to a limited optimization steps which can be conducted at science laboratories as compared to the extensive optimization procedures standardly applied by the industry, this study allowed us to extract useful correlations between materials, technological solutions, degradation protocols, and PV performance and perform a thorough analysis of such solar cell devices. First and foremost, a proper device encapsulation—at times lacking in the devices presented here—appears mandatory to ensure the potentially high lifetime of the PCDTBT-based devices. In addition, the vast laboratory cross-comparison sheds some light on the most suitable combinations out of the wide variety of available interlayer materials, to point toward a finer device optimization. The device architecture and choice of interlayers strongly affect the long-term device performance, and their impact on the device stability is strongly correlated with the aging conditions used. The implemented interlayers should always be carefully chosen also on the basis of their stability, as well as the final device application. In general, a Ca-based electrode proved to contribute to an early failure of the device, likely due to its instability toward moisture and water, therefore other top contacts should be preferred. As well, ZnO-based cells performed better than those comprising PEDOT:PSS, especially under ISOS-L2 aging protocol. This could provide an indication for material selection, once certain specific applications for OPV have been targeted.

On the other hand, despite differences originating from these factors, which are not directly related to the active layer materials, some conclusions on the physical properties of the PCDTBT polymer could also be made. The molecular weight seems to be a significant factor for determining both the cell burn-in time and the time of stabilization (T_S), as the radical defect density is expected to be inversely proportional to the molecular weight, and as such found to dictate the trend of the initial degradation process to a significant extent. An optimum combination of molecular weight and active layer thickness appears to exist in terms of achieving the longest T_{80} period, regardless of the ISOS degradation protocol used.

We expect that the observations made in this study on the physical properties of the materials as well as on the importance of the choice of optimal interlayer materials and cell architectures will contribute to the enhancement of the stabilities of organic solar devices developed in the future, both those employing the materials tested in the study, but also applied to those comprising novel materials and employing innovative fabrication methods, such as for example NFAs and more stable encapsulation formulations similar to those currently used for the commercialized OLED devices.

Bibliography

[1] A. E. Becquerel, *Comptes Rendus De L'Académie Des Sciences*, 1839, 9, 145.

[2] A. E. Becquerel, *Comptes Rendus De L'Académie Des Sciences*, 1839, 9, 561.

[3] W. Shockley and H. J. Queisser, Detailed Balance Limit of Efficiency of P-N Junction Solar Cells, *J. Appl. Phys.*, 1961, 32, 510-519.

[4] M. C. Hanna and A. J. Nozik, Solar conversion efficiency of photovoltaic and photo electrolysis cells with carrier multiplication absorbers*, J. Appl. Phys.*, 2006, 100, 074510.

[5] M. A. Green, K. Emery, Y. Hishikawa, and W. Warta, Solar Cell Efficiency Tables (Version 34), *Prog. Photovolt: Res. Appl.*, 2009, 17, 320-326.

[6] M. Gratzel, Photoelectrochemical cells, Nature, 15-11-2001, 414, 338-344.

[7] M. K. Nazeeruddin, A. Kay, I. Rodicio, R. Humphry-Baker, E. Mueller, P. Liska, N. Vlachopoulos, and M. Graetzel, *J. Am. Chem. Soc.*, 1-5-2002, 115, 6382-6390.

[8] https://www.nrel.gov/pv/cell-efficiency.html

[9] J. Nelson, *The Physics of Solar Cells* **2004**, Imperial College Press.

[10] P.T. Landsberg, Recombination in Semiconductors 1991, Cambridge University Press.

[11] Landsberg, P. T. (2003). Recombination in semiconductors. Cambridge University Press.

[12] Li, L. (2011). Determination of Electrostatic Potential and Charge Distribution of Semiconductor Nanostructures using Off-axis Electron Holography (Doctoral dissertation, Arizona State University).

[13] www.researchgate.net/publication/297569438_PhD_Thesis_The_stability_of_third_generation_solar_cells

[14] G. A. Chamberlain, Solar Cells, 1983, 8, 47-83.

[15] C. W. Tang, Appl. Phys. Lett., 1986, 48, 183-185.

[16] N. S. Sariciftci, L. Smilowitz, A. J. Heeger and F. Wudl, Science 1992, 258, 1474-1476.

[17] G. Yu and A. J. Heeger, J. Appl. Phys. 1995, 78, 4510-4515.

[18] P. Peumans and S. R. Forrest, Appl. Phys. Lett. 2001, 79, 126-128.

[19] Yong Cui, Nature Com., 2019, 10, 2515.

[20] K.S. Novoselov, A.K. Geim, S.V. Morozov, D. Jiang, Y. Zhang, S.V. Dubonos, I.V. Grigorieva and A.A. Firsov, Science 2004, 306, 666 – 669.

[21] F. Schwierz and Nat. Nanotechnol. 2010, 5, 487 – 496.

[22] F. Bonaccorso, Z. Sun, T. Hassan and A. Ferrari, Nat. Photonics 2010, 4, 611 – 622.

[23] M. Pumera, Energy Environ. Sci. 2011, 4, 668 – 674.

[24] D. Chen, H. Zhang, Y. Liu and J. Li, Energy Environ. Sci., 2013, 6, 1362–1387; b) B.J. Schultz, R.V. Dennis, V. Lee and S. Banerjee, Nanoscale 2014, 6, 3444 – 3466.

[25] Z. Chen, W. Ren, L. Gao, B. Liu, S. Pei and H.-M. Cheng, Nat. Mater. 2011, 10, 424–428.

[26] C.K. Chua and M. Pumera, Chem. Soc. Rev. 2014, 43, 291–312.

[27] X. Mei, X. Meng and F. Wu, Phys. E Low-dimens. Syst. Nanostruct. 2015, 68, 81–86.

[28] W. Lv, D. Tang, Y. He, C. You, Z. Shi, X. Chen, C.-M. Chen, P.-X. Hou, C. Liu and Q.-H. Yang, ACS Nano 2009, 3, 3730–3736.

[29] M. Lotya, Y. Hernandez, P.J. King, R.J. Smith, V. Nicolosi, L.S. Karlsson, F.M. Blighe, S. De, Z. Wang and I.T. McGovern, J. Am. Chem. Soc. 2009, 131, 3611–3620.

[30] W.S. Hummers and R.E. Offeman, J. Am. Chem. Soc. 1958, 80, 1339.

[31] S.F. Pei and H.M. Cheng, Carbon 2012, 50, 3210–3228.

[32] Rajesh Kumar Singh, Rajesh Kumar and Dinesh Pratap Singh, RSC Adv., 2016,6, 64993-65011.

[33] C. Petridis, G. Kakavelakis and E. Kymakis, Energy Environ. Sci. 2018, DOI:10.1039/C7EE03620E.

[34] M. M. Stylianakis, D. Konios, C. Petridis, G. Kakavelakis, E. Stratakis and E. Kymakis, 2D Mater. 2017.

[35] M. Inagaki and F.Y. Kang, J. Mater. Chem. A 2014, 2, 13193–13206.

[36] https://socratic.org/questions/how-do-pi-bonds-overlap.

[37] http://cleanenergywiki.org/index.php?title=The_Polyene_Series.

[38] N. C. Greenham and R. H. Friend, Solid State Physics 1995, 49, 1.

[39] S. Mazumbar, M. Chandross, and N. S. Sariciftci, Primary photoexcitations in conjugated polymers (World Scientific, Singapore, 1997).

[40] E. M. Conwell and H. A. Mizes, Physical Review B 1995, 51, 6953.

[41] R. N. Marks, J. J. Halls, D. D. C. Bradley, R. H. Friend, and A. B. Holmes, Journal of Physics-Condensed Matter 1994, 6, 1379.

[42] B.R. Saunders, J. Colloid Interface Sci. 2012, 369, 1-15.

[43] Tzung-Han Lai, Sai-Wing Tsang, Jesse R. Manders, Song Chen and Franky So, Materials Today, 2013, 16 (11), 424.

[44] W. Cai, X. Gong and Y. Cao, Sol. Energy Mater Sol. Cells 2010, 94, 114-127.

[45] G. Garcia-Belmonte, A. Munar, E.M. Barea, J. Bisquert, I. Ugarte and R. Pacios, Org. Electron. 2008, 9, 847-851.

[46] N.S. Sariciftci, L. Smilowitz, A.J. Heeger and F. Wudl, Science 1992, 258, 1474-1476.

[47] C.J. Brabec, S. Gowrisanker, J.J.M. Halls, D. Laird, S. Jia, S.P. Williams, Adv. Mater. 2010, 22, 3839-3856.

[48] 92 T.A. Bull, L.S.C. Pingree, S.A. Jenekhe, D.S. Ginger and C.K. Luscombe, ACS Nano 2009, 3, 627-636.

[49] G. Yu, J. Gao, J.C. Hummelen, F. Wudl and A.J. Heeger, Science 1995, 270, 1789-1791.

[50] Hsing-Ju Wang, Chih-Ping Chen and Ru-Jong Jeng, Materials 2014, 7(4), 2411-2439.

[51] Qishi Liua Yufan Jiang, Ke Jin, Jianqiang Qin, Jingui Xu, Wenting Li, Ji Xiong, Jinfeng Liu, Zuo Xiao, Kuan Sun, hangfeng Yang, Xiaotao Zhang and Liming Ding, Science Bulletin, Vol. 65, 2020, 272.

[52] L. Meng, Y. Zhang, X. Wan, et al. Science, 361 (2018), pp. 1094-1098 .

[53] Y. Cui, H. Yao, L. Hong, et al., Natl Sci Rev (2019), 10.1093/nsr/nwz200.

[54] Y. Wu, Y. Zheng, H. Yang, et al. Sci China Chem (2019), 10.1007/s11426-019-9599-1.

[55] B. Fan, D. Zhang, M. Li, et al. Sci China Chem, 62 (2019), pp. 746-752.

[56] . Xiong, K. Jin, Y. Jiang, et al. Sci Bull, 64 (2019), pp. 1573-1576.

[57] T. Wang, J. Qin, Z. Xiao, et al. Sci Bull, 65 (2020), pp. 179-181.

[58] G. Li, V. Shrotriya, J. S. Huang, Y. Tao, T. Moriarty, L. Emery and Y. Yang, Nat. Mater. 2005, 4, 864.

[59] C. Groves, Energy Environ. Sci. 2013, 6, 1546.

[60] Y. F. Li, Acc. Chem. Res. 2012, 45, 723.

[61] H. L. Lip and A. K. Y. Jen, Energy Environ. Sci. 2012, 5, 5994.

[62] M. Jorgensen, K. Norrman, S. A. Gevorgyan, T. Tromholt, B. Andreasen and F. C. Krebs, Adv. Mater. 2012, 24, 580.

[63] T. Ameri, P. Khoram, J. Min and C. J. Brabec, Adv. Mater. 2013, 25, 4245.

[64] Q. An, F. Zhang, J. Zhang, W. Tang, Z. Denga and B. Hu, Energy Environ. Sci. 2016, 9, 281.

[65] Huiting Fu, Zhaohui Wang and Yanming Sun, Solar RRL, Vol. 2, January 2018, 1700158.

[66] Q. Sun, F. Zhang, J. Hai, J. Yu, H. Huang, F. Teng and W. Tang, Electron. Mater. Lett. 2015, 11, 236.

[67] S. J. Ko, W. Lee, H. Choi, B. Walker, S. Yum, S. Kim, T. J. Shin, H. Y. Woo and J. Y. Kim, Adv. Energy Mater. 2015, 5, 1401687.

[68] Z. Zhuo, F. Zhang, J. Wang, X. Xu, Z. Xu, Y. Wang and W. Tang, Sol. State Electron. 2011, 68, 83.

[69] Q. An, F. Zhang, J. Zhang, W. Tang, Z. Wang, L. Li, Z. Xu, F. Teng and W. Tang, Sol. Energy Mater. Sol. Cells 2013, 118, 30.

[70] M. Koppe, H. J. Egelhaaf, G. Dennler, M. C. Scharber, C. J. Brabec, P. Schilinsky and C. N. Hoth, Adv. Funct. Mater. 2010, 20, 338.

[71] L. Yang, L. Yan and W. You, J. Phys. Chem. Lett. 2013, 4, 1802.

[72] https://www.pveducation.org/pvcdrom/solar-cell-operation/iv-curve

[73] http://org.ntnu.no/solarcells/pages/introduction.php

[74] http://org.ntnu.no/solarcells/pages/introduction.php

[75] http://www.ni.com/white-paper/7230/en/

[76] Zhongfu Zhou and John Macaulaym, Energies 2017, 10(12), 2075.

[77] Davide Bartesaghi, Irene del Carmen Pérez, Juliane Kniepert, Steffen Roland, Mathieu Turbiez, Dieter Neher & L. Jan Anton Koster, Nature Communications volume 6, Article number: 7083 (2015).

[78] https://www.pveducation.org/pvcdrom/solar-cell-operation/quantum-efficiency

[79] Xiaodong Liu,ab Yiwei Lin,ab Yingjie Liao,ab Jiazun Wuab and Yonghao Zheng, J. Mater. Chem. C, 2018, 6, 3499-3513.

[80] Cao, W.; Xue, J. Recent progress in organic photovoltaics: Device architecture and optical design. Energy Environ. Sci. 2014, 7, 2123–2144

[81] Li, Y.F. Molecular design of photovoltaic materials for polymer solar cells: Toward suitable electronic energy levels and broad absorption. Acc. Chem. Res. 2012, 45, 723–733.

[82] Li, G.; Zhu, R.; Yang, Y. Polymer solar cells. Nat. Photon. 2012, 6, 153–161.

[83] Mikroyannidis, J.A.; Stylianakis, M.M.; Sharma, G.D.; Balraju, P.; Roy, M.S. A novel alternating phenylenevinylene copolymer with perylene bisimide units: Synthesis, photophysical, electrochemical, and photovoltaic properties. J. Phys. Chem. C 2009, 113, 7904–7912.

[84] Lu, L.; Yu, L. Understanding low bandgap polymer PTB7 and optimizing polymer solar cells based on it. Adv. Mater. 2014, 26, 4413–4430.

[85] Mikroyannidis, J.A.; Stylianakis, M.M.; Suresh, P.; Roy, M.S.; Sharma, G.D. Synthesis of perylene monoimide derivative and its use for quasi-solid-state dye-sensitized solar cells based on bare and modified nano-crystalline ZnO photoelectrodes. Energy Environ. Sci. 2009, 2, 1293–1301.

[86] Sharma, G.D.; Suresh, P.; Mikroyannidis, J.A.; Stylianakis, M.M. Efficient bulk heterojunction devices based on phenylenevinylene small molecule and perylene-pyrene bisimide. J. Mater. Chem. 2010, 20, 561–567.

[87] Zhang, S.; Ye, L.; Hou, J. Breaking the 10% efficiency barrier in organic photovoltaics: Morphology and device optimization of well-known PBDTTT polymers. Adv. Energy Mater. 2016, 6, 1502529.

[88] Guo, X.; Zhou, N.; Lou, S.J.; Smith, J.; Tice, D.B.; Hennek, W. Polymer solar cells with enhanced fill factors. Nat. Photon. 2013, 7, 825–833.

[89] Liu, Q.; Toudert, J.; Li, T.; Kramarenko, M.; Martínez-Denegri, G.; Ciammaruchi, L.; Zhan, X.; Martorell, J. nverse optical cavity design for ultrabroadband light absorption beyond the conventional limit in low-bandgap nonfullerene acceptor–based solar cells. Adv. Energy Mater. 2019, 9, 1900463.

[90] Liu, Q.; Romero-Gomez, P.; Mantilla-Perez, P.; Colodrero, S.; Toudert, J.; Martorell, J. A two-resonance tapping avity for an optimal light trapping in thin-film solar cells. Adv. Energy Mater. 2017, 7, 1700356.

[91] Kakavelakis, G.; Vangelidis, I.; Jungemann, H.; Kanaras, A.G.; Lidorikis, E.; Stratakis, E.; Kymakis, E. Photovoltaic devices: Plasmonic backscattering effect in high-efficient organic photovoltaic devices. Adv. Energy Mater. 2015, 6, 1501640.

[92] Noori, K.; Konios, D.; Stylianakis, M.M.; Kymakis, E.; Giustino, F. Energy-level alignment and open-circuit voltage at graphene/polymer interfaces: Theory and experiment. 2D Mater. 2016, 3, 015003.

[93] Tiwari, S.; Tiwari, T.; Carter, S.; Scott, J.; Yakhmi, J. Advances in polymer-based photovoltaic cells: Review of pioneering materials, design, and device physics. In Handbook of Ecomaterials, 1st ed.; Martínez, L., Kharissova, O., Kharisov, B., Eds.; Springer: Cham, Switzerland, 2019; pp. 1055–1101.

[94] Huang, W.; Cheng, P.; Yang, Y.; Li, G.; Yang, Y. High-performance organic bulk-heterojunction solar cells based on multiple-donor or multiple-acceptor components. Adv. Mater. 2018, 30, 1705706.

[95] Anagnostou, K.; Stylianakis, M.M.; Petridis, K.; Kymakis, E. Building an organic solar cell: Fundamental procedures for device fabrication. Energies 2019, 12, 2188.

[96] Marrocchi, A.; Lanari, D.; Facchetti, A.; Vaccaro, L. Poly(3-hexylthiophene): Synthetic methodologies and properties in bulk heterojunction solar cells. Energy Environ. Sci. 2012, 5, 8457–8474.

[97] Liang, Y.; Feng, D.; Wu, Y.; Tsai, S.T.; Li, G.; Ray, C.; Yu, L. Highly efficient solar cell polymers developed via fine-tuning of structural and electronic properties. J. Am. Chem. Soc. 2009, 131, 7792–7799.

[98] Matsumoto, F.; Moriwaki, K.; Takao, Y.; Ohno, T. Synthesis of thienyl analogues of PCBM and investigation of morphology of mixtures in P3HT. Beilstein J. Org. Chem. 2008, 4, 33.

[99] Li, C.Z.; Yip, H.L.; Jen, A.K.Y. Functional fullerenes for organic photovoltaics. J. Mater. Chem. 2012, 22, 4161–4177.

[100] Berger, P.; Kim, R.; Kim, M. Polymer solar cells: P3HT: PCBM and beyond. J. Renew. Sustain. Energy 2018, 10, 013508.

[101] Chen, C.P.; Lee, I.; Tsai, C.; Huang, Y.; Chen, C.L.; Huang, G.W. Efficient organic solar cells based on PTB7:$PC_{71}BM$ blend film with embedded different shapes silver nanoparticles into PEDOT: PSS as hole transporting layers. Org. Electron. 2018, 62, 95–101.

[102] Cui, Y.; Yao, H.; Hong, L.; Zhang, T.; Tang, Y.; Lin, B.; Xian, K.; Gao, B.; An, C.; Bi, P.; et al. 17% efficiency organic photovoltaic cell with superior processability. Nat. Sci. Rev. 2019, nwz200.

[103] Cui, Y.; Yao, H.; Zhang, J.; Zhang, T.; Wang, Y.; Hong, L.; Xian, K.; Xu, B.; Zhang, S.; Peng, J.; et al. Over 16% efficiency organic photovoltaic cells enabled by a chlorinated acceptor with increased open-circuit voltages. Nat. Commun. 2019, 10, 2515.

[104] Fan, B.; Zhang, D.; Li, M.; Zhong, W.; Zeng, Z.; Ying, L.; Huang, F.; Cao, Y. Achieving over 16% efficiency for single-junction organic solar cells. Sci. China Chem. 2019, 62, 746–752.

[105] Doumon, N.Y.; Dryzhov, M.V.; Houard, F.V.; Le Corre, V.M.; Rahimi Chatri, A.; Christodoulis, P.; Koster, L.J.A. Photostability of fullerene and non-fullerene polymer solar cells: The role of the acceptor. ACS Appl. Mater. Interfaces 2019, 11, 8310–8318.

[106] Li, N.; McCulloch, I.; Brabec, C.J. Analyzing the efficiency, stability and cost potential for fullerene-free organic photovoltaics in one figure of merit. *Energy Environ. Sci.* **2018**, *11*, 1355–1361.

[107] Liu, Q.; Toudert, J.; Liu, F.; Mantilla-Perez, P.; Bajo, M.M.; Russell, T.P.; Martorell, J. Circumventing UV light induced nanomorphology disorder to achieve long lifetime PTB7-Th:PCBM based solar cells. Adv. Energy Mater. 2017, 7, 1701201.

[108] Lu, L.; Kelly, M.A.; You, W.; Yu, L. Status and prospects for ternary organic photovoltaics. Nat. Phot. 2015, 9, 491–500.

[109] Gupta, V.; Bharti, V.; Kumar, M.; Chand, S.; Heeger, A.J. Polymer-polymer Förster resonance energy transfer significantly boosts the power conversion efficiency of bulk-heterojunction solar cells. Adv. Mater. 2015, 27, 4398–4404.

[110] Felekidis, N.; Melianas, A.; Kemerink, M. Design rule for improved open-circuit voltage in binary and ternary organic solar cells. ACS Appl. Mater. Interfaces 2017, 9, 37070–37077.

[111] Gasparini, N.; Salleo, A.; McCulloch, I.; Baran, D. The role of the third component in ternary organic solar cells. Nat. Rev. Mater. 2019, 4, 229–242.

[112] Lu, L.; Chen, W.; Xu, T.; Yu, L. High-performance ternary blend polymer solar cells involving both energy transfer and hole relay processes. Nat. Comm. 2015, 6, 7327.

[113] Liu, T.; Huo, L.; Sun, X.; Fan, B.; Cai, Y.; Kim, T. Ternary organic solar cells based on two highly efficient polymer donors with enhanced power conversion efficiency. Adv. Energy Mater. 2016, 6, 1502109.

[114] Gasparini, N.; Lucera, L.; Salvador, M.; Prosa, M.; Spyropoulos, G.D.; Kubis, P. High-performance ternary organic solar cells with thick active layer exceeding 11% efficiency. Energy Environ. Sci. 2017, 10, 885–892.

[115] Cha, H.; Chung, D.S.; Bae, S.Y.; Lee, M.J.; An, T.K.; Hwang, J. Complementary absorbing star-shaped small molecules for the preparation of ternary cascade energy structures in organic photovoltaic cells. Adv. Funct. Mater. 2013, 23, 1556–1565.

[116] Zhang, Y.; Deng, D.; Lu, K.; Zhang, J.; Xia, B.; Zhao, Y. Synergistic effect of polymer and small molecules for high-performance ternary organic solar cells. Adv. Mater. 2015, 27, 1071–1076.

[117] Zhang, S.; Zuo, L.; Chen, J.; Zhang, Z.; Mai, J.; Lau, T.K. Improved photon-to-electron response of ternary blend organic solar cells with a low band gap polymer sensitizer and interfacial modification. J. Mater. Chem. A 2016, 4, 1702–1707.

[118] Nian, L.; Gao, K.; Liu, F.; Kan, Y.; Jiang, X.; Liu, L. 11% efficient ternary organic solar cells with high composition tolerance via integrated near-IR sensitization and interface engineering. Adv. Mater. 2016, 28, 8184–8190.

[119] Zhang, J.; Zhao, Y.; Fang, J.; Yuan, L.; Xia, B.; Wang, G. Enhancing performance of large-area organic solar cells with thick film via ternary strategy. Small 2017, 13, 1700388.

[120] Zhang, G.; Zhang, K.; Yin, Q.; Jiang, X.F.; Wang, Z.; Xin, J. High-performance ternary organic solar cell enabled by a thick active layer containing a liquid crystalline small molecule donor. J. Am. Chem. Soc. 2017, 139, 2387–2395.

[121] Kai, Z.; Dandan, T.; Kaicheng, Z.; Zhaowei, W.; Lan, D.; Yanfeng, L.; Ligang, Y.; Jian, F.; Bo, S.; Zhou, Y.; et al. A two-dimension-conjugated small molecule for efficient ternary organic solar cells. Org. Electron. 2017, 48, 179–187.

[122] Wenzhan, X.; Chao, Y.; Xiang, Y.; Lili, J.; Xiong, G.; Yong, C. Efficient organic solar cells with polymer-small molecule: Fullerene ternary active layers. ACS Omega 2017, 2, 1786–1794.

[123] Pan, F.; Zhang, L.; Jiang, H.; Yuan, D.; Nian, Y.; Cao, Y.; Chen, J. As-cast ternary polymer solar cells based on a non-fullerene acceptor and its fluorinated counterpart showing improved efficiency and good thickness tolerance. J. Mater. Chem. A 2019, 7, 9798–9806.

[124] Rodríguez Seco, C.; Ferran, A.V.; Misra, R.; Sharma, G.D.; Palomares, E. Efficient non-polymeric heterojunctions in ternary organic solar cells. ACS Appl. Energy Mater. 2018, 1, 4203–4210.

[125] Mohapatra, A.A.; Kim, V.; Puttaraju, B.; Sadhanala, A.; Jiao, X.; McNeill, C.R.; Friend, R.H.; Patil, S. Förster resonance energy transfer drives higher efficiency in ternary blend organic solar cells. ACS Appl. Energy Mater. 2018, 1, 4874–4882.

[126] Ruiping, Q.; Guo, D.; Li, M.; Li, G.; Bo, Z.; Wu, J. Perylene monoimide dimers enhance ternary organic solar cells efficiency by induced D–A crystallinity. ACS Appl. Energy Mater. 2019, 2, 305–311.

[127] . Fu, H.; Li, C.; Bi, P.; Hao, X.; Liu, F.; Li, Y.; Wang, Z.; Sun, Y. Efficient ternary organic solar cells enabled by the integration of nonfullerene and fullerene acceptors with a broad composition tolerance. Adv. Funct. Mater. 2019, 29, 1807006

[128] Song, X.; Gasparini, N.; Nahid, M.M.; Harish, S.; Paleti, K.; Wang, J.L.; Ade, H.; Baran, D. Dual sensitizer and processing-aid behavior of donor enables efficient ternary organic solar cells. Joule 2019, 3, 1–12.

[129] Ke, L.; Gasparini, N.; Min, J.; Zhang, H.; Adam, M.; Rechberger, S. Panchromatic ternary/quaternary polymer/fullerene BHJ solar cells based on novel silicon naphthalocyanine and silicon phthalocyanine dye sensitizers. J. Mater. Chem. A 2017, 5, 2550–2562.

[130] Grant, T.M.; Gorisse, T.; Dautel, O.; Wantz, G.; Lessard, B.H. Multifunctional ternary additive in bulk heterojunction OPV: Increased device performance and stability. J. Mater. Chem. A 2017, 5, 1581–1587.

[131] Stylianakis, M.M.; Konios, D.; Viskadouros, G.; Vernardou, D.; Katsarakis, N.; Koudoumas, E.; Anastasiadis, S.H.; Stratakis, E.; Kymakis, E. Ternary organic solar cells incorporating zinc phthalocyanine with improved performance exceeding 8.5%. Dyes Pigm. 2017, 146, 408–413.

[132] Cheng, P.; Li, Y.; Zhan, X. Efficient ternary blend polymer solar cells with indene C60 bis-adduct as an electron-cascade acceptor. Energy Environ. Sci. 2014, 7, 2005–2011.

[133] Sygletou, M.; Tzourmpakis, P.; Petridis, C.; Konios, D.; Fotakis, C.; Kymakis, E.; Stratakis, E. Laser induced nucleation of plasmonic nanoparticles on two-dimensional nanosheets for organic photovoltaics. J. Mater. Chem. A 2016, 4, 1020–1027.

[134] Bonaccorso, F.; Balis, N.; Stylianakis, M.M.; Savarese, M.; Adamo, C.; Gemmi, M.; Pellegrini, V.; Stratakis, E.; Kymakis, E. Functionalized graphene as an electron-cascade acceptor for air-processed organic ternary solar cells. Adv. Funct. Mater. 2015, 25, 3870–3880.

[135] Stylianakis, M.M.; Konios, D.; Kakavelakis, G.; Charalambidis, G.; Stratakis, E.; Coutsolelos, A.G.; Kymakis, E.; Anastasiadis, S.H. Efficient ternary organic photovoltaics incorporating a graphene-based porphyrin molecule as a universal electron cascade material. Nanoscale 2015, 7, 17827–17835.

[136] Kakavelakis, G.; Esau, A.; Del Rio, C.; Pellegrini, V.; Ansaldo, A.; Tzourmpakis, P.; Brescia, R.; Prato, M.; Stratakis, E.; Kymakis, E.; et al. Size-tuning of WSe2 flakes for high efficiency inverted organic solar cells. ACS Nano 2017, 11, 3517–3531.

[137] Stylianakis, M.M.; Kosmidis, D.M.; Anagnostou, K.; Polyzoidis, C.; Krassas, M.; Kenanakis, G.; Viskadouros, G.; Kornilios, N.; Petridis, K.; Kymakis, E. Emphasizing the operational role of a novel graphene-based ink into high performance ternary organic solar cells. Nanomaterials 2020, 10, 89.

[138] Balis, N.; Konios, D.; Stratakis, E.; Kymakis, E. Ternary organic solar cells with reduced graphene oxide–Sb2S3 hybrid nanosheets as the cascade material. ChemNanoMat 2015, 1, 5346–5352.

[139] Kozycz, L.M.; Gao, D.; Hollinger, J.; Seferos, D.S. Donor–donor block copolymers for ternary organic solar cells. Macromolecules 2012, 45, 5823–5832.

[140] You, J.; Dou, L.; Hong, Z.; Li, G.; Yang, Y. Recent trends in polymer tandem solar cells research. Prog. Polym. Sci. 2013, 38, 1909–1928.

[141] Yang, Y.M.; Chen, W.; Dou, L.; Chang, W.H.; Duan, H.S.; Bob, B. High-performance multiple-donor bulk heterojunction solar cells. Nat. Photon. 2015, 9, 190–198.

[142] Mancilha, F.S.; DaSilveira Neto, B.A.; Lopes, A.S.; Moreira, P.F.; Quina, F.H.; Gonçalves, R.S.; Dupont, J. Are molecular 5,8-π-extended quinoxaline derivatives good chromophores for photoluminescence applications? Eur. J. Org. Chem. 2006, 2006, 4924–4933.

[143] Yuan, J.; Zhang, Y.; Zhou, L.; Zhang, G.; Yip, H.L.; Lau, T.K.; Lu, X.; Zhu, C.; Peng, H.; Johnson, P.A.; et al. Single-junction organic solar cell with over 15% efficiency using fused-ring acceptor with electron-deficient core. Joule 2019, 3, 1140–1151.

[144] Akhtaruzzaman, M.; Tomura, M.; Nishida, J.; Yamashita, Y. New narrow-bandgap polymer composed of benzobis(1,2,5-thiadiazole) and thiophenes. J. Am. Chem. Soc. 1995, 117, 6791.

[145] Van Mullekom, H.A.; Vekemans, J.A.J.M.; Meijer, E.W. Band-gap engineering of donor–acceptor-substituted π-conjugated polymers. Chem. Eur. J. 1998, 4, 1235–1243.

[146] Park, S.H.; Roy, A.; Beaupre', S.; Cho, S.; Coates, N.; Moon, J.S.; Moses, D.; Leclerc, M.; Lee, K.; Heeger, A.J. Bulk heterojunction solar cells with internal quantum efficiency approaching 100%. Nat. Photon. 2009, 3, 297–302.

[147] Halls, J.J.M.; Walsh, C.A.; Greenham, N.C.; Marseglla, E.A.; Friend, R.H.; Moratti, S.C.; Holmes, A.B. Efficient photodiodes from interpenetrating polymer networks. Nature 1995, 376, 498–500.

[148] Mikroyannidis, J.A.; Stylianakis, M.M.; Dong, Q.; Zhou, Y.; Tian, W. New 4,7-dithienebenzothiadiazole derivatives with cyano-vinylene bonds: Synthesis, photophysics and photovoltaics. Synth. Met. 2009, 159, 1471–1477.

[149] Mancilha, F.S.; DaSilveira Neto, B.A.; Lopes, A.S.; Moreira, P.F.; Quina, F.H.; Gonçalves, R.S.; Dupont, J. Are Molecular 5,8-π-Extended Quinoxaline Derivatives Good Chromophores for Photoluminescence Applications? Eur. J. Org. Chem. 2006, 2006, 4924-4933. doi: 10.1002/ejoc.200600376.

[150] Kitamura, C.; Tanaka, S.; Yamashita, Y. Design of Narrow-Bandgap Polymers. Syntheses and Properties of Monomers and Polymers Containing Aromatic-Donor and o-Quinoid-Acceptor Units. Chem. Mater. 1996, 8, 570-578. doi: 10.1021/cm950467m.

[151] Roquet, S.; Cravino, A.; Leriche, P.; Alévêque, O.; Frère, P.; Roncali, J. Triphenylamine–Thienylenevinylene Hybrid Systems with Internal Charge Transfer as Donor Materials for Heterojunction Solar Cells. J. Am. Chem. Soc. 2006, 128, 3459-3466. doi: 10.1021/ja058178e.

[152] Mikroyannidis, J.A.; Stylianakis, M.M.; Dong, Q.; Zhou, Y.; Tian, W. New 4,7-dithienebenzothiadiazole derivatives with cyano-vinylene bonds: Synthesis, photophysics and photovoltaics. Synth. Met. 2009, 159, 1471–1477. doi: 10.1016/j.synthmet.2009.04.002.

[153] Kraft, A.; Grimsdale, A.C.; Holmes, A.B. Electroluminescent conjugated polymers—Seeing polymers in a new light. Angew. Chem. Int. Ed. 1998, 37, 402–428.

[154] Cho, N.S.; Hwang, D.H.; Jung, B.J.; Oh, J.; Chu, H.Y.; Shim, H.K. Synthesis and light emitting properties of fluorene–carbazole-based conjugated copolymers. Synth. Met. 2004, 143, 277–282.

[155] Ochiai, S.; Imamura, S.; Kannappan, S.; Palanisamy, K.; Shin, P.K. Characteristics and the effect of additives on the nanomorphology of PTB7/PC71BM composite films. Cur. Appl. Phys. 2013, 13, S58–S63.

[156] Konios, D.; Kakavelakis, G.; Petridis, C.; Savva, K.; Stratakis, E.; Kymakis, E. Highly efficient organic photovoltaic devices utilizing work-function tuned graphene oxide derivatives as the anode and cathode charge extraction layers. J. Mater. Chem. A 2016, 4, 1612–1623.

[157] Zhang, G.C.; Zhou, C.; Sun, C.; Jia, X.; Xu, B.; Ying, L.; Huang, F.; Cao, Y. An open-circuit voltage and power conversion efficiency study of fullerene ternary organic solar cells based on oligomer/oligomer and oligomer/polymer. Macromol. Rapid Commun. 2017, 38, 1700090.

[158] Campbell, A.J.; Bradley, D.D.C. Quantifying the efficiency of electrodes for positive carrier injection into poly(9,9-dioctylfluorene) and representative copolymers. J. Appl. Phys. 2001, 89, 3343.

[159] Kim, H.I.; Kim, M.; Park, C.W.; Kim, H.U.; Lee, H.-K.; Park, T. Morphological control of donor/acceptor interfaces in all-polymer solar cells using a pentafluorobenzene-based additive. Chem. Mater. 2017, 29, 6793–6798.

[160] Inganäs, O. Organic Photovoltaics over Three Decades. Adv. Mater. 2018, 30, 1800388. doi: 10.1002/adma.201800388.

[161] Lee, C.; Lee, S.; Kim, G.U.; Lee, W.; Kim, B.J. Recent Advances, Design Guidelines, and Prospects of All Polymer Solar Cells. Chem. Rev. 2019, 119, 8028–8086. doi: 10.1021/acs.chemrev.9b00044.

[162] Zhang, J.; Tan, H.S.; Guo, X.; Facchetti, A.; Yan, H. Material Insights and Challenges for Non-Fullerene Organic Solar Cells Based on Small Molecular Acceptors. Nat. Energy 2018, 3, 720–731. doi: 10.1002/adma.201800388.

[163] Meng, L.; Zhang, Y.; Wan, X.; Li, C.; Zhang, X.; Wang, Y.; Ke, X.; Xiao, Z.; Ding, L.; Xia, R.; Yip, H.L.; Cao, Y.; Chen, Y. Organic and Solution-Processed Tandem Solar Cells with 17.3% Efficiency. Science 2018, 361, 1094–1098. doi: 10.1126/science.aat2612.

[164] Yuan, J.; Zhang, Y.; Zhou, L.; Zhang, G.; Yip, H.L.; Lau, T.K.; Lu, X.; Zhu, C.; Peng, H.; Johnson, P.A.; Leclerc, M.; Cao, Y.; Ulanski, J.; Li, Y.; Zou, Y. Single-Junction Organic Solar Cell with over 15% Efficiency Using Fused-Ring Acceptor with Electron-Deficient Core. Joule 2019, 3, 1140–1151. doi: 10.1016/j.joule.2019.01.004.

[165] Liu, T.; Luo, Z.; Chen, Y.; Yang, T.; Xiao, Y.; Zhang, G.; Ma, R.; Lu, X.; Zhan, C.; Zhang, M.; Yang, C.; Li, Y.; Yao, J.; Yan, H. A Nonfullerene Acceptor with a 1000 Nm Absorption Edge Enables Ternary Organic Solar Cells with Improved Optical and Morphological Properties and Efficiencies over 15%. Energy Environ. Sci. 2019, 12, 2529–2536. doi: 10.1039/C9EE01030K.

[166] Liu, X.; Yan, Y.; Yao, Y.; Liang, Z. Ternary Blend Strategy for Achieving High-Efficiency Organic Solar Cells with Nonfullerene Acceptors Involved. Adv. Funct. Mater. 2018, 28, 1–20. doi: 10.1002/adfm.201802004.

[167] Gasparini, N.; Salleo, A.; McCulloch, I.; Baran, D. The Role of the Third Component in Ternary Organic Solar Cells. Nat. Rev. Mater. 2019, 4, 229–242. doi: 10.1038/s41578-019-0093-4.

[168] Song, X.; Gasparini, N.; Nahid, M.M.; Paleti, S.H.K.; Wang, J.L.; Ade, H.; Baran, D. Dual Sensitizer and Processing-Aid Behavior of Donor Enables Efficient Ternary Organic Solar Cells. Joule 2019, 3, 846–857. doi: 10.1016/j.joule.2019.01.009.

[169] Seco, C.R.; Vidal-Ferran, A.; Misra, R.; Sharma, G.D.; Palomares, E. Efficient Non-Polymeric Heterojunctions in Ternary Organic Solar Cells. ACS Appl. Energy Mater. 2018, 1, 4203–4210. doi: 10.1021/acsaem.8b00828.

[170] Qin, R.; Guo, D.; Li, M.; Li, G.; Bo, Z.; Wu, J. Perylene Monoimide Dimers Enhance Ternary Organic Solar Cells Efficiency by Induced D-A Crystallinity. ACS Appl. Energy Mater. 2019, 2, 305–311. doi: 10.1021/acsaem.8b01320.

[171] Fu, H.; Li, C.; Bi, P.; Hao, X.; Liu, F.; Li, Y.; Wang, Z.; Sun, Y. Efficient Ternary Organic Solar Cells Enabled by the Integration of Nonfullerene and Fullerene Acceptors with a Broad Composition Tolerance. Adv. Funct. Mater. 2019, 29, 1–8. doi: 10.1002/adfm.201807006.

[172] Cheng, P.; Li, Y.; Zhan, X. Efficient Ternary Blend Polymer Solar Cells with Indene-C60 Bisadduct as an Electron-Cascade Acceptor. Energy Environ. Sci. 2014, 7, 2005–2011. doi: 10.1039/C3EE44202K.

[173] Lu, L.; Chen, W.; Xu, T.; Yu, L. High-Performance Ternary Blend Polymer Solar Cells Involving Both Energy Transfer and Hole Relay Processes. Nat. Commun. 2015, 6, 1–7. doi: 10.1038/ncomms8327.

[174] . Gasparini, N.; Lucera, L.; Salvador, M.; Prosa, M.; Spyropoulos, G.D.; Kubis, P.; Egelhaaf, H.J.; Brabec, C.J.; Ameri, T. High-Performance Ternary Organic Solar Cells with Thick Active Layer Exceeding 11% Efficiency. Energy Environ. Sci. 2017, 10, 885-892. doi: 10.1039/C6EE03599J.

[175] Ke, L.; Gasparini, N.; Min, J.; Zhang, H.; Adam, M.; Rechberger, S.; Forberich, K.; Zhang, C.; Spiecker, E.; Tykwinski, R.R.; Brabec, C.J.; Ameri, T. Panchromatic Ternary/Quaternary Polymer/Fullerene BHJ Solar Cells Based on Novel Silicon Naphthalocyanine and Silicon Phthalocyanine Dye Sensitizers. J. Mater. Chem. A 2017, 5, 2550–2562. doi: 10.1039/C6TA08729A.

[176] Bonaccorso, F.; Balis, N.; Stylianakis, M.M.; Savarese, M.; Adamo, C.; Gemmi, M.; Pellegrini, V.; Stratakis, E.; Kymakis, E. Functionalized Graphene as an Electron-Cascade Acceptor for Air-Processed Organic Ternary Solar Cells. Adv. Funct. Mater. 2015, 25, 3870–3880. doi: 10.1002/adfm.201501052.

[177] Kakavelakis, G.; Del Rio Castillo, A.E.; Pellegrini, V.; Ansaldo, A.; Tzourmpakis, P.; Brescia, R.; Prato, M.; Stratakis, E.; Kymakis, E.; Bonaccorso, F. Size-Tuning of WSe2 Flakes for High Efficiency Inverted Organic Solar Cells. ACS Nano 2017, 11, 3517–3531. doi: 10.1021/acsnano.7b00323.

[178] Nagarjuna, P.; Bagui, A.; Gupta, V.; Singh, S.P. A Highly Efficient PTB7-Th Polymer Donor Bulk HeteroJunction Solar Cell with Increased Open Circuit Voltage Using Fullerene Acceptor CN-PC70BM. Org. Electron. 2017, 43, 262–267. doi: 10.1016/j.orgel.2017.01.015.

[179] Fan, R.; Huai, Z.; Sun, Y.; Li, X.; Fu, G.; Huang, S.; Wang, L.; Yang, S. Enhanced Performance of Polymer Solar Cells Based on PTB7-Th:PC 71 BM by Doping with 1-Bromo-4-Nitrobenzene. J. Mater. Chem. C 2017, 5, 10985-10990. doi: 10.1039/C7TC04062H.

[180] Zhu, Y.; Murali, S.; Cai, W.; Li, X.; Suk, J.W.; Potts, J.R.; Ruoff, R.S. Graphene and Graphene Oxide: Synthesis, Properties, and Applications. Adv. Mater. 2010, 22, 3906–3924. doi: 10.1002/adma.201001068.

[181] Tang, X.Z.; Li, W.; Yu, Z.Z.; Rafiee, M.A.; Rafiee, J.; Yavari, F.; Koratkar, N. Enhanced thermal stability in graphene oxide covalently functionalized with 2-amino-4, 6-didodecylamino-1, 3, 5-triazine. Carbon 2011, 49, 1258-1265. doi: 10.1016/j.carbon.2010.11.044.

[182] Cardona, C.M.; Li, W.; Kaifer, A.E.; Stockdale, D.; Bazan, G.C. Electrochemical considerations for determining absolute frontier orbital energy levels of conjugated polymers for solar cell applications. Adv. Mater. 2011, 23, 2367-2371. doi: 10.1002/adma.201004554.

[183] Azimi, H.; Senes, A.; Scharber, M.C.; Hingerl, K.; Brabec, C.J. Charge Transport and Recombination in Low- Bandgap Bulk Heterojunction Solar Cell using Bis-adduct Fullerene. Adv. Energy Mater. 2011, 1, 1162-1168. doi: 10.1002/aenm.201100331.

[184] L. Dou, Y. Liu, Z. Hong, G. Li, Y. Yang, Chem. Rev. 2015, 115, 12633.

[185] X. Guo, M. Baumgarten, K. Mullen, € Prog. Polym. Sci. 2013, 38, 1832.

[186] J. D. Yuen, R. Kumar, D. Zakhidov, J. Seifter, B. Lim, A. J. Heeger, F. Wudl, Adv. Mater. 2011, 23, 3780.

[187] X. Guo, A. Facchetti, T. J. Marks, Chem. Rev. 2014, 114, 8943.

[188] C. B. Nielsen, M. Turbiez, I. McCulloch, Adv. Mater. 2013, 25, 1859.

[189] K. H. Hendriks, G. H. L. Heintges, V. S. Gevaerts, M. M. Wienk, R. A. J. Janssen, Angew. Chem. Int. Ed. 2013, 52, 8341.

[190] R. S. Ashraf, I. Meager, M. Nikolka, M. Kirkus, M. Planells, B. C. Schroeder, S. Holliday, M. Hurhangee, C. B. Nielsen, H. Sirringhaus, I. McCulloch, J. Am. Chem. Soc. 2015, 137, 1314.

[191] H. Choi, S.-J. Ko, T. Kim, P.-O. Morin, B. Walker, B. H. Lee, M. Leclerc, J. Y. Kim, A. J. Heeger, Adv. Mater. 2015, 27, 3318.

[192] J. Y. Back, H. Yu, I. Song, I. Kang, H. Ahn, T. J. Shin, S.-K. Kwon, J. H. Oh, Y.-H. Kim, Chem. Mater. 2015, 27, 1732.

[193] B. Sun, W. Hong, Z. Yan, H. Aziz, Y. Li, Adv. Mater. 2014, 26, 2636.

[194] M. M. Wienk, M. Turbiez, J. Gilot, R. A. J. Janssen, Adv. Mater. 2008, 20, 2556.

[195] W. Li, K. H. Hendriks, M. M. Wienk, R. A. J. Janssen, Acc. Chem. Res. 2016, 49, 78.

[196] C. L. Chochos, S. A. Choulis, Prog. Polym. Sci. 2011, 36, 1326.

[197] T. Lei, J.-Y. Wang, J. Pei, Chem. Mater. 2014, 26, 594.

[198] Wang, H. Dong, W. Hu, Y. Liu, D. Zhu, Chem. Rev. 2012, 112, 2208.

[199] L. Ding, H.-B. Li, T. Lei, H.-Z. Ying, R.-B. Wang, Y. Zhou, Z. M. Su, J. Pei, Chem. Mater. 2012, 24, 1944.

[200] W. Li, K. H. Hendriks, A. Furlan, W. S. C. Roelofs, S. C. J. Meskers, M. M. Wienk, R. A. J. Janssen, Adv. Mater. 2014, 26, 1565.

[201] T. Lei, J.-H. Dou, J. Pei, Adv. Mater. 2012, 24, 6457.

[202] L. Biniek, S. Fall, C. L. Chochos, D. V. Anokhin, D. A. Ivanov, N. Leclerc, P. Lev ——————————————————— eque, T. Heiser, ^ Macromolecules. 2010, 43, 9779.

[203] C. L. Chochos, A. Katsouras, N. Gasparini, C. Koulogiannis, T. Ameri, C. J. Brabec, A. Avgeropoulos, Macromol. Rapid Commun. 2017, 38, 1600614.

[204] X.-Y. Wang, F.-D. Zhuang, X. Zhou, D.-C. Yang, J.-Y. Wang, J. Pei, J. Mater. Chem. C 2014, 2, 8152.

[205] H. Bronstein, D. S. Leem, R. Hamilton, P. Woebkenberg, S. King, W. Zhang, R. S. Ashraf, M. Heeney, T. D. Anthopoulos, J. d. Mello, I. McCulloch, Macromolecules. 2011, 44, 6649.

[206] Q. Wu, M. Wang, X. Qiao, Y. Xiong, Y. Huang, X. Gao, H. Li, Macromolecules. 2013, 46, 3887.

[207] R. J. Kline, D. M. DeLongchamp, D. A. Fischer, E. K. Lin, L. J. Richter, M. L. Chabinyc, M. F. Toney, M. Heeney, I. McCulloch, Macromolecules. 2007, 40, 7960.

[208] L. Biniek, S. Fall, C. L. Chochos, N. Leclerc, P. Lev ——————————————————— eque, T. Heiser, Org. Electron. 2012, 13, 114.

[209] F. Zhang, Y. Hu, T. Schuettfort, C. Di, X. Gao, C. R. McNeill, L. Thomsen, S. C. B. Mannsfeld, W. Yuan, H. Sirringhaus, D. Zhu, J. Am. Chem. Soc. 2013, 135, 2338.

[210] I. Meager, R. S. Ashraf, S. Mollinger, B. C. Schroeder, H. Bronstein, D. Beatrup, M. S. Vezie, T. Kirchartz, A. Salleo, J. Nelson, I. McCulloch, J. Am. Chem. Soc. 2013, 135, 11537.

[211] Y. Li, P. Sonar, L. Murphy, W. Hong, Energy Environ. Sci. 2013, 6, 1684.

[212] S. Y. Qu, H. Tian, Chem. Commun. 2012, 48, 3039.

[213] M. A. Naik, S. Patil, J. Polym. Sci. Part A: Polym. Chem. 2013, 51, 4241.

[214] C. H. Woo, P. M. Beaujuge, T. W. Holcombe, O. P. Lee, J. M. J. Frechet, ——————————————————— J. Am. Chem. Soc. 2010, 132, 15547.

[215] H. Bronstein, Z. Chen, R. S. Ashraf, W. Zhang, J. Du, J. R. Durrant, P. S. Tuladhar, K. Song, S. E. Watkins, Y. Geerts, M. M. Wienk, R. A. J. Janssen, T. Anthopoulos, H. Sirringhaus, M. Heeney, I. McCulloch, J. Am. Chem. Soc. 2011, 133, 3272.

[216] H. H. Fong, V. A. Pozdin, A. Amassian, G. G. Malliaras, D. M. Smilgies, M. He, S. Gasper, F. Zhang, M. Sorensen, J. Am. Chem. Soc. 2008, 130, 13202.

[217] M. J. Frisch, G. W. Trucks, H. B. Schlegel, G. E. Scuseria, M. A. Robb, J. R. Cheeseman, J. A. Montgomery, Jr., T. Vreven, K. N. Kudin, J. C. Burant, J. M. Millam, S. S. Iyengar, J. Tomasi, V. Barone, B. Mennucci, M. Cossi, G. Scalmani, N. Rega, G. A. Petersson, H. Nakatsuji, M. Hada, M. Ehara, K. Toyota, R. Fukuda, J. Hasegawa, M. Ishida, T. Nakajima, Y. Honda, O. Kitao, H. Nakai, M. Klene, X. Li, J. E. Knox, H. P. Hratchian, J. B. Cross, V. Bakken, C. Adamo, J. Jaramillo, R. Gomperts, R. E. Stratmann, O. Yazyev, A. J. Austin, R. Cammi, C. Pomelli, J. W. Ochterski, P. Y. Ayala, K. Morokuma, G. A. Voth, P. Salvador, J. J. Dannenberg, V. G. Zakrzewski, S. Dapprich, A. D. Daniels, M. C. Strain, O. Farkas, D. K. Malick, A. D. Rabuck, K. Raghavachari, J. B. Foresman, J. V. Ortiz, Q. Cui, A. G. Baboul, S. Clifford, J. Cioslowski, B. B. Stefanov, G. Liu, A. Liashenko, P. Piskorz, I. Komaromi, R. L. Martin, D. J. Fox, T. Keith, M. A. Al-Laham, C. Y. Peng, A. Nanayakkara, M. Challacombe, P. M. W. Gill, B. Johnson, W. Chen, M. W. Wong, C. Gonzalez, J. A. Pople, GAUSSIAN 03, Revision E.01; Gaussian, Inc.: Wallingford, CT, 2004.

[218] L. Biniek, C. L. Chochos, N. Leclerc, O. Boyron, S. Fall, P. Leve^que, T. Heiser, J. Polym. Sci. Part A: Polym. Chem. 2012, 50, 1861.

[219] J. Ku, Y. Lansac, Y. H. Jang, J. Phys. Chem. C 2011, 115, 21508.

[220] C. Risko, M. D. McGehee, J.-L. Bredas, Chem. Sci. 2011, 2, 1200.

[221] B. Carsten, F. He, H. J. Son, T. Xu, L. Yu, Chem. Rev. 2011, 111, 1493.

[222] S. Roquet, A. Cravino, P. Leriche, O. Aleveque, P. Fre ^ ` re, J. Roncali, J. Am. Chem. Soc. 2006, 128, 3459.

[223] X. Zhan, A. Facchetti, S. Barlow, T. J. Marks, M. A. Ratner, M. R. Wasielewski, S. R. Marder, Adv. Mater. 2011, 23, 268.

[224] J. Mei, Y. Diao, A. L. Appleton, L. Fang, Z. Bao, J. Am. Chem. Soc. 2013, 135, 6724.

[225] C. L. Chochos, R. Singh, M. Kim, N. Gasparini, A. Katsouras, C. Kulshreshtha, V. G. Gregoriou, P. E. Keivanidis, T. Ameri, C. J. Brabec, K. Cho, A. Avgeropoulos, Adv. Funct. Mater. 2016, 26, 1840.

[226] C. L. Chochos, S. Drakopoulou, A. Katsouras, B. M. Squeo, C. Sprau, A. Colsmann, V. G. Gregoriou, A.-P. Cando, S. Allard, U. Scherf, N. Gasparini, N. Kazerouni, T. Ameri, C. J. Brabec, A. Avgeropoulos, Macromol. Rapid Commun. 2017, 38, 1600720.

[227] M. M. Wienk, J. M. Kroon, W. J. H. Verhees, J. Knol, J. C. Hummelen, P. A. van Hal, R. A. J. Janssen, Angew. Chem. Int. Ed. 2003, 42, 3371.

[228] M.O. Reese, S.A. Gevorgyan, M. Jorgensen, E. Bundgaard, S.R. Kurtz, D.S. Ginley, D.C. Olson, M.T. Lloyd, P. Moryillo, E.A. Katz, A. Elschner, O. Haillant, T.R. Currier, V. Shrotriya, M. Hermenau, M. Riede, K.R. Kirov, G. Trimmel, T. Rath, O. Inganas,F.L. Zhang, M. Andersson, K. Tvingstedt, M. Lira-Cantu, D. Laird, C. McGuiness, S. Gowrisanker, M. Pannone, M. Xiao, J. Hauch, R. Steim, D.M. DeLongchamp, R. Rosch, H. Hoppe, N. Espinosa, A. Urbina, G. Yaman-Uzunoglu, J.B. Bonekamp, A. van Breemen, C. Girotto, E. Voroshazi, F.C. Krebs, Consensus stability testing protocols for organic photovoltaic materials and devices, Sol. Energy Mater. Sol. Cells 95 (2011) 1253–1267.

[229] L. Ciammaruchi, S. Penna, A. Reale, T.M. Brown, A. Di Carlo, Acceleration factor for ageing measurement of dye solar cells, Microelectron. Reliab. 53 (2013) 279–281.

[230] E.A. Katz, D. Faiman, S.M. Tuladhar, J.M. Kroon, M.M. Wienk, T. Fromherz, F. Padinger, C.J. Brabec, N.S. Sariciftci, Temperature dependence for the photovoltaic device parameters of polymer-fullerene solar cells under operating conditions, J. Appl. Phys. 90 (2001) 5343–5350.

[231] T.-A. Chen, X. Wu, R.D. Rieke, Regiocontrolled synthesis of poly(3-alkylthiophenes) mediated by Rieke zinc: their characterization and solid-state properties, J. Am. Chem. Soc. 117 (1995) 233–244.

[232] D.K. Susarova, N.P. Piven, A.V. Akkuratov, L.A. Frolova, M.S. Polinskaya, S.A. Ponomarenko, S.D. Babenko, P.A. Troshin, ESR spectroscopy as a powerful tool for probing the quality of conjugated polymers designed for photovoltaic applications, Chem. Commun. (J. Chem. Soc. Sect. D) 51 (2015) 2239–2241.

[233] S. Das, F. Herrmann-Westendorf, F.H. Schacher, E. Tauscher, U. Ritter, B. Dietzek, M. Presselt, Controlling electronic transitions in fullerene van der Waals aggregates via supramolecular assembly, ACS Appl. Mater. Interfaces 8 (2016), 21512–21521.

[234] W.B. Jackson, N.M. Amer, A.C. Boccara, D. Fournier, Photothermal deflection spectroscopy and detection, Appl. Optic. 20 (1981) 1333–1344.

[235] M.T. Neukom, S. Züfle, B. Ruhstaller, Reliable extraction of organic solar cell parameters by combining steady-state and transient techniques, Org. Electron. 13 (2012), 2910–2916.

[236] S. Züfle, M.T. Neukom, S. Altazin, M. Zinggeler, M. Chrapa, T. Offermans, B. Ruhstaller, An effective area approach to model lateral degradation in organic solar cells, Adv. Energ. Mater. 5 (2015) 1500835.

[237] R.D. McCullough, R.D. Lowe, Enhanced electrical conductivity in regioselectively synthesized poly(3-alkylthiophenes), J. Chem. Soc., Chem. Commun. (1992) 70–72.

[238] T.A. Chen, R.D. Rieke, The first regioregular head-to-tail poly(3-hexylthiophene- 2,5-diyl) and a regiorandom isopolymer: nickel versus palladium catalysis of 2(5)- bromo-5(2)-(bromozincio)-3-hexylthiophene polymerization, J. Am. Chem. Soc. 114 (1992) 10087–10088.

[239] R.S. Loewe, S.M. Khersonsky, R.D. McCullough, A simple method to prepare headto-tail coupled, regioregular poly(3-alkylthiophenes) using grignard metathesis, Adv. Mater. 11 (1999) 250–253.

[240] A. Marrocchi, D. Lanari, A. Facchetti, L. Vaccaro, Poly(3-hexylthiophene): synthetic methodologies and properties in bulk heterojunction solar cells, Energ, Environ. Sci. 5 (2012) 8457–8474.

[241] I. Osaka, R.D. McCullough, Advances in molecular design and synthesis of regioregular polythiophenes, Accounts Chem. Res. 41 (2008) 1202–1214.

[242] N. Gasparini, M. Salvador, S. Strohm, T. Heumueller, I. Levchuk, A. Wadsworth, J.H. Bannock, J.C. de Mello, H.-J. Egelhaaf, D. Baran, I. McCulloch, C.J. Brabec, Burn-in free nonfullerene-based organic solar cells, Adv. Energy Mater. 7 (2017), 1700770.

[243] M.V. Khenkin, A.K. M, I. Visoly-Fisher, Y. Galagan, F. Di Giacomo, B.R. Patil, G. Sherafatipour, V. Turkovic, H.-G. Rubahn, M. Madsen, T. Merckx, G. Uytterhoeven, J.P.A. Bastos, T. Aernouts, F. Brunetti, M. Lira-Cantu, E.A. Katz, Reconsidering figures of merit for performance and stability of perovskite photovoltaics, Energy Environ. Sci. 11 (2018) 739–743.

[244] M.O. Reese, S.A. Gevorgyan, M. Jørgensen, E. Bundgaard, S.R. Kurtz, D.S. Ginley, D.C. Olson, M.T. Lloyd, P. Morvillo, E.A. Katz, A. Elschner, O. Haillant, T.R. Currier, V. Shrotriya, M. Hermenau, M. Riede, K.R. Kirov, G. Trimmel, T. Rath, O. Inganäs, F. Zhang, M. Andersson, K. Tvingstedt, M. LiraCantu, D. Laird, C. McGuiness, S. Gowrisanker, M. Pannone, M. Xiao, J. Hauch, R. Steim, D.M. DeLongchamp, R. Rösch, H. Hoppe, N. Espinosa, A. Urbina, G. Yaman-Uzunoglu, J-B. Bonekamp, A.J.J.M. van Breemen, C. Girotto, E. Voroshazi, and F.C. Krebs: Consensus stability testing protocols for organic photovoltaic materials and devices. Sol. Energy Mater. Sol. Cells 95, 1253–1267 (2011).

[245] J. Kettle, N. Bristow, D.T. Gethin, Z. Tehrani, O. Moudam, B. Li, E.A. Katz, G.A. dos Reis Benatto, and F.C. Krebs: Printable luminescent down shifter for enhancing efficiency and stability of organic photovoltaics. Sol. Energy Mater. Sol. Cells 144(Suppl. C), 481–487 (2016).

[246] Q. Burlingame, G. Zanotti, L. Ciammaruchi, E.A. Katz, and S.R. Forrest: Outdoor operation of small-molecule organic photovoltaics. Org. Electron. 41(Suppl. C), 274–279 (2017).

[247] S.A. Gevorgyan, N. Espinosa, L. Ciammaruchi, B. Roth, F. Livi, S. Tsopanidis, S. Zufle, S. Queiros, A. Gregori, G.A.D. Benatto, M. Corazza, M.V. Madsen, M. Hosel, M.J. Beliatis, T.T. LarsenOlsen, F. Pastorelli, A. Castro, A. Mingorance, V. Lenzi, D. Fluhr, R. Roesch, M.M.D. Ramos, A. Savva, H. Hoppe, L.S.A. Marques, I. Burgues, E. Georgiou, L. Serrano-Lujan, and F.C. Krebs: Baselines for lifetime of organic solar cells. Adv. Energy Mater. 6, 1600910 (2016).

[248] S.A. Gevorgyan, M.V. Madsen, B. Roth, M. Corazza, M. Hösel, R.R. Søndergaard, M. Jørgensen, and F.C. Krebs: Lifetime of organic photovoltaics: Status and predictions. Adv. Energy Mater. 6, 1501208 (2016).

[249] H.J. Son, B. Carsten, I.H. Jung, and L. Yu: Overcoming efficiency challenges in organic solar cells: Rational development of conjugated polymers. Energy Environ. Sci. 5, 8158–8170 (2012).

[250] . A. Zen, J. Pflaum, S. Hirschmann, W. Zhuang, F. Jaiser, U. Asawapirom, J.P. Rabe, U. Scherf, and D. Neher: Effect of molecular weight and annealing of poly(3-hexylthiophene)s on the performance of organic field-effect transistors. Adv. Funct. Mater. 14, 757–764 (2004).

[251] W. Ma, J.Y. Kim, K. Lee, and A.J. Heeger: Effect of the molecular weight of poly(3-hexylthiophene) on the morphology and performance of polymer bulk heterojunction solar cells. Macromol. Rapid Commun. 28, 1776–1780 (2007).

[252] M. Koppe, C.J. Brabec, S. Heiml, A. Schausberger, W. Duffy, M. Heeney, and I. McCulloch: Influence of molecular weight distribution on the gelation of P3HT and its impact on the photovoltaic performance. Macromolecules 42, 4661–4666 (2009).

[253] M. Koppe, C.J. Brabec, S. Heiml, A. Schausberger, W. Duffy, M. Heeney, and I. McCulloch: Influence of molecular weight distribution on the gelation of P3HT and its impact on the photovoltaic performance. Macromolecules 42, 4661–4666 (2009).

[254] Z. Ding, J. Kettle, M. Horie, S.W. Chang, G.C. Smith, A.I. Shames, and E.A. Katz: Efficient solar cells are more stable: The impact of polymer molecular weight on performance of organic photovoltaics. J. Mater. Chem. A 4, 7274–7280 (2016).

[255] L.A. Frolova, N.P. Piven, D.K. Susarova, A.V. Akkuratov, S.D. Babenko, and P.A. Troshin: ESR spectroscopy for monitoring the photochemical and thermal degradation of conjugated polymers used as electron donor materials in organic bulk heterojunction solar cells. Chem. Commun. 51, 2242–2244 (2015).

[256] D.K. Susarova, N.P. Piven, A.V. Akkuratov, L.A. Frolova, M.S. Polinskaya, S.A. Ponomarenko, S.D. Babenko, and P.A. Troshin: ESR spectroscopy as a powerful tool for probing the quality of conjugated polymers designed for photovoltaic applications. Chem. Commun. 51, 2239–2241 (2015).

[257] D.K. Susarova, N.P. Piven, A.V. Akkuratov, L.A. Frolova, M.S. Polinskaya, S.A. Ponomarenko, S.D. Babenko, and P.A. Troshin: ESR spectroscopy as a powerful tool for probing the quality of conjugated polymers designed for photovoltaic applications. Chem. Commun. 51, 2239–2241 (2015).

[258] T.S. Glen, N.W. Scarratt, H. Yi, A. Iraqi, T. Wang, J. Kingsley, A.R. Buckley, D.G. Lidzey, and A.M. Donald: Dependence on material choice of degradation of organic solar cells following exposure to humid air. J. Polym. Sci., Part B: Polym. Phys. 54, 216–224 (2016).

[259] B. Paci, A. Generosi, V. Rossi Albertini, P. Perfetti, R. de Bettignies, and C. Sentein: Time-resolved morphological study of organic thin film solar cells based on calcium/aluminium cathode material. Chem. Phys. Lett. 461, 77–81 (2008).

[260] Z.Y. Liu, M.M. Tian, and N. Wang: Influences of Alq3 as electron extraction layer instead of Ca on the photo-stability of organic solar cells. J. Power Sources 250, 105–109 (2014).

[261] S. Cros, M. Firon, S. Lenfant, P. Trouslard, and L. Beck: Study of thin calcium electrode degradation by ion beam analysis. Nucl. Instrum. Methods Phys. Res., Sect. B 251, 257–260 (2006).

[262] T.S. Glen, N.W. Scarratt, H. Yi, A. Iraqi, T. Wang, J. Kingsley, A.R. Buckley, D.G. Lidzey, and A.M. Donald: Grain size dependence of degradation of aluminium/calcium cathodes in organic solar cells following exposure to humid air. Sol. Energy Mater. Sol. Cells 140(Suppl. C), 25–32 (2015).

[263] M.T. Lloyd, D.C. Olson, P. Lu, E. Fang, D.L. Moore, M.S. White, M.O. Reese, D.S. Ginley, and J.W.P. Hsu: Impact of contact evolution on the shelf life of organic solar cells. J. Mater. Chem. 19, 7638–7642 (2009).

[264] N. Karst and J.C. Bernède: On the improvement of the open circuit voltage of plastic solar cells by the presence of a thin aluminium oxide layer at the interface organic/aluminium. Phys. Status Solidi A 203, R70–R72 (2006).

[265] M.T. Lloyd, C.H. Peters, A. Garcia, I.V. Kauvar, J.J. Berry, M.O. Reese, M.D. McGehee, D.S. Ginley, and D.C. Olson: Influence of the hole-transport layer on the initial behavior and lifetime of inverted organic photovoltaics. Sol. Energy Mater. Sol. Cells 95, 1382–1388 (2011).

[266] D.M. Tanenbaum, H.F. Dam, R. Roesch, M. Jorgensen, H. Hoppe, and F.C. Krebs: Edge sealing for low cost stability enhancement of roll-to-roll processed flexible polymer solar cell modules. Sol. Energy Mater. Sol. Cells 97, 157–163 (2012).

[267] Y.W. Zhang, E. Bovill, J. Kingsley, A.R. Buckley, H.N. Yi, A. Iraqi, T. Wang, and D.G. Lidzey: PCDTBT based solar cells: One year of operation under real-world conditions. Sci. Rep. 6, 21632 (2016).

[268] A. Tournebize, P.O. Bussiere, P. Wong-Wah-Chung, S. Therias, A. Rivaton, J.L. Gardette, S. Beaupre, and M. Leclerc: Impact of UV-visible light on the morphological and photochemical behavior of a low-bandgap poly(2,7-carbazole) derivative for use in high-performance solar cells. Adv. Energy Mater. 3, 478–487 (2013).

[269] A. Tournebize, A. Rivaton, J-L. Gardette, C. Lombard, B. PepinDonat, S. Beaupre, and M. Leclerc: How photoinduced crosslinking under operating conditions can reduce PCDTBT-based solar cell efficiency and then stabilize it. Adv. Energy Mater. 4, 1 (2014).

[270] L.N. Inasaridze, A.I. Shames, I.V. Martynov, B. Li, A.V. Mumyatov, D.K. Susarova, E.A. Katz, and P.A. Troshin: Light-induced generation of free radicals by fullerene derivatives: An important degradation pathway in organic photovoltaics? J. Mater. Chem. A 5, 8044–8050 (2017).

[271] Z. Li, K.H. Chiu, R.S. Ashraf, S. Fearn, R. Dattani, H.C. Wong, C.H. Tan, J.Y. Wu, J.T. Cabral, and J.R. Durrant: Toward improved lifetimes of organic solar cells under thermal stress: Substrate-dependent morphological stability of PCDTBT:PCBM films and devices. Sci. Rep. 5, 15149 (2015).

[272] E. Voroshazi, B. Verreet, A. Buri, R. Mueller, D. Di Nuzzo, and P. Heremans: Influence of cathode oxidation via the hole extraction layer in polymer:fullerene solar cells. Org. Electron. 12, 736– 744 (2011).

[273] M. Salvador, N. Gasparini, J.D. Perea, S.H. Paleti, A. Distler, L.N. Inasaridze, P.A. Troshin, L. Luer, H-J. Egelhaaf, and C. Brabec: Suppressing photooxidation of conjugated polymers and their blends with fullerenes through nickel chelates. Energy Environ. Sci. 10, 2005–2016 (2017).

[274] V. Turkovic, S. Engmann, N. Tsierkezos, H. Hoppe, M. Madsen, H-G. Rubahn, U. Ritter, and G. Gobsch: Long-term stabilization of organic solar cells using hydroperoxide decomposers as additives. Appl. Phys. A 122, 1–6 (2016).

[275] V. Turkovic, S. Engmann, N. Tsierkezos, H. Hoppe, U. Ritter, and G. Gobsch: Long-term stabilization of organic solar cells using hindered phenols as additives. ACS Appl. Mater. Interfaces 6, 18525–18537 (2014).

[276] V. Turkovic, S. Engmann, N.G. Tsierkezos, H. Hoppe, M. Madsen, H.G. Rubahn, U. Ritter, and G. Gobsch: Long-term stabilization of organic solar cells using UV absorbers. J. Phys. D: Appl. Phys. 49, 125604 (2016).